AIC
Advances in Industrial Control

Ship Motion Control

COURSE KEEPING AND ROLL STABILISATION USING RUDDER AND FINS

Tristan Perez

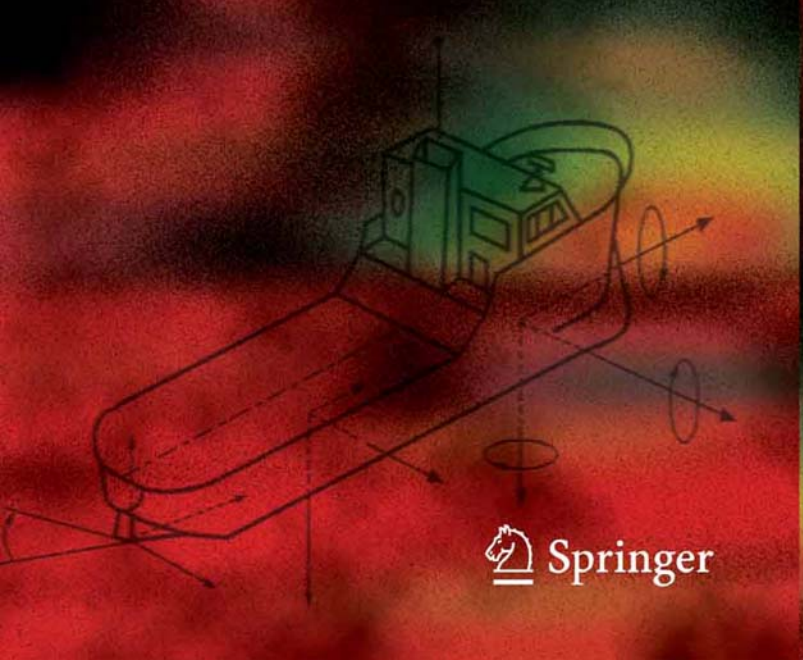

Springer

Advances in Industrial Control

Other titles published in this series:

Data-driven Techniques for Fault Detection and Diagnosis in Chemical Processes
Evan L. Russell, Leo H. Chiang and Richard D. Braatz

Nonlinear Identification and Control
Guoping Liu

Digital Controller Implementation and Fragility
Robert S.H. Istepanian and James F. Whidborne (Eds.)

Optimisation of Industrial Processes at Supervisory Level
Doris Sáez, Aldo Cipriano and Andrzej W. Ordys

Applied Predictive Control
Huang Sunan, Tan Kok Kiong and Lee Tong Heng

Hard Disk Drive Servo Systems
Ben M. Chen, Tong H. Lee and Venkatakrishnan Venkataramanan

Robust Control of Diesel Ship Propulsion
Nikolaos Xiros

Hydraulic Servo-systems
Mohieddine Jelali and Andreas Kroll

Model-based Fault Diagnosis in Dynamic Systems Using Identification Techniques
Silvio Simani, Cesare Fantuzzi and Ron J. Patton

Strategies for Feedback Linearisation
Freddy Garces, Victor M. Becerra, Chandrasekhar Kambhampati and Kevin Warwick

Robust Autonomous Guidance
Alberto Isidori, Lorenzo Marconi and Andrea Serrani

Dynamic Modelling of Gas Turbines
Gennady G. Kulikov and Haydn A. Thompson (Eds.)

Control of Fuel Cell Power Systems
Jay T. Pukrushpan, Anna G. Stefanopoulou and Huei Peng

Fuzzy Logic, Identification and Predictive Control
Jairo Espinosa, Joos Vandewalle and Vincent Wertz

Optimal Real-time Control of Sewer Networks
Magdalene Marinaki and Markos Papageorgiou

Process Modelling for Control
Benoît Codrons

Computational Intelligence in Time Series Forecasting
Ajoy K. Palit and Dobrivoje Popovic

Modelling and Control of mini-Flying Machines
Pedro Castillo, Rogelio Lozano and Alejandro Dzul

Manufacturing Systems Control Design
Stjepan Bogdan, Frank L. Lewis and Zdenko Kovačić
Publication due September 2005

Tristan Perez

Ship Motion Control

Course Keeping and Roll Stabilisation Using Rudder and Fins

With 89 Figures

Springer

Tristan Perez, PhD
Centre for Ships and Ocean Structures (CeSOS),
Norwegian University of Science and Technology (NTNU),
Marine Technology Centre,
NO-7491, Trondheim, Norway

British Library Cataloguing in Publication Data
Perez, Tristan
Ship motion control : autopilots with rudder roll
stabilisation and combined rudder-fin stabilisers. -
(Advances in industrial control)
1. Motion control devices 2. Automatic pilot (Ships)
3. Steering-gear 4. Stability of ships
I. Title
623.8'63
ISBN-10: 1852339594

Library of Congress Control Number: 2005924305

Advances in Industrial Control series ISSN 1430-9491
ISBN-10: 1-85233-959-4
ISBN-13: 978-1-85233-959-3
Springer Science+Business Media
springeronline.com

Typesetting: Electronic text files prepared by author
Production: LE-TEX Jelonek, Schmidt & Vöckler GbR, Leipzig, Germany
Printed in Germany
69/3141-543210 Printed on acid-free paper SPIN 11316978

Advances in Industrial Control

Professor Emeritus O.P. Malik
Department of Electrical and Computer Engineering
University of Calgary
2500, University Drive, NW
Calgary
Alberta
T2N 1N4
Canada

Professor K.-F. Man
Electronic Engineering Department
City University of Hong Kong
Tat Chee Avenue
Kowloon
Hong Kong

Professor G. Olsson
Department of Industrial Electrical Engineering and Automation
Lund Institute of Technology
Box 118
S-221 00 Lund
Sweden

Professor A. Ray
Pennsylvania State University
Department of Mechanical Engineering
0329 Reber Building
University Park
PA 16802
USA

Professor D.E. Seborg
Chemical Engineering
3335 Engineering II
University of California Santa Barbara
Santa Barbara
CA 93106
USA

Doctor I. Yamamoto
Technical Headquarters
Nagasaki Research & Development Center
Mitsubishi Heavy Industries Ltd
5-717-1, Fukahori-Machi
Nagasaki 851-0392
Japan

To Professors Graham Goodwin and Mogens Blanke,

who guided me unfailingly during my first steps into research.

Series Editors' Foreword

The series *Advances in Industrial Control* aims to report and encourage technology transfer in control engineering. The rapid development of control technology has an impact on all areas of the control discipline. New theory, new controllers, actuators, sensors, new industrial processes, computer methods, new applications, new philosophies…, new challenges. Much of this development work resides in industrial reports, feasibility study papers and the reports of advanced collaborative projects. The series offers an opportunity for researchers to present an extended exposition of such new work in all aspects of industrial control for wider and rapid dissemination.

In marine control systems, it is the demand for better motion control performance across a wide range of operational situations that has motivated researchers to the investigation and, in some cases, field sea trialling of new advanced control schemes. Marine operations such as pipe-laying, drilling operations, cargo transportation, passenger transportation, marine airstrips, helicopter platforms and car-ferry operations may each require specialist vessels but within this variety is a small set of marine control problems. It is the generic set of marine problems including course-keeping, roll-stabilisation, path-following, vertical motion control, station-keeping and dynamic positioning that taxes the ingenuity of the marine control engineer. Ingenuity and inspiration are required because the marine vessel set-up usually comprises only a few actuators – rudders, fins and, maybe, thrusters, to accomplish a primary objective like course-keeping – to travel from A to B – and possible secondary objectives like reduction in wave-induced roll so that passengers have a pleasant ride – good levels of passenger comfort. An additional problem with the available actuators is that they have the non-linear characteristic of saturation. Rudders and fins usually have both a maximum rate of travel, and a maximum angular range. Similarly, thrusters will have maximum power outputs as well as effective angular range limits. Consequently, marine control system problems are invariable constrained actuator control problems.

Tristan Perez's *Ship Motion Control* is a comprehensive contribution to the marine control literature and to the *Advances in Industrial Control* monograph series. The author has assimilated the past thirty-years' work of marine control

engineers into a single volume whilst concentrating on two important research control design problems:

- autopilots with rudder-roll stabilization and
- fin and combined rudder-fin stabilization.

He has been guided by some of the leading marine control academics, in particular Mogens Blanke and Thor Fossen; indeed Chapters 3 and 4 on kinematics and kinetics of ship motion are jointly authored with Professor Fossen. There are some 240 cited references – an invaluable resource for interested readers.

The volume is likely to appeal to a wide range of readers who will each be able to extract something different from the various parts of the monograph. Part I has some four chapters on the modelling fundamentals including kinematics, dynamics and actuators. Part II is a very useful survey of the ship roll stabilization problem and how ship roll performance is measured and assessed. This clearly motivates the human necessity for roll-reduction and roll stabilization. Parts III and IV move on to the control systems aspects of the various stabilization designs. Valuable material here includes a study of system performance limitations as caused by the presence of non-minimum phase characteristics and actuator saturation. Chapter 10 has an interesting historical review of these marine control problems stretching back some thirty-years into the 1970s. Given the constrained nature of marine actuators it is perhaps not surprising that the solutions proposed in this volume, presented in Chapter 12 and 13, are based on the Model Predictive Control paradigm. Appendix B which closes the volume is a very useful item, being a fully documented benchmark model for a naval vessel.

The *Advances in Industrial Control* monograph series has always tried to include volumes which chart the progress of advanced systems techniques as applied to marine control problems. This volume by Dr. Perez continues our tradition and makes a valuable contribution to the monograph series.

M.J. Grimble and M.A. Johnson
Industrial Control Centre
Glasgow, Scotland, U.K.

Preface

Motion control systems have a significant impact on the performance of ships and marine structures allowing them to perform tasks in severe sea states and during long periods of time. Ships are designed to operate with adequate reliability and economy, and in order to achieve this, it is essential to control the motion. For each type of ship and operation performed (transit, landing a helicopter, fishing, deploying and recovering loads, *etc.*), there are not only desired motion settings, but also limits on the acceptable (undesired) motion induced by the environment. The task of a ship motion control system is therefore to act on the ship so it follows the desired motion as closely as possible.

This book provides an introduction to the field of ship motion control by studying the control system designs for course-keeping autopilots with rudder roll stabilisation and integrated rudder-fin roll stabilisation. These particular designs provide a good overview of the difficulties encountered by designers of ship motion control systems and, therefore, serve well as an example driven introduction to the field.

The idea of combining the control design of autopilots with that of fin roll stabilisers, and the idea of using rudder-induced roll motion as a sole source of roll stabilisation seems to have emerged in the late 1960s. Since that time, these control designs have been the subject of continuous and ongoing research. This ongoing interest is a consequence of the significant bearing that the control strategy has on the performance and the issues associated with control system design. The challenges of these designs lie in devising a control strategy to address the following issues: underactuation, disturbance rejection with a non-minimum phase system, input and output constraints, model uncertainty, and large unmeasured stochastic disturbances. To date, the majority of the work reported in the literature has focused strongly on some of the design issues whereas the remaining issues have been addressed using *ad hoc* approaches. This has provided an additional motivation for revisiting these control designs and looking at the benefits of applying a contemporary

design framework, which can potentially address the majority of the design issues.

Intended Audience

The book has been written for students, researchers and practitioners of both control engineering and marine technology. Because of the mixed intended audience, much effort has been put into balancing the level of the presentation of topics of control and marine technology. Nevertheless, the reader is assumed to have some background knowledge in linear systems and state-space models, as covered in standard undergraduate control courses.

How Does the Book Fit in with the Related Literature?

With respect to the pioneering books on marine control systems by Prof. Thor I. Fossen [66, 67], this book provides a deeper coverage of hydrodynamic aspects related to control, wave-induced motion modelling and roll stabilisation. In addition, it addresses the fundamental issues of constrained control system design and performance-limitation analysis. Therefore, this book complements [66, 67]. This book also includes extensive references to the literature of ship roll stabilisation of the last 30 years with, plus a complete benchmark example vessel with both manoeuvring and seakeeping model parameters.

Numerical Simulations and Software Support

Throughout the book numerical simulations are used to illustrate the main concepts and results. These simulations have been performed by the author using the *Marine GNC Toolbox*, which is part of the *Marine System Simulator (MSS)* developed at NTNU. This is a Matlab®/Simulink®-based toolbox specially developed for rapid prototyping and evaluation of marine control systems. For further details and free-download versions see `http://www.cesos.ntnu.no/mss`

Book Overview

The key ingredients for a successful control system design are

- A mathematical model of the system to be controlled,
- Understanding of how performance will be assessed,
- Knowledge of fundamental limitations that may prevent any design achieving the desired performance.

The book is thus organised in four parts; the first three parts deal with the above ingredients, and the fourth addresses control system design:

Part I—ship modelling for control. This part introduces the models used to describe environmental disturbances and ship dynamics for control system design. Chapter 2 introduces concepts of related to modelling and simulation of ocean waves. It discusses the principal characteristics of waves relevant to the ship motion control system design and presents different modelling and simulation techniques. The modelling of a marine vehicle is then considered in three parts. Chapter 3 describes the geometrical aspects of ship motion (kinematics): variables, reference frames and transformations of variables. Chapter 4 presents the equations of motion (kinetics); it discusses how these equations are formulated in different theories of ship motion study (manoeuvring and seakeeping), and how the different models are linked to obtain both comprehensive models for control testing and simplified models for control system design. This chapter introduces a novel state-space model for manoeuvring in a seaway, which is believed to be the basis for a new generation of model-based ship motion control systems. Simulation aspects of ship motion are also discussed. Chapter 5 reviews the characteristics and models of actuators: lifting surfaces and the forces and moments they generate. This includes rudders, fins and their associated machinery.

Part II—introduction to ship roll stabilisation. Chapter 6 provides an overview of the roll stabilistion techniques commonly used, and discusses the advantages and disadvantages of each technique. Chapter 7 reviews the methods commonly employed in the marine environment to assess the motion performance of the ship. These methods provide a basis for obtaining control system specifications in agreement with performance assessment methods.

Part III—performance limitations in feedback control with application to ship roll stabilisers. Using the models introduced in Part I, this part addresses the fundamental issue of performance limitations for the particular problems of rudder and fin roll stabilisation. Chapter 8 reviews the fundamental performance limitations of the closed-loop system due to the dynamic characteristics of the ship. A study quantifying the limitations due to the non-minimum phase dynamics and underactuation characteristics of the system is presented. Chapter 9 incorporates the limitations imposed by the limited authority of the actuators into the study and discusses the role of the different limiting factors under different sailing conditions. The material presented in this part contributes to a deeper understanding of the main design issues and provides a method to estimate a benchmark performance prior to the design.

Part IV—control system design for autopilot with RRS and fin stabilisers. Chapter 10 presents a comprehensive review of the previous work on

control of rudder and fin stabilisers. Chapter 11 provides an introduction to constrained control system design, with emphasis on techniques based on optimization; in particular model predictive control. Chapter 12 discusses the constituting parts of contemporary course-keeping autopilots (guidance system, wave filters and controller), and concentrates on control design. Chapter 13 addresses the control system design for fin-based roll stabilisers. It discusses a non-linear phenomena due unsteady hydrodynamics, which appears to affect the performance of stabilisers in moderate to rough sea states. A control strategy based on constrained control is then proposed to address the design issues. Finally, the problem combined rudder-fin stabilisation is discussed.

Acknowledgements

I am obliged to Professors Graham Goodwin (from The University of Newcastle, Australia) and Mogens Blanke (from the Danish Technical University), to whom this book is dedicated for their guidance and support. I believe their approach to control system design is very much reflected in this book.

I owe a great deal to Professors Asgeir J. Sørensen, Thor I. Fossen and Odd Faltinsen (all from the Norwegian University of Science and Technology — NTNU) for our discussions about ship dynamics and hydrodynamics, and also for providing me with such an encouraging working environment. A special thank you goes to Prof. Anna Stefanoupoulou (from the University of Michigan, USA). Her comments and suggestions about my previous work encouraged me to pursue the publication of this book.

I am grateful indeed to all my former colleagues at the Department of Electrical and Computer Engineering of The University of Newcastle in Australia, where this work began. I owe a great deal to Martin Williams and Adam Williams (from ADI-Limited Australia) for the opportunity to work in seakeeping. I would also like to thank Bruce McNeice and Martin Grimm (from Directorate of Naval Platform System Engineering (DNPSE) Department of Defence, Australia) for discussions about my work. Many thanks also to my colleagues at NTNU for proofreading and commenting on early drafts: Dr. Fabio Celani, Ingo Drummen, Anne Marthine Rustad, Øyvind Smogeli, Kari Unneland and Anders S. Wroldsen. Special thank you go to Oliver Jackson from Springer London and to Petra Möws from LE-TeX, Jelonek, Schmidt & Voeckler GbR, Germany for all the support and editorial work.

The work presented in this book started at the Department of Electrical Engineering and Computer Science, The University of Newcastle, Australia, and continued and is ongoing at Centre for Ships and Ocean Structures (CeSOS) at NTNU. Formal acknowledgements go to The Norwegian Research Council—main sponsor of CeSOS; to ADI-Limited Australia for allowing me to use part of the data from one of their vessel designs; and to MARINTEK AS, Trondheim for allowing me to use ShipX-VERES to obtain the hydrodynamic data for the benchmark example.

Finally, a big thank you to my families in both Argentina and Australia for all their love and support. And most importantly, my heartfelt thanks, love, and deepest appreciation go to my lovely wife Jae. Without Jae's love, patience and constant support, it would have been impossible to finish this work.

Trondheim, Norway *Tristan Perez*
April 2005

Contents

1

Introduction to Ship Motion Control

Marine vehicles are designed to operate with adequate reliability and economy, and in order to accomplish this, it is essential to control the motion of the ship. This control task consists in making the ship to follow, as closely as possible, a *desired trajectory*, which can be defined in terms of the ship's position, velocity and acceleration. In most ship operational conditions, the desired trajectory is slowly varying (low-frequency motion) compared to the motion induced by the waves (wave-frequency motion). This results in motion control problems with different objectives:

- Control only the low-frequency motion,
- Control only the wave-frequency motion (motion damping),
- Control both.

Course keeping and dynamic positioning are examples of ship motion control problems in which it is desired to control only the low-frequency motion the ship. Roll stabilisation of surface ships and heave compensation for offshore structures are examples in which it is desired to control the wave-frequency motion. The design of autopilots for simultaneous course keeping and roll stabilisation using only the rudder is an example in which the control objective requires controlling both low-frequency motion (for the course) and the wave-frequency motion (for roll).

For each type of ship and operation performed, there are settings for the desired trajectory, and also limits on the acceptable wave-induced motion under which the operation can be performed. These limits can be imposed on either absolute or relative motions: displacements, velocities and accelerations and also on responses derived from motions, *e.g.* motion sickness incidence and motion induced interruptions. For example, pipe-laying vessels, drilling vessels, air craft carriers and other navy ships handling weapons all require small wave-induced displacements to be able to perform their tasks or missions. Wave-induced accelerations, on the other hand, affect the performance of the crew, and can also produce cargo damage. Long exposures to vertical accelerations, for instance, produce seasickness, which affects crew effectiveness and

passenger comfort. Large lateral accelerations can produce cargo damage and prevent the crew from working on deck. In less extreme cases, lateral accelerations increase the amount of time required by the crew to accomplish their tasks.

This chapter provides a brief introduction to the fundamental problem of ship motion control and the issues associated with control system design. Issues related to control system implementation that may affect the design are also discussed.

1.1 The Fundamental Problem of Ship Motion Control

Goodwin *et al.*[89], give the following general definition for the fundamental problem of control:

Definition 1.1 (Goodwin *et al.*[89]). *The central problem in control is to find a feasible way to act on a given system so it adheres, as closely as possible, to some desired behaviour. Furthermore, this approximate behavior should be achieved in the face of uncertainty of the system to be controlled and in the presence of uncontrollable external disturbances acting on the system.* ○○○

The above definition reveals issues that commonly affect the control system design:

- **Feasibility**. The proposed solution must be technically, economically and environmentally viable. This means that the control design often will be subject to constraints. These constraints often lead to conflicting control objectives.

- **Action**. Acting on the system requires energy, and the amount of energy available to implement the control action may be limited. Therefore, this may also introduce constraints on the design.

- **Desired behaviour**. The behaviour of the system must be properly specified. This may influence decisions about the tools from control theory used for the design.

- **Uncertainty**. Assuming a complete characterization of the behaviour of the system is highly unrealistic, and some magnitudes of interest may not be available for taking measurements. This means that the design must perform well in the presence of uncertainty; understanding this is crucial because feedback control can lead to catastrophic results if uncertainty is not properly accounted for in the design.

- **Disturbances**. Disturbances, in general, cannot be known *a priori*. This introduces further uncertainty into the design.

The fundamental problem of ship motion control can then be defined in terms of Definition 1.1 by replacing the word *system* by *ship*; and specifying the *desired behaviour* in terms of a *desired trajectory*, which may also include *reducing wave-induced motion*.

The solution to a ship motion control problem depends on the requirements of the particular operations performed by the ship, *e.g.* transit, dynamic positioning, assisted position mooring, diving (for underwater vehicles), and it is based on the interconnection of three systems as shown in Figure 1.1. These systems perform the following functions:

- **Guidance system**. This system generates the desired settings: a reference trajectory (position, velocity and acceleration). A guidance system usually has the functions shown in Figure 1.1. The waypoint generator, establish the desired wayponits according to information regarding the mission, operator decision, weather, fleet operations, amount of power available *etc.* The waypoint management system updates the active waypoint based on the current position of the ship. The reference computing algorithms generate a smooth feasible trajectory based on a reference model, the ship actual position, amount of power available, and the active way point.
- **Control system**. This system processes information to infer the state of the ship and to generate an appropriate command for the actuators so as to reduce the difference between the actual and desired trajectories. The controller can have different operation modes, and depending on the type of operation performed by the ship, the controller can combine (or be switched into) the different modes: autopilot mode, dynamic positioning (DP) mode, roll and pitch stabilisation mode, *etc.*
  For some ships and operations, it can happen that the desired control action can be delivered in several ways due to over-actuation, *i.e.* different combinations of actuator demand can yield the same control action. In these cases, the control system must also solve the so-called control allocation problem based on some optimisation criteria.
- **Navigation system**. This system provides reliable measurements. The basic functions of this system are to collect information from the many sensors on the ship (GPS, speed log, compass, gyros, radar, accelerometers *etc.*), perform signal quality checking, and transform the measurements to a common coordinate reference frame used by the control and guidance systems.

Although not explicitly indicated in Figure 1.1, the guidance, navigation, and control systems must also have mechanisms for fault detection, and redundancy. This allows reconfiguring the control so as to minimise the impact of faults on safety and performance.

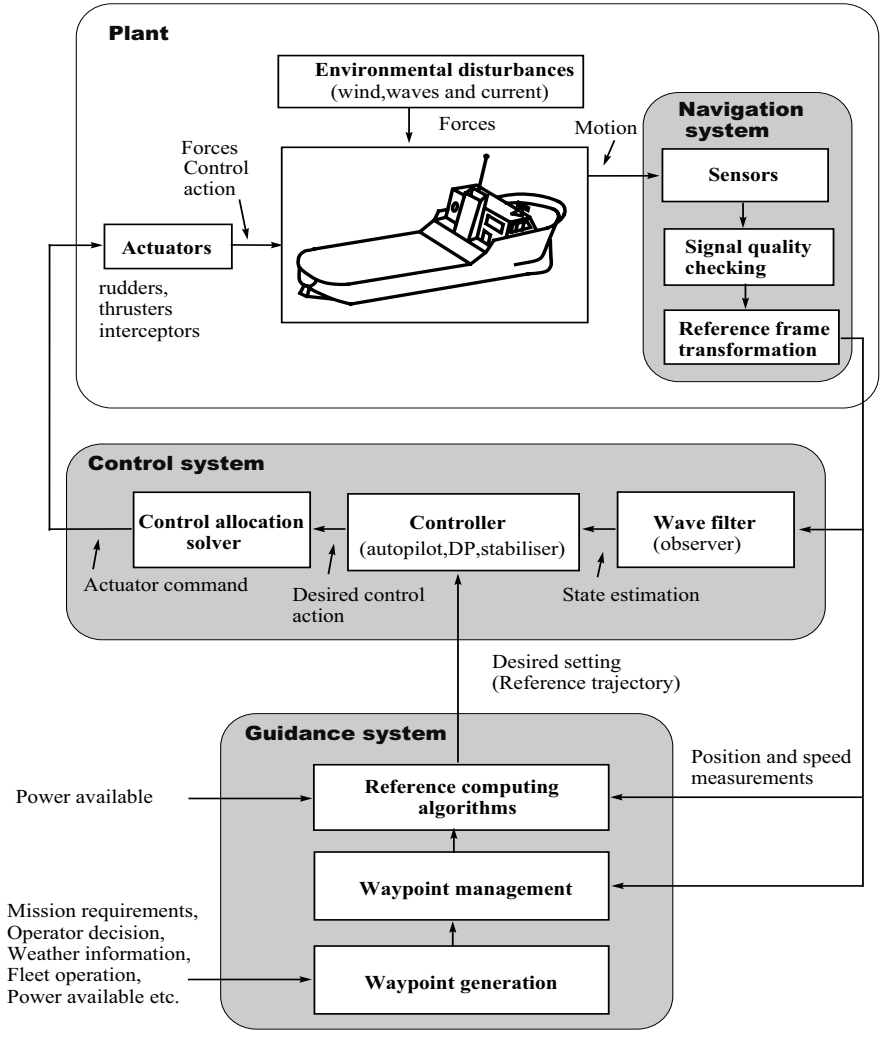

Fig. 1.1. Basic elements of a ship motion control system

1.2 Ship Motion Control Problems and Control Designs Addressed in this Book

In this book, we will focus on design of the control system part of the scheme shown in Figure 1.1. In particular, we will limit our discussion to the ship motion control problems of *course keeping and roll reduction*, and address the design of the following type of controllers:

- Autopilots with rudder roll stabilisation,
- Fin stabilisers,
- Integrated control of rudder and fin stabilisers.

The topics of guidance and navigation of marine systems will not be discussed here, for these have been comprehensively covered in [67].

The autopilot is a controller that regulates the heading of the ship to a desired value provided by the guidance system—see Figure 1.1 (see Section 12.1 for a further review of the functions of contemporary autopilots). Most surface ships use rudders to correct the heading of the ship, and therefore, in these cases, the autopilot generates a rudder angle command.

Apart from affecting the heading, the rudder can induce significant roll motion in some ships, and this characteristic may be exploited to reduce the undesired roll motion induced by the waves. In this case, the autopilot can incorporate a *rudder roll stabilisation* (RRS) function, and the control objectives then become to regulate the heading to a desired value and to reduce the roll angle and roll accelerations as much as possible.

Regarding roll reduction, some vessels can be equipped with fin stabilisers. In general, fin stabilisers only use information of roll motion, and are controlled independently from the rudder. However, due to the coupling between roll and heading, it has long been suggested and recognised (see, for example, [43]) that an integrated control system design for commanding fins and rudder can offer a performance better than that of two independent designs.

The design of autopilots with rudder roll stabilisation and the integrated fin-rudder control have been the subject of ongoing research interest for over 30 years. This is a consequence of the significant bearing the control strategy has on ship performance and also the complexity associated with the control design. Therefore, these designs provide a comprehensive overview of the main difficulties associated with ship motion control; and thus, a good introduction to the topic.

1.3 Mathematical Models for Control

A successful control system design and further description of the design problem requires knowledge of the system to be controlled. This knowledge is captured by a *Mathematical Model (MM)*, *i.e.* mathematical expressions that describe the relationship amongst the magnitudes that characterize the system [156].

In control design, mathematical models allow one to design a controller, to perform numerical simulations of different scenarios, and to obtain a preliminary assessment of the impact that the design can have on the performance of the system. These numerical simulations often preclude any experimental assessment of the design—this is often the case for marine systems due to the high cost of performing both scale-model experiments and full-scale sea trials.

In this book, we use mathematical models to describe the motion of a ship due to the action of the environment and the action of the control system.

When building and using mathematical models, one should bear in mind that the level of complexity of the model and more importantly the assumptions under which the model was developed match the purpose of the model. For control purposes, we usually deal with two types of mathematical models [89, 211]:

- **Control-design models (CD-models)**. These are models used for control system design purposes and analysis of some properties of the system (stability, fundamental limitations, robustness, *etc.*). Control design models capture the essential behaviour of the system. These models are often state-space models (first-order vector ordinary differential equations), or in the case of linear systems they could be transfer functions (Laplace transform domain)—see Section 1.4.

- **High-fidelity models (HFi-models)**. The purpose of these models is to describe the behaviour of the system as accurately as possible. These models are used to test controllers on a more sophisticated model than the one used during the design; but these models can also be used to calibrate the CD-models. In practice, control design can be an iterative process: one always starts with the simplest CD-model as possible so to avoid having a complex controller, and then test the controller with the HFi-models. If the performance is not satisfactory, then one may need to upgrade the CD-models and redesign the controller. Thus, the HFi-models can be used to both assess the quality of the controller and the quality of the CD-models. Oftentimes, HFi-models incorporate features that have a direct bearing on the system behaviour, but render the methods of control theory not applicable [89].

Both these types of models will be used throughout the book to describe the motion of ships.

1.4 State-space and Input-output Models Revisited

Figure 1.2 shows a typical mathematical model representation of the input-output characteristics of the system, in which the following variables are involved:

- $\mathbf{u}(t) \in \mathbb{R}^m$ is the input or manipulated variable—control command.
- $\mathbf{y}_{\mathrm{c}}(t) \in \mathbb{R}^k$ is the controlled output or variable of interest.
- $\mathbf{y}(t) \in \mathbb{R}^p$ is the measured output.
- $\mathbf{w}(t) \in \mathbb{R}^l$ is the disturbance.
- $\mathbf{n}(t) \in \mathbb{R}^p$ is the measurement noise (usually considered additive).
- $\mathbf{h}\langle \circ, \circ \rangle : \mathbb{R}^m \times \mathbb{R}^l \to \mathbb{R}^p$ is an operator (typically an ordinary differential equation).

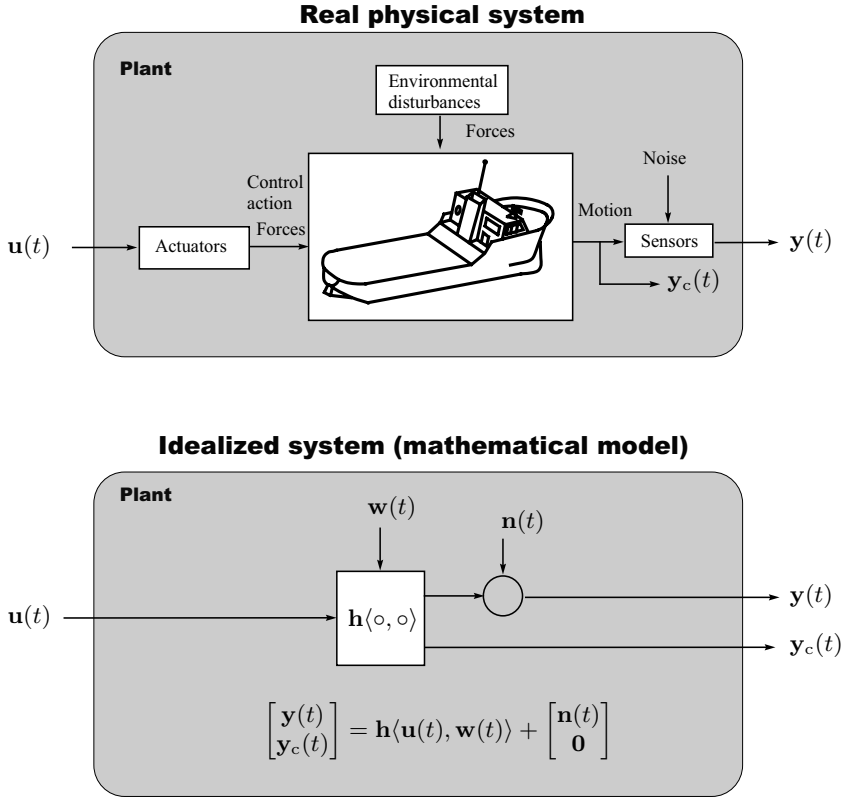

Fig. 1.2. Mathematical models

The controlled output $\mathbf{y}_c(t)$ is the variable for which we would like to specify a behavior (keep it constant or follow a reference)—See Definition 1.1. Oftentimes, the controlled output coincides with the measured output, $\mathbf{y}_c(t) = \mathbf{y}(t)$, but this may not be case in general—indeed, in some cases, we are interested in controlling the behaviour of variables that we do not measure. For example, in the case of ship roll stabilisation, roll angle is the measured output, but depending on the mission performed by the ship, roll acceleration can also be of interest, which is usually not measured.

The manipulated variable $\mathbf{u}(t)$, is related to the action by which the behaviour of the system is modified, *e.g.* a rudder angle, demand of thrust of a thruster, the angle of attack of a fin stabiliser. Apart from the action related to the manipulated variable, there are interactions between the system and its surrounding environment, over which we will have no control, that act on the system and modify its behavior, *e.g.* in the case of a ship these could be the actions of waves, wind and current. These uncontrollable actions are called

disturbances and may be measured or not. In the model shown in Figure 1.2, the disturbances are represented by the disturbance vector $\mathbf{w}(t)$. These magnitudes are often non-deterministic; and therefore, a stochastic description can be used in terms of their power spectral densities and probability density functions.

Another type of disturbance present in control systems is a noise that represents the uncertainty introduced by the limited accuracy of the sensors used to perform the measurements. This is represented by the measurement noise vector $\mathbf{n}(t)$ in Figure 1.2, which is also described in terms of its stochastic characteristics. For example, it usually assumed that the measurement noise is Gaussian and uncorrelated, while the disturbance vector is often assumed Gaussian with a given narrow-banded power spectral density. In some cases, however, the stochastic characteristics of the disturbances may be difficult to establish; then disturbances can be described in terms of set membership, *i.e.* by describing the set in which they take values–this is also referred to as unknown but bounded description [24].

1.4.1 State-Space Models

For control system analysis and design, the operator $\mathbf{h}\langle\circ,\circ\rangle$ in Figure 1.2 usually takes the following general form called a *state-space* representation:

$$\begin{aligned}\dot{\mathbf{x}}(t) &= \mathbf{f}(t,\mathbf{x}(t),\mathbf{u}(t),\mathbf{w}(t))\\ \mathbf{y}_{\mathrm{c}}(t) &= \mathbf{g}_{\mathrm{c}}(t,\mathbf{x}(t),\mathbf{u}(t))\\ \mathbf{y}(t) &= \mathbf{g}_{y}(t,\mathbf{x}(t),\mathbf{u}(t))+\mathbf{n}(t),\end{aligned} \tag{1.1}$$

where $\mathbf{x}(t)\in\mathbb{R}^n$ is the so-called *state vector*. This is a vector of internal variables of the system, called the *state variables*. If the values of the state variables and inputs are known at a particular time instant, then the values of all other variables of interest in the system can be found via static relationships[1] of state and input variables at that same time instant [156].

Example 1 *For ship motion control design problems, the motion of the ship can be conceptually described as a mass-spring-damping system. Let us consider in this example the basic mass-spring-damping system in one degree of freedom.*

Let the offset position of the mass with respect to its equilibrium position be $z(t)$ and consider a control force $F_c(t)$ used to position the mass and an external disturbance force $F_d(t)$ also acting on the system. Then, Newton's second law gives the following ordinary differential equation to describe the motion of the system:

$$M\ddot{z}+D\,\dot{z}(t)+Kz(t)=F_c(t)+F_d(t), \tag{1.2}$$

[1]Static relationships depend on the current value of the variables, but not on past values.

where M is the mass, D is the damping coefficient and K the stiffness characteristic of the spring. Now we can define the auxiliary variables

$$\begin{aligned} x_1(t) &\triangleq z(t) \\ x_2(t) &\triangleq \dot{z}(t). \end{aligned} \tag{1.3}$$

From these definitions and (1.2)*, we can obtain a state-space representation:*

$$\begin{aligned} \dot{x}_1(t) &= x_2(t) \\ \dot{x}_2(t) &= M^{-1}[-Kx_1(t) - Dx_2(t) + F_c(t) + F_d(t)]. \end{aligned} \tag{1.4}$$

If we are interested in the velocity of the mass, and we measure it, then, we can express the system in the form of (1.1) *by considering*

$$\begin{aligned} &\mathbf{x}(t) \triangleq \begin{bmatrix} x_1(t) \\ x_2(t) \end{bmatrix}, \quad \mathbf{u}(t) \triangleq F_c(t), \quad \mathbf{w}(t) \triangleq F_d(t) \\ &\mathbf{y}(t) = x_2(t) + n(t), \end{aligned} \tag{1.5}$$

where $n(t)$ represents the uncertainty introduced by the velocity measurement device.

Notice that if we know $x_1(t)$, $x_2(t)$, $F_c(t)$ and $F_d(t)$ at a particular time instant, we can then calculate any other variable of interest of the system via a static relationship: force of the spring, force of the damper, deformation of the spring, etc. ○ ○ ○

The choice of state variables is not unique. Indeed, following with the example above, we could have chosen as state variables the momentum of the mass ($p = M\dot{z}$) and the force of the spring ($F_s = Kz$), and obtain another state-space representation.

If the value of all the components of the state vector is *necessary and sufficient* to determine the value of any variable of the system at a time instant (together with the knowledge of the input at that instant), the state vector is said to be a *minimal state vector* [156]. The number of components of any minimal state vector is the *order of the system*, which is a unique characteristic of the system. For mechanical systems, the order is twice the number of degrees of freedom. Typically, when we talk about the order of a system or model[2] in control applications, we refer to the number of components of any minimal state vector that can be used to describe the system.

When the system is linear the model (1.1) takes the following form

$$\begin{aligned} \dot{\mathbf{x}}(t) &= \mathbf{A}(t)\mathbf{x}(t) + \mathbf{B}(t)\mathbf{u}(t) + \mathbf{E}(t)\mathbf{w}(t) \\ \mathbf{y}(t) &= \mathbf{C}(t)\mathbf{x}(t) + \mathbf{D}(t)\mathbf{u}(t) + \mathbf{n}(t), \end{aligned} \tag{1.6}$$

[2]Once a mathematical model of the real physical system has been obtained, the mathematical model becomes the subject of study for control design and analysis purposes. Hence, the words model and system are often considered synonyms.

where $\mathbf{A}(t)$, $\mathbf{B}(t)$, $\mathbf{C}(t)$, $\mathbf{D}(t)$, and $\mathbf{E}(t)$ are matrices of appropriate dimensions. For ease of exposition and without much loss of generality, it will be assumed in the rest of this chapter that the measured and controlled output variables are the same, *i.e.* $\mathbf{y}(t) = \mathbf{y}_c(t)$.

When the matrices in (1.6) are constant over time, the model or system is said to be a *Linear Time Invariant (LTI)* model or system.

Example 2 *Following with Example 1, in which the damping and the spring are linear, we can express the state-space model as*

$$\begin{aligned}\begin{bmatrix}\dot{x}_1(t)\\ \dot{x}_2(t)\end{bmatrix} &= \begin{bmatrix}0 & 1\\ -M^{-1}K & -M^{-1}D\end{bmatrix}\begin{bmatrix}x_1(t)\\ x_2(t)\end{bmatrix} + \begin{bmatrix}0\\ M^{-1}\end{bmatrix} F_c(t) + \begin{bmatrix}0\\ M^{-1}\end{bmatrix} F_d(t),\\ \mathbf{y}(t) &= \begin{bmatrix}0\ 1\end{bmatrix}\begin{bmatrix}x_1(t)\\ x_2(t)\end{bmatrix} + \begin{bmatrix}0\\ n(t)\end{bmatrix},\end{aligned} \tag{1.7}$$

with the obvious definitions for the matrices $\mathbf{A}$, $\mathbf{B}$, $\mathbf{C}$, $\mathbf{D}$ *and* $\mathbf{E}$. ∘ ∘ ∘

1.4.2 Laplace-Transform Models

For a LTI system, the application of Laplace Transform gives a zero initial condition input-output representation of the system. In this formulation, the Laplace transforms of the different variables are related as follows when the initial conditions are zero:

$$\mathbf{Y}(s) = \mathbf{H}(s)\mathbf{U}(s) + \mathbf{G}(s)\mathbf{W}(s) + \mathbf{N}(s), \tag{1.8}$$

where

$$\begin{aligned}\mathbf{U}(s) &= [\mathfrak{L}\{u_1(t)\}, ..., \mathfrak{L}\{u_m(t)\}]^{\mathrm{T}}\\ \mathbf{Y}(s) &= [\mathfrak{L}\{y_1(t)\}, ..., \mathfrak{L}\{y_p(t)\}]^{\mathrm{T}}\\ \mathbf{W}(s) &= [\mathfrak{L}\{w_1(t)\}, ..., \mathfrak{L}\{w_l(t)\}]^{\mathrm{T}}\\ \mathbf{N}(s) &= [\mathfrak{L}\{n_1(t)\}, ..., \mathfrak{L}\{n_p(t)\}]^{\mathrm{T}},\end{aligned}$$

with $\mathfrak{L}\{\cdot\}$ being the Laplace transform operator. The matricices $\mathbf{H}(s)$, $\mathbf{G}(s)$ are the so called *transfer function* matrices

$$\mathbf{H}(s) = \begin{bmatrix}H_{11}(s) & \cdots & H_{1m}(s)\\ \vdots & \dots & \vdots\\ H_{p1}(s) & \cdots & H_{pm}(s)\end{bmatrix} \quad \mathbf{G}(s) = \begin{bmatrix}G_{11}(s) & \cdots & G_{1l}(s)\\ \vdots & \dots & \vdots\\ G_{p1}(s) & \cdots & G_{pl}(s)\end{bmatrix}. \tag{1.9}$$

The transfer function matrices can be obtained from the state-space representation (1.6) with constant matrices as follows

$$\begin{aligned}\mathbf{H}(s) &= \mathbf{C}(s\mathbf{I}_{n\times n} - \mathbf{A})^{-1}\mathbf{B} + \mathbf{D}\\ \mathbf{G}(s) &= \mathbf{C}(s\mathbf{I}_{n\times n} - \mathbf{A})^{-1}\mathbf{E} + \mathbf{D},\end{aligned} \tag{1.10}$$

where $\mathbf{I}_{n\times n}$ is the identity matrix of order n.

Example 3 *Following with Example 1,*

$$\mathbf{Y}(s) = \underbrace{\frac{M^{-1}s}{s^2 + \frac{D}{M}s + \frac{K}{M}}}_{H(s)} \mathbf{U}(s) + \underbrace{\frac{M^{-1}s}{s^2 + \frac{D}{M}s + \frac{K}{M}}}_{G(s)} \mathbf{W}(s) + \mathbf{N}(s), \tag{1.11}$$

where $\mathbf{Y}(s) = \mathfrak{L}\{\dot{z}(t)\}$, $\mathbf{U}(s) = \mathfrak{L}\{F_c(t)\}$, $\mathbf{W}(s) = \mathfrak{L}\{F_d(t)\}$ *and* $\mathbf{N}(s) = \mathfrak{L}\{n(t)\}$. ○ ○ ○

One the most important properties of the transfer function description is that it allows one to look at the system from a frequency domain point of view. For example, let us consider only the inputs in (1.8) for simplicity, and assume that these are of the following form:

$$u_k(s) = a_k \cos(\omega_k t + \varepsilon_k), \quad k = 1, ..., m,$$

then if the system is asymptotically stable, the outputs will satisfy

$$y_j(t) = \sum_{k=1}^{m} a_k |H_{jk}(j\omega_k)| \cos[\omega_k t + \varepsilon_k + \arg H_{jk}(j\omega_k)], \quad j = 1, ..., p$$

in steady state, *i.e.* after the transient response extinguishes. With this information, one can design a controller based on frequency domain specifications.

Control theory provides a set of methods for analysis and design of control systems. These methods, however, are often applicable if the controlled system is described using either of the model representations reviewed in this section, *i.e.* state-space models and Laplace transform models. Therefore, one of the tasks of the control system designer is to develop such models or transform other type of models, *e.g.* HFi-models into the these forms. For further description of the models described in this section and their properties see, for example, [62, 89].

1.5 Computer-Controlled Systems

Nowadays, most control systems are implemented using computers, and the data transferred between sensors and the controller and between the controller and the actuators is done in digital form. Figure 1.3 represents a simplified version of a computer controlled system.

Using computers to implement control systems has many advantages over their analog counterparts (usually implemented with analog electronics). For example, in computer control systems, it is easy to upgrade the controller complexity by modifying the software that implements the control algorithm. We can also incorporate the features of fault detection, diagnosis, and modify the controller on-line to account for faults (fault tolerant control). The latter is of paramount importance in practice because it increases safety and reliability.

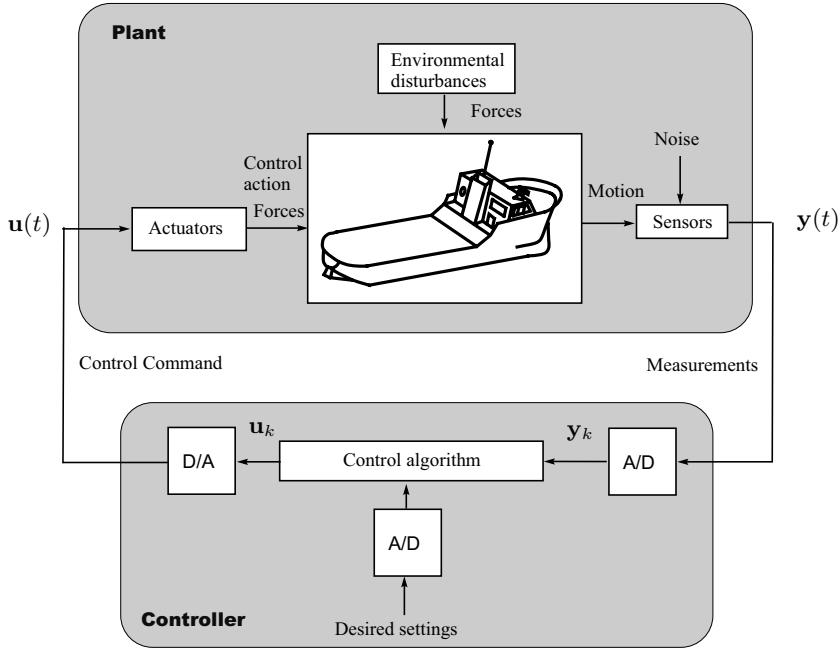

Fig. 1.3. Simplified computer-controlled system

From the control design perspective, one may perform the design in continuous time, and then implement a discrete-time approximation of the resulting controller. This works well when the complexity of the controller is low (and thus requiring short computation time) and all the communications between the controller and sensors and actuators allow a fast sampling rate. However, when this is not the case and the sampling period cannot be small due to economic or technical constraints, the digital nature of the controller can affect the performance of the closed-loop system. In these cases, it can be advantageous to consider the design from a discrete-time point of view *ab initio*.

The decision about considering a discrete-time design framework may not only be based on implementation issues, but also on modelling issues. Indeed, analytical mathematical models obtained from the laws of physics are usually continuous-time models. In many cases, however, such models may not be possible to obtain due to the high complexity of the systems we want to control. Alternatively, even when the structure of the model can be determined analytically, the end result would require the knowledge of parameters whose values are not easy to determine. In these cases, one can use experimental modeling to estimate the parameters or system identification to obtain a simplified model and its parameters from data collected during experiments. If we apply these methods, the model obtained is often a LTI discrete-time model:

$$\begin{aligned} \mathbf{x}_{k+1} &= \mathbf{\Phi}\,\mathbf{x}_k, +\mathbf{\Gamma}\,\mathbf{u}_k + \mathbf{\Gamma}_w\,\mathbf{w}_k \\ \mathbf{y}_k &= \mathbf{C}\,\mathbf{x}_k + \mathbf{D}\,\mathbf{u}_k + \mathbf{n}_k. \end{aligned} \tag{1.12}$$

where the index k denotes that the value of the variables is known at the time instant $t_k = t_0 + T_s\,k$, where T_s is the sampling period, and the index takes the values $k = 0, 1, 2, ...$

If we have access to a continuous LTI model, then there are different methods that we can use to convert it into a discrete-time model. A simple method (although not the one with the best numerical properties [89]) is to approximate the derivative in the state equation in a state space model by an increment:

$$\dot{\mathbf{x}} \approx \frac{\mathbf{x}(t+T_s) - \mathbf{x}(t)}{T_s}, \tag{1.13}$$

which leads to the Euler method for converting continuous to discrete-time systems:

$$\begin{aligned} \mathbf{x}_{k+1} &= (\mathbf{I}_{n\times n} + \mathbf{A}T_s)\,\mathbf{x}_k + T_s\,\mathbf{B}\,\mathbf{u}_k + T_s\,\mathbf{E}\,\mathbf{w}_k \\ \mathbf{y}_k &= \mathbf{C}\,\mathbf{x}_k + \mathbf{D}\,\mathbf{u}_k + \mathbf{n}_k, \end{aligned} \tag{1.14}$$

and hence,

$$\begin{aligned} \mathbf{\Phi} &\triangleq (\mathbf{I}_{n\times n} + \mathbf{A}T_s) \\ \mathbf{\Gamma} &\triangleq T_s\,\mathbf{B} \\ \mathbf{\Gamma}_w &\triangleq T_s\,\mathbf{E}. \end{aligned} \tag{1.15}$$

An alternative representation is obtained by using the zero-order hold method [9, 73, 89]:

$$\begin{aligned} \mathbf{\Phi} &\triangleq \exp(\mathbf{A}T_s) \\ \mathbf{\Gamma} &\triangleq \mathbf{A}^{-1}(\mathbf{\Phi} - \mathbf{I}_{n\times n})\mathbf{B} \\ \mathbf{\Gamma}_w &\triangleq \mathbf{A}^{-1}(\mathbf{\Phi} - \mathbf{I}_{n\times n})\mathbf{E}, \end{aligned} \tag{1.16}$$

which reverts to the Euler representation if the exponential is expressed as a series expansion and only the linear terms are considered.

In this book, we will use both continuous and discrete-time models in the forms presented above. The material presented in this chapter regarding models serves as a description of notation and model structures adopted in the book. Readers requiring a more thorough discussion of state-space models, discrete-time models and computer control systems are referred to [9, 73, 89].

1.6 The Road Ahead

The key ingredients for a successful ship motion control system design are

- A mathematical model of the ship,
- Understanding of how performance will be assessed,
- Knowledge of fundamental limitations, if any.

The rest of the book is therefore organised in four parts; the first three parts deal with the above ingredients, while the fourth part addresses control system design for

- Autopilots with rudder roll stabilisation,
- Fin and combined rudder-fin roll stabilisation.

Part I

Ship Modelling for Control

2

Environmental Disturbances

The undesirable motion of a ship in a seaway is induced by the action of environmental disturbances: waves, wind and current. For the particular ship motion control problem considered in this book (course keeping and roll stabilisation), ocean waves are the dominant environmental disturbance; and hence, the type of disturbances described in this chapter.

From the control system design perspective, the characterization of the disturbances acting on the ship is essential to design good performance ship motion controllers and to understand limitations that may prevent the design achieving the performance specifications. In this chapter, we review models and simulation techniques that characterize the elevation of the sea surface. This serves as a basis for the study of ship motion: response to wave excitation loads—which is covered in Chapter 4.

2.1 Basic Hydrodynamic Assumptions

The description of waves and the interaction between waves and floating objects requires some basic knowledge of fluid flow behaviour. This is the field of study of hydrodynamics. In this section, we review some the elementary concepts.

2.1.1 Fluid Flow and Continuity

To describe most fluid flow phenomena associated with the waves and the motion of ships in waves, we need to know the velocity of the fluid and the pressure at different locations. The velocity of the fluid at the location

$$\mathbf{x} = \begin{bmatrix} x_1, & x_2, & x_3 \end{bmatrix}^{\mathrm{T}} \tag{2.1}$$

is given by the *fluid flow velocity vector*:

$$\mathbf{v}(\mathbf{x}, t) = \begin{bmatrix} v_1(\mathbf{x}, t), & v_2(\mathbf{x}, t), & v_3(\mathbf{x}, t) \end{bmatrix}^{\mathrm{T}}. \tag{2.2}$$

This vector is described relative to the, so-called, hydrodynamic reference frame (h-frame) that has its origin in the mean free surface of the water with the vertical coordinate z taken positive upwards.

For the flow velocities involved in ship motion, the fluid can be considered *incompressible*, *i.e.* of constant density ρ. Under this assumption, the net volume rate at a volume V enclosed by a closed surface S is

$$\iint_S \mathbf{v} \cdot \mathbf{n}\, ds = \iiint_V \mathbf{div}(\mathbf{v})\, dV = 0, \tag{2.3}$$

where we have used the divergence theorem—see [3] for different identities derived from (2.3). Since (2.3) is valid for all the regions V in the fluid, then by assuming that $\nabla \cdot \mathbf{v}$ is continuous, we obtain

$$\mathbf{div}(\mathbf{v}) = \nabla \cdot \mathbf{v} = \frac{\partial v_1}{\partial x} + \frac{\partial v_2}{\partial y} + \frac{\partial v_3}{\partial z} = 0, \tag{2.4}$$

which is the *continuity equation* for incompressible flows.

2.1.2 Material Derivative

Let $f(x, y, z, t)$ be a scalar function and $\mathbf{f}(t, x, y, z)$ a vector function, which describe some properties of interest of the fluid; then,

$$\begin{aligned} \frac{df}{dt} &= \frac{\partial f}{\partial t} + \frac{\partial f}{\partial x}\frac{dx}{dt} + \frac{\partial f}{\partial y}\frac{dy}{dt} + \frac{\partial f}{\partial z}\frac{dz}{dt} \\ \frac{d\mathbf{f}}{dt} &= \frac{\partial \mathbf{f}}{\partial t} + \frac{\partial \mathbf{f}}{\partial x}\frac{dx}{dt} + \frac{\partial \mathbf{f}}{\partial y}\frac{dy}{dt} + \frac{\partial \mathbf{f}}{\partial z}\frac{dz}{dt}. \end{aligned} \tag{2.5}$$

If these are taken for the function $\mathbf{x}(t)$ s.t. $\dot{\mathbf{x}}(t) = \mathbf{v}(t)$, then we have a special notation, and the derivatives are called *material derivatives*:

$$\begin{aligned} \frac{Df}{Dt} &= \frac{\partial f}{\partial t} + \frac{\partial f}{\partial x}v_1 + \frac{\partial f}{\partial y}v_2 + \frac{\partial f}{\partial z}v_3 \\ \frac{D\mathbf{f}}{Dt} &= \frac{\partial \mathbf{f}}{\partial t} + \frac{\partial \mathbf{f}}{\partial x}v_1 + \frac{\partial \mathbf{f}}{\partial y}v_2 + \frac{\partial \mathbf{f}}{\partial z}v_3, \end{aligned} \tag{2.6}$$

or

$$\frac{Df}{Dt} = \frac{\partial f}{\partial t} + \mathbf{v} \cdot \nabla f, \qquad \frac{D\mathbf{f}}{Dt} = \frac{\partial \mathbf{f}}{\partial t} + (\mathbf{v} \cdot \nabla)\mathbf{F}. \tag{2.7}$$

The first terms on the right-hand side account for the rate of change at a fixed location, whereas the second terms account for the rate of change following the fluid at the local flow velocity $\mathbf{v}(t)$.

2.1.3 Navier-Stokes Equations

The conservation of momentum in the flow is described by the *Navier-Stokes Equations* (see, for example, [3])

$$\rho \frac{D\mathbf{v}}{Dt} = \rho\,\mathbf{F} - \nabla p + \mu \nabla^2 \mathbf{v}, \tag{2.8}$$

where $\mathbf{F}$ are accelerations due to volumetric forces, from which only the gravity it is often considered; *i.e.* $\mathbf{F} = [0\,0\,-g]^{\mathrm{T}}$, $p = p(\mathbf{x}, t)$ is the pressure, and μ is the viscosity coefficient of the fluid.

To describe the real flow of ships, it is then necessary to solve the Navier-Stokes equations (2.8) together with the continuity equation (2.4). These form a system of non-linear partial differential equations, which unfortunately, do not have analytical solution, and the numerical solutions are still far from being feasible with current computing power. One approximation used consists in decomposing the unknowns, $\mathbf{v}$ and p, into a steady part which is a time average and a fluctuating part. This gives rise to the Reynolds Averaged Navier-Stokes equations (RANS), which can be solved numerically [23].

2.1.4 Potential Flows and The Bernoulli Equation

If we neglect viscosity, we have what we call an *ideal fluid*. This is a commonly made assumption to calculate ship flows because viscosity often matters only in a thin layer close to the ship hull. By disregarding the last term in (2.8), we obtain the *Euler* equations of fluid motion:

$$\rho \frac{D\mathbf{v}}{Dt} = \rho\,\mathbf{F} - \nabla p. \tag{2.9}$$

A further simplification of the flow description is obtained by assuming that the flow is *irrotational*, this is

$$\mathbf{curl}(\mathbf{v}) = \nabla \times \mathbf{v} = 0. \tag{2.10}$$

The term *potential flow* is used to describe irrotational flows of invisid-incompressible fluids. Under this assumption, there exists a scalar function $\Phi(t, x, y, z)$ called *potential* such that

$$\mathbf{v} = \nabla \Phi. \tag{2.11}$$

Hence, if we know the potential, we can calculate the velocities:

$$v_1 = \frac{\partial \Phi}{\partial x}, \qquad v_2 = \frac{\partial \Phi}{\partial y}, \qquad v_3 = \frac{\partial \Phi}{\partial z}. \tag{2.12}$$

For this case, the continuity equation reverts to the Laplace Equation of the potential:

$$\nabla^2 \Phi = \frac{\partial^2 \Phi}{\partial x^2} + \frac{\partial^2 \Phi}{\partial y^2} + \frac{\partial^2 \Phi}{\partial z^2} = 0. \tag{2.13}$$

The potential can then be obtained by solving the Laplace equation (2.13) subject to appropriate boundary conditions, *i.e.* by solving a boundary value problem.

The Euler equation of fluid motion (2.9) can be expressed as

$$\frac{\partial \mathbf{v}}{\partial t} + (\mathbf{v} \cdot \nabla)\mathbf{v} = -\nabla \left(\frac{p}{\rho} + \Upsilon \right), \tag{2.14}$$

where $-\nabla \Upsilon = \mathbf{F}$, *i.e.* $\Upsilon = gz$. Using properties of vector calculus (see, for example, [3]), this becomes

$$\frac{\partial \mathbf{v}}{\partial t} + (\nabla \times \mathbf{v}) \times \mathbf{v} = -\nabla \left(\frac{p}{\rho} + \frac{1}{2}\mathbf{v}^2 + \Upsilon \right) \tag{2.15}$$

If the flow is irrotational, then the second term of the left-hand side vanishes, and we can express the above as

$$\nabla \left(\frac{p}{\rho} + \frac{\partial \Phi}{\partial t} + \frac{1}{2}(\nabla \Phi)^2 + \Upsilon \right) = 0. \tag{2.16}$$

This expression is valid in the whole fluid. Hence,

$$\frac{p}{\rho} + \frac{\partial \Phi}{\partial t} + \frac{1}{2}(\nabla \Phi)^2 + gz = C, \tag{2.17}$$

which is the *Bernoulli equation*.

By setting the constant $C = p_0/\rho$, we can obtain the relative pressure from

$$p - p_0 = -\rho g z - \rho \frac{\partial \Phi}{\partial t} - \rho (\nabla \Phi)^2. \tag{2.18}$$

For simplicity, the atmospheric pressure p_0 is often considered zero.

Potential flows offer a great simplification, which can be see from (2.11) and (2.18), *i.e.* if we know the potential, then we know the velocity and the pressure in the fluid, from which we can calculate the forces acting on a floating body. For *most* problems related ship motion in waves, potential theory is sufficient to obtain results with appropriate accuracy for engineering purposes. For further discussions on the topics presented in this section, see [3], [23], [63], [114] and [159].

2.2 Regular Waves in Deep Water

The term *regular wave* refers to a harmonic wave travelling on the surface of the fluid:

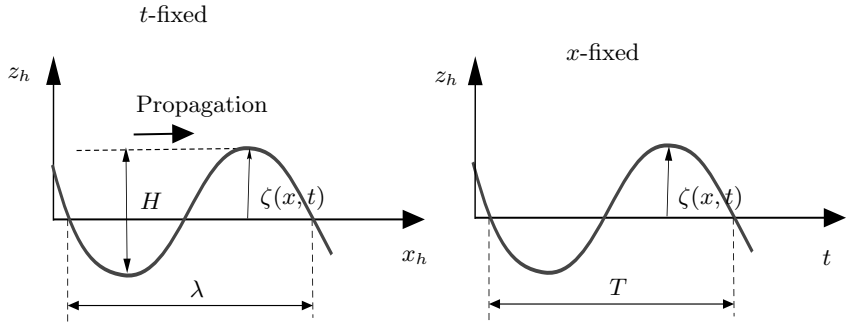

Fig. 2.1. Regular wave parameters.

$$\zeta(x,t) = \bar{\zeta}\sin(\omega t - kx + \varepsilon). \tag{2.19}$$

Figure 2.1 depicts the main parameters defining a harmonic wave traveling in the x-direction with respect to the hydrodynamic reference frame (x_h, y_h, z_h). The sea surface elevation is denoted by $\zeta(x,t)$. This is characterised by a sinusoid of constant amplitude $\bar{\zeta}$ as described in (2.19). The *double amplitude* or *wave height* is denoted by $H = 2\bar{\zeta}$, λ is the *wave length*, and ω is the circular *wave frequency* related to the wave period T via $\omega = 2\pi/T$. The speed at which the crest of the wave travels over the surface is called the *wave celerity* $c = \lambda/T$.

A mathematical description of the fluid flow velocities and the pressure distribution due to a travelling wave can be obtained from potential theory. Indeed, if $\Phi_w(t,x,y,z)$ is the potential due to the traveling wave, then, the following equation is satisfied in the fliud:

$$\nabla^2\Phi_w = 0. \tag{2.20}$$

By solving this, the velocity of the fluid particles is given by $\nabla\Phi_w$, and the pressure can be calculated from the Bernoulli equation (2.18).

To obtain the potential, we need to solve Equation (2.20) together with the following boundary conditions (see, for example, [63]):

1. **Kinematic free-surface boundary condition.** This condition establishes that a fluid particle on the free surface remains on the free surface. Mathematically, this is expressed though the material derivative $D(z-\zeta(x,y,t))/Dt = 0$. Using a Taylor expansion and taking only the linear terms, this condition becomes

$$\frac{\partial\zeta}{\partial t} = \frac{\partial\Phi_w}{\partial z} \quad \texttt{on} \quad z = 0. \tag{2.21}$$

2. **Dynamic free-surface condition.** This condition establishes that the water pressure equals the atmospheric pressure on the free surface. By considering the linear terms in the Bernoulli equation (2.18), this condition becomes
$$g\zeta + \frac{\partial \Phi_w}{\partial t} = 0 \quad \texttt{on} \quad z = 0. \tag{2.22}$$
3. **Sea bed condition.** This condition establishes that there is no flow velocity component normal to the sea bottom. Assuming a flat sea bed this is
$$\frac{\partial \Phi_w}{\partial z} = 0 \quad \texttt{on} \quad z = -h, \tag{2.23}$$
where h is the depth.

The solution of the above boundary value problem with $h \to \infty$ that is consistent with the physics of the problem for a wave propagating in the x_h direction is [159, 63, 3]

$$\Phi_w(t, x, y, z) = \frac{g\bar{\zeta}}{\omega} e^{kz} \cos(\omega t - kx + \varepsilon). \tag{2.24}$$

The parameter $\bar{\zeta}$ is the amplitude of the wave, ε is the initial phase and k is the *wave number*. For the deep water conditions being considered ($h \geq \lambda/2$), the following *dispersion relationships* hold:

$$k = \frac{\omega^2}{g} \qquad \lambda = \frac{g}{2\pi} T^2. \tag{2.25}$$

Also, the fact that only the linear terms are considered in the free-surface boundary conditions means that the solution will be valid for waves of small steepness, *i.e.* $\bar{\zeta}/\lambda \ll 1$ (see [3]).

If the waves propagate at an angle χ with respect to the positive axis x_h, then the potential can be expressed as

$$\Phi_w(t, x, y, z) = \frac{g\bar{\zeta}}{\omega} e^{kz} \cos(\omega t - kx\cos(\chi) - ky\sin(\chi) + \varepsilon). \tag{2.26}$$

From the dynamic free-surface condition, we obtain the wave elevation:

$$\zeta(x, y, t) = \bar{\zeta} \sin[\omega t + \varepsilon - kx\cos(\chi) - ky\sin(\chi)]. \tag{2.27}$$

Also, $\nabla \Phi_w$ gives the velocity components of a particle in the fluid:

$$\begin{aligned} v_1(x, y, z, t) &= \omega \cos(\chi) e^{kz} \bar{\zeta} \sin[\omega t + \varepsilon - kx\cos(\chi) - ky\sin(\chi)] \\ v_2(x, y, z, t) &= \omega \sin(\chi) e^{kz} \bar{\zeta} \sin[\omega t + \varepsilon - kx\cos(\chi) - ky\sin(\chi)] \\ v_3(x, y, z, t) &= \omega e^{kz} \bar{\zeta} \cos[\omega t + \varepsilon - kx\cos(\chi) - ky\sin(\chi)] \end{aligned} \tag{2.28}$$

The behaviour of waves is significantly affected by the depth. For the particular applications considered in this book, only deep water characteristics

will be considered. Shallow water effects are discussed, for example, in [159, 163].

The wave description presented above corresponds to the, so-called, first-order wave theory or linear wave theory. The linearity follows from the Laplace equation and the boundary conditions considered: the principle of superposition holds for the potentials; and thus, for the surface elevation and fluid particle velocities. Second-order theory, for example, accounts for non-linearities related to the square of the wave amplitude. This gives a more accurate description of mean drift forces and slowly-varying wave induced loads on ships and marine structures, which is important for the analysis of moored ships and structures and to evaluate added resistance in waves [63, 23]. First-order wave theory only describes zero mean phenomena, and this is sufficient for the problems of autopilot and fins stabiliser control design.

2.3 Encounter Frequency

In the previous section, we have described regular waves from a stationary reference frame. When the ship is at zero speed, the frequency at which the waves excite the ship coincides with the wave frequency; and thus, the previous description is valid. However, when the ship moves, the frequency observed from the ship differs from the wave frequency. The frequency experienced by the ship is called the *encounter frequency*, and it is denoted by ω_e.

If the ship moves forwards with an average speed U, the sea can be more conveniently described relative to a frame (o_h, x_h, y_h) that moves at the average speed of the vessel as shown in Figure 2.2. This figure also shows the adopted convention for the, so-called, *encounter angle* χ, and also the usual denomination for the different sailing conditions:

- Following seas (χ= 0 or 360 deg),
- Quartering seas ($0 < \chi < 90$ deg or $270 < \chi < 360$ deg),
- Beam seas ($\chi = 90$ deg—port or 270 deg—starboard),
- Bow seas ($90 < \chi < 180$ deg or $180 < \chi < 270$ deg),
- Head seas ($\chi = 180$ deg).

From Figure 2.2, it follows that the relative speed at which the waves overtake the ship is $c - U\cos(\chi)$. Then, we can express the encounter frequency as

$$\omega_e = \frac{2\pi}{T_e} = \frac{2\pi}{\lambda}[c - U\cos(\chi)],$$

or

$$\omega_e = \omega - \frac{\omega^2 U}{g}\cos(\chi). \tag{2.29}$$

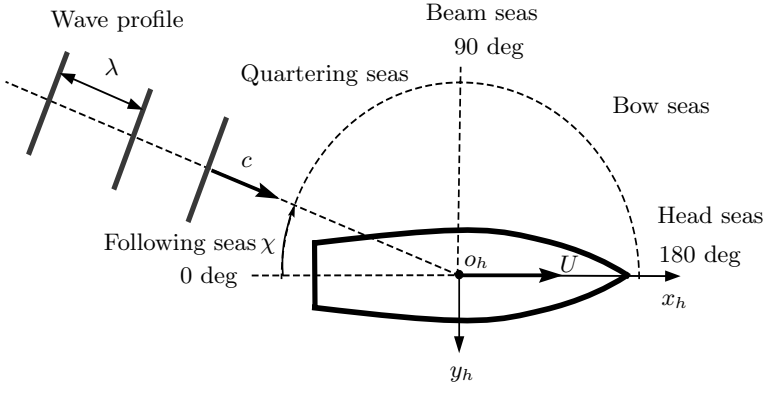

Fig. 2.2. Encounter angle definition and usual denomination for sailing conditions.

Expression (2.29) represents the transformation in frequency that a regular wave goes through when it is observed either from a stationary frame or from a frame moving with the forward speed of the vessel. Figure 2.3 shows a schematic representation of the transformation between ω and ω_e. From this figure, we can see that when the vessel is sailing in bow or head seas the wave frequencies are mapped into higher frequencies. In beam seas, however, there is no change and both ω and ω_e are the same. In following and quartering seas, the situation becomes more involved as different wave frequencies can be mapped into the same encounter frequency.

From the development in the previous section, we can also see that long waves travel faster than short waves in deep water:

$$c = \sqrt{\frac{g\lambda}{2\pi}}. \tag{2.30}$$

Hence, in following and quartering seas, long waves overtake the vessel whereas short waves are overtaken by the vessel. Indeed, for $0 < \omega < \frac{g}{U\cos(\chi)}$ the waves overtake the vessel. The wave frequency $\omega = \frac{g}{U\cos(\chi)}$, at which $\omega_e = 0$, corresponds to the situation in which the component of the ship velocity in the direction of wave propagation is the same as the wave celerity. In this case, the wave pattern observed from the ship remains stationary and travels along with the ship. Finally, for high-frequency waves, the encounter frequency is negative, meaning that the ship overtakes the waves.

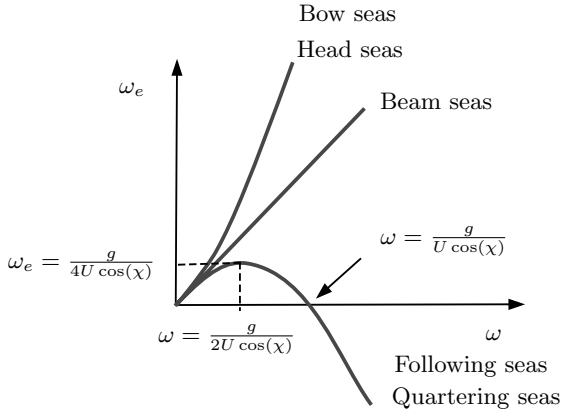

Fig. 2.3. Transformation from wave to encounter frequency under different sailing conditions for U fixed.

The motion of a ship in waves is the result of the wave excitation due to the varying distribution of pressure on the hull. From the material presented in this section, it can be envisaged that the wave excitation, as well as the vessel response, will depend not only on the characteristics of the waves—amplitude and frequency—but also on the *sailing conditions*: encounter angle and speed.

2.4 Ocean Waves and Wave Spectra

Ocean waves are random in both time and space. These characteristics are often summarised by the term *irregular* in the marine literature. The stochastic description is, therefore, the most appropriate approach to characterise them. In practice, it is usually assumed that the variations of a stochastic nature of the sea are much slower than the variations of the sea surface itself—stationarity is assumed. Due to this assumption, the elevation of the sea, $\zeta(x, y, t)$, at a position x, y, can be considered a realisation of a stationary stochastic process. The following simplifying assumptions regarding the underlying stochastic model are usually made [99, 213]:

- The observed sea surface, at a certain location and for short periods of time, is considered a realisation of a stationary and homogeneous zero mean Gaussian stochastic process.
- A standard formula for the Power Spectral Density (PSD) of the wave sea surface elevation, $\mathbf{S}_{\zeta\zeta}(\omega)$, is adopted. This PSD is commonly referred to as *wave spectrum*, and describes how the energy of the sea surface is distributed in the frequency domain. Under a Gaussian assumption, the process, in a statistical sense, is completely characterised by the PSD $\mathbf{S}_{\zeta\zeta}(\omega)$.

The above implies that

$$\begin{aligned} \mathbf{E}[\zeta(t)] &= 0 \\ \mathbf{E}[\zeta(t)^2] &= \int_0^\infty S_{\zeta\zeta}(\omega)\, d\omega. \end{aligned} \tag{2.31}$$

The validity of the hypotheses of stationarity and Gaussianity has been investigated via extensive analysis of time series recorded from wave-riding buoys. For example, [99] report the following results from studies performed in the North Atlantic Ocean:

- For low and moderate sea states (significant wave height[1] $\mathrm{H}_{1/3} < 4$ m), the sea can be considered stationary for periods over 20 min. For more severe sea states, stationarity can be questioned even for periods of 20 min.
- For medium states ($4 < \mathrm{H}_{1/3} < 8$ m), Gaussian models are still accurate, but deviations from Gaussianity slightly increase with the increasing severity of the sea state.

The deviations from Gaussianity are related to the severity of the sea state and the depth. If the water is sufficiently deep, however, the sea surface elevation can be considered Gaussian regardless of the sea state [163].

In some applications, the wave slope spectrum may be necessary; this refers to the spacial derivative. For example, for the regular wave described by (2.19), the *wave slope* is given by

$$\zeta'(t,x) = \frac{d\zeta(t,x)}{dx} = -k\bar{\zeta}\cos(\omega t - kx + \varepsilon). \tag{2.32}$$

From this, it follows that the *wave slope spectrum* is given by (see [133])

$$S'_{\zeta\zeta}(\omega) = k^2 S_{\zeta\zeta}(\omega) = \frac{\omega^4}{g^2} S_{\zeta\zeta}(\omega). \tag{2.33}$$

In the case of roll and pitch motion of ships, it is the slope of the waves rather than the height what excites the motion; and due to this the roll and pitch frequency responses are often given relative to the wave slope rather than the amplitude—we will further comment on this in Chapter 4.

[1] Average of the heights of largest 1/3rd of the waves.

2.4.1 Statistics of Wave Period

Let us assume that the waves propagate in one direction, so the spectrum depends on the frequency only, *i.e.* $S_{\zeta\zeta}(\omega)$ (this assumption will be removed in a later section). The statistical moments of the spectrum (or spectral moments) of order n of the process $\zeta(t)$ are defined as

$$m_\zeta^n = \int_0^\infty \omega^n \mathbf{S}_{\zeta\zeta}(\omega) d\omega. \tag{2.34}$$

The moments of the spectrum are used to define several quantities related to the statistics of wave period. Rice [186, 187] showed that for Gaussian processes the following relationships hold:

- **Average wave period** (1/average frequency of the spectrum)

$$\bar{T} \quad \texttt{or} \quad T_1 = 2\pi \frac{m_\zeta^0}{m_\zeta^1}. \tag{2.35}$$

- **Zero-crossing wave period** (average period of zero up-crossings)

$$T_z = 2\pi \sqrt{\frac{m_\zeta^0}{m_\zeta^2}}. \tag{2.36}$$

- **Average period between response maxima** (crests)

$$T_c = 2\pi \sqrt{\frac{m_\zeta^2}{m_\zeta^4}}. \tag{2.37}$$

Note that the 2π factor in the expressions above appears only if the moments are calculated using a PSD given in terms of the circular frequency (2.34). For a discussion on the units of the PSD, see Section 2.4.3.

2.4.2 Statistics of Maxima

The Gaussian assumption for the sea surface elevation implies that the elevation is statistically symmetrical with respect to the zero level. This assumption also implies that the maxima and minima of a wave record (or realisation) are statistically symmetrical about the zero level. Practical wave records usually present short-period oscillations on top of long-period oscillations. Therefore, we can expect to have more than one maximum within a positive excursion of the realisation, which implies that there will be also positive minima.

A maximum of a realization of a stochastic process $\zeta(t)$ occurs when the realisation of $\dot{\zeta}(t)$ is zero and the realisation $\ddot{\zeta}(t)$ is negative simultaneously.

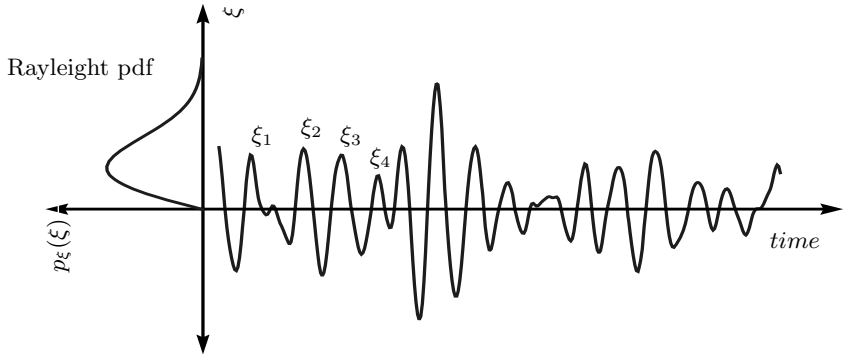

Fig. 2.4. Illustration of statistics of maxima of a narrow banded Gaussian process.

The information about the distribution of the maxima can then be obtained from the joint probability functions of $\zeta(t)$, $\dot{\zeta}(t)$ and $\ddot{\zeta}(t)$. If the maxima are modeled as realisations of a random variables ξ, the probability density function (pdf) $p_\xi(\xi)$ depends on the value of the so-called *spectral broadness*:

$$\epsilon = \sqrt{1 - \frac{T_c}{T_z}}. \tag{2.38}$$

For $\epsilon \approx 0$, *i.e.* $T_c \approx T_z$, there are no multiple maxima and minima within an excursion above or below zero; then, the spectrum is referred to as *narrow banded*. For this case, $p_\xi(\xi)$ can be approximated by a Rayleigh pdf with parameter $b = \sqrt{m_\zeta^0}$. That is,

$$p_\xi(\xi) = \frac{\xi}{m_\zeta^0} \exp(\frac{-\xi^2}{2m_\zeta^0}) \qquad \text{if} \quad \epsilon = 0. \tag{2.39}$$

This case is illustrated in Figure 2.4. When $\epsilon \to 1$,*i.e.* $T_c \ll T_z$, there is a large number of maxima and minima within an excursion of the realisation of the process above or below zero; then, the spectrum is referred to as *broad banded*, and $p_\xi(\xi)$ is Gaussian. See [182] for details. Except for the two cases mentioned above, the pdf of maxima is neither Rayleigh nor Gaussian; this pdf is given by the, so-called, Rice Distribution—see [182] and [155].

Using the Ralyleigh pdf to describe the statistics of maxima of the wave elevation realisations, we can calculate the probability of exceeding a particular wave height. One statistic of particular interest is the average of the $1/n$-th highest observations of the peaks of the random process. The probability of exceeding an amplitude $\xi_{1/n}$ is given by

$$\mathbf{Pr}[\xi > \xi_{1/n}] = \frac{1}{n} = \int_{\xi_{1/n}}^{\infty} \frac{\xi}{m_\xi^0} \exp(\frac{-\xi^2}{2m_\xi^0}) \quad d\xi. \tag{2.40}$$

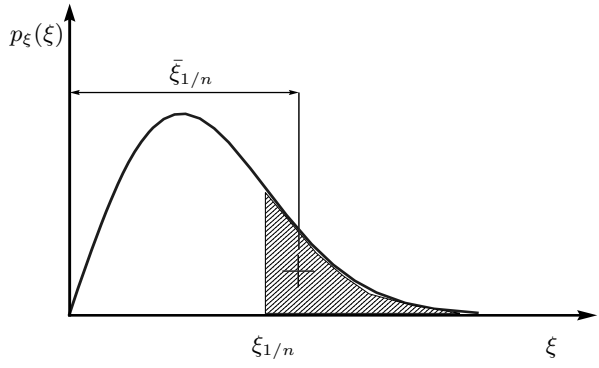

Fig. 2.5. Definition of $1/n$-th highest observation.

Then, the average of the $1/n$-th highest observations is defined as

$$\bar{\xi}_{1/n} = n \int_{\xi_{1/n}}^{\infty} \frac{\xi^2}{m_\xi^0} \exp(\frac{-\xi^2}{2m_\xi^0}) \quad d\xi. \tag{2.41}$$

Figure 2.5 depicts a graphical interpretations of this definition.

Typical values of ϵ arising from records of ocean waves or ship motion are less than 0.6. In practice, the statistics of maxima are calculated assuming $\epsilon \approx 0$; this gives an error of about 10% when estimating $\bar{\xi}_{1/3}$ and $\bar{\xi}_{1/10}$ (the most commonly used statistics) [133]. Consequently, the assumption of a narrow-banded wave spectrum is commonly made to evaluate the statistics related to waves and ship motion.

Using (2.41), the following quantities are defined [135, 182]:

- **Mean value of wave amplitude**

$$\overline{\zeta} = 1.5\sqrt{m_\zeta^0}. \tag{2.42}$$

- **Significant wave amplitude**

$$\zeta_{1/3} = 2\sqrt{m_\zeta^0}. \tag{2.43}$$

- **Significant wave height** (average of the heights of largest 1/3rd of the waves)

$$H_{1/3}\,(\text{or } Hs) = 4\sqrt{m_\zeta^0}\sqrt{1 - \frac{\epsilon^2}{1}}. \tag{2.44}$$

In practice, the significant wave height is estimated as $H_{1/3} = 4\sqrt{m_\zeta^0}$. As already mentioned, for marine applications the spectral broadness is of order

0.6, and for this value, the third factor in (2.44) is 0.9055, which justifies the approximation.

The significant wave height is used to define the sea state. Table 2.1 shows the sea state code commonly used to describe the seaway in marine applications.

Table 2.1. World meteorological sea state definitions.

Sea state code	$H_{1/3}$ lower limit	$H_{1/3}$ upper limit	Seaway description
0	0	0	Calm (glassy)
1	0	0.1	Calm (rippled)
2	0.1	0.5	Smooth (wavelets)
3	0.5	1.25	Slight
4	1.25	2.5	Moderate
5	2.5	4	Rough
6	4	6	Very rough
7	6	9	High
8	9	14	Very high
9	14	>14	Phenomenal

Although here we have considered the statistics of wave elevation, the concepts apply to Gaussian narrow-banded processes in general. As we will see in the next chapters, the motion response of a vessel to the wave excitations can be considered to certain extent within a linear framework. Therefore, under the Gaussian assumption for the wave elevation and the linearity of the response, the resulting ship motion can also be considered Gaussian; and all the above statistics can also be used to characterise ship motion.

2.4.3 A Note on the Units of the Spectral Density

Very often we have to deal with spectra expressed as a function of either frequency f (Hz) or circular frequency ω (rad/s). This mix usually arises when we need to compare data from different disciplines, or when using some simulation tools. The conversion, although simple, can result in errors.

As stated by Newland [158], a way to avoid potential blunders is to note that the energy is maintained regardless of the frequency units. Thus, if $S_{\zeta\zeta}(\omega)$ and $W_{\zeta\zeta}(f)$ are spectra of the same magnitude $\zeta(t)$ expressed in different frequency units, it follows that

$$S_{\zeta\zeta}(\omega)\, d\omega = W_{\zeta\zeta}(f)\, df,$$

with $d\omega = 2\pi df$. Then,

$$S_{\zeta\zeta}(\omega)\, d\omega = W_{\zeta\zeta}(\frac{\omega}{2\pi})\, \frac{d\omega}{2\pi},$$

which leads to

$$S_{\zeta\zeta}(\omega) = \frac{1}{2\pi} W_{\zeta\zeta}(\frac{\omega}{2\pi}).$$

Similarly,

$$W_{\zeta\zeta}(f) = 2\pi S_{\zeta\zeta}(2\pi f).$$

Another factor that could lead to erroneous results when calculating the energy from the PSD is the scaling adopted for the Fourier transform. The Wiener-Khintchine theorem establishes that the PSD $\mathbf{S}_{\zeta\zeta}(\omega)$ of a continuous-time stationary stochastic process $\zeta(t)$ and its autocorreltation function $\mathbf{R}_{\zeta\zeta}[\tau] = \mathbf{E}[\zeta(t)\zeta(t-\tau)]$ are a fourier transform pair:

$$\mathbf{S}_{\zeta\zeta}(\omega) = c_1 \int_{-\infty}^{\infty} \mathbf{R}_{\zeta\zeta}[\tau] \exp(-j\omega\tau) \quad d\tau \tag{2.45}$$

$$\mathbf{R}_{\zeta\zeta}[\tau] = c_2 \int_{-\infty}^{\infty} \mathbf{S}_{\zeta\zeta}(\omega) \exp(j\omega\tau) \quad d\omega, \tag{2.46}$$

where the values of the constants c_1 and c_2 must satisfy the following condition:

$$c_1 c_2 = \frac{1}{2\pi}. \tag{2.47}$$

Typical choices are

$$c_1 = 1, \qquad c_2 = \frac{1}{2\pi},$$

or

$$c_1 = \frac{1}{\pi}, \qquad c_2 = \frac{1}{2}.$$

The first choice is commonly adopted in control engineering because the Laplace transform reduces to the Fourier transform when $s = j\omega$ [39]. The second choice is commonly adopted in marine technology to describe waves [163]. In this framework, the following relations hold:

$$\mathbf{var}[\zeta] = \mathbf{E}[\zeta^2] = \mathbf{R}_{\zeta\zeta}[0] = \frac{1}{2} \int_{-\infty}^{\infty} \mathbf{S}_{\zeta\zeta}(\omega)\, d\omega = \int_{0}^{\infty} \mathbf{S}_{\zeta\zeta}(\omega)\, d\omega. \tag{2.48}$$

One should be careful and find which one is the the appropriate constant c_2 when calculating the variance by integrating a given PSD.

2.5 Standard Spectrum Formulae

After the wind has blown constantly for a certain period of time, the sea elevation can be assumed statistically stable. In this case, the sea is referred to as *fully developed* . If the irregularity of the observed waves is only in the dominant wind direction, so that there are mainly uni-directional wave crests with varying separation but remaining parallel to each other, the sea

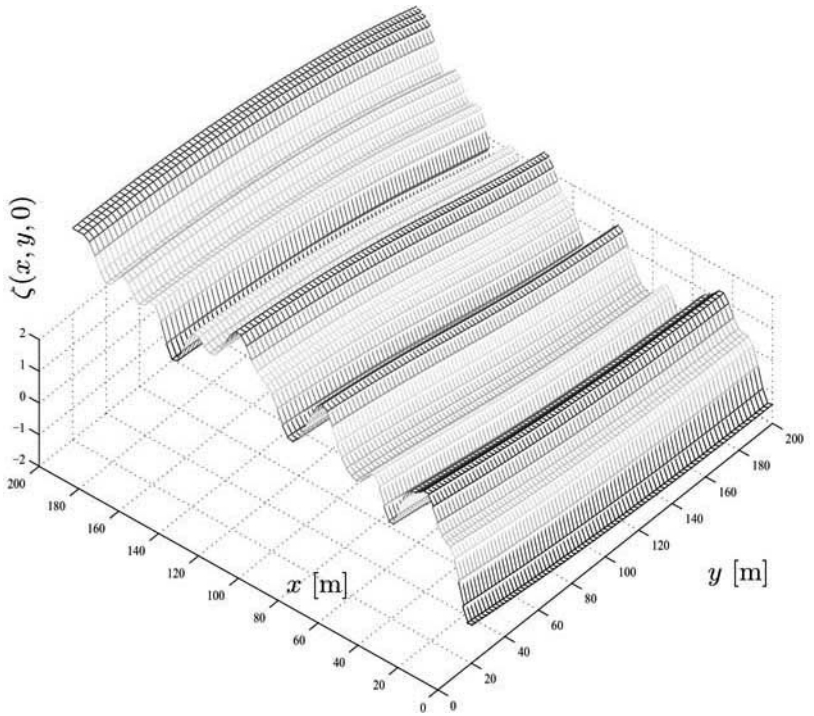

Fig. 2.6. Snapshot of a simulation of a long-crested sea.

is referred to as a *long-crested* irregular sea [182]—see Figure 2.6. If there are data available from wave ride buoys, the sea spectrum can be determined using spectral estimation techniques—see, for example, [220]. In cases where no wave records are available, standard, idealized, formulae can be used.

One family of idealised spectra is the *Bretschneither* family, which was developed in early 1950s [38]:

$$\mathbf{S}_{\zeta\zeta}(\omega) = \frac{A}{\omega^5} \exp\left(\frac{-B}{\omega^4}\right) \quad [\mathrm{m}^2\mathrm{s}]. \tag{2.49}$$

The parameters A and B are related to the modal frequency and the spectral moments. The modal frequency satisfies,

$$\omega_0 = \left(\frac{4B}{5}\right)^{\frac{1}{4}}, \tag{2.50}$$

where

$$\left.\frac{d\mathbf{S}_{\zeta\zeta}(\omega)}{d\omega}\right|_{\omega=\omega_0} = 0$$

and

$$m_\zeta^0 = \frac{A}{4B} \qquad m_\zeta^1 = 0.3\frac{A}{B^{3/4}} \qquad m_\zeta^2 = \sqrt{\frac{\pi A^2}{16B}}. \tag{2.51}$$

This family can be used to represent rising and falling seas, as well as fully developed seas with no swell[2] and unlimited fetch[3]—see [133] and references therein for further details.

In the 1960s, the *Pierson-Moskowitz* family was developed to forecast storm waves at a single point in fully developed seas with no swell using wind data [181]. This family relates the parameters A and B to the average wind speed at 19.5m above the sea surface $\bar{V}_{19.5}$:

$$A = 8.1 \times 10^{-3} g^2 \qquad B = \frac{0.74g}{\bar{V}_{19.5}}. \tag{2.52}$$

The 15th International Towing Tank Conference (ITTC) in 1978 recommended the use of the *Modified Pierson-Moskowitz* family. For this family, the significant wave height and different wave period statistics are used to parameterize each spectrum:

$$A = \frac{487H_{1/3}^2}{T_0^4} = \frac{173H_{1/3}^2}{T_1^4} = \frac{123H_{1/3}^2}{T_z^4},$$
$$B = \frac{1949}{T_0^4} = \frac{691}{T_1^4} = \frac{495}{T_z^4}. \tag{2.53}$$

Figure 2.7, shows a plot of the ITTC sea spectrum and the wave slope spectrum for a particular wave height and different wave mean periods.

There are other families that account for the case of limited fetch like the JONSWAP spectra (see [133] for [220] for this version), and also spectra that account for both wind waves and swell like the empirical double-peak Torsethaugen spectra (see [67] and references therein for details.)

[2] This term is commonly used to describe long wave components that are the result of storms of great intensity occurring, or that have occurred, in areas far away (order of thousand of kilometres) from the observation point. When these low-frequency components contaminate the local wind waves, double-peaked spectra need to be considered.

[3] *Fetch* is the distance between the point at which the waves are observed and a windward boundary, such as a shore or the edge of a storm area. The fetch gives a notion of the area of interaction between the wind and sea surface with respect to the observation point [133].

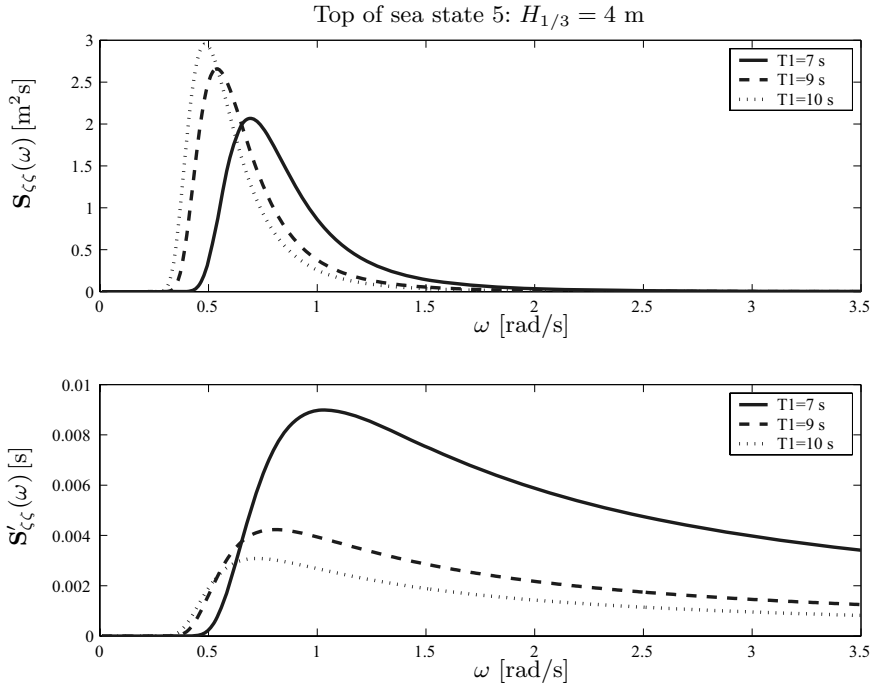

Fig. 2.7. Example of ITTC PSD for the wave elevation and wave slope for $H_{1/3} = 4m$ and T_1 =7, 9 and 10 s.

2.6 Linear Representation of Long-crested Irregular Seas

If white noise[4] w is passed through a linear filter with transfer function $H(j\omega)$, then it follows from the linearity of the filter that the PSD $\mathbf{S}_{yy}$ of the output y is given by

$$\mathbf{S}_{yy}(j\omega) = |H(j\omega)|^2 \mathbf{S}_{ww}, \tag{2.54}$$

where $\mathbf{S}_{ww}$ is the intensity of the white noise (constant height of the PSD.) The filter $H(j\omega)$ is called a *shaping filter* because it can be designed so that $\mathbf{S}_{yy}$ approximates the shape of the PSD of the signal of interest. Equation (2.54) is the spectral factorization of $\mathbf{S}_{yy}(j\omega)$. This method is commonly used in control for analysis and simulation of the disturbances acting on the system (see, for example, [8], [24] or [128]), and can be used to approximate the sea spectrum.

As commented by Fossen [66], spectral factorisation methods were first applied in the marine environment to model high-frequency ship motions in dynamic positioning applications in the 1970s. Since then, several authors have

[4] A signal with constant power spectral density over all frequencies of interest.

proposed different orders and structure for the filter $H(j\omega)$ to model wave-induced motion on ships and marine structures—see, for example, [79] and [96]. The most commonly used filter to model these effects is a second-order filter of the form [66]:

$$H(j\omega) = \frac{2\xi\omega_n(j\omega)}{(j\omega)^2 + 2\xi\omega_n(j\omega) + \omega_n^2}. \tag{2.55}$$

This particular filter has the property that

$$|H(j\omega)|^2 = \frac{4(\xi\omega_n\omega)^2}{(\omega_n^2 - \omega^2)^2 + 4(\xi\omega_n\omega)^2}; \tag{2.56}$$

and then,

$$\max_{\omega} \mathbf{S}_{yy} = |H(j\omega)|^2 \mathbf{S}_{ww} = \mathbf{S}_{nn}. \tag{2.57}$$

To approximate a given spectrum, the parameters of the filter can be chosen according to the following rules:

1- The intensity of the noise driving the filter is obtained from

$$\mathbf{S}_{ww} = \max_{\omega} \mathbf{S}_{yy}(\omega). \tag{2.58}$$

2- The natural frequency of the filter is obtained from

$$\omega_n \approx \arg\max_{\omega} \mathbf{S}_{yy}(\omega). \tag{2.59}$$

3- The damping coefficient $0 < \xi < 1$ is calculated such that the variance of the output of the filter matches the variance of the original spectrum, *i.e.*

$$\int_0^\infty |H(\xi, \omega)|^2 \mathbf{S}_{ww} d\omega \approx m_y^0. \tag{2.60}$$

The last equation can be solved using a simple bi-section algorithm [41]. Equation (2.60) ensures that the energy of the approximation equals the energy of the spectrum being approximated.

A state-space representation of (2.55) that can be used for time domain simulations is

$$\begin{aligned} \begin{bmatrix} \dot{x}_1 \\ \dot{x}_2 \end{bmatrix} &= \begin{bmatrix} 0 & 1 \\ -\omega_n^2 & -2\xi\omega_n \end{bmatrix} \begin{bmatrix} x_1 \\ x_2 \end{bmatrix} + \begin{bmatrix} 0 \\ 2\xi\omega_n \end{bmatrix} w, \\ y &= \begin{bmatrix} 0 & 1 \end{bmatrix} \begin{bmatrix} x_1 \\ x_2 \end{bmatrix} \end{aligned} \tag{2.61}$$

2.7 The Encounter Spectrum

When a ship is moving with a certain speed, the frequencies observed from the ship differ from those observed in a stationary frame: the frequencies change according to (2.29). This Doppler effect changes not only the frequency range of the spectrum but also its shape. The wave spectrum seen from the ship is called the *wave encounter spectrum* $\mathbf{S}(\omega_e)$.

Since the power of any magnitude is invariant with respect to the reference frame from which it is observed, for any PSD the following holds:

$$\mathbf{S}(\omega_e)\, d\omega_e = \mathbf{S}(\omega)\, d\omega.$$

From this, it follows that

$$\mathbf{S}(\omega_e) = \frac{\mathbf{S}(\omega)}{\left|\frac{d\omega}{d\omega_e}\right|} = \frac{\mathbf{S}(\omega)}{\left|1 - \frac{2\omega U}{g}\cos(\chi)\right|}. \tag{2.62}$$

For beam seas, the transformation is trivial, *i.e.* since $\cos(\pi/2) = 0$, then $\mathbf{S}(\omega_e) = \mathbf{S}(\omega)$. In bow seas, the encounter spectrum is a spread version of the wave spectrum shifted towards higher frequencies. For quartering and following seas the situation becomes complex since expression (2.62) is singular at $\bar{\omega}_w = g/(2U\cos\chi)$ where the denominator vanishes, and also because the transformation from the wave frequency to the encounter frequency is not one to one.

Figure 2.8, shows a schematic representation of the transformation in quartering seas from a particular PSD $\mathbf{S}(\omega)$ to the corresponding encounter PSD $\mathbf{S}(\omega_e)$. In this figure, the absolute value of the transformation ω to ω_e has been taken.

From Figure 2.8, we can see that the energy at low encounter frequency usually arises from the energy of three different frequency ranges in the wave frequency domain. This is depicted by the area A_{e1}. Moreover, a large amount of energy corresponding to the wave frequencies close to $\bar{\omega}$ is mapped into a small range of encounter frequencies. This effect, depicted by A_{e2}, can often result in an integrable singularity—see [182].

2.8 Short-crested Irregular Seas

When irregularities are apparent along the wave crests at right angles to the direction of the wind, the sea is referred to as *short crested* or *confused* [182]—see Figure 2.9. In this case, the waves propagate in different directions with a dominant direction (spreading). This is the most likely situation encountered at sea. As commented by Lloyd [135], a wave spectrum derived from data recorded at sea, at a particular point, will invariably contain contributions from different directions, but in most applications this can be ignored (and

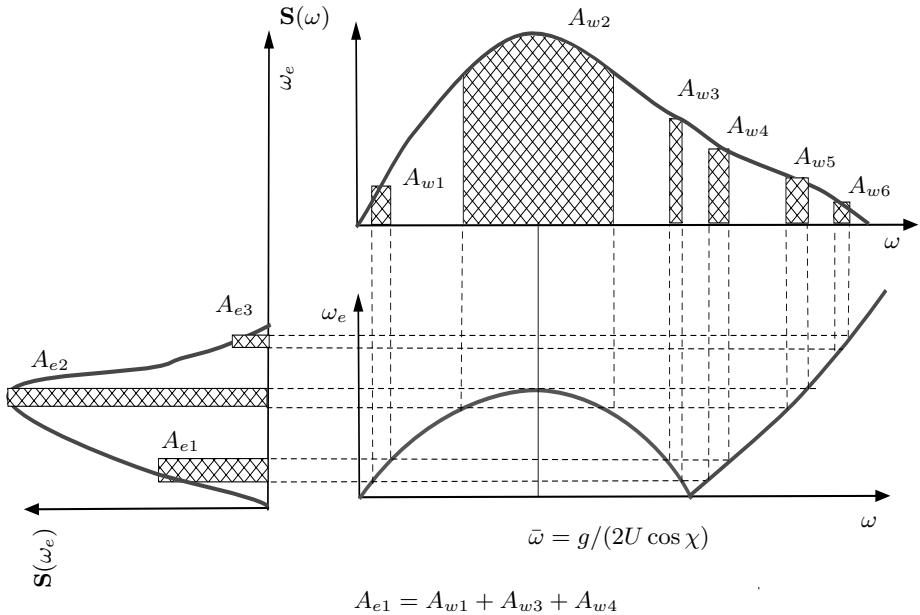

$$A_{e1} = A_{w1} + A_{w3} + A_{w4}$$

$$A_{e2} = A_{w2} + A_{w5}$$

$$A_{e3} = A_{w6}$$

Fig. 2.8. Schematic transformation between wave and encounter frequency domain PSD in quartering and following seas.

considered that the sea is described by a long-crested sea). For example, Figure 2.13 shows simulated time series of a long-crested and a short-crested sea, but both could be considered realisations of a sea described by a long-crested spectrum. Nevertheless, the degree of spreading is important to describe ship motions due to wave loads because the response depends on how much energy there is at the different encounter angles.

For simulation and analysis purposes, it is a common practice to consider the directional spectrum as a product of two functions:

$$\mathbf{S}_{\zeta\zeta}(\omega, \chi) = \mathbf{S}(\omega) M(\chi), \tag{2.63}$$

where the function $M(\chi)$ is the so-called spreading function. This function, as its name indicates, spreads the energy of the spectrum $S(\omega)$, and hence the following relation is satisfied [213]:

$$m_\zeta^0 = \int_0^\infty \int_{-\pi}^{\pi} S_{\zeta\zeta}(\omega, \chi) d\chi \, d\omega = \int_0^\infty S(\omega) \, d\omega. \tag{2.64}$$

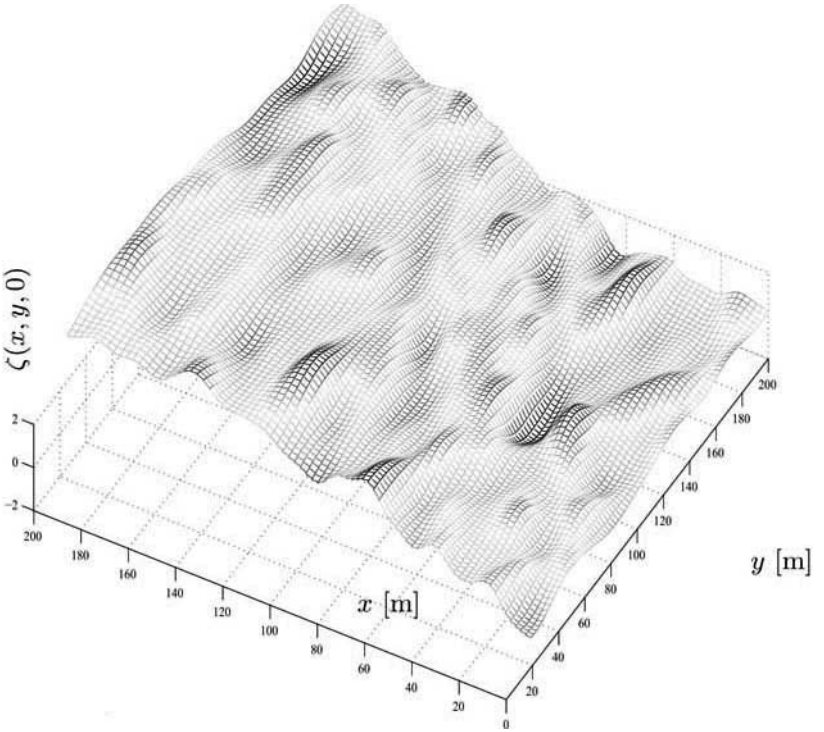

Fig. 2.9. Snapshot of a simulation of a short-crested sea.

A commonly used spreading function is of the form [155]:

$$M(\chi) = \begin{cases} \frac{2^{(2n-1)}n!(n-1)!}{\pi(2n-1)!}\cos^{2n}(\chi - \chi_0) & \text{for } -\frac{\pi}{2} < \chi - \chi_0 < \frac{\pi}{2}, \\ 0 & \text{otherwise.} \end{cases} \tag{2.65}$$

where χ_0 is the dominant wave propagation direction, and the values of $n = 1, 2$ are commonly used. See [135] for a more general form where $|\chi - \chi_0| < \alpha$; with α not necessarily equal to $\pi/2$. Figure 2.10 shows a plot of (2.65) for $n = 1, 2, 3$. Note that the higher the value of n, the larger the concentration of energy around the main direction of wave propagation. Finally, Figure 2.11 shows an example of a directional spectrum based on the ITTC spectrum and $n = 2$.

2.9 Long-term Statistics of Ocean Waves

In the previous sections, we have seen that the sea spectrum can be parameterised in terms of the significant wave height and the wave period. The sea

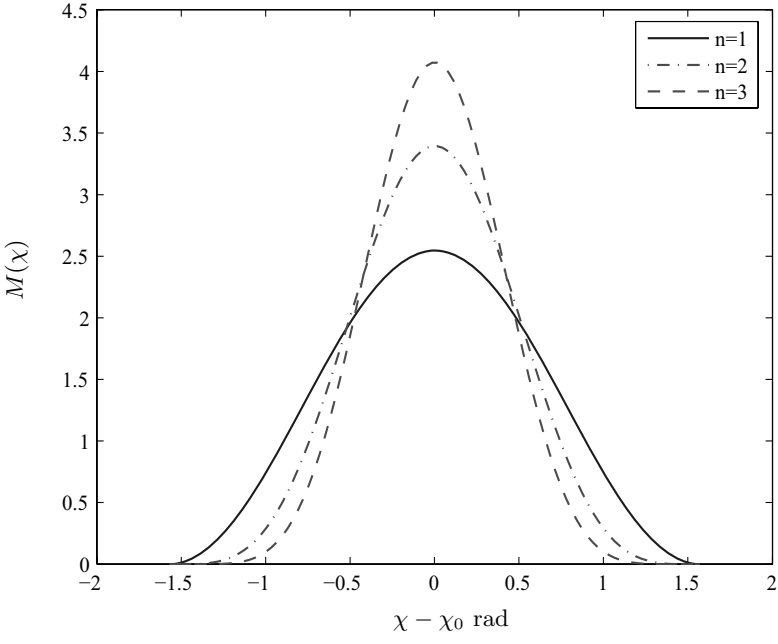

Fig. 2.10. Example of spreading function for commonly used values of n.

spectrum and all the statistics, which can be derived from it, are called *short-term statistics* because they can be used to describe the properties of the sea environment only for minutes or hours at most.

The so-called long-term statistics, by contrast, describe the probability occurrence of a particular wave height and wave period at a particular location and for a particular time of the year. These data are used to find values of wave height and period relevant to the region of operation of a particular ship. As an example, consider the data for the south-east Indian Ocean shown in Table 2.2. Similar data for different areas can be found in [107].

2.10 Simulation of Wave Elevation

As we have seen, the sea surface elevation can be considered an aperiodic wave system having a continuous energy spectrum. Using this representation, if $\zeta(t)$ is stationary on time interval $[0, T]$, its realisations can be approximated to any degree of accuracy by [186]

$$\zeta(t) = \sum_{n=1}^{N} \bar{\zeta}_n \cos(\omega_n t + \varepsilon_n), \tag{2.66}$$

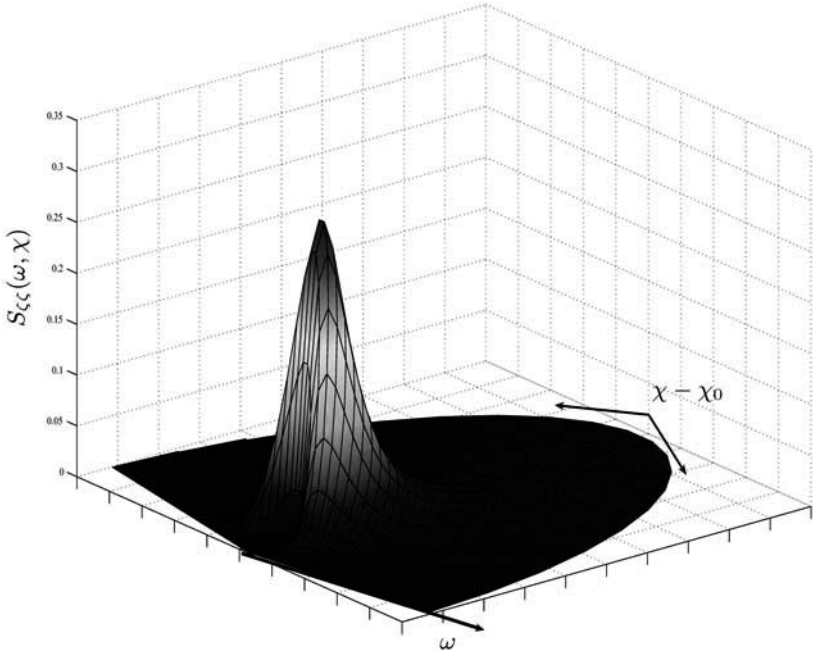

Fig. 2.11. Example of directional spectrum based on the ITTC spectrum for significant wave height of 2 m, peak frequency of 1 rad/sec and spreading with $n = 2$.

with N being sufficiently large, where $\bar{\zeta}_n$ are constants, and the phases ε_n are independent identically distributed random variables with uniform distribution in $[0, 2\pi]$. This choice of random phases ensures that $\zeta(t)$ is a Gaussian process [84, 186, 213]. This sum represents an ensemble of realisations of the process.

The autocorrelation of the process defined above is given by (see [97] for details)

$$\mathbf{R}_{\zeta\zeta}(\tau) = \mathbf{E}[\zeta(t)\zeta(t+\tau)] = \sum_{n=1}^{N} \frac{\bar{\zeta}_n^2}{2} \cos(\omega_n \tau). \tag{2.67}$$

Since the autocorrelation for $\tau = 0$ gives the energy of $\eta(t)$, it follows that

$$\int_0^\infty \mathbf{S}_{\zeta\zeta}(\omega)\, d\omega \approx \sum_{n=1}^{N} \frac{\bar{\zeta}_n^2}{2}, \tag{2.68}$$

and we can write

Table 2.2. Long-term statistics: wave height and wave period joint probability distribution. Area 100 south-east Indian Ocean. Reproduced from [185] and published with permission of the Director of Navy Platform Systems (DNPS), Department of Defence, Australia.

$H_{1/3}$[m],T_z[s] |	<4	4–5	5–6	6–7	7–8	8–9	9–10	10–11	11–12	12–13	>13
>14									0.1	0.1	
13-14									0.1		
12-13								0.1	0.1		
11-12							0.1	0.1	0.1		
10-11						0.1	0.1	0.1	0.1	0.1	
9-10						0.1	0.2	0.3	0.2	0.1	
8-9						0.2	0.4	0.5	0.3	0.1	
7-8					0.1	0.4	0.8	0.8	0.5	0.2	0.1
6-7					0.2	0.9	1.6	1.3	0.7	0.2	0.1
5-6				0.1	0.7	2.1	2.9	2.1	0.9	0.3	0.1
4-5				0.2	1.7	4.4	4.8	2.8	1.0	0.3	0.1
3-4				0.7	4.0	7.5	6.2	2.8	0.8	0.2	
2-3			0.1	2.0	7.0	8.5	4.9	1.6	0.3	0.1	
1-2			0.5	3.2	5.8	3.9	1.3	0.3			
0-1		0.1	0.4	0.9	0.6	0.2					

$$\sum_{n=1}^{N} \int_{\omega_n - \Delta\omega/2}^{\omega_n + \Delta\omega/2} \mathbf{S}_{\zeta\zeta}(\omega)\, d\omega = \sum_{n=1}^{N} \frac{\bar{\zeta}_n^2}{2}, \tag{2.69}$$

and take

$$\frac{\bar{\zeta}_n^2}{2} = \int_{\omega_n - \Delta\omega/2}^{\omega_n + \Delta\omega/2} \mathbf{S}_{\zeta\zeta}(\omega)\, d\omega = \mathbf{S}_{\zeta\zeta}(\omega^*)\Delta\omega \tag{2.70}$$

for some

$$\omega^* \in [\omega_n - \frac{\Delta\omega}{2}, \omega_n + \frac{\Delta\omega}{2}].$$

The later follows from the mean-value theorem for integrals of continuous functions under the assumption that $\mathbf{S}_{\zeta\zeta}(\omega)$ is continuous. From (2.70), it follows that

$$\bar{\zeta}_n = \sqrt{2\mathbf{S}_{\zeta\zeta}(\omega^*)\Delta\omega}. \tag{2.71}$$

In practice, small errors are incurred if we take $\omega^* = \omega_n$. Nevertheless, since the value of N is finite, one should bear in mind that we are approximating the realisation of a stochastic process by a finite sum of periodic signals, which is periodic. Indeed, if $\omega^* = \omega_n$, the realisation will repeat itself after after $2\pi/\Delta\omega$. By choosing ω^* randomly within the interval $[\omega_n - \frac{\Delta\omega}{2}, \omega_n + \frac{\Delta\omega}{2}]$, the fundamental period is increased. Therefore, the following steps can be applied, in some cases, to determine the appropriate number of sinusoids:

1. If a simulation requires $Tsim$ seconds, choose
$$\Delta\omega < \frac{2\pi}{Tsim}.$$
2. The number of sinusoids will then depend on the range of frequencies over which the spectrum is significant. If the energy is negligible outside the frequency range $[\omega_{min}, \omega_{max}]$, then one can take
$$N > \frac{(\omega_{max} - \omega_{min})}{\Delta\omega}.$$
3. Choose ω^* random in each interval $[\omega_n - \frac{\Delta\omega}{2}, \omega_n + \frac{\Delta\omega}{2}]$ to ensure that the fundamental period of the realizations is larger than $Tsim$.

This is summarised in Figure 2.12.

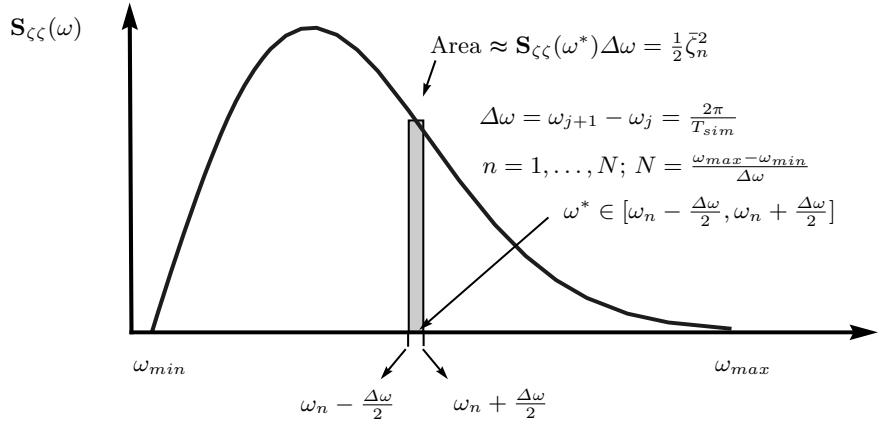

Fig. 2.12. Obtention of regular component amplitudes for time series simulations.

Using the results given above, we can then generate the time series for numerical simulations as follows:

- for long-crested seas:

$$\zeta(x,y,t) = \sum_{n=1}^{N} \sqrt{2\mathbf{S}_{\zeta\zeta}(\omega^*)\Delta\omega}\cos(\omega^* t + \varepsilon_n - k_n(x\cos\chi - y\sin\chi)), \tag{2.72}$$

  with ω^* taken randomly in each interval $[\omega_n - \frac{\Delta\omega}{2}, \omega_n + \frac{\Delta\omega}{2}]$.
- for short-crested seas:

$$\zeta(x,y,t) = \sum_{n=1}^{N}\sum_{m=1}^{M} \sqrt{2\mathbf{S}_{\zeta\zeta}(\omega^*,\chi^*)\Delta\omega\Delta\chi} \cos(\omega^* t + \varepsilon_{n,m} - k_n(x\cos\chi_m - y\sin\chi_m)). \tag{2.73}$$

  with ω^* and χ^* taken randomly in each of the intervals $[\omega_n - \frac{\Delta\omega}{2}, \omega_n + \frac{\Delta\omega}{2}]$ and $[\chi_m - \frac{\Delta\chi}{2}, \chi_m + \frac{\Delta\chi}{2}]$ respectively.

Figures 2.6, 2.9 and 2.13 show the numerical results of expressions (2.72) and (2.73) for a simulation example. In this example, we have used the ITTC spectrum with significant wave height of 2 m and modal period of 1 rad/s. Figure 2.6 shows a snapshot of the sea surface elevation for the long-crested case, whereas Figure 2.9 shows the results for the short-crested case. The latter was obtained using the spreading function with spreading factor $n = 2$. Figure 2.13 shows the corresponding time series at the location $x = 0, y = 0$.

As commented at the beginning of Section 2.8, if we derive a wave spectrum from the data of a particular point (for example, using the data shown in Figure 2.13), the directionality can be ignored in most applications, and we could consider that the sea is described by a long-crested sea. This is clear from the two realisations shown in Figure 2.13; both could be considered realisations of a sea described by a long-crested spectrum. However, as we will see in Chapter 4, the degree of spreading is important to describe ship motion.

Similar results can be obtained using the linear approximations presented in Section 2.6. In the case of long-crested seas, we simply have to filter white noise. For the short-crested case, however, we need to tune as many shaping filters as there are directions being considered. Hence, the simplicity of the linear method for this case can be argued.

Finally, in the case of simulation in the encounter frequency domain, for the case of a ship moving with forward speed, expressions (2.72) and (2.73) remain valid by substituting ω^* by ω_e^* and the corresponding wave numbers k_e. In the case of using linear approximations, the directions need to be discretised and then the filters need to be tuned for each encounter spectrum. We shall

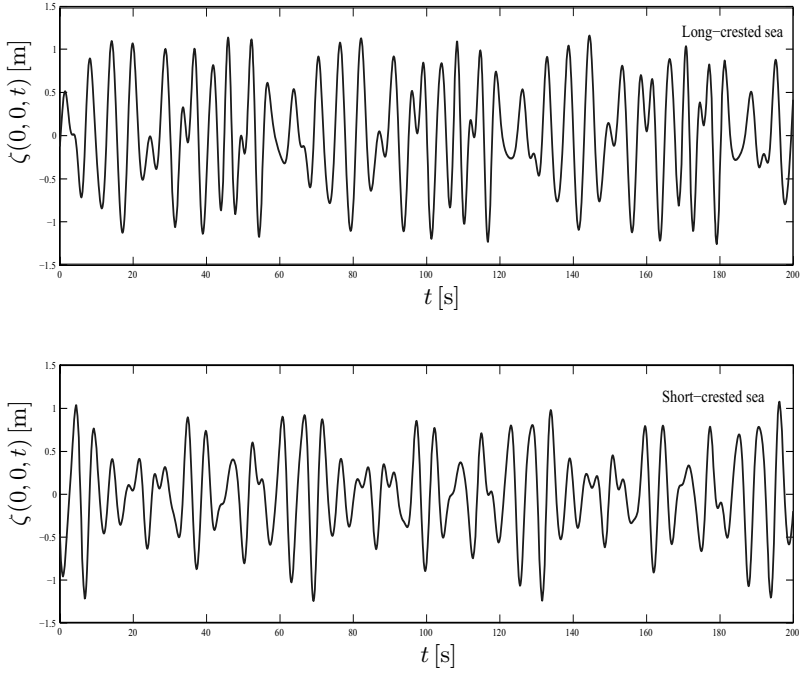

Fig. 2.13. Time series at the origin for an ITTC spectrum for significant wave height of 2 m, peak frequency of 1 rad/s. Long crested (top plot); short crested for 10 directions with spreading factor $n = 2$ (bottom plot.)

see, in the second part of the book, that the latter is a useful analysis tool for the study of performance limitations.

3

Kinematics of Ship Motion

by T. Perez and T.I. Fossen

Within the discipline of mechanics, *dynamics* refers to the branch that studies the motion of particles and bodies under the action of forces. This study can be divided into two parts [203]:

- Kinematics,
- Kinetics.

Kinematics describes geometrical aspects of motion without considering mass and forces: reference frames, variables and transformations. *Kinetics* describes the effects of forces on the motion. This chapter introduces the kinematics of ship motion while kinetics are discussed in Chapter 4.

3.1 Reference Frames

A ship in a seaway moves in six degrees of freedom (6DOF). Thus, to describe its motion, we need to consider three coordinates to define translations and three coordinates to define the orientation. These coordinates are defined using two type of reference frames: *inertial frames* and *body-fixed frames*. The following right-hand reference frames are usually considered for marine vehicles—see Figures 3.1 and 3.2:

- **North-east-down frame (*n*-frame)**. The n-frame (o_n, x_n, y_n, z_n) is fixed to the Earth. The positive x_n-axis points towards the North, the positive y_n-axis towards the East, and the positive z_n-axis towards the centre of the Earth. The origin, o_n, is located on mean water free-surface at an appropriate location. This frame is considered inertial. This is a reasonable assumption because the velocity of marine vehicles is small enough

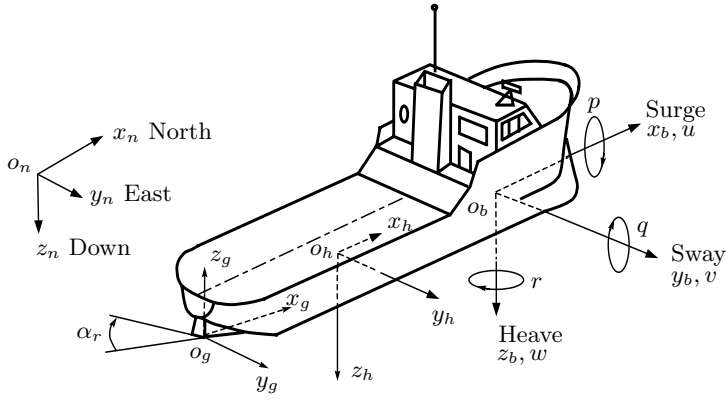

Fig. 3.1. Notation and sign conventions for ship motion description.

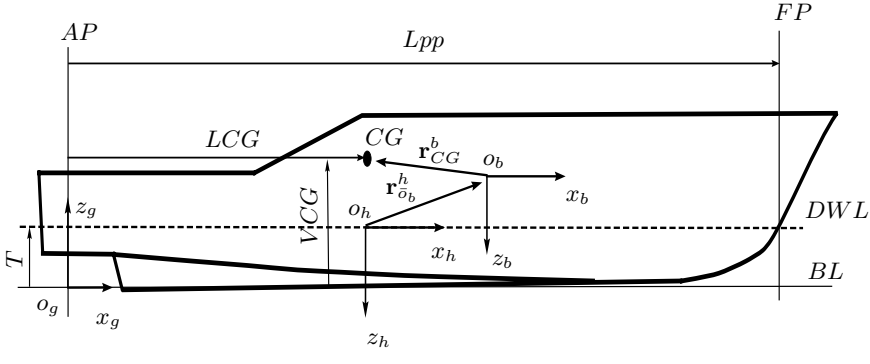

Fig. 3.2. Main particulars and reference frames: geometric (origin o_g); hydrodynamic (origin o_h); and body-fixed (origin o_b); CG—centre of gravity; LCG—lateral centre of gravity (distance); VCG—vertical centre of gravity (distance); AP—aft perpendicular; FP—front perpendicular; L_{pp}—length between perpendiculars; T—draught; DWL—design waterline and BL–baseline.

for the forces due to the rotation of the Earth being negligible compared to the hydrodynamic forces acting on the vehicle [67].

- **Geometric frame (*g*-frame; forward-starboard-up)**. The g-frame (o_g, x_g, y_g, z_g) is fixed to the hull. The positive x_g-axis points towards the bow, the positive y_g-axis points towards starboard and the positive z_g-axis points upwards. The origin of this frame is located along the centre line and at the intersection of the baseline (BL) and the aft perpendicular (AP), which is taken at the rudder stock – see Figure 3.2.

- **Body-fixed frame (*b*-frame; forward-starboard-down)**. The b-frame (o_b, x_b, y_b, z_b) is fixed to the hull. The positive x_b-axis points towards the bow, the positive y_b-axis points towards starboard and the positive z_b-axis points downwards. For marine vehicles, the axes of this frame are chosen to coincide with the principal axes of inertia; this determines the position of the origin of the frame, o_b, [67]. We will further discuss the location of o_b in Chapter 4.

- **Hydrodynamic frame (*h*-frame; forward-starboard-down)**. The h-frame (o_h, x_h, y_h, z_h) is not fixed to the hull; it moves at the average speed of the vessel following its path. The x_h-y_h plane coincides with the mean-water free surface. The positive x_h-axis points forward and it is aligned with the low-frequency yaw angle $\overline{\psi}$ [1]. The positive y_h-axis points towards starboard, and the positive z_h-axis points downwards. The origin o_h is determined such that the z_h-axis passes through the time-average position of the centre of gravity. This frame is usually considered when the vessel travels at a constant average speed (which also includes the case of zero speed); and therefore, the wave-induced motion makes the vessel oscillate with respect to the h-frame. This frame is considered inertial.

Each of these frames has a specific use. For example, the g-frame is commonly used by naval architects to define the geometry of hull, main particulars, location of the centre of gravity, location of o_b *etc.* The n-frame is used to define the position of the vessel, and together with the b-frame it also defines the orientation of the vessel. All the measurements taken on board (velocities, accelerations, *etc.*) are referred to the b-frame, which is also used to formulate the equations of motion. The h-frame is used in hydrodynamics to compute the forces and motion due to the interaction between the hull and the waves—these data are important for preliminary ship and ship motion control system design. This frame is also used to define local wave-induced accelerations, which are used to calculate indices related to performance of the crew or comfort of passengers—see Chapter 7.

[1] The angle $\bar{\psi}$ is obtained by filtering out the 1st-order wave-induced motion (oscillatory motion), and keeping the low frequency motion, which can be either equilibrium or slowly-varying. Hence, $\bar{\psi}$ is constant for a ship sailing in a straight-line path.

3.2 Vector Notation

Because of the use of different reference frames, it is necessary establish a mathematical notation that allows us to identify position, velocity, and acceleration of different points of interest on the ship and to express them in the different frames considered. Thus, for a generic point of interest x on the ship,

- $\mathbf{r}_x^f$ denotes the *position* of x with respect to a frame f, *i.e.*

$$\mathbf{r}_x^f = x_x^f \mathbf{f}_x + y_x^f \mathbf{f}_y + z_x^f \mathbf{f}_z \equiv \begin{bmatrix} x_x^f \\ y_x^f \\ z_x^f \end{bmatrix} = [x_x^f, y_x^f, z_x^f]^{\mathrm{T}}. \tag{3.1}$$

- $\mathbf{v}_x^f$ denotes the *velocity* of x with respect to a frame f.
- $\dot{\mathbf{v}}_x^f$ denotes the *acceleration* of x with respect to a frame f.
- $\boldsymbol{\Theta}_{ab}$ Euler angles that take the a-frame into the orientation of the b-frame. Rotations are considered positive when made counter clockwise.
- $\boldsymbol{\omega}_{ab}^c$ denotes the relative angular velocity of the frame b with respect to the frame a, decomposed in the frame c.

The cross product of the vectors will be written as [62, 67]:

$$\mathbf{a} \times \mathbf{b} \triangleq \mathbf{S}(\mathbf{a})\mathbf{b}, \tag{3.2}$$

where the skew-symmetric matrix $\mathbf{S}$ is defined as:

$$\mathbf{S}(\boldsymbol{\lambda}) = -\mathbf{S}^{\mathrm{T}}(\boldsymbol{\lambda}) \triangleq \begin{bmatrix} 0 & -\lambda_3 & \lambda_2 \\ \lambda_3 & 0 & -\lambda_1 \\ -\lambda_2 & \lambda_1 & 0 \end{bmatrix}, \quad \boldsymbol{\lambda} \triangleq \begin{bmatrix} \lambda_1 \\ \lambda_2 \\ \lambda_3 \end{bmatrix}. \tag{3.3}$$

3.3 Coordinates Used to Describe Ship Motion

3.3.1 Manoeuvring and Seakeeping

Surface vessel operations are performed under different environmental conditions, and different assumptions are made during the study of hydrodynamics in each case. As a consequence of this, the study of ship dynamics has traditionally been separated into two main areas:

- Manoeuvring,
- Seakeeping.

Manoeuvring deals with the the motion of a ship in the absence of wave-excitation (calm water) [2]. The motion results from the action of control devices: control surfaces and propulsion units. Manoeuvring is associated with course changes, stopping, *etc.* Seakeeping, on the other hand, is associated with motion sue to wave excitation, while the vessel keeps its course and its speed constant.

These two areas of study of ship motion are well established with accurate models to describe the motion characteristics according to the assumptions made in each of them. Due to the independent development of manoeuvring and seakeeping, different reference frames and coordinates are used to describe the motion of the ship.

3.3.2 Manoeuvring Coordinates and Reference Frames

The north-east-down *position* of a ship is defined by the coordinates of the origin of the b-frame, o_b, relative to the n-frame:

$$\mathbf{r}_{o_b}^{n} \triangleq \begin{bmatrix} n \\ e \\ d \end{bmatrix}.$$

The *attitude* of a ship is defined by the orientation of the b-frame relative to the n-frame. This is given by the three consecutive rotations that take the n-frame into the b-frame. The rotations are performed in the following order:

1. Rotation about the z_n axis; the rotation angle is called *yaw* ψ,
2. Rotation about the y_n axis; the rotation angle is called *pitch* θ,
3. Rotation about the x_n axis; the rotation angle is called *roll* ϕ.

With the rotations performed in this particular order, the rotation angles are called Euler angles. The *vector of Euler angles* is defined as

$$\mathbf{\Theta}_{nb} \triangleq \begin{bmatrix} \phi \\ \theta \\ \psi \end{bmatrix}. \tag{3.4}$$

Following the notation of Fossen [66, 67], the *position-orientation vector* (or *generalised position vector*) is defined as:

$$\boldsymbol{\eta} \triangleq \begin{bmatrix} \mathbf{r}_{o_b}^{n} \\ \mathbf{\Theta}_{nb} \end{bmatrix} = [n, e, d, \phi, \theta, \psi]^{\mathrm{T}}. \tag{3.5}$$

The linear and angular velocities of the ship are more conveniently expressed in the b-frame. The *linear-angular velocity vector* (or simply *generalised velocity vector*) given in the b-frame is defined as:

$$\boldsymbol{\nu} \triangleq \begin{bmatrix} \mathbf{v}_{o_b}^{b} \\ \boldsymbol{\omega}_{nb}^{b} \end{bmatrix} = [u, v, w, p, q, r]^{\mathrm{T}}, \tag{3.6}$$

where

- $\mathbf{v}_{o_b}^{b} = [u, v, w]^{\mathrm{T}}$ is the linear velocity of the point o_b expressed in the b-frame.

- $\boldsymbol{\omega}_{nb}^{b} = [p, q, r]^{\mathrm{T}}$ is the angular velocity of the b-frame with respect to the n-frame expressed in the frame b.

Table 3.1 summarises the adopted notation. The reader should be aware of the differences in nomenclature and reference frames used to describe ship motion in different areas of study (manoeuvring and seakeeping), and be careful when combining data and results. A further discussion on these topics can be found in [67].

Table 3.1. Adopted nomenclature for the description of ship motion, and reference frames in which the components are defined.

Component	Name	Definition frame
n	North position	n-frame
e	East position	n-frame
d	Down position	n-frame
ϕ	Roll angle	Euler angle
θ	Pitch angle	Euler angle
ψ	Heading or yaw angle	Euler angle
u	Surge velocity	b-frame
v	Sway velocity	b-frame
w	Heave velocity	b-frame
p	Roll rate	b-frame
q	Pitch rate	b-frame
r	Yaw rate	b-frame

3.3.3 Seakeeping Coordinates and Reference Frames

In seakeeping, the study ship motion is performed under the assumption that the ship is moving on a steady course and at a constant-average forward speed (which includes the case of zero speed). This defines a state of equilibrium of motion, and the action of the waves makes the ship oscillate with respect to this equilibrium (1st-order wave-induced motion). This fundamental assumption is the basis of the *seakeeping theory of ship motion*—see [28, 63, 135, 159].

In seakeeping theory, the motion of the ship is commonly described using the h-frame, which is fixed with respect to the equilibrium of motion. Here, however, we will also allow the ship to manoeuvre, but under the assumption that the manoeuvring is much slower than the motion induced by the waves. This way the h-frame can still be used to describe the motion.

Once the origin o_h is chosen, it coincides with the slowly-varying location of a point s in the ship, *i.e.* $o_h \equiv \bar{s}$, where the notation $\bar{s}$ indicates either *equilibrium* or *slowly varying component*. Thus, $o_h \equiv \bar{s} = s$ when there are no waves (see Figure 3.3). The set of *generalised perturbation coordinates or*

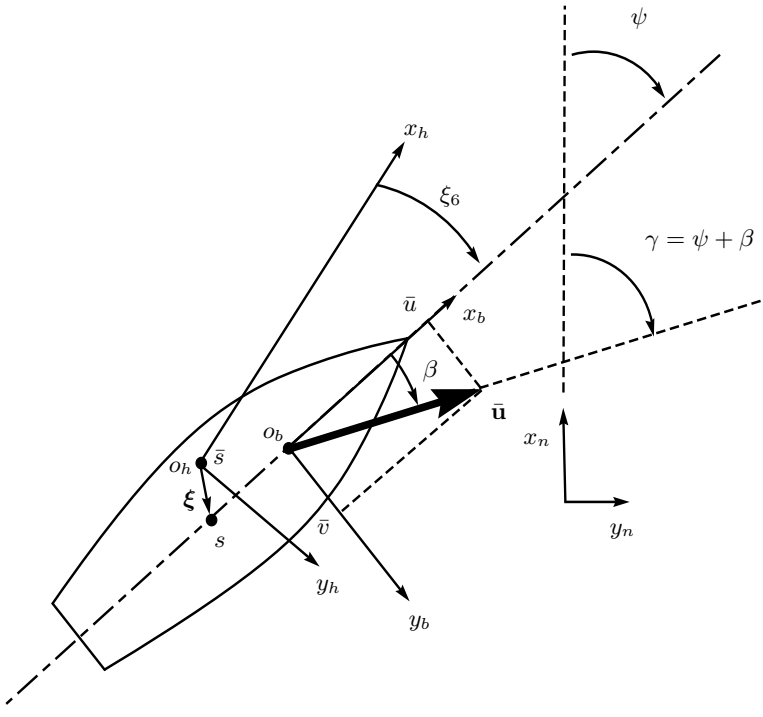

Fig. 3.3. Angles for the horizontal plane.

seakeeping coordinates defined in the h-frame will be denoted by:

$$\boldsymbol{\xi} = [\xi_1, \xi_2, \xi_3, \xi_4, \xi_5, \xi_6]^{\mathrm{T}}. \tag{3.7}$$

When these coordinates[2] describe the position of s (see Figure 3.3), the linear coordinates are normally referred to as

- ξ_1—surge displacement,
- ξ_2—sway displacement,
- ξ_3—heave displacement,

whereas the angular coordinates ξ_4, ξ_5, ξ_6 are the Euler angles that take the h-frame into the orientation of the b-frame:

[2]Note that in some of the hydrodynamic and seakeeping literature (*e.g.* [63, 133]), the above variables are usually denoted by η_i. Unfortunately, this is in conflict with the variables (3.5), which are already well accepted in the literature of guidance, navigation and control of marine systems [66, 67]. For this reason we have adopted the notation ξ_i.

$$\boldsymbol{\Theta}_{hb} \triangleq \begin{bmatrix} \xi_4 \\ \xi_5 \\ \xi_6 \end{bmatrix} = \begin{bmatrix} \phi \\ \theta \\ \psi - \overline{\psi} \end{bmatrix}. \tag{3.8}$$

These angles are referred to as

- ξ_4—roll perturbation angle,
- ξ_5—pitch perturbation angle,
- ξ_6—yaw perturbation angle.

The perturbation coordinates can be used to describe the oscillatory position of any point of interest with respect to h-frame. Indeed, for the generic point of interest x with equilibrium position $\bar{x}$ with respect to o_h, the following relationships hold:

$$\begin{aligned} \mathbf{r}_x^h &= [\xi_1, \xi_2, \xi_3]^{\mathrm{T}} + [\xi_4, \xi_5, \xi_6]^{\mathrm{T}} \times \mathbf{r}_{\bar{x}}^h \\ \mathbf{v}_x^h &= [\dot{\xi}_1, \dot{\xi}_2, \dot{\xi}_3]^{\mathrm{T}} + [\dot{\xi}_4, \dot{\xi}_5, \dot{\xi}_6]^{\mathrm{T}} \times \mathbf{r}_{\bar{x}}^h \\ \dot{\mathbf{v}}_x^h &= [\ddot{\xi}_1, \ddot{\xi}_2, \ddot{\xi}_3]^{\mathrm{T}} + [\ddot{\xi}_4, \ddot{\xi}_5, \ddot{\xi}_6]^{\mathrm{T}} \times \mathbf{r}_{\bar{x}}^h. \end{aligned} \tag{3.9}$$

This, for example, allows one to evaluate vertical accelerations at different locations on the ship and calculate the motion sickness incidence (MSI) index—see Chapter 7.

3.3.4 Angles About the z-axis

Let us define the *total ship velocity vector* (in the b-frame) as

$$\bar{\mathbf{u}} = [\bar{u}, \bar{v}, \bar{w}]^{\mathrm{T}}, \tag{3.10}$$

such that

$$\begin{aligned} u &= \bar{u} + \delta u \\ v &= \bar{v} + \delta v \\ w &= \bar{w} + \delta w. \end{aligned}$$

For surface vessels $\bar{w}$ =0, and for slow manoeuvring the surge and sway velocities $\bar{u}$ and $\bar{v}$ are the approximately the same in both the b- and the h-frame. In this case, the surge velocity is denoted

$$U \equiv \bar{u}^h \approx \bar{u},$$

which is the notation commonly used in seakeeping and hydrodynamics.

Then, for the angles about the z-axis of surface ships, it is convenient to distinguish between the following (see Figure 3.3):

- **Heading or yaw angle** ψ. This is the first rotation of the sequence of rotations (Euler angles) that take the n- into the b-frame—see Section 3.3.2.

- **Seakeeping or yaw perturbation angle** ξ_6. This is the first rotation of the sequence of rotations (Euler angles) that take the h- into the b-frame—see Section 3.3.3.

- **Drift angle** β. This is the angle between the positive x-axis of the b-frame and the average ship velocity vector $\bar{\mathbf{u}}$, *i.e.*

$$\beta = \arctan\left(\frac{\bar{v}}{\bar{u}}\right), \tag{3.11}$$

  provided $\bar{u}$ is not zero.

- **Course angle** γ. This is the angle between the positive x-axis of the n-frame the ship velocity vector $\bar{\mathbf{u}}$.

3.4 Velocity Transformations

3.4.1 Rotation Matrices

The transformation of vector coordinates between different frames is performed via appropriate transformation matrices. Following [62], the generic vector $\mathbf{r}$, can be expressed in either the frame a or the frame b as

$$\mathbf{r} = \sum_{i=1}^{3} r_i^a \mathbf{a}_i \quad \text{and} \quad \mathbf{r} = \sum_{i=1}^{3} r_i^b \mathbf{b}_i, \tag{3.12}$$

where the vectors $\mathbf{a}_i$ and $\mathbf{b}_i$ are the unit vectors along the axis of the reference frames a and b respectively, and $r_i^a = \mathbf{r} \cdot \mathbf{a}_i$ and $r_i^b = \mathbf{r} \cdot \mathbf{b}_i$. Then,

$$r_i^a = \mathbf{r} \cdot \mathbf{a}_i = \left(\sum_{i=1}^{3} r_i^b \mathbf{b}_i\right) \cdot \mathbf{a}_i = \sum_{i=1}^{3} r_i^b (\mathbf{a}_i \cdot \mathbf{b}_i). \tag{3.13}$$

This leads to the notation $\mathbf{R}_b^a$ for transformation matrix with entries $\{\mathbf{a}_i \cdot \mathbf{b}_i\}$, which takes vectors expressed in the frame b to the frame a:

$$\mathbf{r}^a = \mathbf{R}_b^a \, \mathbf{r}^b. \tag{3.14}$$

This matrix is called the *rotation matrix* from b to a.
Rotation matrices are elements in $SO(3)$, the *special orthogonal group of order 3:*

$$SO(3) = \left\{ \mathbf{R} | \mathbf{R} \in \mathbb{R}^{3\times 3},\ \mathbf{R}\mathbf{R}^{\mathrm{T}} = \mathbf{I}_{3\times 3}, \text{and} \det(\mathbf{R}){=}1 \right\}. \tag{3.15}$$

Thus,

$$(\mathbf{R}_b^a)^{-1} = (\mathbf{R}_b^a)^{\mathrm{T}} = \mathbf{R}_a^b.$$

3.4.2 Kinematic Transformation Between the *b*- and the *n*-frame

The transformation between the body-fixed linear velocities and the time derivative of the positions in the n-frame can be expressed as

$$\begin{bmatrix} \dot{n} \\ \dot{e} \\ \dot{d} \end{bmatrix} = \mathbf{R}_b^n(\mathbf{\Theta}_{nb}) \begin{bmatrix} u \\ v \\ w \end{bmatrix}, \tag{3.16}$$

where *linear-velocity transformation matrix* $\mathbf{R}_b^n(\mathbf{\Theta}_{nb})$ is given by [66, 67]

$$\mathbf{R}_b^n(\mathbf{\Theta}_{nb}) = \begin{bmatrix} c\psi c\theta & -s\psi c\phi + c\psi s\theta s\phi & s\psi s\phi + c\psi c\phi s\theta \\ s\psi c\theta & c\psi c\phi + s\phi s\theta s\psi & -c\psi s\phi + s\psi c\phi s\theta \\ -s\theta & c\theta s\phi & c\theta c\phi \end{bmatrix}, \tag{3.17}$$

where $s \equiv \sin(\cdot)$ and $c \equiv \cos(\cdot)$, and

$$\mathbf{R}_n^b(\mathbf{\Theta}_{nb}) = \mathbf{R}_b^n(\mathbf{\Theta}_{nb})^{-1} = \mathbf{R}_b^n(\mathit{\Theta}_{nb})^{\mathrm{T}}. \tag{3.18}$$

This transformation is the result of three consecutive rotations about the principal axes [67]:

$$\mathbf{R}_b^n(\mathbf{\Theta}_{nb}) \triangleq \mathbf{R}_{z,\psi}\mathbf{R}_{y,\theta}\mathbf{R}_{x,\phi}, \tag{3.19}$$

with,

$$\mathbf{R}_{x,\phi} \triangleq \begin{bmatrix} 1 & 0 & 0 \\ 0 & \mathrm{c}\phi & -\mathrm{s}\phi \\ 0 & \mathrm{s}\phi & \mathrm{c}\phi \end{bmatrix}, \quad \mathbf{R}_{y,\theta} \triangleq \begin{bmatrix} \mathrm{c}\theta & 0 & \mathrm{s}\theta \\ 0 & 1 & 0 \\ -\mathrm{s}\theta & 0 & \mathrm{c}\theta \end{bmatrix}, \quad \mathbf{R}_{z,\psi} \triangleq \begin{bmatrix} \mathrm{c}\psi & -\mathrm{s}\psi & 0 \\ \mathrm{s}\psi & \mathrm{c}\psi & 0 \\ 0 & 0 & 1 \end{bmatrix}. \tag{3.20}$$

The transformation between the body-fixed angular velocity $\boldsymbol{\omega}_{nb}^b$ and the time derivative of the Euler angles $\dot{\mathbf{\Theta}}_{nb}$ can be expressed as

$$\dot{\boldsymbol{\Theta}}_{nb} = \mathbf{T}_{\boldsymbol{\Theta}}(\boldsymbol{\Theta}_{nb})\,\boldsymbol{\omega}_{nb}^{b}, \quad \text{or} \quad \begin{bmatrix}\dot{\phi}\\ \dot{\theta}\\ \dot{\psi}\end{bmatrix} = \mathbf{T}_{\boldsymbol{\Theta}}(\boldsymbol{\Theta}_{nb}) \begin{bmatrix}p\\ q\\ r\end{bmatrix}, \tag{3.21}$$

where *angular-velocity transformation matrix* $\mathbf{T}_{\boldsymbol{\Theta}}(\boldsymbol{\Theta}_{nb})$ and its inverse are given by

$$\mathbf{T}_{\boldsymbol{\Theta}}(\boldsymbol{\Theta}_{nb}) \triangleq \begin{bmatrix}1 & s\phi t\theta & c\phi t\theta\\ 0 & c\phi & -s\phi\\ 0 & s\phi/c\theta & c\phi/c\theta\end{bmatrix}, \quad \mathbf{T}_{\boldsymbol{\Theta}}(\boldsymbol{\Theta}_{nb})^{-1} \triangleq \begin{bmatrix}1 & 0 & -s\theta\\ 0 & c\phi & c\theta s\phi\\ 0 & -s\phi & c\phi c\theta\end{bmatrix} \tag{3.22}$$

with $t \equiv \tan(\cdot)$ and $c\theta \neq 0$.

This transformation can be obtained from [67]:

$$\boldsymbol{\omega}_{nb}^{b} = \begin{bmatrix}p\\ q\\ r\end{bmatrix} = \begin{bmatrix}\dot{\phi}\\ 0\\ 0\end{bmatrix} + \mathbf{R}_{x,\phi}^{\mathrm{T}} \begin{bmatrix}0\\ \dot{\theta}\\ 0\end{bmatrix} + \mathbf{R}_{x,\phi}^{\mathrm{T}}\mathbf{R}_{y,\theta}^{\mathrm{T}} \begin{bmatrix}0\\ 0\\ \dot{\psi}\end{bmatrix} \triangleq \mathbf{T}_{\boldsymbol{\Theta}}(\boldsymbol{\Theta}_{nb})^{-1}\,\dot{\boldsymbol{\Theta}}. \tag{3.23}$$

Notice that $\mathbf{T}_{\boldsymbol{\Theta}}(\boldsymbol{\Theta}_{nb})^{-1} \neq \mathbf{T}_{\boldsymbol{\Theta}}(\boldsymbol{\Theta}_{nb})^{\mathrm{T}}$, and also that, $\mathbf{T}_{\boldsymbol{\Theta}}(\boldsymbol{\Theta}_{nb})$ is not defined for $\theta = \pm\pi/2$. This is never a problem for surface vessels, but could be of concern for underwater vehicles in some cases. In such cases, the singularity can be avoided using unit quaternions [67].

Using the above, we can define the following *kinematic transformation for the manoeuvring coordinates*:

$$\dot{\boldsymbol{\eta}} = \mathbf{J}_{b}^{n}(\boldsymbol{\Theta}_{nb})\,\boldsymbol{\nu} = \begin{bmatrix}\mathbf{R}_{b}^{n}(\boldsymbol{\Theta}_{nb}) & \mathbf{0}_{3\times 3}\\ \mathbf{0}_{3\times 3} & \mathbf{T}_{\boldsymbol{\Theta}}(\boldsymbol{\Theta}_{nb})\end{bmatrix}\boldsymbol{\nu}. \tag{3.24}$$

To transform the accelerations, we need to consider the time derivatives of (3.16) and (3.21). For example,

$$\begin{aligned}[\dot{u},\dot{v},\dot{w}]^{\mathrm{T}} &= \mathbf{R}_{n}^{b}(\boldsymbol{\Theta}_{nb})\,[\ddot{n},\ddot{e},\ddot{d}]^{\mathrm{T}} + \dot{\mathbf{R}}_{n}^{b}(\boldsymbol{\Theta}_{nb})\,[\dot{n},\dot{e},\dot{d}]^{\mathrm{T}}\\ [\dot{p},\dot{q},\dot{r}]^{\mathrm{T}} &= \mathbf{T}_{\boldsymbol{\Theta}}(\boldsymbol{\Theta})\,[\ddot{\phi},\ddot{\theta},\ddot{\psi}]^{\mathrm{T}} + \dot{\mathbf{T}}_{\boldsymbol{\Theta}}(\boldsymbol{\Theta})\,[\dot{\phi},\dot{\theta},\dot{\psi}]^{\mathrm{T}}.\end{aligned} \tag{3.25}$$

3.4.3 Kinematic Transformation Between the *b*- and the *h*-frame

The transformation for the generalized velocity vector $\boldsymbol{\nu}$ (given in the b-frame) into the generalised velocity vector $\dot{\boldsymbol{\xi}} = [(\mathbf{v}_{o_h}^{h})^{\mathrm{T}}, (\boldsymbol{\omega}_{hb}^{h})^{\mathrm{T}}]^{\mathrm{T}}$ in the h-frame is performed in two steps: *a translation* and *a rotation*.

Let us consider the case of zero forward speed first. The linear velocity of $\bar{o}_h$ in the b-frame is given by

$$\mathbf{v}_{\bar{o}_h}^{b} = \mathbf{v}_{o_b}^{b} + \boldsymbol{\omega}_{nb}^{b} \times \mathbf{r}_{\bar{o}_h}^{b}, \tag{3.26}$$

where $\bar{o}_h$ is the equilibrium position of o_h with respect to to the b-frame (remember that the h-frame is not fixed to the ship and therefore the vector $\mathbf{r}^b_{o_h}$ is time varying, so we consider $\mathbf{r}^b_{\bar{o}_h}$).

Since the h-frame is considered inertial and its relative angular velocity with respect to the n-frame is approximately zero (*i.e.* $\boldsymbol{\omega}^b_{nh} \approx \mathbf{0}$), the following relationship holds:

$$\boldsymbol{\omega}^b_{hb} = \boldsymbol{\omega}^b_{nb} - \boldsymbol{\omega}^b_{nh} \approx \boldsymbol{\omega}^b_{nb}. \tag{3.27}$$

By expressing the cross product in (3.26) in terms of a skew-symmetric matrix

$$\mathbf{S}(\mathbf{r}^b_{\bar{o}_h}) = -\mathbf{S}(\mathbf{r}^b_{\bar{o}_h})^{\mathrm{T}} = \begin{bmatrix} 0 & -z^b_{\bar{o}_h} & y^b_{\bar{o}_h} \\ z^b_{\bar{o}_h} & 0 & -x^b_{\bar{o}_h} \\ -y^b_{\bar{o}_h} & x^b_{\bar{o}_h} & 0 \end{bmatrix}, \tag{3.28}$$

Expressions (3.26) and (3.27) can be combined as

$$\begin{bmatrix} \mathbf{v}^b_{\bar{o}_h} \\ \boldsymbol{\omega}^b_{hb} \end{bmatrix} = \mathbf{H}(\mathbf{r}^b_{\bar{o}_h}) \begin{bmatrix} \mathbf{v}^b_{o_b} \\ \boldsymbol{\omega}^b_{nb} \end{bmatrix}, \tag{3.29}$$

where is the *screw transformation*:

$$\mathbf{H}(\boldsymbol{\lambda}) \triangleq \begin{bmatrix} \mathbf{I}_{3\times 3} & \mathbf{S}(\lambda)^{\mathrm{T}} \\ \mathbf{0}_{3\times 3} & \mathbf{I}_{3\times 3} \end{bmatrix}, \qquad \boldsymbol{\lambda} \in \mathbb{R}^3. \tag{3.30}$$

The linear velocity transformation between the b- and the h-frame is given by the following rotation

$$\mathbf{v}^h_{\bar{o}_h} = \mathbf{R}^h_b(\boldsymbol{\Theta}_{hb})\mathbf{v}^b_{\bar{o}_h}, \tag{3.31}$$

where $\mathbf{R}^h_b(\boldsymbol{\Theta}_{hb})$ is of the form of (3.17).

In a similar way, the angular velocity transformation is given by

$$\boldsymbol{\omega}^h_{hb} = \mathbf{R}^h_b(\boldsymbol{\Theta}_{hb})\boldsymbol{\omega}^b_{hb}, \tag{3.32}$$

where $\mathbf{T}_{\boldsymbol{\Theta}}(\boldsymbol{\Theta}_{hb})$ is of the form of (3.22).

By combining (3.31), (3.32) and (3.29), we obtain

$$\begin{bmatrix} \mathbf{v}^h_{\bar{o}_h} \\ \boldsymbol{\omega}^h_{hb} \end{bmatrix} = \begin{bmatrix} \mathbf{R}^h_b(\boldsymbol{\Theta}_{hb}) & \mathbf{0}_{3\times 3} \\ \mathbf{0}_{3\times 3} & \mathbf{R}^h_b(\boldsymbol{\Theta}_{hb}) \end{bmatrix} \mathbf{H}(\mathbf{r}^b_{\bar{o}_h}) \begin{bmatrix} \mathbf{v}^b_{o_b} \\ \boldsymbol{\omega}^b_{nb} \end{bmatrix}. \tag{3.33}$$

Thus, the sought transformation is obtained by combining the above expression with $\dot{\boldsymbol{\Theta}}_{hb} = \mathbf{T}_{\boldsymbol{\Theta}}(\boldsymbol{\Theta}_{hb})\boldsymbol{\omega}^b_{nb}$:

$$\dot{\boldsymbol{\xi}} = \mathbf{J}^h_b(\boldsymbol{\Theta}_{hb}, \mathbf{r}^b_{\bar{o}_h})\boldsymbol{\nu}, \tag{3.34}$$

with

$$\mathbf{J}^h_b(\boldsymbol{\Theta}_{hb}, \mathbf{r}^b_{\bar{o}_h}) \triangleq \begin{bmatrix} \mathbf{R}^h_b(\boldsymbol{\Theta}_{hb}) & \mathbf{R}^h_b(\boldsymbol{\Theta}_{hb})\mathbf{S}(\mathbf{r}^b_{\bar{o}_h})^{\mathrm{T}} \\ \mathbf{0}_{3\times 3} & \mathbf{T}_{\boldsymbol{\Theta}}(\boldsymbol{\Theta}_{hb}) \end{bmatrix}. \tag{3.35}$$

For the case of forward velocity, let us separate the body-fixed velocity into a slowly-varying component and an oscillatory component induced by the wave motion:

$$\boldsymbol{\nu} = \bar{\boldsymbol{\nu}} + \delta\boldsymbol{\nu}, \tag{3.36}$$

with

$$\begin{aligned} \bar{\boldsymbol{\nu}} &= [U, 0, 0, 0, 0, 0]^{\mathrm{T}} \\ \delta\boldsymbol{\nu} &= [\delta u, \delta v, \delta w, \delta p, \delta q, \delta r]^{\mathrm{T}} \\ &= [\delta u, v, w, p, q, r]^{\mathrm{T}}. \end{aligned} \tag{3.37}$$

Then the kinematic transformation between the b- and the h-frame for the case of forward speed is given by

$$\boxed{\dot{\boldsymbol{\xi}} = \mathbf{J}_b^h(\boldsymbol{\Theta}_{hb}, \mathbf{r}_{\bar{o}_h}^b)(\boldsymbol{\nu} - \bar{\boldsymbol{\nu}}),} \tag{3.38}$$

with $\mathbf{J}_b^h(\delta\boldsymbol{\Theta}, \mathbf{r}_{\bar{o}_h}^b)$ given in (3.35).

Note that for small angles, *i.e.* $\boldsymbol{\Theta}_{hb} \approx \mathbf{0}$ small, the following approximations can be used:

$$\begin{aligned} \mathbf{R}_b^h(\boldsymbol{\Theta}_{hb}) &\approx \mathbf{I}_{3\times 3} \\ \mathbf{T}_{\boldsymbol{\Theta}}(\boldsymbol{\Theta}_{hb}) &\approx \mathbf{I}_{3\times 3} \\ \mathbf{J}_b^h(\boldsymbol{\Theta}_{hb}, \mathbf{r}_{\bar{o}_h}^b) &\approx \mathbf{H}(\mathbf{r}_{\bar{o}_h}^b). \end{aligned} \tag{3.39}$$

If we expand the this kinematic transformation, consider small angles, assume a slender ship (so the DOF 1,3,5 can be decoupled from 2,4,6) and keep only the linear terms, we obtain

$$\dot{\xi}_1 \approx \delta u + z_{oh}^b \delta q \tag{3.40}$$

$$\dot{\xi}_2 \approx \delta v + x_{oh}^b \delta r - z_{oh}^b \delta p + U\delta\psi \tag{3.41}$$

$$\dot{\xi}_3 \approx \delta w - x_{oh}^b \delta q - U\delta\theta \tag{3.42}$$

$$\dot{\xi}_4 = \delta p \tag{3.43}$$

$$\dot{\xi}_5 = \delta q \tag{3.44}$$

$$\dot{\xi}_6 = \delta r. \tag{3.45}$$

The time derivative of (3.40)-(3.45) gives

$$\ddot{\xi}_1 = \dot{\delta u} + z_{oh}^b \dot{\delta q} \tag{3.46}$$

$$\ddot{\xi}_2 = \dot{\delta v} + x_{oh}^b \dot{\delta r} - z_{oh}^b \dot{\delta p} + U\delta r \tag{3.47}$$

$$\ddot{\xi}_3 = \dot{\delta w} - x_{oh}^b \dot{\delta q} - U\delta q \tag{3.48}$$

$$\ddot{\xi}_4 = \dot{\delta p} \tag{3.49}$$

$$\ddot{\xi}_5 = \dot{\delta q} \tag{3.50}$$

$$\ddot{\xi}_6 = \dot{\delta r}. \tag{3.51}$$

If we assume *sinusoidal* motions, the following relationships hold for yaw (and similarly for pitch):

$$\begin{aligned} \delta\psi &= \sin\omega_e t \\ r &= \omega_e \cos\omega_e t \\ \dot{r} &= -\omega_e^2 \sin\omega_e t = -\omega_e^2 \delta\psi, \end{aligned} \tag{3.52}$$

which can be used to express

$$\delta\psi = -\frac{1}{\omega_e^2}\dot{r}, \quad \delta\theta = -\frac{1}{\omega_e^2}\dot{q}. \tag{3.53}$$

Substituting these in (3.40)-(3.45), we obtain

$$\dot{\xi}_1 \approx \delta u + z_{oh}^b \delta q \tag{3.54}$$

$$\dot{\xi}_2 \approx \delta v + x_{oh}^b \delta r - z_{oh}^b \delta p - U\frac{1}{\omega_e^2}\dot{\delta r} \tag{3.55}$$

$$\dot{\xi}_3 \approx \delta w - x_{oh}^b \delta q + U\frac{1}{\omega_e^2}\dot{\delta q} \tag{3.56}$$

$$\dot{\xi}_4 = \delta p \tag{3.57}$$

$$\dot{\xi}_5 = \delta q \tag{3.58}$$

$$\dot{\xi}_6 = \delta r. \tag{3.59}$$

Expressions (3.54)-(3.59) and (3.46)-(3.51) represent a linear approximation of (3.38), and can be written in a compact form as follows:

$$\dot{\boldsymbol{\xi}} = \mathbf{J}_b^h \boldsymbol{\delta\nu} - \frac{U}{\omega_e^2}\mathbf{L}\dot{\boldsymbol{\delta\nu}} \tag{3.60}$$

$$\ddot{\boldsymbol{\xi}} = \mathbf{J}_b^h \dot{\boldsymbol{\delta\nu}} + U\mathbf{L}\boldsymbol{\delta\nu}, \tag{3.61}$$

where

$$\mathbf{J}_b^h \triangleq \mathbf{J}_b^h(\mathbf{0}, \mathbf{r}_{\bar{o}_h}^b) = \mathbf{H}(\mathbf{r}_{\bar{o}_h}^b), \tag{3.62}$$

with $\mathbf{H}(\mathbf{r}_{\bar{o}_h}^b)$ given in (3.30), and

$$\mathbf{L} \triangleq \begin{bmatrix} 0&0&0&0&0&0 \\ 0&0&0&0&0&1 \\ 0&0&0&0&-1&0 \\ 0&0&0&0&0&0 \\ 0&0&0&0&0&0 \\ 0&0&0&0&0&0 \end{bmatrix}. \tag{3.63}$$

4

Ship Kinetics

by T. Perez and T.I. Fossen

Chapter 3 reviewed the kinematics of ship motion, *i.e.* the geometrical aspects of motion: variables, reference frames and transformations. This chapter reviews the kinetics of ship motion, *i.e.* the study of the forces acting on the ship and the motion they produce. By combining the material presented Chapter 3 with that of this chapter, one can obtain ship dynamic models for control design and testing (*cf.* Section 1.3).

4.1 An Overview of Ship Modeling for Control

As discussed in [174], the models for ship motion control system design use superposition of either motion or force. Therefore in each case, magnitudes can be conceptually decomposed as

$$X = X_{\mathrm{w}} + \bar{X}, \qquad \bar{X} = X_{\mathrm{s-vd}} + X_{\mathrm{c}}. \tag{4.1}$$

- **First-order wave-induced force/motion (w)**. This force/motion is oscillatory. This is commonly modelled as a time series disturbance obtained by combining the wave spectrum with the vessel *Force Response Amplitude Operators* (Force RAO) or the *Motion Response Amplitude Operators* (Motion RAO), which are transfer functions that map the wave elevation or wave slope into force and motion.
- **Slowly-varying disturbance force/motion (s-vd)**. This force/motion is produced by second-order wave effects (wave mean-drift and slowly-varying forces), current and wind.
- **Control-induced force/motion (c)**. This is the force/motion induced by the control system, which is usually designed to counteract only the the effect of the slowly-varying disturbances.

The motion superposition model is the most commonly adopted model for control system design—see Figure 4.1. In this model, a manoeuvring model is used to describe the relationship between the control action and the motion induced by this control action whereas seakeeping models are used to describe the motion due to the waves.

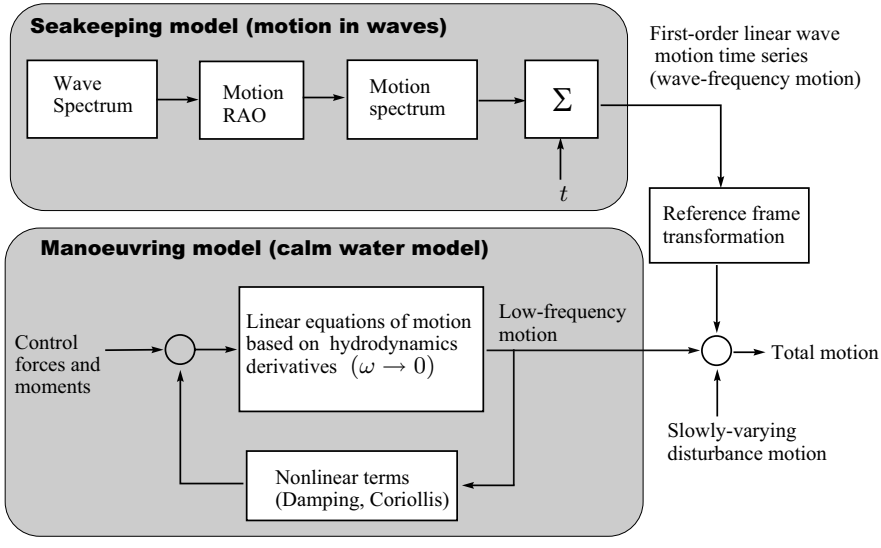

Fig. 4.1. Motion superposition model of a marine vessel [174].

The type of model shown in Figure 4.1 presents two shortcomings. The first one is that the model may not be used for multibody system interactions. This requires energy exchange, *i.e.,* it requires elements with common forces and speeds, and this is not captured by a models that uses wave-induced motion as a disturbance. This issue, however, is more relevant to marine operations like up-loading and deploying heavy equipment, pipe-lying, positioning of deep suspended loads, than to the problems considered in this book. The second shortcoming of this type of model is that the manoeuvring part does not incorporate fluid memory effects associated with the wave-frequency induced motion. Indeed, the radiation forces due to the frequency dependent mass and damping of the ship are only considered in the seakeeping model (this is embedded in the motion RAO). This results in miss-modelled dynamics, which are of interest for ship motion control in a seaway.

An alternative approach consists of using a model with force superposition rather than motion superposition, as illustrated in Figure 4.2. In this model, the Force RAO are combined with the sea spectrum to give the wave-excitation forces. Also, a time-domain representation is used for the fluid memory effects

associated with the wave-frequency motion of the ship. This time domain representation uses a convolution integral to compute the radiation damping forces. Therefore, these forces are computed using both the wave- and control-induced motion instead of only the wave-induced motion as in the model shown in Figure 4.1. This is key issue for obtaining good models for wave-motion damping control problems like roll stabilisation.

The model shown in Figure 4.2 is well known in marine technology and it is part of the state of art time-domain ship motion simulators. However, its use for control system design has not yet been widely adopted. Recent reported results [127] proposed a state-space representation for the convolution integral which results in model amenable to control system design tools.

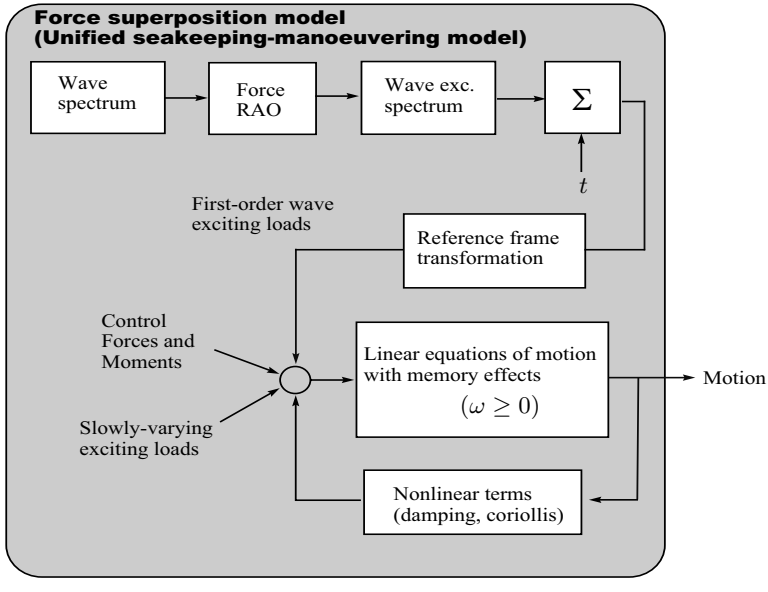

Fig. 4.2. Force superposition model of a marine vessel [174].

In the rest of the chapter, we will present and discuss the elements shown in Figures 4.1 and 4.2. We will first describe the seakeeping and manoeuvring models so as to obtain the classical motion superposition model shown in Figure 4.1. Then, we will discuss the elements of the force superposition model shown in Figure 4.2.

4.2 Seakeeping Theory Models

As already mentioned in Section 3.3.3, seakeeping theory studies the motion of surface vessels in waves. The motion of a ship in a seaway is the response to sea loads, which are forces and moments that arise due to changes in pressure over the surface of the hull. If the sea state is not extreme, the motion responses can be considered within a linear framework. This allows one to apply the principle of superposition to study ship motion: the motion due to an irregular sea can be described as the summation of the responses to many regular waves. This concept was introduced to the field of ship motion study by St. Denis and Pierson in the 1950s [213], as a method to predict ship responses in a realistic seaway.

The *linear seakeeping theory* of ship motion makes three essential assumptions:

- The sea surface elevation is assumed to be a realisation of an ergodic Gaussian stochastic process with zero mean. Thus, the process is entirely described by its power spectral density—the sea spectrum.
- The wave-excitation loads and ship motion response are assumed to be linear.
- The ship keeps a steady course and moves at a constant average speed (which includes the case of zero speed).

The first assumption was already discussed in Chapter 2. The second assumption allows one to obtain the power spectral density of the wave-excitation loads and the motion components by multiplying the response amplitude operators (force and motion RAO) by the wave spectrum. Since the excitation is Gaussian and the motion response linear, the motion is also Gaussian; then, once the motion spectrum is obtained, all the statistics of motion can be calculated and data for time series generation be obtained.

The linear assumption is a limitation since it neglects viscous effects (which need to be incorporated separately) and characteristics of a real free surface. Despite this, linear theory has proven to be a tool that yields reasonable predictions for analysis at preliminary stages of both ship and ship motion control system design. For roll motion, in particular, viscous effects play a very important role because of bilge keels and appendages, and these effects cannot be neglected for they provide most of the total roll damping. This leads to nonlinearities, which can be reduced to linear equivalent terms via stochastic or equivalent linearisation [135, 182, 192]; and hence, the problem can be still considered within a linear framework.

4.2.1 Equations of Motion and Hydrodynamic Forces in the *h*-frame

A distinctive characteristic of seakeeping theory is the use the hydrodynamic frame, h-frame (x_h, y_h, z_h), to describe the motion of the fluid and the ship—see Section 3.1. Since, the h-frame is inertial, the *vector equation of motion* in this frame is

$$\mathbf{M}^h_{RB}\ddot{\boldsymbol{\xi}} = \boldsymbol{\tau}^h_{\text{hyd}}. \tag{4.2}$$

The coordinates $\boldsymbol{\xi}$ are the generalised perturbation coordinates or seakeeping coordinates given in the h-frame defined in Section 3.3.3. The components of the vector $\boldsymbol{\tau}^h_{\text{hyd}}$ are the generalised hydrodynamic forces (forces and moments) for the six degrees of freedom expressed in the h-frame. The matrix $\mathbf{M}^h_{RB}$ is the generalised rigid-body mass matrix (mass and inertia) with respect to the h-frame:

$$\begin{aligned}\mathbf{M}^h_{RB} &\triangleq \begin{bmatrix} m\mathbf{I}_{3\times 3} & -m\mathbf{S}(\mathbf{r}^h_g) \\ m\mathbf{S}(\mathbf{r}^h_g) & \mathbf{I}^h \end{bmatrix} \\ &= \begin{bmatrix} m & 0 & 0 & 0 & mz^h_g & -my^h_g \\ 0 & m & 0 & -mz^h_g & 0 & mx^h_g \\ 0 & 0 & m & my^h_g & -mx^h_g & 0 \\ 0 & -mz^h_g & my^h_g & I^h_x & -I^h_{xy} & -I^h_{xz} \\ mz^h_g & 0 & -mx^h_g & -I^h_{yx} & I^h_y & -I^h_{yz} \\ -my^h_g & mx_g & 0 & -I^h_{zx} & -I^h_{zy} & I^h_z \end{bmatrix}. \end{aligned} \tag{4.3}$$

The mass of the ship m can be calculated as the product of the water density and the displaced volume ∇, *i.e.* $m = \rho\nabla$ (where ρ is the water density). The coordinates of the centre of gravity with respect to the h-frame are given by the vector $\mathbf{r}^h_g = [x^h_g, y^h_g, z^h_g]^{\mathrm{T}}$, and $\mathbf{S}(\cdot)$ is the skew-symmetric matrix defined in (3.3). The inertia tensor with respect to the h-frame $\mathbf{I}^h$ is

$$\mathbf{I}^h \triangleq \begin{bmatrix} I^h_{xx} & -I^h_{xy} & -I^h_{xz} \\ -I^h_{yx} & I^h_{yy} & -I^h_{yz} \\ -I^h_{zx} & -I^h_{zy} & I^h_{zy} \end{bmatrix}, \quad \mathbf{I}^h = (\mathbf{I}^h)^{\mathrm{T}} > 0, \tag{4.4}$$

where the moments and products of inertia can be calculated using the displaced volume as follows:

$$\begin{aligned} I_{xx} &= \int_\nabla [(y^h)^2 + (x^h)^2]\rho dV, \qquad I_{xy} = I_{yx} = \int_\nabla (y^h x^h)\rho dV, \\ I_{yy} &= \int_\nabla [(z^h)^2 + (x^2]\rho dV, \qquad I_{xz} = I_{zx} = \int_\nabla (x^h z^h)\rho dV, \\ I_{zz} &= \int_\nabla [(y^h)^2 + (z^h)^2]\rho dV, \qquad I_{yz} = I_{zy} = \int_\nabla (y^h z^h)\rho dV. \end{aligned} \tag{4.5}$$

The total *hydrodynamic force vector* $\boldsymbol{\tau}_H$ is assumed to be the linear combinations of the following components [63]:

$$\boldsymbol{\tau}_{\text{hyd}} = \boldsymbol{\tau}_{1\text{w}} + \boldsymbol{\tau}_{2\text{w}} + \boldsymbol{\tau}_{\text{r}} + \boldsymbol{\tau}_{\text{v}} + \boldsymbol{\tau}_{\text{hs}}. \tag{4.6}$$

- **First-order wave excitation forces** ($\boldsymbol{\tau}_{1\text{w}}$). These forces are the zero-mean oscillatory forces caused by the waves, which are separated into two components. The first component gives the, so-called, *Froude-Kriloff forces*, which are forces due to the incident waves under the assumption that the hull is restrained from moving and that the presence of the hull does not disturb the flow field. The second effect is a correction to account for the modification of the flow field due to the hull; otherwise there would be water mass transfer through the hull. This second component gives the so-called *diffraction forces*.

- **Second-order wave excitation forces** ($\boldsymbol{\tau}_{2\text{w}}$). These forces include mean wave-drift loads, slowly varying (difference frequencies) and rapidly varying (sum frequencies) wave loads. Depending on the ship motion control problem considered these forces represent a significant contribution of the wave excitation loads.

- **Radiation forces** ($\boldsymbol{\tau}_{\text{r}}$). These forces appear as a consequence of the change in the momentum of the fluid and the waves generated due to the motion of the hull. These forces are proportional to the accelerations of and velocities the ship. Due to this, the radiation forces are separated into the so-called *added-mass forces* (forces proportional to accelerations) and *potential-damping forces* (forces proportional to velocities).

- **Viscous forces** ($\boldsymbol{\tau}_{\text{v}}$). These are nonlinear damping forces that appear due to nonlinear non-conservative phenomena by which kinetic energy of the hull is transferred to the fluid due to viscous effects (skin friction, flow separation and eddy making). These forces are depend nonlinearly on the relative velocities between the hull and the fluid.

- **Hydrostatic forces** ($\boldsymbol{\tau}_{\text{hs}}$). These are restoring forces due to gravity and buoyancy that tend to preserve the equilibrium of the ship.

Except for the viscous forces, the rest can be studied within a linear framework. Indeed, the wave excitation forces can be obtained by considering linear potential flow theory. As already discussed in Section 2.1.4, this theory seeks a potential function $\Phi(x, y, z, t)$, that satisfies the Laplace equation in the fluid and boundary conditions on the surface of the hull, on the free surface of the water and at the seafloor. Due to linearity, this potential is separated into a radiation potential and a wave-excitation potential:

$$\Phi = \Phi_{\mathrm{r}} + \Phi_{\mathrm{w}}. \tag{4.7}$$

The pressure can be calculated by substituting the potential into the linearised Bernoulli Equation (see Section 2.1.4), and the hydrodynamic forces and moments are obtained by integrating the pressure over the wetted surface Sw of the hull. Thus, the components, for each degree of freedom, of the radiation forces can obtained as follows:

$$\tau_{\mathrm{r}i}^{h} = \begin{cases} -\iint_{Sw} \left(\frac{\partial \Phi_{\mathrm{r}}}{\partial t} + gz\right)(\mathbf{n})_i \, ds & i = 1, 2, 3. \\ -\iint_{Sw} \left(\frac{\partial \Phi_{\mathrm{r}}}{\partial t} + gz\right)(\mathbf{r} \times \mathbf{n})_i \, ds & i = 4, 5, 6. \end{cases} \tag{4.8}$$

Where $\mathbf{n} = [n_1, n_2, n_3]^{\mathrm{T}}$ is a unit vector normal to the wetted surface of the hull and positive into the fluid. The notation $(\mathbf{n})_i$ and $(\mathbf{r} \times \mathbf{n})_i$ refers to the i-th component of $\mathbf{n}$ and $\mathbf{r} \times \mathbf{n}$ respectively.

The first-order wave excitation forces and moments are obtained in a similar way using the wave-excitation potential:

$$\tau_{1\mathrm{w}i}^{h} = \begin{cases} -\iint_{Sw} \left(\frac{\partial \Phi_{1\mathrm{w}}}{\partial t} + gz\right)(\mathbf{n})_i \, ds & i = 1, 2, 3. \\ -\iint_{Sw} \left(\frac{\partial \Phi_{1\mathrm{w}}}{\partial t} + gz\right)(\mathbf{r} \times \mathbf{n})_i \, ds & i = 4, 5, 6. \end{cases} \tag{4.9}$$

The first-order wave excitation potential is further separated into the incident potential and the diffraction potential $\Phi_{1\mathrm{w}} = \Phi_{\mathrm{I}} + \Phi_{\mathrm{D}}$. The incident potential corresponds to the undisturbed incident waves, *cf.* (2.26). The integration of the pressure due to this potential gives the so-called Froude-Kriloff forces, whereas the integration of the pressure due to diffraction potential gives the wave diffraction forces—see [195, 63] for details. Within the first order potential theory, these forces depend linearly on the magnitude of the waves.

As we shall see in the next section, expressions (4.8) and (4.9) can be evaluated numerically for sinusoidal waves using hydrodynamic programs. Because of the linearity assumption made, these forces are proportional to the amplitude of the sinusoidal waves, and the data obtained is tabulated as transfer-function model (force RAO)—see Section 4.2.2.

The second-order wave excitation forces are obtained by integration the pressure due to second order potentials, but this goes beyond the scope of this book. These forces, however, have a little impact for the ship motion control problems considered in this book. The reader is referred to [195, 63] for further details of second-order wave excitation forces.

Finally, the hydrostatic forces and moments are proportional to the displacements $\boldsymbol{\xi}$. Thus, the linearised forces and moments can be expressed as

$$\boldsymbol{\tau}_{\mathrm{hs}}^{h} = \mathbf{G}^{h} \boldsymbol{\xi}. \tag{4.10}$$

The only non-zero linear restoring coefficients are [63]

$$
\begin{aligned}
G^h_{33} &= \rho g A_{WP} \\
G^h_{35} &= C^h_{53} = -\rho g \iint_{A_{WP}} x^h \, ds \\
G^h_{44} &= \rho g \nabla GMt \\
G^h_{55} &= \rho g \nabla GMl,
\end{aligned}
\tag{4.11}
$$

where A_{WP} is the water-plane area, ∇ is the displaced volume, and GMt and GMl are the transverse and longitudinal metacentric heights. Figure 4.3 illustrates the components involved in the roll restoring moment ($\tau^h_{4\text{hs}} = G^h_{44}\xi_4$). In this case, the restoring moment is the product of the righting arm $GZ \approx GMt\,\xi_4$ times the force due to the displaced volume $\rho g \nabla$.

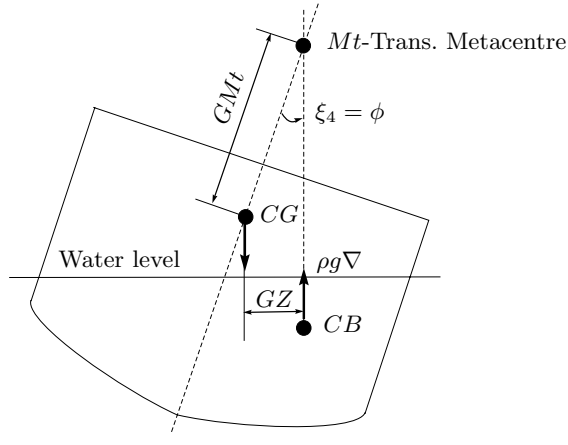

Fig. 4.3. Transverse metacentric height GMt and transverse righting arm GZ.

4.2.2 Wave Force Response Amplitude Operator (Force RAO)

As already mentioned, the wave-excitation forces can be studied using superposition due to the linearity assumption made in seakeeping theory. Therefore, it is common to study the forces and the motion only for sinusoidal excitations and use the frequency domain approach to calculate force transfer functions, which can then be combined with the wave spectrum to obtain the loads for a particular sea state and sailing condition.

If the sea elevation at the origin of the h-frame is given by

$$
\zeta(t) = \bar{\zeta}\cos(\omega_e t + \epsilon), \tag{4.12}
$$

using complex notation we can express the harmonic wave, the wave excitations and the components of motion in terms of the complex variables $\tilde{\zeta}$, $\tilde{\tau}^h_{1\text{w}i}$ and $\tilde{\xi}_i$, such that

$$\begin{aligned}
\zeta(t) &= \Re\left\{\tilde{\zeta} e^{j\omega_e t}\right\} = \Re\left\{\bar{\zeta} e^{j\epsilon} e^{j\omega_e t}\right\} \\
\tau^h_{1\mathrm{w}i}(t) &= \Re\left\{\tilde{\tau}^h_{1\mathrm{w}i}\, e^{j\omega_e t}\right\} = \Re\left\{|\tilde{\tau}^h_{1\mathrm{w}i}|\, e^{j(\arg\tilde{\tau}^h_{1\mathrm{w}i}+\epsilon)}\, e^{j\omega_e t}\right\}, \\
\xi_i(t) &= \Re\left\{\tilde{\xi}_i\, e^{j\omega_e t}\right\} = \Re\left\{|\tilde{\xi}_i|\, e^{j(\arg\tilde{\xi}_i+\epsilon)}\, e^{j\omega_e t}\right\},
\end{aligned} \tag{4.13}$$

where $\Re\{\cdot\}$ denotes the real part of the argument. Using these, we can define the *wave-force response amplitude operators* (Force RAO) for each degree of freedom as

$$F_i(\omega_e, \chi) = \left|\frac{\tilde{\tau}^h_{1\mathrm{w}i}(\omega_e, \chi)}{\tilde{\zeta}}\right| e^{j \arg \tilde{\tau}^h_{1\mathrm{w}i}(\omega_e, \chi)}, \tag{4.14}$$

or, expressed in the wave frequency domain,

$$F_i(\omega, U, \chi) = \left|\frac{\tilde{\tau}^h_{1\mathrm{w}i}(\omega, U, \chi)}{\tilde{\zeta}}\right| e^{j \arg \tilde{\tau}^h_{1\mathrm{w}i}(\omega, U, \chi)}. \tag{4.15}$$

Note that the complex wave excitation forces $\tilde{\tau}^h_{1\mathrm{w}i}$ depend on the encounter frequency ω_e and also the encounter angle χ.

These force transfer functions can be obtained from standard seakeeping programs, which calculate them based on the geometry of the hull and loading condition. Details of this are beyond the scope of this book; here we will only use of the results of these programs, but the interested reader can see for example [64, 115, 144] and references therein. As an example, Figure 4.4 shows the magnitude of the force RAO in sway for different headings corresponding to the benchmark example given in Appendix B at 15kt.

With these force RAO, one can obtain the power spectral density of the wave loads given the sea spectrum $\mathbf{S}_{\zeta\zeta}(\omega_e, \chi)$:

$$\mathbf{S}_{\tau_{1W}\tau_{1W}i}(\omega_e) = |F_i(\omega_e, \chi)|^2\, \mathbf{S}_{\zeta\zeta}(\omega_e, \chi), \tag{4.16}$$

or simulate first-order wave excitation loads due to irregular seas as

$$\tau^h_{1\mathrm{w}i}(t) = \sum_j |F_i(\omega_{ej}, \chi)|\, \zeta_j \cos(\omega_{ej} + \epsilon + \arg[F_i(\omega_{ej}, \chi)]), \tag{4.17}$$

for $i = 1, 2, \ldots, 6$.

4.2.3 Motion Response Amplitude Operator (Motion RAO)

Apart from evaluating the force RAO, as discussed in the previous section, one can also use the frequency domain approach to evaluate the radiation forces, and then the equation of motion (4.2). This leads to the so-called *motion response amplitude operators* (motion RAO)

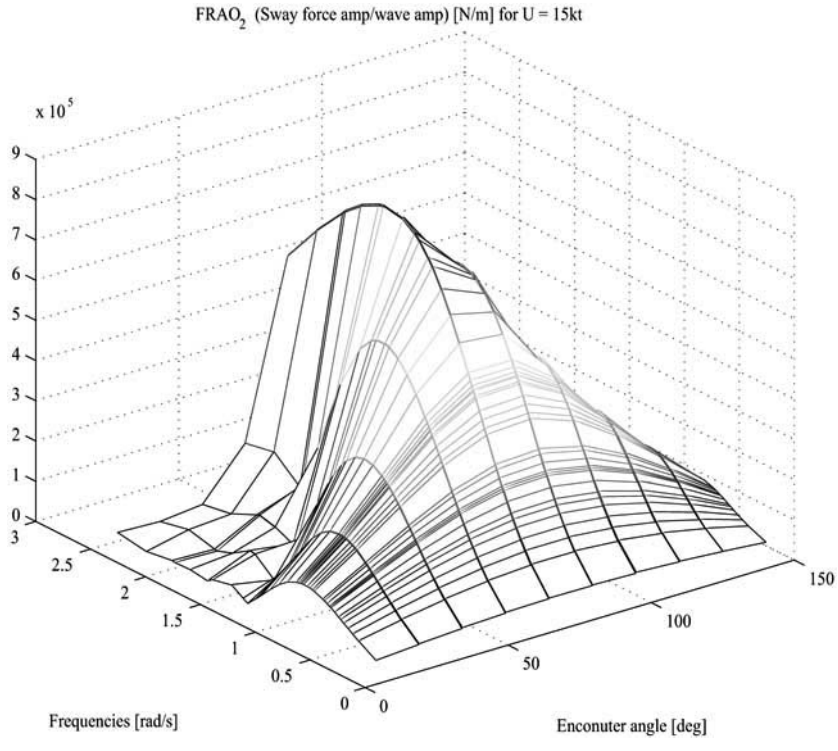

Fig. 4.4. Sway force RAO of the naval vessel benchmark at 15kts for different headings. The data is given as a function of the wave frequency. These force RAO were obtained using by ShipX-VERES [64].

The radiation forces are proportional to the accelerations and velocities of the ship motion. For *sinusoidal* motion, the vector of radiation forces (with components given in Expression (4.8)) can be expressed as follows [195, 63]:

$$\boldsymbol{\tau}_{\mathrm{r}}^{h} = -\mathbf{A}^{h}(\omega_e)\ddot{\boldsymbol{\xi}} - \mathbf{B}^{h}(\omega_e)\dot{\boldsymbol{\xi}}, \tag{4.18}$$

where—if the ship is symmetric with respect to the x_h-z_h plane—the matrix $\mathbf{A}^{h}(\omega_e)$ is of the form [195]:

$$\mathbf{A}^{h}(\omega_e) = \begin{bmatrix} A^h_{11}(\omega_e) & 0 & A^h_{13}(\omega_e) & 0 & A^h_{15}(\omega_e) & 0 \\ 0 & A^h_{22}(\omega_e) & 0 & A^h_{24}(\omega_e) & 0 & A^h_{26}(\omega_e) \\ A^h_{31}(\omega_e) & 0 & A^h_{33}(\omega_e) & 0 & A^h_{35}(\omega_e) & 0 \\ 0 & A^h_{42}(\omega_e) & 0 & A^h_{44}(\omega_e) & 0 & A^h_{46}(\omega_e) \\ A^h_{51}(\omega_e) & 0 & A^h_{53}(\omega_e) & 0 & A^h_{55}(\omega_e) & 0 \\ 0 & A^h_{62}(\omega_e) & 0 & A^h_{64}(\omega_e) & 0 & A^h_{66}(\omega_e) \end{bmatrix}, \tag{4.19}$$

and the damping matrix $\mathbf{B}^h(\omega_e)$ is similar to (4.19) modulo substitution A^h_{ik} by B^h_{ik}.

Due to the relationship (4.18), the matrix $\mathbf{A}(\omega_e)^h$ is called *added-mass matrix*, and the first term in (4.18) gives the so-called *added mass forces*. The added mass forces reflect the change of momentum in the fluid due to the motion of the hull—it does not mean that the water moves along with the ship. The matrix $\mathbf{B}(\omega_e)^h$ is called *potential-damping matrix* . Since potential theory does not account for viscous effects (skin friction and flow separation effects), the second term in (4.18) represents the transfer of kinetic energy of the hull into the generated waves that appear due to the motion of the hull.

In the case of roll and surge motion, the potential damping is very small and corrections need to be made to account for viscous effects. These corrections are based on empirical approaches, and can be incorporated into the equations of motion via an equivalent linear viscous damping coefficient B^h_{11visc} and B^h_{44visc} such that the energy dissipated through viscous effects is the same as that dissipated by the linear viscous term [135, 182].

By substituting the wave-excitation, radiation and hydrostatic forces into (4.2), and using the complex notation (4.13), we obtain the *frequency-domain equations of motion*:

$$-\omega_e^2[\mathbf{M}^h_{RB} + \mathbf{A}^h(\omega_e)]\tilde{\boldsymbol{\xi}} + j\omega_e\mathbf{B}^h(\omega_e)\tilde{\boldsymbol{\xi}} + \mathbf{G}^h\tilde{\boldsymbol{\xi}} = \tilde{\boldsymbol{\tau}}^h_{1\mathrm{w}}(\omega_e, \chi), \qquad (4.20)$$

from which the the responses can be evaluated:

$$\tilde{\boldsymbol{\xi}} = [-\omega_e^2(\mathbf{M}^h_{RB} + \mathbf{A}^h(\omega_e)) + j\omega_e\mathbf{B}^h(\omega_e) + \mathbf{G}^h]^{-1}\tilde{\boldsymbol{\tau}}^h_{1\mathrm{w}}(\omega_e, \chi). \qquad (4.21)$$

It should be emphasised that by multiplying both sides of Expression (4.20) by $e^{j\omega_e t}$ and taking the real part, one would not obtain the true equations of motion. Indeed, this would result in time-domain equations which describe the motion of the ship *only if* the wave excitation forces are sinusoidal, and provided the coefficients assume a proper value according to the frequency of the excitation. The true time-domain equations of motion (valid for any type excitation) have constant added mass and the damping is given by a convolution integral. This will be further discussed in Section 4.4.

In practice, Equation (4.21) is evaluated numerically only for a discrete set of frequencies (usually between 20 and 40). Details on how this is calculated is beyond the scope of the book, and interested reader should consult, for example, the hydrodynamic programs described in [64, 115, 144].

Due to the linearity of (4.21) and also the linearity of the wave excitation forces, the results give the amplitude and phase of each component of motion per unit of wave height or wave slope. These give the frequency response of the ship, which is represented in terms of the so-called *Motion Response Amplitude Operators* motion RAO:

$$H_i(\omega_e, \chi) = \left| \frac{\tilde{\xi}_i(\omega_e)}{\tilde{\zeta}} \right| e^{j \arg \tilde{\xi}_i(\omega_e)} \quad (\text{for} \quad i = 1, 2, \ldots, 6) \tag{4.22}$$

Note that it is also common practice to give the motion RAO of rotational motions (roll, pitch and yaw) normalised in terms of the wave slope ($k_e\bar{\zeta}$). In this case, the motion RAO is defined as

$$H_i(\omega_e, \chi) = \left| \frac{\tilde{\xi}_i(\omega_e)}{k_e\tilde{\zeta}} \right| e^{j \arg \tilde{\xi}_i(\omega_e)} \quad (\text{for} \quad i = 4, 5, 6), \tag{4.23}$$

where $k_e = \omega_e^2/g$ is the regular wave number—see Section 2.2.

The motion RAO can be expressed either in the wave frequency domain or in the encounter frequency domain:

$$H_i(\omega_e, \chi) \equiv H_i(\omega, U, \chi).$$

Then, for example, if the sea elevation, at the origin of the h-frame is described by

$$\zeta(t) = \bar{\zeta} \cos(\omega_e t + \epsilon), \tag{4.24}$$

the motion components are, then, obtained as

$$\xi_i(t) = \bar{\zeta}|H_i(\omega_e, \chi)| \ \cos(\omega_e t + \arg[H_i(\omega_e, \chi)] + \epsilon) \quad \text{for} \quad i = 1, 2, \ldots, 6 \tag{4.25}$$

If the motion RAO of the rotational components are normalised by the wave slope, (4.25) can be replaced by

$$\xi_i(t) = \bar{\zeta}|H_i(\omega_e, \chi)|k_e \sin(\omega_e t + \arg[H_i(\omega_e, \chi)] + \epsilon) \quad \text{for} \quad i = 4, 5, 6. \tag{4.26}$$

In the formulation presented thus far, the motion RAO obtained are given at the origin of the h-frame. To obtain the motion RAO at any other location point of interest x on the ship given by the vector $\mathbf{r}_x^h = [x_x^h, y_x^h, z_x^h]$, relative to the h-frame, the following relationship can be used:

$$[H_1^x, H_2^x, H_3^x]^{\mathrm{T}} = [H_1, H_2, H_3]^{\mathrm{T}} + [H_4, H_5, H_6]^{\mathrm{T}} \times \mathbf{r}_x^h, \tag{4.27}$$

where H_1^x, H_2^x, and H_3^x are the motion RAO at the desired location.

Figure 4.5 shows the roll, sway and yaw motion RAO, at the center of gravity, for one speed and different encounter angles of the benchmark example vessel described in Appendix B.

When the phases are negative, it means that the motion lags the wave elevation (or slope) at the origin of the h-frame. As described in Chapter 2,

when sailing in beam seas, the encounter and wave frequency are the same, and we can see from Figure 4.5 that the roll natural frequency is close to 1 rad/s. When sailing in bow seas, wave frequencies are mapped in to higher frequencies. This is why in Figure 4.5 the wave frequencies that are close to the resonance in roll are lower than those in the case of beam seas. For the sailing conditions shown, no wave frequencies are close to the roll resonance in quartering seas. Figures 4.6, 4.7 and 4.8 show the motion RAO for encounter angles with increments of 15 deg.

It should be noted from these examples that for the sway and yaw motion RAO in quartering seas with encounter angles of 30 deg and 45 deg, the encounter frequency approaches zero for the wave frequencies approaching 1.5 rad/s and 2.5 rad/s respectively, and then the response in sway and yaw increases rapidly. This can be seen from (4.21), by noting that there are singularities when $\omega_e \to 0$ because there are no restoring coefficients G_{2k} or G_{6k}, and. For simulations in irregular seas, this may not be a problem if the wave spectrum has low energy close to those frequencies. In practice, the helmsman or the autopilot will always limit these large motions [135].

4.2.4 Ship Motion Spectra and Statistics of Ship Motion

The motion RAO can be combined with the sea elevation or sea slope spectrum to obtain the motion spectra:

$$\mathbf{S}_{\xi\xi_i}(\omega_e) = |H_i(\omega_e, \chi)|^2 \mathbf{S}_{\zeta\zeta}(\omega_e) \quad \text{for} \quad i = 1, 2, \ldots, 6. \tag{4.28}$$

If the motion RAO of the rotational components are normalised by the wave slope, a similar expression holds for the wave slope spectrum (*cf.* (2.33)):

$$\mathbf{S}_{\xi\xi_i}(\omega_e) = |H_i(\omega_e, \chi)|^2 \mathbf{S}'_{\zeta\zeta}(\omega_e) \quad \text{for} \quad i = 4, 5, 6. \tag{4.29}$$

Since the power of any magnitude is invariant with respect to the reference frame from which it is observed, it follows that the spectral moments of order n of the motion components can be computed either in the encounter or in the wave frequency domain:

$$\begin{aligned} m^n_{\xi i} &= \int_0^\infty \omega_e^n |H_i(\omega_e, \chi)|^2 \mathbf{S}_{\zeta\zeta}(\omega_e)\, d\omega_e \\ &= \int_0^\infty \omega^n |H_i(\omega, U, \chi)|^2 \mathbf{S}_{\zeta\zeta}(\omega)\, d\omega. \end{aligned} \tag{4.30}$$

It is implicitly assumed in the above that either the wave spectrum or the wave slope spectrum should be used according to the definition of the MRAO of each motion component, and we will not make any explicit difference henceforth.

The factor $|H_i(\omega, U, \chi)|^2 \mathbf{S}_{\zeta\zeta}(\omega)$ in the second line of (4.30) is called a *pseudo-spectrum* and will be denoted by

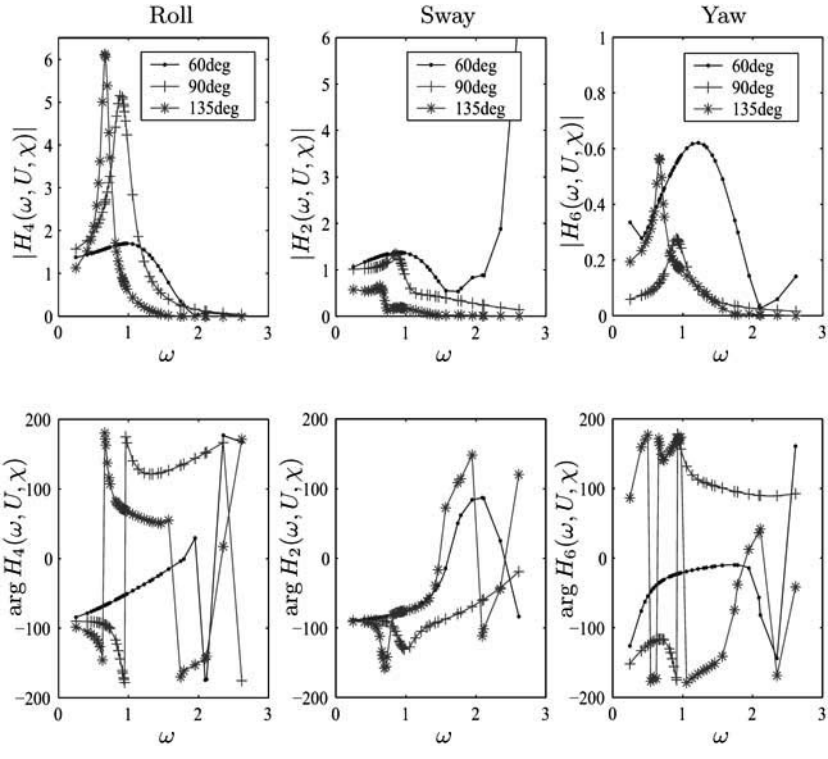

Fig. 4.5. Roll, sway and yaw motion RAO of the naval vessel benchmark at 15kts for different encounter angles. The motion RAO are given as a function of the wave frequency.

$$\mathbf{S}^{\star}_{\eta\eta i}(\omega) = |H_i(\omega, U, \chi)|^2 \mathbf{S}_{\zeta\zeta}(\omega). \tag{4.31}$$

The pseudo-spectrum can be used to determine the moments of the motion component as readily seen in (4.30), yet it is not the actual psd of the motion component observed from the ship. To obtain the latter, the pseudo-spectrum must be converted to the encounter frequency, using (2.62).

Figure 4.9 depicts a particular example for roll motion in quartering seas. The top and middle plots on the left hand side show the ITTC spectrum and the corresponding wave slope spectrum for a particular significant wave height and average wave period. The bottom left plot shows the square of the magnitude of the roll motion RAO for the particular sailing condition. The top plot on the right-hand side shows the roll pseudo-spectrum according to (4.31).

The middle plot on the right hand side shows the transformation between wave and encounter frequency for the adopted sailing condition according to

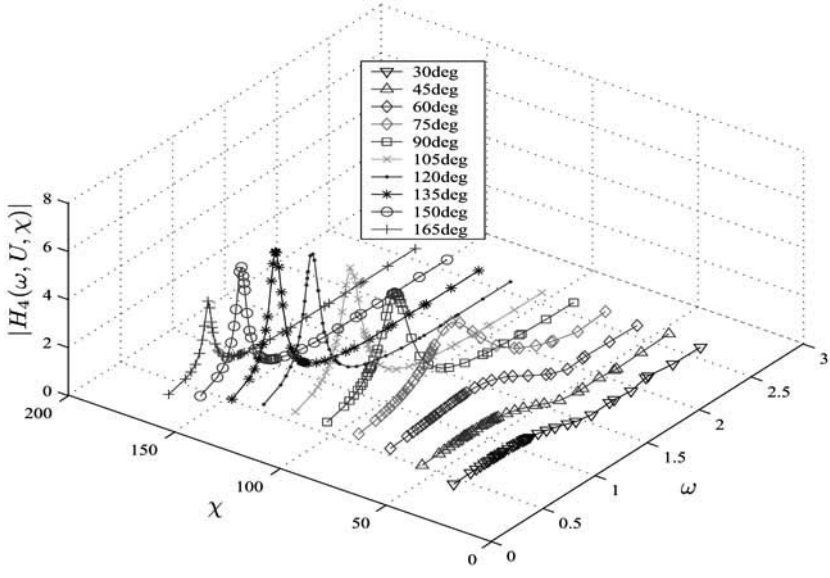

Fig. 4.6. motion RAO Roll of the naval vessel benchmark at 15 kt for different encounter angles. The motion RAO are given as a function of the wave frequency.

(2.29), and the bottom plot shows the roll power spectral density, which is the transformation of the pseudo-spectrum according to (2.62). Because of the frequency content of the pseudo-spectrum and the transformation to the encounter frequency for the particular sailing condition, most of the frequency components falls close to ω_e =4.5 rad/s—see Figure 2.3 for details on how to calculate this value. Due to the singularity that can appear in the case of quartering seas, as shown in Figure 4.9, the encounter spectrum is seldom used in computations; all statistics are calculated using the pseudo-spectrum. We will see in the next section that the encounter spectrum is not necessary to simulate the time series or motion. Figure 4.10 shows a similar example but for the bow sea case. As we can see from these two examples, the roll power spectral density can vary significantly depending on sea state, speed and encounter angle. This can result in problems for rudder-based roll stabilisers as we shall see in the second part of the book.

4.2.5 Time-series of Ship Motion using Seakeeping Models

The ship motion in a seaway can be simulated by time series. The method is the same as that presented in Chapter 2, Section 2.10, to simulate sea surface elevation.

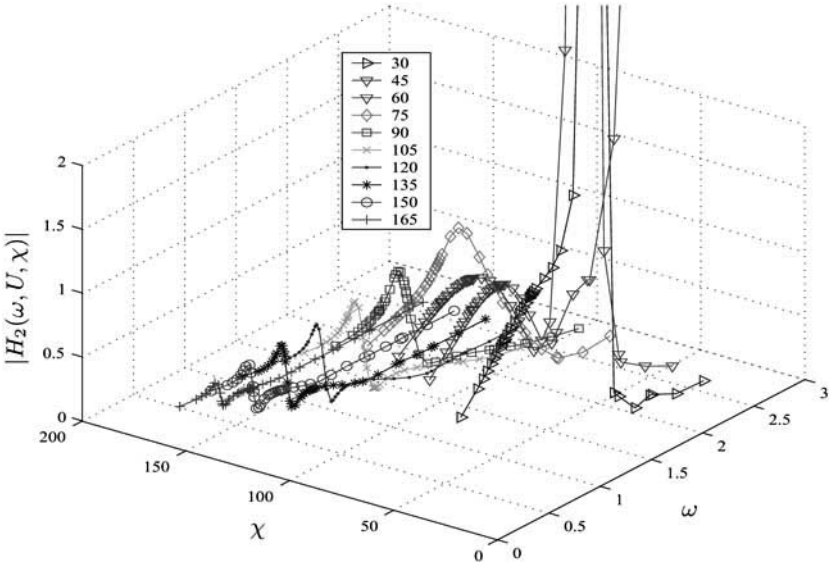

Fig. 4.7. motion RAO sway of the naval vessel benchmark at 15 kt for different encounter angles. The motion RAO are given as a function of the wave frequency.

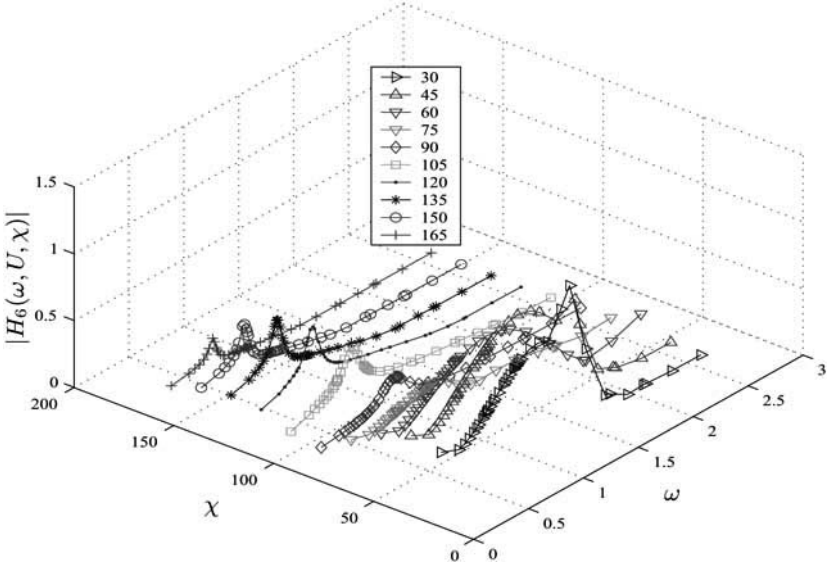

Fig. 4.8. motion RAO yaw of the naval vessel benchmark at 15 kt for different encounter angles. The motion RAO are given as a function of the wave frequency.

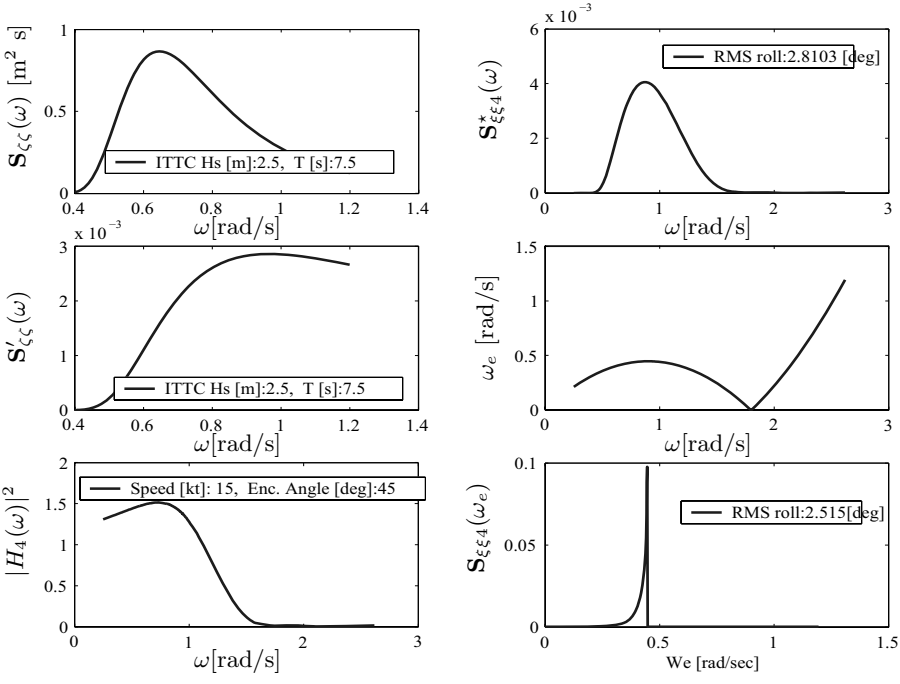

Fig. 4.9. Roll motion encounter psd in quartering seas.

By formulating the problem in the wave encounter frequency domain, the time series for the different components can be generated as indicated in the following:

$$\xi_i(t) = \sum_{n=1}^{N} \sum_{m=1}^{M} \bar{\eta}_{inm}(\omega_n) \cos\left[\left(\omega_n - \frac{\omega_n^2 U}{g}\cos(\chi_m)\right) t + \vartheta_{inm}(\omega) + \epsilon_n\right], \tag{4.32}$$

for $i = 1, 2, \ldots 6$, with

$$\bar{\eta}_{inm}(\omega_n^*) = \sqrt{2|H_i(\omega_n^*, U, \chi_m)|^2 \mathbf{S}_{\zeta\zeta}(\omega_n^*, \chi_m^*) \Delta\chi \Delta\omega}. \tag{4.33}$$

$$\vartheta_{inm}(\omega) = \arg H_i(\omega_n^*, U, \chi_m^*), \tag{4.34}$$

and ω_n^* chosen randomly in the interval

$$\left[\omega_n - \frac{\Delta\omega}{2}, \omega_n + \frac{\Delta\omega}{2}\right].$$

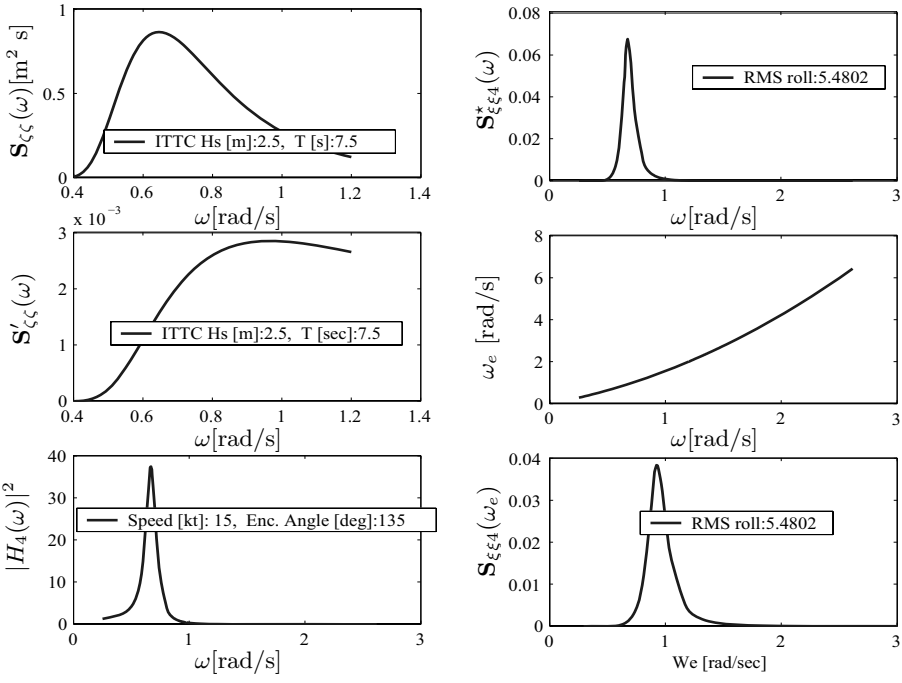

Fig. 4.10. Roll motion encounter psd in bow seas.

The phases ϵ_n are independent and identically distributed with uniform pdf in the interval $[0,\ 2\pi]$, and once chosen, these are the same for all the different motion components. If the motion RAO of the rotational components are normalised by the wave slope, one can use the following expression for $i = 4, 5, 6$:

$$\xi_i(t) = \sum_{n=1}^{N} \sum_{m=1}^{M} \bar{\eta}_{inm}(\omega_n) k_n \sin\left[\left(\omega_n - \frac{\omega_n^2 U}{g}\cos(\chi_m)\right) t + \vartheta_{inm}(\omega) + \epsilon_n\right]. \tag{4.35}$$

The expressions given above are valid for the general case of short-crested seas, provided the directions are discretised and the RAO are calculated for each of the discrete directions χ_m. For the case of a long-crested sea $M = 1$, and $\Delta\chi = 1$. To chose the number of components N and $\Delta\omega$, the rules given in Section 2.10 can be used.

As an example of time series, using the MRAO consider the results shown in Figures 4.11 and 4.12 for long-crested seas. These figures show the time series for roll, sway and yaw for beam seas, and roll time series for quartering, beam and bow seas. For the simulation of the wave excitation force times

series, a similar procedure can be followed by combining the sea spectrum with FRAO.

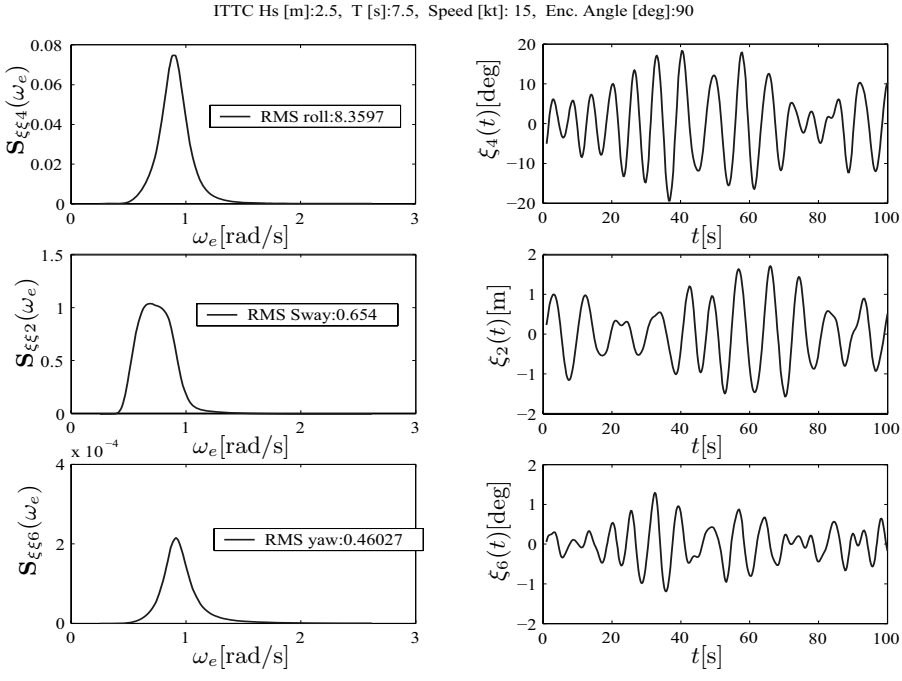

Fig. 4.11. Roll sway and yaw motion power spectral densities and time series for beam seas at 15kts. The wave spectrum used is ITTC with $H_{1/3} = 2.5$ m and $T = 7.5$ s.

It should be noted that the time series can also be implemented using linear shaping filters driven by white noise as described in Section 2.6. Depending on the vessel and sailing conditions the, psd of the motion components can be approximated by simple second-order shaping filters. For these cases, the algorithm given in Section 2.6 can be used to tune such filters according to the given sea state and sailing conditions. For cases in which the second-order approximation does not yield good results, higher order models should be estimated—see, for example, [37].

With this, we have defined all the elements of the seakeeping model indicated in Figure 4.1. The following summarises the properties of the seakeeping models [174]:

- The motion is described from an equilibrium frame traveling with the average speed of the ship—that is to say, fixed speed and heading.

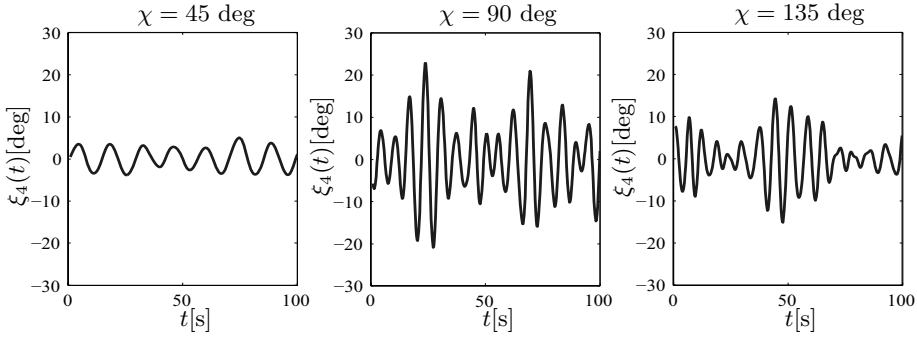

Fig. 4.12. Roll motion time series under different encounter angles for the benchmark example at 15 kt. The wave spectrum used is ITTC with $H_{1/3} = 2.5$ m and $T = 7.5$ s.

- Linearity is assumed between the motion responses and the wave amplitude; the problem is analysed in the frequency domain, *i.e.* the frequency-domain equations of motion are analysed in *steady state* and for sinusoidal waves excitations.

- To calculate the hydrodynamic radiation-induced forces, potential flow theory is used, and corrections for viscous effects are made based on empirical procedures.

- The mass and damping coefficients of the frequency-domain equations of motion are frequency dependent, and the equations are solved for a discrete set of frequencies. Since for a fixed frequency the equations are linear, the results give the amplitude and phase of the motion components per unit of wave amplitude as a function of the frequency—the motion RAO.

- By combining the motion RAO with the sea spectrum, all the statistics of motion can be calculated, and time series can be obtained for time domain simulations, but only describe steady-state motion.

- Depending on the hydrodynamic program used, the models may not accurate at low frequency. This is characteristic of strip theory codes (2D potential Theory) [195]. Despite all the apparent limitations of the method, it should be emphasised that the potential flow formulation solved by strip theory gives very good results compared to other, more complex formulations and more importantly, compared to experimental results. See [195, 160] for strip theory formulations, and [18] for details

about other computational methods for ship motion in seaway.

- The linearity assumption limits the validity of the model to waves of small steepness and small motion amplitudes, so superposition can be applied to the potential.

4.3 Manoeuvring Theory Models

In manoeuvring theory, as well as in guidance and navigation [67], the equations of motion are described using the variables $\boldsymbol{\eta}$ defined in the north-east-down frame (n-frame) and the variables $\boldsymbol{\nu}$ defined in the body-fixed frame (b-frame)—see Section 3.3. Using the notation of Fossen [66, 67], the vector equation to describe the motion of a marine vehicle using these variables can be expressed as

$$\begin{aligned}[\mathbf{M}^b_{RB} + \mathbf{M}^b_A]\dot{\boldsymbol{\nu}} + \mathbf{C}^b(\boldsymbol{\nu})\boldsymbol{\nu} + \mathbf{D}^b(\boldsymbol{\nu})\boldsymbol{\nu} + \mathbf{g}^b(\boldsymbol{\eta}) &= \boldsymbol{\tau}^b \\ \dot{\boldsymbol{\eta}} &= \mathbf{J}^n_b(\boldsymbol{\Theta}_{nb})\boldsymbol{\nu},\end{aligned} \tag{4.36}$$

where

- $\mathbf{M}^b_{RB}$ is the rigid-body generalised mass matrix (mass and inertia) with respect to the origin of the b-frame,
- $\mathbf{M}^b_A$ is the generalised added-mass matrix,
- $\mathbf{C}^b(\boldsymbol{\nu})$ is the total (rigid body and added mass) Coriolis and centripetal acceleration matrix,
- $\mathbf{D}^b(\boldsymbol{\nu})$ is the damping matrix,
- $\mathbf{g}^b(\boldsymbol{\eta})$ is the restoring function,
- $\mathbf{J}^n_b(\boldsymbol{\Theta}_{nb})$ is the velocity transformation matrix given in (3.24),
- $\boldsymbol{\tau}^b$ is the vector of forces and moments acting on the hull originated by the control devices, the propulsion system, and hydrodynamic effects.

Because the motion is described in a non-inertial frame (b-frame), the equations of motion include fictitious accelerations. We will next describe the different elements of equation (4.36).

4.3.1 Rigid Body Dynamics in the *b*-frame

The rigid-body equations of motion expressed in the body-fixed reference frame or b-frame are:

$$\mathbf{M}^b_{RB}\dot{\boldsymbol{\nu}} + \mathbf{C}^b_{RB}(\boldsymbol{\nu})\boldsymbol{\nu} = \boldsymbol{\tau}^b, \tag{4.37}$$

where $\mathbf{M}_{RB}$ is the generalised mass matrix

$$\mathbf{M}^b_{RB} \triangleq \begin{bmatrix} m\mathbf{I}_{3\times 3} & -m\mathbf{S}(\mathbf{r}^b_g) \\ m\mathbf{S}(\mathbf{r}^b_g) & \mathbf{I}^b \end{bmatrix}, \tag{4.38}$$

which is of the form of (4.3). The Coriollis and centripetal acceleration matrix can be expressed in different ways; one representation is

$$\mathbf{C}^b_{RB}(\boldsymbol{\nu}) \triangleq \begin{bmatrix} m\mathbf{S}(\boldsymbol{\nu}_2) & -m\mathbf{S}(\boldsymbol{\nu}_2)\mathbf{S}(\mathbf{r}^b_g) \\ m\mathbf{S}(\mathbf{r}^b_g)\mathbf{S}(\boldsymbol{\nu}_2) & -\mathbf{S}(\mathbf{I}^b\boldsymbol{\nu}_2) \end{bmatrix}, \tag{4.39}$$

where $\boldsymbol{\nu}_2 \triangleq [p, q, r]^{\mathrm{T}}$—see [67] for alternative representations of (4.39). The terms in $\mathbf{C}_{RB}(\boldsymbol{\nu})\boldsymbol{\nu}$ (4.37) are fictitious forces and moments arising from expressing the equations of motion in the non-inertial b-frame.

The components of (4.37) are [66]

$$\begin{aligned}
m\left[\dot{u} - vr + wq - x^b_g(q^2 + r^2) + y^b_g(pq - \dot{r}) + z^b_g(pr + \dot{q})\right] &= \tau^b_1 \\
m\left[\dot{v} - wp + ur - y^b_g(r^2 + p^2) + z^b_g(qr - \dot{p}) + x^b_g(qp + \dot{r})\right] &= \tau^b_2 \\
m\left[\dot{w} - uq + vp - z^b_g(p^2 + q^2) + x^b_g(rp - \dot{q}) + y^b_g(rq + \dot{p})\right] &= \tau^b_3 \\
I^b_x\dot{p} + (I^b_z - I^b_y)qr - (\dot{r} + pq)I^b_{xz} + (r^2 - q^2)I^b_{yz} + (pr - \dot{q})I^b_{xy} & \\
+m\left[y^b_g(\dot{w} - uq + vp) - z^b_g(\dot{v} - wp + ur)\right] &= \tau^b_4 \\
I^b_y\dot{q} + (I^b_x - I^b_z)rp - (\dot{p} + qr)I^b_{xy} + (p^2 - r^2)I^b_{zx} + (qp - \dot{r})I^b_{yz} & \\
+m\left[z^b_g(\dot{u} - vr + wq) - x^b_g(\dot{w} - uq + vp)\right] &= \tau^b_5 \\
I^b_z\dot{r} + (I^b_y - I^b_x)pq - (\dot{q} + rp)I^b_{yz} + (q^2 - p^2)I^b_{xy} + (rq - \dot{p})I^b_{zx} & \\
+m\left[x^b_g(\dot{v} - wp + ur) - y^b_g(\dot{u} - vr + wq)\right] &= \tau^b_6
\end{aligned} \tag{4.40}$$

For the motion control problem addressed in this book (course keeping and roll stabilisation), it is a common practice to neglect the pitch and heave motion components. This yields a model in four degrees of freedom (4DOF): *surge*, *sway*, *roll* and *yaw*. Under this assumption,

$$\begin{aligned}
m[\dot{u} - vr - x^b_g r^2 - y^b_g\dot{r} + z^b_g pr] &= \tau^b_1 \\
m[\dot{v} + ur - y^b_g(r^2 + p^2) - z^b_g\dot{p} + x^b_g\dot{r}] &= \tau^b_2 \\
I^b_x\dot{p} - \dot{r}I^b_{xz} + r^2 I^b_{yz} + prI^b_{xy} + m[y^b_g vp - z^b_g(\dot{v} + ur)] &= \tau^b_4 \\
I^b_z\dot{r} - rpI^b_{yz} - p^2 I^b_{xy} - \dot{p}I^b_{zx} + m[x^b_g(\dot{v} + ur) - y^b_g(\dot{u} - vr)] &= \tau^b_6.
\end{aligned} \tag{4.41}$$

The position of the origin o_b of the b-frame can be chosen so as to simplify the equations of motion. For instance, if o_b coincides with CG, and the axes x_b, y_b, z_b coincide with the principal axes of inertia; then, the simplest form of the equations of motion (4.41) is obtained. Some disadvantages of this choice, however, are that the axes x_b, y_b, z_b may differ from the symmetry axes of the ship and also that the location of the CG may vary with the loading condition. These effects has to be compensated for by the control system if such equations of motion are used for control applications [66]. As a consequence, it is often more convenient to chose the origin o_b such that

the inertia products are negligible and the axes x_b, y_b, z_b correspond to the longitudinal, lateral and normal direction of the vehicle. As shown by Fossen, [66], this can be achieved by choosing o_b such that the coordinates of CG satisfy the following relationships:

$$\begin{aligned} mI^g_{yz}x^2_g &= -I^g_{xy}I^g_{xz} \\ mI^g_{xz}y^2_g &= -I^g_{xy}I^g_{yz} \\ mI^g_{yz}x^2_g &= -I^g_{xz}I^g_{yz} \end{aligned}$$

where the superscript ^{g} denotes that the moments of inertia are taken with the body frame fixed at CG. The relationship between moments of inertia with respect to the b-frame and those located at CG are related via

$$\begin{aligned} I^b_{xx} &= I^g_{xx} + m[(y^b_g)^2 + (z^b_g)^2] \\ I^b_{yy} &= I^g_{yy} + m[(z^b_g)^2 + (z^b_g)^2] \\ I^b_{zz} &= I^g_{zz} + m[(x^b_g)^2 + (y^b_g)^2]. \end{aligned}$$

The following equations of motion are valid when body-fixed axes correspond to the longitudinal, lateral, and normal directions [66]:

$$\begin{aligned} m\left[\dot{u} - vr + wq - x^b_g(q^2 + r^2) + y^b_g(pq - \dot{r}) + z^b_g(pr + \dot{q})\right] &= \tau^b_1 \\ m\left[\dot{v} - wp + ur - y^b_g(r^2 + p^2) + z^b_g(qr - \dot{p}) + x^b_g(qp + \dot{r})\right] &= \tau^b_2 \\ m\left[\dot{w} - uq + vp - z^b_g(p^2 + q^2) + x^b_g(rp - \dot{q}) + y^b_g(rq + \dot{p})\right] &= \tau^b_3 \\ I^b_{xx}\dot{p} + (I^b_{zz} - I_{yy})qr + m\left[y^b_g(\dot{w} - uq + vp) - z^b_g(\dot{v} - wp + ur)\right] &= \tau^b_4 \\ I^b_{yy}\dot{q} + (I^b_{xx} - I^b_{zz})rp + m\left[z^b_g(\dot{u} - vr + wq) - x^b_g(\dot{w} - uq + vp)\right] &= \tau^b_5 \\ I^b_{zz}\dot{r} + (I^b_{yy} - I^b_{yx})pq + m\left[x^b_g(\dot{v} - wp + ur) - y^b_g(\dot{u} - vr + wq)\right] &= \tau^b_6 \end{aligned} \tag{4.42}$$

and in 4DOF

$$\begin{aligned} m[\dot{u} - y^b_g\dot{r} - vr - x^b_g r^2 + z^b_g pr] &= \tau^b_1 \\ m[\dot{v} - z^b_g\dot{p} + x^b_g\dot{r} + ur - y^b_g(r^2 + p^2)] &= \tau^b_2 \\ I^b_{xx}\dot{p} - mz^b_g\dot{v} + m[y^b_g vp - z^b_g ur] &= \tau_4 \\ I^b_{zz}\dot{r} + mx^b_g\dot{v} - my^b_g\dot{u} + m[x^b_g ur + y^b_g vr] &= \tau^b_6 \end{aligned} \tag{4.43}$$

Expression (4.43) is the model that will be adopted for the rigid-body dynamics in the sequel.

The total vector of forces and moments $\boldsymbol{\tau}$—appearing in the right-hand side of expression (4.43)—is generated by different phenomena and can be

separated into components according to their originating effects as, and the total effect be studied using superposition [133]:

$$\boldsymbol{\tau}^b = \boldsymbol{\tau}^b_{\text{hyd}} + \boldsymbol{\tau}^b_{\text{hs}} + \boldsymbol{\tau}^b_{\text{c}} + \boldsymbol{\tau}^b_{\text{p}},$$

where subscripts stand for

- Hydrodynamic forces and moments,
- Hydrostatic forces and moments,
- Control devices forces and moments,
- Propulsion forces and moments.

In this book, it will be assumed that $\boldsymbol{\tau}^b_{\text{p}}$ compensates for the hydrodynamic resistance of the hull, and also that the dynamics associated with the surge component of motion are much slower than the dynamics of the other motion components. This assumption allows us to decouple the surge component and to treat the variable u as a constant equal to the ship service speed $\bar{u}$, *i.e.* in the sequel it will be assumed that $\dot{u} \approx 0$ and $u \approx U$.

4.3.2 Manoeuvring Hydrodynamics

Due to the complex phenomena associated with the hydrodynamics forces during manoeuvring, these forces motions are usually determined from experimental scaled-model tests. In this approach, The forces are modelled as a general nonlinear functions:

$$\boldsymbol{\tau}^b_{\text{hyd}} = \mathbf{f}_{\text{hyd}}(\dot{\boldsymbol{\nu}}, \boldsymbol{\nu}, \boldsymbol{\eta}). \tag{4.44}$$

These are the radiation and viscous forces *at low frequency*, and the hydrostatic or restoring forces. The only restoring force relevant to manoeuvring is the roll restoring moment is the roll moment:

$$\tau^b_{4\text{hs}} = GZ(\phi)\rho g \nabla, \tag{4.45}$$

where $GZ(\phi)$ is the so-called roll righting arm shown in Figure 4.3. If data for $GZ(\phi)$ is not available, the linear approximation given in (4.11) is sufficient for surface vessels.

The first term in (4.44) is often expanded in a series. There are two approaches to express such a series. The first approach, proposed by Abkowitz, [1], consists in using a truncated Taylor series with only odd terms of third order. The second approach, uses the, so-called *second-order modulus terms*. This method was proposed by Fedyaevsky and Sobolev [65], and later by Norrbin [162]. The manoeuvring model of the benchmark example (see Appendix B) is given in this latter form [33]:

Sway terms

$$\begin{aligned}\tau^b_{2\text{hyd}} &= Y_{\dot v}\dot v + Y_{\dot r}\dot r + Y_{\dot p}\dot p \\ &\quad + Y_{|u|v}\,|U|\,v + Y_{ur}Ur + Y_{v|v|}v\,|v| + Y_{v|r|}v\,|r| + Y_{r|v|}r\,|v| \\ &\quad + Y_{\phi|uv|}\phi\,|Uv| + Y_{\phi|ur|}\phi\,|Ur| + Y_{\phi uu}\phi\,U^2.\end{aligned} \tag{4.46}$$

Roll terms

$$\begin{aligned}\tau^b_{4\text{hyd}} &= K_{\dot v}\dot v + K_{\dot p}\dot p \\ &\quad + K_{|u|v}\,|U|\,v + K_{ur}Ur + K_{v|v|}v\,|v| + K_{v|r|}v\,|r| + K_{r|v|}r\,|v| \\ &\quad + K_{\phi|uv|}\phi\,|Uv| + K_{\phi|ur|}\phi\,|Ur| + K_{\phi uu}\phi\,U^2 + K_{|u|p}\,|U|\,p \\ &\quad + K_{p|p|}p\,|p| + K_p p + K_{\phi\phi\phi}\phi^3 - \rho g\nabla GZ(\phi).\end{aligned} \tag{4.47}$$

Yaw terms

$$\begin{aligned}\tau^b_{6\text{hyd}} &= N_{\dot v}\dot v + N_{\dot r}\dot r \\ &\quad + N_{|u|v}\,|U|\,v + N_{|u|r}\,|U|\,r + N_{r|r|}r\,|r| + N_{r|v|}r\,|v| \\ &\quad + N_{\phi|uv|}\phi\,|Uv| + N_{\phi u|r|}\phi\,U\,|r| + N_p p + N_{|p|p}|p|p + N_{|u|p}|U|p \\ &\quad + N_{\phi u|u|}\phi\,U\,|U|\,.\end{aligned} \tag{4.48}$$

The linear coefficients in expressions (4.46) to (4.48) are called the *hydrodynamic derivatives* since, for example,

$$Y_{\dot p} = \frac{\partial \tau^b_{2\text{hyd}}}{\partial \dot p}, \quad \text{and} \quad K_p = \frac{\partial \tau^b_{4\text{hyd}}}{\partial p}$$

are the force in sway due to the roll rate derivative (added mass term), and the roll moment due to the roll rate (damping term).

The hydrodynamic derivatives proportional to the accelerations are the added masses and moments of inertia similarly to the seakeeping theory. The difference, however, is that in manoeuvring, these are measured by making the scale model oscillate at low frequencies.

The coefficients of the nonlinear terms are simply obtained from curve fitting and therefore should not be called hydrodynamic derivatives. The use of second-order modulus terms have proven to represent the cross-flow drag at large angles of attack [50]. As mentioned by Clarke [50] it has been found that for simulation purposes, it is much more straightforward to store the data and use look-up tables to interpolate rather than to fit explicit curves. For a recent review on the foundations of the manoeuvring equations, see [50].

4.3.3 Nonlinear Manoeuvring State-space Models

In order to perform time domain numerical simulations and to design model based control strategies, it is convenient to use state-space methods. From the models provided in the previous section, the components of vector equation (4.36) in sway, roll and yaw can be expressed as

$$
\begin{aligned}
(m - Y_{\dot{v}})\dot{v} - (mz_G + Y_{\dot{p}})\dot{p} + (mx_G - Y_{\dot{r}})\dot{v} &= \tau^{-}_{2\text{hyd}} - mur + \tau_{2\text{c}} \\
-(mz_G + K_{\dot{v}})\dot{v} + (I_x - K_{\dot{p}})\dot{p} - K_{\dot{r}}\dot{p} &= \tau^{-}_{4\text{hyd}} + mz_G ur + \tau_{4\text{c}} \\
(mx_G - N_{\dot{v}})\dot{v} - N_{\dot{p}}\dot{p} + (I_z - N_{\dot{r}})\dot{r} &= \tau^{-}_{6\text{hyd}} - mx_G ur + \tau_{6\text{c}} \\
\dot{\phi} &= p \\
\dot{\psi} &= r\cos(\phi)
\end{aligned}
\tag{4.49}
$$

Here, the terms $\tau^{-}_{i\text{hyd}}$, $i = 2, 4, 6$ correspond to the nonlinear hydrodynamic terms, for example, given in Expressions (4.46) to (4.48) without the terms that are proportional to the accelerations—which have been included on the left-hand side of (4.49). The forces and moments produced by the control surfaces, reviewed in Chapter 5, are represented by the terms

$$
\boldsymbol{\tau}^b_{\text{c}} = \begin{bmatrix} \tau^b_{2\text{c}} & \tau^b_{4\text{c}} & \tau^b_{6\text{c}} \end{bmatrix}^{\text{T}}. \tag{4.50}
$$

Equations (4.49) are already in a form similar to a state-space form. Indeed, by defining the state vector vector

$$
\mathbf{x} \triangleq \begin{bmatrix} v & p & r & \phi & \psi \end{bmatrix}^{\text{T}},
$$

then Expression (4.49) can be written as

$$
\dot{\mathbf{x}} = \begin{bmatrix} \mathbf{M}^{-1} & \mathbf{0} \\ \mathbf{0} & \mathbf{I}_{2\times 2} \end{bmatrix} \mathbf{f}(\mathbf{x}) + \begin{bmatrix} \mathbf{M}^{-1} \\ \mathbf{0}_{1\times 3} \\ \mathbf{0}_{1\times 3} \end{bmatrix} \boldsymbol{\tau}^b_{\text{c}}, \tag{4.51}
$$

with

$$
\mathbf{M} \triangleq \begin{bmatrix} (m - Y_{\dot{v}}) & -(mz^b_g + Y_{\dot{p}}) & (mx^b_g - Y_{\dot{r}}) \\ -(mz^b_g + K_{\dot{v}}) & (I^b_{xx} - K_{\dot{p}}) & -K_{\dot{r}} \\ (mx^b_g - N_{\dot{v}}) & -N_{\dot{p}} & (I^b_{zz} - N_{\dot{r}}) \end{bmatrix} \tag{4.52}
$$

and

$$
\mathbf{f}(\mathbf{x}) = \mathbf{f}_{\text{hyd}}(\mathbf{x}) + \mathbf{f}_{\text{c}}(\mathbf{x}). \tag{4.53}
$$

with the obvious definitions for the functions $\mathbf{f}_{hyd}(x)$ and $\mathbf{f}_{\text{c}}(\mathbf{x})$:

$$
\mathbf{f}_{\text{hyd}}(\mathbf{x}) = \begin{bmatrix} \tau^{-}_{2\text{hyd}} \\ \tau^{-}_{4\text{hyd}} \\ \tau^{-}_{6\text{hyd}} \\ 0 \\ 0 \end{bmatrix} \qquad \mathbf{f}_{c}(\mathbf{x}) = \begin{bmatrix} -mur \\ mz^b_g ur \\ -mx^b_g ur \\ 0 \\ 0 \end{bmatrix} \tag{4.54}
$$

4.3.4 Linear Manoeuvring State-space Models

The model presented in the previous subsection is a comprehensive model that can be used as a calibration model to test different control strategies. In order to design a control system and to draw conclusions about intrinsic limitations, it is convenient to work with a linear model:

$$\dot{\mathbf{x}} = \mathbf{A}\,\mathbf{x} + \mathbf{B}\,\boldsymbol{\tau}_{\mathrm{c}}. \tag{4.55}$$

By taking the first term of the Taylor expansion around the equilibrium point $\overline{\mathbf{x}} = 0, u = \overline{u}$, the matrices of this linearised model are defined as:

$$\mathbf{A} \triangleq \begin{bmatrix} \mathbf{M}^{-1} & \mathbf{0} \\ \mathbf{0} & \mathbf{I}_{2\times 2} \end{bmatrix} \left.\frac{\partial \mathbf{f}(\mathbf{x})}{\partial \mathbf{x}}\right|_{\overline{\mathbf{x}}=0} \qquad \mathbf{B} \triangleq \begin{bmatrix} \mathbf{M}^{-1} \\ \mathbf{0}_{1\times 3} \\ \mathbf{0}_{1\times 3} \end{bmatrix}, \tag{4.56}$$

where, for example, by using (4.46)–(4.48)

$$\left.\frac{\partial \mathbf{f}(\mathbf{x})}{\partial \mathbf{x}}\right|_{\overline{\mathbf{x}}=0} = \begin{bmatrix} Y_{|u|v}|\overline{u}| & 0 & (Y_{ur}-m)\overline{u} & Y_{\phi uu}\overline{u}^2 & 0 \\ K_{|u|v}|\overline{u}| & K_p + K_{|u|p}|\overline{u}| & (K_{ur}+mz_G)\overline{u} & K_{\phi uu}\overline{u}^2 - \rho g \nabla GMt & 0 \\ N_{|u|v}|\overline{u}| & N_p + N_{|u|p}|\overline{u}| & N_{|u|r}|\overline{u}| - mx_G\overline{u} & N_{\phi u|u|}\overline{u}|\overline{u}| & 0 \\ 0 & 1 & 0 & 0 & 0 \\ 0 & 0 & 1 & 0 & 0 \end{bmatrix}. \tag{4.57}$$

Model (4.55) incorporates all the relevant couplings of interest between roll, sway and yaw to analyze the problem of rudder-based stabiliser control system design [33]. This is an important characteristic for studying design performance limitations associated with the dynamics of the ship. This topic will be the subject of the second part of this book.

With this, we have completely defined all the elements of the manoeuvring model indicated in Figure 4.1. The following summarises the properties of the manoeuvring models [174]:

- The equations of motion are formulated in a reference frame fixed to the ship (b-frame), and not in an equilibrium frame like in seakeeping (h-frame).

- The equations can be linear or non-linear depending on the application. For autopilots (course-keeping), and autopilots with rudder rudder roll stabilisation, linear models are usually sufficient, since large deviations requiring non-linear terms can be regarded as poor course-keeping [50].

- The coefficients of the equations are estimated from captive scale-model tests, by measuring forces while the model is subjected to *low* frequency forced oscillations in 3DOF (surge, sway and yaw) or 4DOF (with the addition of roll). These coefficients can also be obtained using hydrodynamic programs combined with look-up tables, or by scalling data from known models [208].

- The model is valid in calm water conditions because the coefficients are estimated from data collected from low frequency experiments. Therefore, if there is a significant motion induced by the waves, the memory effects associated with the radiation forces are not accounted for.

We finish this section by showing some simulations results obtained using the manoeuvring models presented. Figure 4.13, shows the value of the state variables for the linear and the non-linear model of our benchmark example (see Appendix B) under a zig-zag test [133]. All the coefficients are given in Appendix B.

4.4 A Force-superposition Model for Slow Manoeuvring in a Seaway

As commented in Section 4.1, the combination of seakeeping model as an output disturbance for the manoeuvring model is the commonly used approached to model ships for control system design, but this approach suffers from two drawbacks. The first one is that the model may not be used for multibody system interactions, and the second is that there is some uncertainty in the response to the control actions because of miss-modelled dynamics related to changes in added mass and damping with the frequency of the wave excitation. A more realistic description it that shown in Figure 4.2, in which the wave excitation loads are used as input disturbance and a unified model that accounts for memory effects is used. This type of model can therefore be used for slow manoeuvring in a seaway. The slow manoeuvring restriction is because the hydrodynamic frame h is used to obtain the wave-excitation and radiation forces. Thus, it is implicitly assumed that the speed of the manoeuvre is much slower than the wave-induced motion so the h-frame can be considered inertial. This is a reasonable assumption at least for large vessels. In this section, we further describe the elements of such model. The material that follows has been motivated by the work of Bailey *et al.*[11] and Kristansen and Egeland [127].

4.4.1 Time Domain Seakeeping Models in the h-frame

We have seen that for *sinusoidal* wave excitation forces, the linear equations of motion in the h-frame can be expressed as [195, 63],

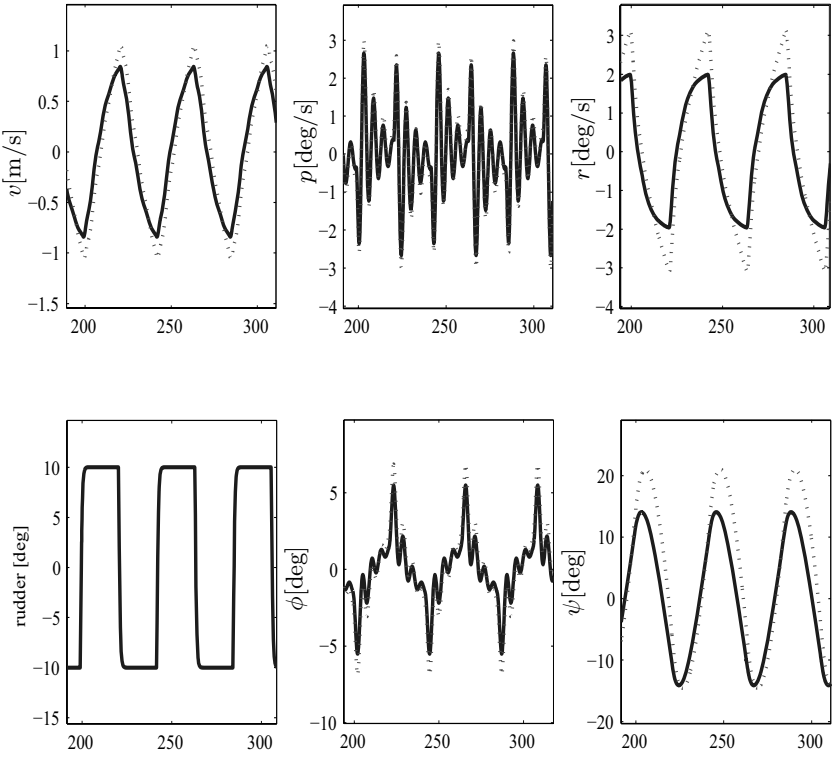

Fig. 4.13. Simulation results corresponding to the naval vessel under an IMO 10 deg zig-zag test. Nonlinear model (solid). Linearised model (dotted).

$$[\mathbf{M}^h_{RB} + \mathbf{A}^h(\omega_e)]\ddot{\boldsymbol{\xi}} + \mathbf{B}^h(\omega_e)\dot{\boldsymbol{\xi}} + \mathbf{G}^h\boldsymbol{\xi} = \boldsymbol{\tau}^h_{\mathrm{w}}. \tag{4.58}$$

However, as already mentioned, these are not truly equations of motion, because they are valid only if the wave excitation forces are sinusoidal, and provided the coefficients assume an appropriate value according to the frequency of the excitation. Further, these equations describe motion only in steady state.

Cummins, in 1962 [58] considered the behaviour of the fluid and the ship in the time domain. He made the assumption of linearity, and considered impulses in the components of motion. This resulted in a boundary value problem in which the potential was separated into two parts; one valid during the duration of the impulses and the other valid after the impulses extinguished. By expressing the pressure as a function of these potentials and integrating it over the wetted surface of the vessel, he obtained a vector integro-differential equation, which is known as the *Cummins Equation*:

$$[\mathbf{M}^h_{RB} + \bar{\mathbf{A}}^h]\ddot{\boldsymbol{\xi}} + \int_{-\infty}^{t} \bar{\mathbf{K}}^h(t-\tau)\,\dot{\boldsymbol{\xi}}(\tau)\,d\tau + \mathbf{G}^h\boldsymbol{\xi} = \boldsymbol{\tau}^h_{\mathrm{w}}. \tag{4.59}$$

The matrix $\mathbf{A}^h$ is constant and depends only on the ship geometry. The entries of the matrix $\bar{\mathbf{K}}^h(t-\tau)$, in the convolution integral, are retardation functions of time, which depend on the forward speed and geometry of the vessel; this functions are the impulse response functions of the velocities.

The Cummings equation reveal the structure of the true equations of motion of a ship and are valid for any bounded excitation $\boldsymbol{\tau}^h_{\mathrm{w}}$. Since equation (4.59) is valid for arbitrary excitations, this includes sinusoids as a particular case. Ogilvie, [168], took the Fourier transform of equation (4.59) for sinusoidal excitations, and found the following relationships

$$\mathbf{A}^h(\omega_e) = \bar{\mathbf{A}}^h - \frac{1}{\omega_e}\int_0^{\infty} \bar{\mathbf{K}}^h(\tau)\sin(\omega_e\tau)d\tau \tag{4.60}$$

$$\mathbf{B}^h(\omega_e) = \int_0^{\infty} \bar{\mathbf{K}}^{\mathbf{h}}(\tau)\cos(\omega_e\tau)d\tau \tag{4.61}$$

Since the first equation must be valid for all ω_e, it follows that

$$\bar{\mathbf{A}}^h = \lim_{\omega_e\to\infty} \mathbf{A}^h(\omega_e) \equiv \mathbf{A}^h(\infty) \tag{4.62}$$

The second equation is rewritten using the inverse Fourier transform giving:

$$\bar{\mathbf{K}}^h(t) = \frac{2}{\pi}\int_0^{\infty} \mathbf{B}^h(\omega_e)\cos(\omega_e\tau)d\omega_e \tag{4.63}$$

This expression is recognized as a matrix of *retardation functions*. Thus, the Cummins Equation (4.59) can be expressed as

$$[\mathbf{M}^h_{RB} + \mathbf{A}^h(\infty)]\ddot{\boldsymbol{\xi}} + \int_{-\infty}^{t} \bar{\mathbf{K}}^h(t-\tau)\dot{\boldsymbol{\xi}}(\tau)d\tau + \mathbf{G}^h\boldsymbol{\xi} = \boldsymbol{\tau}^h_{\mathrm{w}}. \tag{4.64}$$

An alternative representation is

$$[\mathbf{M}^h_{RB} + \mathbf{A}^h(\infty)]\ddot{\boldsymbol{\xi}} + \mathbf{B}^h(\infty)\dot{\boldsymbol{\xi}} + \int_{-\infty}^{t} \mathbf{K}^h(t-\tau)\dot{\boldsymbol{\xi}}(\tau)d\tau + \mathbf{g}^h(\boldsymbol{\xi}) = \boldsymbol{\tau}^h_{\mathrm{w}}. \tag{4.65}$$

where

$$\mathbf{K}^h(t) = \frac{2}{\pi}\int_0^{\infty} [\mathbf{B}^h(\omega_e) - \mathbf{B}^h(\infty)]\cos(\omega\tau)d\omega_e, \tag{4.66}$$

The term $\mathbf{g}^h(\boldsymbol{\xi})$ indicates that nonlinear restoring forces may be used, instead of the linear approximation $\mathbf{G}^h\boldsymbol{\xi}$.

The above form of the equations of motion results in better numerical properties for the convolution integral because $[\mathbf{B}^h(\omega_e) - \mathbf{B}^h(\infty)]$ goes to zero as ω_e goes to infinity.

4.4.2 Seakeeping Model in the *b*-frame

Using the transformations for the velocities and accelerations (3.60), the equations of motion (4.58) expressed in the *b*-frame become

$$(\mathbf{J}_b^h)^{\mathrm{T}}[\mathbf{M}_{RB}^h + \mathbf{A}^h(\omega_e)]\,[\mathbf{J}_b^h\dot{\boldsymbol{\delta\nu}} + U\mathbf{L}\boldsymbol{\delta\nu}] + \mathbf{B}^h(\omega_e)\left[\mathbf{J}_b^h\boldsymbol{\delta\nu} - \frac{U}{\omega_e^2}\mathbf{L}\dot{\boldsymbol{\delta\nu}}\right] + (\mathbf{J}_b^h)^{\mathrm{T}}\mathbf{g}^h(\boldsymbol{\xi}) = (\mathbf{J}_b^h)^{\mathrm{T}}\boldsymbol{\tau}_{\mathrm{w}}^h. \quad (4.67)$$

The transformation of the generalised mass matrix from the *h*-frame to the *b*-frame is given by

Then,

$$[\mathbf{M}_{RB}^b + \mathbf{M}_A^b(\omega_e)]\,\dot{\boldsymbol{\delta\nu}} + [\mathbf{C}_{RB}^b + \mathbf{C}_A^b(\omega_e)]\boldsymbol{\delta\nu} + \mathbf{B}^b(\omega_e)\boldsymbol{\delta\nu} + \mathbf{g}^b(\boldsymbol{\eta}) = \boldsymbol{\tau}_{\mathrm{w}}^b, \quad (4.68)$$

where

$$\begin{aligned}
\mathbf{M}_{RB}^b &= (\mathbf{J}_b^h)^{\mathrm{T}}\mathbf{M}_{RB}^h\mathbf{J}_b^h,\\
\mathbf{B}^b(\omega_e) &= (\mathbf{J}_b^h)^{\mathrm{T}}\mathbf{B}^h(\omega_e)\mathbf{J}_b^h\\
\mathbf{M}_A^b(\omega_e) &= (\mathbf{J}_b^h)^{\mathrm{T}}\mathbf{A}^h(\omega_e)\mathbf{J}_b^h - \frac{U}{\omega_e^2}(\mathbf{J}_b^h)^{\mathrm{T}}\mathbf{B}^h(\omega_e)\mathbf{J}_b^h,\\
\mathbf{C}_{RB}^b &= U\mathbf{M}_{RB}^b,\\
\mathbf{C}_A^b &= U(\mathbf{J}_b^h)^{\mathrm{T}}\mathbf{A}^h(\omega_e)\mathbf{J}_b^h\\
\mathbf{g}^b(\boldsymbol{\eta}) &= (\mathbf{J}_b^h)^{\mathrm{T}}\mathbf{g}^h(\boldsymbol{\xi}),\\
\boldsymbol{\tau}_{\mathrm{w}}^b &= (\mathbf{J}_b^h)^{\mathrm{T}}\boldsymbol{\tau}_{\mathrm{w}}^h.
\end{aligned} \quad (4.69)$$

Notice that this transformation of (4.58) to the *b*-frame generates two new matrices $\mathbf{C}_{RB}^b$ and $\mathbf{C}_A^b(\omega_e)$, which are recognized as the *Coriolis and centripetal matrices* due to rigid-body and frequency dependent added mass. There matrices appear as a consequence of expressing the equations of motion in a non-inertial frame.

Let us for convenience define the term

$$\begin{aligned}
\mathbf{N}^b(\omega_e) &\triangleq \mathbf{C}_A^b(\omega_e) + \mathbf{B}^b(\omega_e),\\
&= (\mathbf{J}_b^h)^{\mathrm{T}}[\mathbf{B}^h(\omega_e) + U\mathbf{A}^h(\omega_e)\mathbf{L}]\mathbf{J}_b^h
\end{aligned} \quad (4.70)$$

and express (4.68) as

$$[\mathbf{M}_{RB}^b + \mathbf{M}_A^b(\omega_e)]\,\dot{\boldsymbol{\delta\nu}} + \mathbf{N}^b(\omega_e)\boldsymbol{\delta\nu} + \mathbf{D}^b(\omega_e)\boldsymbol{\delta\nu} + \mathbf{g}^b(\boldsymbol{\eta}) = \boldsymbol{\tau}_{\mathrm{w}}^b, \quad (4.71)$$

Therefore, a time-domain representation for the above model valid for any type of excitation is the *Cummins equation in the b-frame*:

$$[\mathbf{M}^b_{RB} + \mathbf{M}^b_A(\infty)]\dot{\boldsymbol{\delta\nu}} + \mathbf{C}^b_{RB}\boldsymbol{\delta\nu} + \mathbf{N}^b(\infty)\boldsymbol{\delta\nu} + \int_0^t \mathbf{K}^b(t-\tau)\boldsymbol{\delta\nu}(\tau)\,d\tau + \mathbf{g}^b(\boldsymbol{\eta}) = \boldsymbol{\tau}^b_{\mathrm{w}}, \quad (4.72)$$

where

$$\mathbf{M}^b_{RB} = (\mathbf{J}^h_b)^{\mathrm{T}}\mathbf{M}^h_{RB}\mathbf{J}^h_b, \quad (4.73)$$

$$\mathbf{M}^b_A(\infty) = (\mathbf{J}^h_b)^{\mathrm{T}}\mathbf{A}^h(\infty)\mathbf{J}^h_b, \quad (4.74)$$

$$\mathbf{N}^b(\infty) = (\mathbf{J}^h_b)^{\mathrm{T}}[\mathbf{B}^h(\infty) + U\mathbf{A}^h(\infty)\mathbf{L}]\mathbf{J}^h_b, \quad (4.75)$$

$$\mathbf{K}^b(t) = \frac{2}{\pi}\int_0^\infty (\mathbf{N}^b(\omega) - \mathbf{N}^b(\infty))\cos(\omega t)d\omega, \quad (4.76)$$

The above is a unified model that can be used for slow manoeuvring in a seaway. Indeed, the classical linear manoeuvring model—linear version of (4.36)—can be obtained from (4.71), by taking the limit $\omega_e \to 0$. By doing this, we find the relationship between the added masses and potential damping obtained from strip theory and the hydrodynamic derivatives:

$$\mathbf{M}_A = (\mathbf{J}^h_b)^{\mathrm{T}}\mathbf{A}^h(0)\mathbf{J}^h_b - \lim_{\omega_e\to 0}\frac{U}{\omega_e^2}(\mathbf{J}^h_b)^{\mathrm{T}}\mathbf{B}^h(\omega_e)\mathbf{J}^h_b$$

$$= -\begin{bmatrix} X_{\dot u} & X_{\dot v} & X_{\dot w} & X_{\dot p} & X_{\dot q} & X_{\dot r} \\ Y_{\dot u} & Y_{\dot v} & Y_{\dot w} & Y_{\dot p} & Y_{\dot q} & Y_{\dot r} \\ Z_{\dot u} & Z_{\dot v} & Z_{\dot w} & Z_{\dot p} & Z_{\dot q} & Z_{\dot r} \\ K_{\dot u} & K_{\dot v} & K_{\dot w} & K_{\dot p} & K_{\dot q} & K_{\dot r} \\ M_{\dot u} & M_{\dot v} & M_{\dot w} & M_{\dot p} & M_{\dot q} & M_{\dot r} \\ N_{\dot u} & N_{\dot v} & N_{\dot w} & N_{\dot p} & N_{\dot q} & N_{\dot r} \end{bmatrix}$$

$$\mathbf{D}^b_{\mathrm{lin}} = (\mathbf{J}^h_b)^{\mathrm{T}}[\mathbf{B}^h(0) + U\mathbf{A}^h(0)\mathbf{L}]\mathbf{J}^h_b$$

$$= -\begin{bmatrix} X_u & X_v & X_w & X_p & X_q & X_r \\ Y_u & Y_v & Y_w & Y_p & Y_q & Y_r \\ Z_u & Z_v & Z_w & Z_p & Z_q & Z_r \\ K_u & K_v & K_w & K_p & K_q & K_r \\ M_u & M_v & M_w & M_p & M_q & M_r \\ N_u & N_{vp} & N_w & N_p & N_q & N_r \end{bmatrix},$$

where $\mathbf{D}^b_{\mathrm{lin}}\boldsymbol{\nu}$ is the linear part of $\mathbf{D}^b(\boldsymbol{\nu})\boldsymbol{\nu}$ in (4.36).

It should be noticed, however, that if coefficients in $\mathbf{A}^h(\omega_e)$ and $\mathbf{B}^h(\omega_e)$ calculated using strip-theory codes (2D potential theory), they are not accurate as $\omega_e \to 0$, because this is not contemplated in the assumptions used to derive strip theory—see, for example, [195] for details.

4.4.3 A Unified Nonlinear State-pace Model

Kristiansen and Egeland, [127], have proposed a state-space formulation for the convolution term in (4.72). If we consider:

$$\boldsymbol{\gamma}(t) = \int_{-\infty}^{t} \mathbf{K}^b(t-\tau)\boldsymbol{\delta\nu}(\tau)d\tau \overset{\text{causal}}{=} \int_{0}^{t} \mathbf{K}^b(t-\tau)\boldsymbol{\delta\nu}(\tau)d\tau; \tag{4.77}$$

Then, for causal systems it follows that:

$$\mathbf{K}^b(t-\tau) = \mathbf{0} \text{ for } t < 0 \tag{4.78}$$

If $\boldsymbol{\delta\nu}$ as a unit impulse, then (4.77) will be an *impulse response* function. Consequently, $\boldsymbol{\gamma}(t)$ can be represented by a linear state-space model:

$$\dot{\boldsymbol{\mu}} = \mathbf{A}_r^b\boldsymbol{\mu} + \mathbf{B}_r^b\boldsymbol{\delta\nu}, \qquad \boldsymbol{\mu}(0) = \mathbf{0} \tag{4.79}$$

$$\boldsymbol{\gamma} = \mathbf{C}_r^b\boldsymbol{\mu} + \mathbf{D}_r^b\boldsymbol{\delta\nu} \tag{4.80}$$

where $(\mathbf{A}_r^b, \mathbf{B}_r^b, \mathbf{C}_r^b, \mathbf{D}_r^b)$ are constant matrices of appropriate dimensions—see [127] for details on how matrices of the state-space can be obtained. As stated in [68], a good approximation to the convolution term is obtained using typically 5 states per entry of the matrix $\mathbf{K}^b$. For example, if we would like to design an autopilot with this model, we could consider the sway velocity, the yaw angle and the entries K_{66}^b, and K_{22}^b. Thus the control design model will have 13 states.

Using these results, we can obtain a state-space representation in the b-frame that is valid for *slow manoeuvring (slow turning) in a seaway with forward speed*:

$$\begin{aligned}
[\mathbf{M}_{RB}^b + \mathbf{M}_A^b(\infty)]\dot{\boldsymbol{\nu}} &= -(\mathbf{N}^b(\infty) + \mathbf{D}_r^b + \mathbf{C}_{RB}^b)(\boldsymbol{\nu} - \bar{\boldsymbol{\nu}}) - \mathbf{C}_r^b\boldsymbol{\mu} - \mathbf{g}^b(\boldsymbol{\eta}) \\
&\quad + \boldsymbol{\tau}_W^b + \boldsymbol{\tau}_P^b, \\
\dot{\boldsymbol{\mu}} &= \mathbf{A}_r^b\boldsymbol{\mu} + \mathbf{B}_r^b(\boldsymbol{\nu} - \bar{\boldsymbol{\nu}}), \\
\dot{\boldsymbol{\eta}} &= \mathbf{J}_b^n(\boldsymbol{\Theta}_{hb})\boldsymbol{\nu},
\end{aligned} \tag{4.81}$$

The term $\boldsymbol{\tau}_P^b$ represents the propulsion forces that take the ship to the speed $\bar{\boldsymbol{\nu}}$. In the first equation in (4.81), we can now add the control action forces $\boldsymbol{\tau}_C^b$ and slowly-varying environmental forces $\boldsymbol{\tau}_E^b$ (due to wind, current and second order wave excitation loads) and additional viscous damping terms $\mathbf{D}_V^b(\boldsymbol{\nu})\boldsymbol{\nu}$. The second equation in (4.81) provides additional dynamics associated with the radiation potential, *i.e.* fluid memory effects.

The following summarises the characteristics of the model given above:

- Compared to the motion superposition model shown in Figure 4.1, the model (4.81) provides a more accurate calculation of the radiation forces when manoeuvering in a seaway. Indeed, in the motion superposition model, the radiation forces are computed using only the motion induced by the waves (this is embedded in the motion RAO), whereas in the force superposition model (4.81), the radiation forces are computed using the motion induced by the combination of the wave and the control forces. This is well known in marine technology, but the state-space representation proposed in [127], and the formulation of the model in the body-fixed frame presented in this chapter, allows one to use the model for control system design. To the best of the authors' knowledge, these high-order models have never before been used for model-based control system design .

- The model uses data readily available from standard seakeeping programs. This is an advantage to the designer of motion control systems because a *preliminary* control design and evaluation can be performed before doing system identification. The only data required by these programs are the drawing of the hull and the loading condition.

- Different corrections to incorporate viscous effects can be included either in the time domain or in the frequency domain (by modifying $\mathbf{B}^h(\omega_e)$) before calculating retardation functions [11, 68, 69]. Also, if the potential theory data are complemented by data from a PMM test, the combination of these can contribute to improve the quality of the model, especially at low frequency. Details about this can be seen in [11, 68].

- A limitation of the model is that it is valid for slow manoeuvring (slow turning). The reason for this is that the wave-excitation forces and the retardation functions are obtained using programs based on seakeeping theory. Therefore, the model is limited to slow turning so that the h-frame can be considered approximately inertial.

- Other limitations of the model are heavily dependent on the seakeeping software used. These are related to the type of ship, the theory, and the code implementation. Therefore, one should be aware of these limitaions. For example, if a strip theory software is used (2D potential theory), there may be limitations in the accuracy of the data at low encounter frequency, and the maximum Froude number should be limited to 0.3, which means that the speed of the vessel should be restricted to

$$U < 0.3\sqrt{gLpp}. \tag{4.82}$$

5

Control Surfaces (Actuators)

The motion of a ship can be affected, to certain extent, by devices that impart forces and moments, *e.g.* rudders, fins, flaps, thrusters and propellers. These devices together with their commanding machinery constitute what in control engineering is known as *actuators*—see figure 5.1. Actuators play a very important role within the control system structure because they provide the link between the controller and the controlled system.

Due to the particular problems considered in this book, we will only focus on the principle of operation and models of the so-called control surfaces—fins and rudders—and their commanding machinery.

5.1 Geometry of Fin and Rudder Hydrofoils

Stabilizer fins and rudders usually present the geometry of a trapezoidal foil similar to that shown in Figure 5.2, in which the main dimensions of the foil are also shown: c_R—*root cord*, c_T—*tip cord* and sp—*span* or *outreach*.

The mean cord $\bar{c}$, foil area A_f and effective aspect ratio a are used to define the hydrodynamic characteristics of the foil. For the particular geometry shown in figure 5.2, these parameters are defined as follows:

$$\bar{c} = \frac{c_R + c_T}{2} \qquad A_f = sp\,\bar{c} \qquad a = \frac{2sp}{\bar{c}}. \tag{5.1}$$

5.2 Hydrodynamic Forces Acting on a Foil

When the fluid moves relative to the foil and there is a small angle of incidence (or effective angle of attack) α_e between the flow and the foil, the flow remains attached to the surface of the foil, and there appear forces on the foil—see Figure 5.3. In this condition, there is a distribution of the flow velocity field $\mathbf{v}$

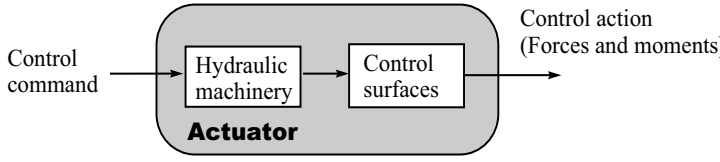

Fig. 5.1. Block diagram of a stabiliser actuator.

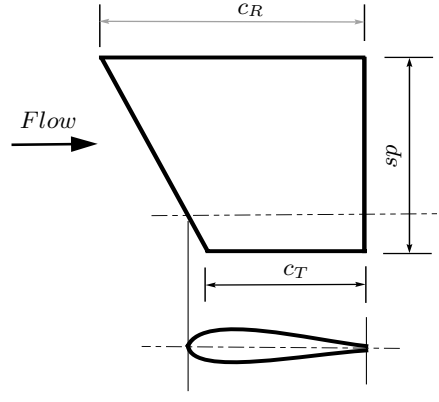

Fig. 5.2. Geometry of a hydrofoil or lifting surface.

along the sides of the foil, and this velocity distribution induces a distribution of pressure on the surface of the foil. The latter results in a force called *lift*, L, directed perpendicular to the flow velocity vector v_∞ far ahead of the foil—see Figure 5.3.

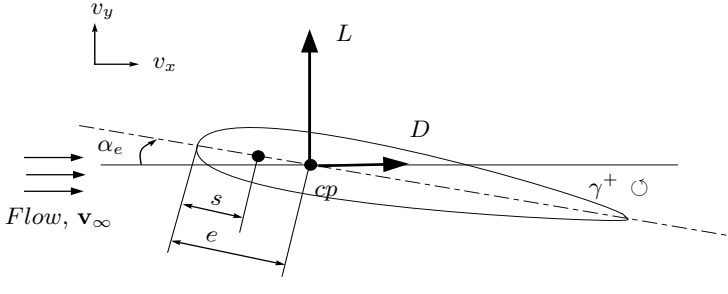

Fig. 5.3. Lift and drag forces on a hydrofoil at an angle of attack.

The above *qualitatively* described effect is usually referred to as two-dimensional (2D) foil theory in steady conditions, since it can be described by studying irrotational flows of an inviscid fluid with velocities confined in the plane perpendicular to the foil (*i.e.* $\mathbf{v} = [v_x\, v_y,\, 0]^{\mathrm{T}}$) as shown in figure 5.3. The corresponding quantitative result is known as the Kutta-Jowkousky theorem [3], which establishes that

$$L = -\rho |\mathrm{v}_\infty| \Gamma_C. \tag{5.2}$$

In expression (5.2), ρ is the density of the fluid, and Γ_C is the so-called *circulation*—defined as the line integral of the velocity field along a closed and positive-oriented curve γ^+ enclosing the foil (see Figure 5.3):

$$\Gamma_C = \oint_{\gamma^+} \mathrm{v} \cdot dl. \tag{5.3}$$

The reason for a non-zero value of circulation (*i.e.* difference between the average flow speed on the sides of the foil) in steady conditions is related to the history of the fluid: in particular, the generating or starting vortex. This vortex is generated due to the viscosity of the fluid which induce flow separation at the sharp trailing edge when the foil starts moving with respect to the fluid. The vorticity generated creates the amount of circulation necessary to shift the rear stagnation point to the trailing edge. Once this condition is reached, the vortex passes to the wake, and the distribution of velocity attains steady conditions provided that v_∞ and α_e keep constant. Once the foil is in steady-state flow, the behaviour of the foil can be study using potential flows. For further details see, for example, [3, 17, 159].

The 2D foil theory accurately describes the behavior of real foils of very high aspect ratio (*cf.* (5.1)) for which the approximation of a 2D flow is valid. However, as the aspect ratio reduces, the flow is no longer two-dimensional but three-dimensional (3D) due to cross flow at the tip of the foil (and also at the root of the foil.) Due to mechanical constraints and space restrictions, high aspect ratio rudders and fins are not viable for every ship. Therefore, most of the control surfaces in marine applications are of low aspect ratio.

The study of 3D flows reveals that the lift reduces with respect to that described by the 2D theory (*cf.* 5.2) and another force appears acting on the foil. This force is called *drag* D, and it is directed in the same direction as v_∞–see figure 5.3. The drag is a consequence of the energy carried away by the trailing vortexes emanating from the tip of the foil [3, 142].

Both resulting forces, L and D, are assumed to act on a point called *centre of pressure* (CP), which is located at the mid-span $sp/2$ and at a distance e from the leading edge of the foil—see Figure 5.3. The position of the CP varies with the angle of attack. This variation is relevant to the mechanical design of the rudder or fin because of the moments these must withstand. However, the effects this variation produces in ship motion can be neglected; and thus, we can consider a fixed position for it. Then, provided $sp > \bar{c}$, the CP is located at $e \approx 0.25\,\bar{c}$ for small angles of attack.

For practical reasons, it is common to express the lift and drag in non-dimensional form:

$$C_L = \frac{L}{0.5\rho V_f^2 A_f} \qquad C_D = \frac{D}{0.5\rho V_f^2 A_f}, \tag{5.4}$$

where $V_f = |\mathrm{v}_\infty|$. From experimental results, Whicker and Fehlner [237] obtained the following formulae to estimate the non-dimensional lift and drag [133]:

$$C_L = \left.\frac{\partial C_L}{\partial \alpha_e}\right|_{\alpha_e=0} \alpha_e + \frac{C_{Dc}}{a}\left(\frac{\alpha_e}{57.3}\right)^2, \tag{5.5}$$

$$C_D = C_{D0} + \frac{C_L^2}{0.9\pi a}, \tag{5.6}$$

where α_e is measured in degrees, C_{Dc} is the cross-flow drag coefficient, and C_{D0} is the minimum section drag (*e.g.* for a NACA 15 profile $C_{D0} = 0.0065$.) Because drag is an undesirable effect, expression (5.6) is often used to interpret drag as the *price paid for obtaining lift* [142].

Figure 5.4 shows typical steady characteristics of lift and drag for a foil with a profile similar to that shown in Figure 5.3. From this figure, we can see

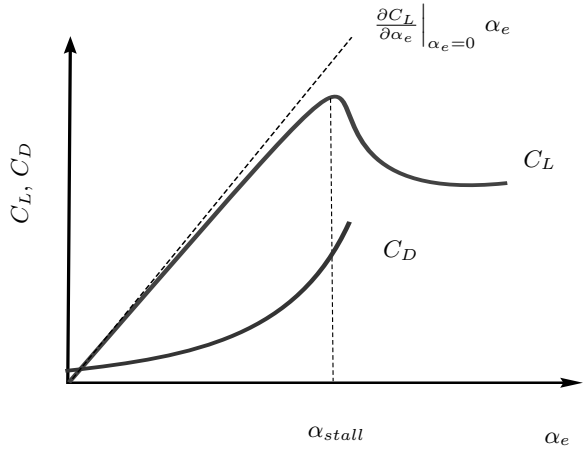

Fig. 5.4. Typical steady free-stream lift and drag characteristic of a hydrofoil.

that the lift develops in an approximately linear manner with an increasing

angle of attack. This linear behaviuor can be approximated using only the first term in the expression for C_L given in (5.5). Also, we can see that the growth of lift with an increasing angle of attack breaks for a particular angle called the *stall angle* α_{stall}. At this angle, flow separation occurs, and the drag increases significantly.

The above presents the characteristic behaviuor of a foil in steady conditions, *i.e.* $\dot{\alpha}_e = 0$ and $\dot{\mathrm{v}}_\infty = \mathbf{0}$. In applications of manoeuvering studies and autopilot design, these models are often deemed satisfactory. However, due to the operation mode of stabilisers, there are situations in which dynamic effects should be considered. These dynamic effects have been reported to affect significantly the performance of fin stabilisers [80]; these are, therefore, the subject of current research interest. In the following section, we introduce unsteady hydrodynamic effects and their implications for stabiliser design.

5.3 Unsteady Hydrodynamics

Recent experimental studies on performance of fin stabilisers reported in [80] seem to indicate that, in mild sea conditions, the static characteristics of foils may be appropriate to describe fin stabiliser behaviuor. As the sea conditions become rough, however, highly nonlinear effects appear that deteriorate the performance of the stabiliser. Quoting Galliarde [80]: [In these conditions] *the dynamic behavior of fins differs significantly from their static behavior; and the efficiency of the stabiliser can be reduced to such extent that the ship behaves as if no stabiliser was present.*

Unsteady hydrodynamic characteristics of foils arise due to time-varying effects. As stated in [92], these effects can be classified in two groups: *foil motion* and *unsteady flow-field structure*. For the case of fin and rudder stabilisers, these effects can be further specified as follows:

- **Foil motion**. Due to the principle of operation of stabilisers, the angle of the foil with respect to the hull is varied permanently as demanded by the controller. This angle, in the sequel identified as the *mechanical angle* (α), is the angle describing the pitch motion of the foil. In addition, the motion of the hull induces foil motion which forces the latter to plunge or heave in the fluid. For example, roll motion induces a local flow velocity component tangential to the hull which acts perpendicular to fins when the mechanical angle is zero. This velocity is often more significant in fins than in rudders due to the larger distance from the ship's centre of roll to the CP of the fins. The local roll-induced velocity, together with the forward velocity of the ship, produce an angle of incidence, which we call *flow angle* (α_{fl}); the combination of mechanical and flow angles modifies the effective angle of attack (α_e) used to give the hydrodynamic characteristics of the fin. To illustrate this, Figure 5.5 depicts the magnitudes involved in an example where the ship rolls to starboard (ϕ, $p > 0$). In this figure, we

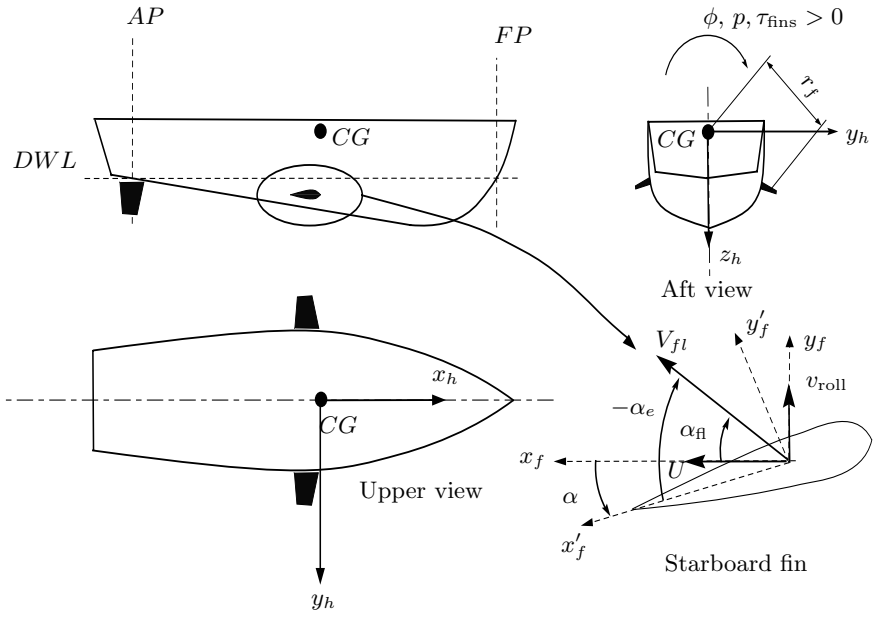

Fig. 5.5. Fin motion due to roll motion.

can see the coordinate frame x_f-y_f in which the mechanical angle and flow angle are defined and also the frame x'_f-y'_f in which the effective angle of attack is defined. The frame x_f-y_f is positioned so that the cord of the fin coincides with the x_f axis when the mechanical angle is zero, while the frame x'_f-y'_f is fixed to the fin. Figure 5.5 also shows the flow velocity V_{fl}, which has been resolved into two components: U surge velocity and v_{roll} roll induced velocity. The roll-induced velocity depends on the roll rate p and the position of the fin relative to the roll center[1] indicated by r_f in Figure 5.5. Using the convention shown in Figure 5.5, we can define

$$\alpha_{\text{fl}} = \arctan\left(\frac{v_{\text{roll}}}{U}\right) = \arctan\left(\frac{r_f\, p}{U}\right) \qquad \alpha_e = -\alpha_{\text{fl}} - \alpha, \tag{5.7}$$

where $\alpha_e > 0$ will induce a positive roll moment: $\tau_{4\text{fins}} > 0$.

- **Flow-field structure**. This takes into account the time-varying incident velocity due to the flow motion. In the case of a ship, the waves that move relative to the hull affect the flow speed and angle due to the elliptical orbital motion of the water particles in the region close to the fin [80].

At low effective angles of attack, with fully attached flow, the unsteady hydrodynamic effects result in small variations of the lift coefficient C_L with respect

[1]For simplicity we will take the roll centre to coincide with the centre of gravity [135]. For a discussion regarding the definition of roll centre see, for example, [110].

to the static hydrodynamic characteristics. For example, Figure 5.6(a) shows a schematic of the hydrodynamic characteristics of a foil in both steady and unsteady conditions.

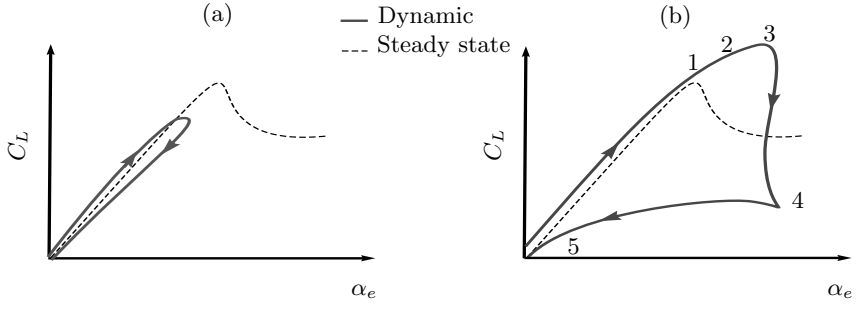

Fig. 5.6. Schematic hydrodynamic characteristic of a foil in steady and unsteady conditions. (a) For small effective angle of attack. (b) For large effective angle of attack.

The phenomena depicted in Figure 5.6(a) have been studied extensively in the field of helicopter rotor aerodynamics[2]. Different theories and models have been proposed in this branch of engineering to study this phenomenon. This behavior can be represented with a second-order linear state-space model, in which the input is the effective angle of attack and the output the lift coefficient C_L—see [92] for further details:

$$\begin{aligned} \dot{\mathbf{x}} &= \mathbf{A}\mathbf{x} + \mathbf{B}\alpha_e \\ C_L &= \mathbf{C}\mathbf{x} + D\alpha_e. \end{aligned} \tag{5.8}$$

When the effective angle of attack is large, however, the unsteady hydrodynamic effects develop into the so called dynamic stall . As stated in [92]: *dynamic stall occurs when a foil or any lifting surface is subject to time-dependent pitching, heaving or other type of unsteady motion that takes the effective angle of attack beyond normal stall conditions.* The resulting flow separation in dynamic stall conditions is significantly different from that found in steady conditions. Due to the nonlinear phenomena involved, there are no simple models such as (5.8) to quantitatively describe and predict this effect suitable for engineering analysis in aerodynamics. To the best of the author's

[2]The rotor blades (foils) of a helicopter are subject of cyclic pitching to account for the difference in flow speed between the blade that is advancing and the blade that is retreating; and therefore, balance the lift they produce.

knowledge, these models are also under development in the area of hydrodynamics. In the following, we present a qualitative description of the physical characteristics of dynamic stall relevant to our purposes.

Figure 5.6(b) shows a schematic for the lift developed by a foil under dynamic stall together with the associated static characteristic. To facilitate the description, this figure also shows points of interest identified by numbers (1 to 5). We will use these points to describe the associated physical phenomena. Following [92]:

- (1) At this point, the foil reaches the steady stall angle.

- (2) The first indication of dynamic stall appears as the lift developed is still increasing with the effective angle of attack beyond steady stall angle. This effect is the result of a delay in flow separation due to the formation of a vortex at the leading edge of the foil. At this stage, it is usually said that the lift overshoots [106]. This overshoot can be up to 100% of the static maximum lift [92].

- (2-3) Here the vortex generated at the leading edge travels towards the trailing edge and the lift still increases until point 3 when the vortex reaches the trailing edge and the lift finally stalls.

- (3-4) After the vortex reaches the trailing edge and passes to the wake, the flow separates completely.

- (4-5) The angle of attack reduces until the flow becomes reattached at point 5.

As we will see in Chapter 13, the effects represented in Figure 5.6(b), together with the above description, will serve to define some of the control system specifications. As a motivation example, Figure 5.7(a) shows the lift coefficient characteristic recently obtained in model tank testing experiments reported in [80]. Apart from the effects already described, it is interesting to note in this figure that once the fin stalls, reduction in the effective angle of attack can result in a change in the lift sign before the sign of the effective angle of attack changes. Figure 5.7(b) shows the non-linearity in a time series of the measured lift.

There is an important characteristic of the dynamic behaviour of foils relevant to stabiliser control design which has not been depicted in the presented diagrams. This is the dynamic characteristic when the maximum effective angle of attack is close to the static stall angle. This situation is an intermediate case between what is shown in Figures 5.6(a) and 5.6(b). Figure 5.8 shows a schematic of the behaviour of the foil in this situation. The work presented in [116] shows experimental data in a form similar to that presented in Figure 5.8.

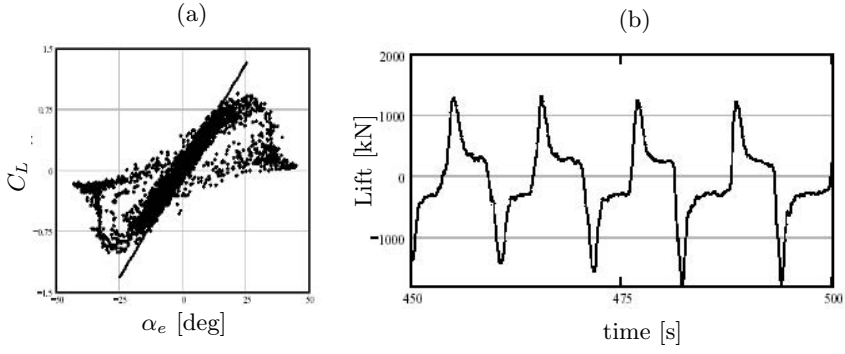

Fig. 5.7. Model tank testing results of fin stabilisers with a linear controller performed at MARIN-Maritime Research Institute Netherlands on a 1:40 model of a 180 m fast ferry at 35 kt in quartering regular seas. (a) Lift coefficient C_L. (b) Time series of the measured lift force. Courtesy of MARIN.

The relevance of this issue to the stabiliser control system design is stated in the following hypothesis:

According to experimental results, it seems that even in dynamic conditions, the behaviour of the foil can be predicted by its static characteristic provided the effective angle of attack is not taken beyond the static stall angle.

The above will be used to define an additional specification for the design of the control system in Chapter 13.

5.4 Forces and Moments Acting on the Hull

Summarising the material presented in the previous sections, there is a total hydrodynamic force F induced on the fin resulting from L and D acting on the centre of pressure CP . This total hydrodynamic force can also be resolved, for convenience, into the components N and T, which are normal and tangential to the foil respectively:

$$\begin{aligned} N &= L\cos\alpha_e + D\sin\alpha_e \\ T &= D\cos\alpha_e - L\sin\alpha_e, \end{aligned} \tag{5.9}$$

such that $F = \sqrt{L^2 + D^2} = \sqrt{N^2 + T^2}$. Furthermore, from expressions (5.5) and (5.6), it follows that

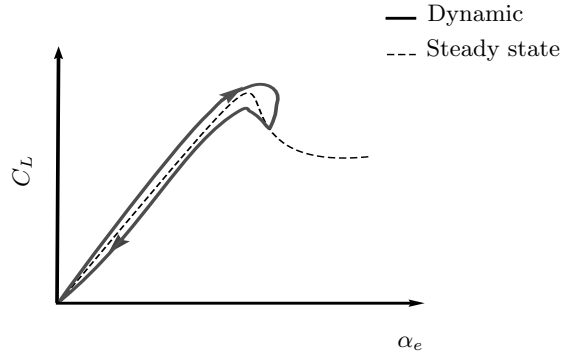

Fig. 5.8. Schematic hydrodynamic characteristic of a foil in dynamic and steady conditions when the maximum effective angle attack is close to static stall angle.

$$L = \frac{1}{2}\rho V_f^2 A_f C_L(\alpha_e) \qquad D = \frac{1}{2}\rho V_f^2 A_f \left(C_{D0} + \frac{C_L(\alpha_e)^2}{0.9\pi a} \right), \quad (5.10)$$

where $C_L(\alpha_e)$ can be either the steady state or the dynamic characteristic of the foil. Expressions (5.9) and (5.10) hold for any foil whether the latter be a rudder or a stabiliser fin. However, the effective angle of attack and the forces and moments appearing on the hull depend on the location of the foil. In the following, we establish these relationships between forces and moments on the hull and hydrodynamic components for both rudders and fins.

5.4.1 Rudder

In manoeuvering applications, the effective angle of attack of the rudder depends on the mechanical angle, surge velocity (u), sway velocity (v) and the sway velocity astern induced by the rate of turn of the vessel ($v_a \approx -LCG\, r$)[3]. However, for rudder-based stabilisers, the problem can be simplified by taking the effective angle of attack to be identical to the mechanical angle, which is defined positive when the rudder moves to port—see Figure 5.9.

The assumption leading to this simplification is that rudder roll stabilisation is not used in manoeuvring situations; and therefore, the sway velocity can be neglected. In addition, due to frequency separation between the roll

[3] In naval architecture, the distance from the rudder stock to the center of gravity is commonly referred to as the Lateral Centre of Gravity (LCG)—see Figure 5.9.

dynamics (which in this case determine the rudder motion) and the yaw dynamics, the sway velocity astern induced by the rate of turn can also be neglected in most situations. Therefore, under these assumptions, the rudder induced forces and moments in 4DOF can be expressed in the body-fixed frame as

$$\begin{aligned} \tau_{1\text{rudder}} &\approx -D \\ \tau_{2\text{rudder}} &\approx \quad L \\ \tau_{4\text{rudder}} &\approx -r_r\, L \\ \tau_{6\text{rudder}} &\approx -LCG\, L \end{aligned} \tag{5.11}$$

where r_r is the rudder roll arm (distance CG-CP), and LCG is defined in Figure 5.9, and L and D given in (5.10). Note that the positive convention shown in Figure 5.9 is in agreement with that presented in Chapter 3: right-hand or right-hand curl rule.

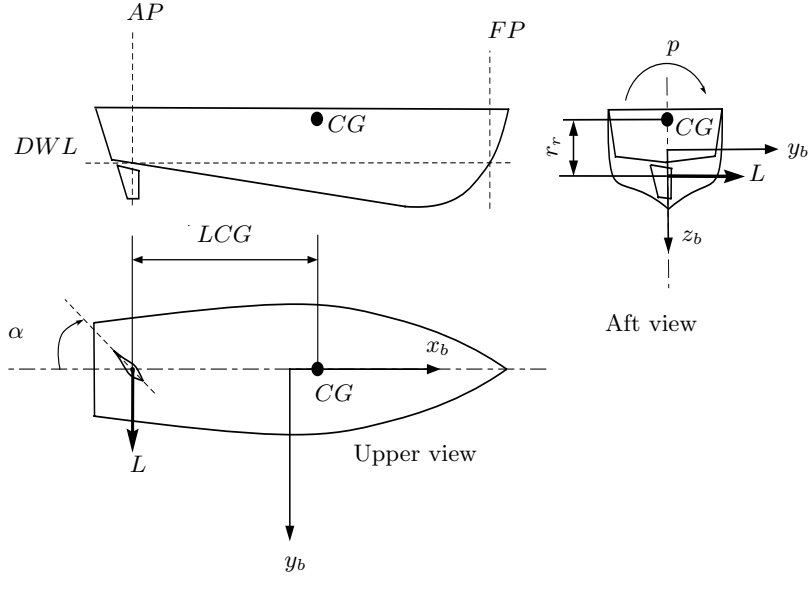

Fig. 5.9. Rudder-induced forces and moments.

5.5 Rudder-Propeller Interaction

To evaluate the lift and the drag produced by the rudder (*cf.* (5.10)), we need to estimate the flow velocity over the rudder u_r. Because the rudder is located in the race of the propeller, the flow velocity over the rudder will be different than the forward velocity of the vessel. To estimate this, we can consider the momentum theory of propellers.

The momentum theory is based on the principle that thrust is generated as a consequence of accelerating the fluid. This approach treats the propeller as a disk that produces a sudden increase in pressure when the fluid passes from one side of the disk to the other.

In the simplified scheme shown in Figure 5.10, the propeller is considered as a disk of area A_p that advances through the undisturbed fluid at a speed u_a. This disk produces a sudden increase in the pressure of the water that passes through it, as indicated in the plot at the bottom of the figure. This figure also shows the streamlines, *i.e.* lines that are tangent to the velocity vector of the fluid; hence, there is no flow across the the streamlines. Under

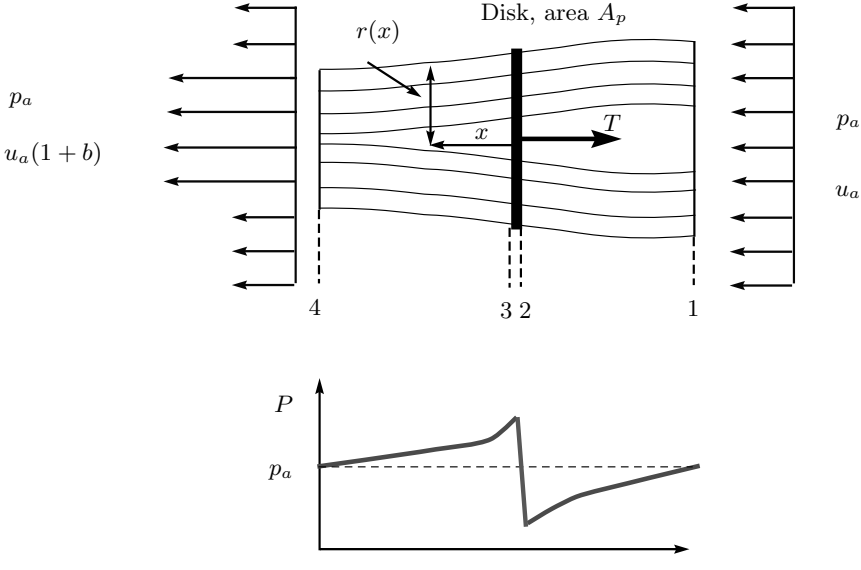

Fig. 5.10. Momentum theory of propeller action

the assumption that the propeller imparts uniform acceleration to all the fluid passing through it, there is a contraction of the tube of fluid; hence, there must be a gradual change in the speed of the fluid. It will be further assumed that there is no rotational motion of the fluid. Then, at the cross section 1, ahead

of the propeller, the fluid has a velocity u_a (*advance velocity* relative to the propeller), and in the wake, section 4, well behind the propeller, the fluid has a speed which may be written as $u_a(1+b)$. The velocity of the fluid at section 2 will be greater than u_a, and this can be written as $u_p = u_a(1+a)$.

If the disk is considered of negligible width, then the speeds on each side equal $u_a(1+a)$, and the volumetric flow rate passing through the disc is

$$Q_f = A_p u_p = A_p u_a(1+a). \tag{5.12}$$

If the flow is steady, the pressure in the tube will be reduced from p_a as the flow speed increases towards the disk—Bernoulli's law. At section 3, the pressure is increased, and at section 4 the pressure will again be p_a. Consequently, by considering the volume between sections 1 and 4, we can apply the momentum equation to the volume in the tube, and the thrust is equal and opposite to the force on the fluid—see [145]:

$$X_T = \rho\, Q_f(u_a(1+b) - u_a). \tag{5.13}$$

Further, the thrust is the result of the difference in pressure between the sides of the disk:

$$X_T = (p_3 - p_2)A_p. \tag{5.14}$$

By applying Bernoulli's law between sections 1 and 2 and between sections 3 and 4 (it cannot be applied between sections 2 and 3 because the flow is unsteady):

$$p_1 + \frac{1}{2}\rho u_1^2 = p_2 + \frac{1}{2}\rho u_2^2$$
$$p_4 + \frac{1}{2}\rho u_4^2 = p_3 + \frac{1}{2}\rho u_3^2,$$

and noting that $u_2 = u_3 = ua(1+a)$, $u_4 = u_a(1+b)$ and $p_1 = p_4 = p_a$, it follows that

$$p_3 - p_2 = \frac{1}{2}\rho(u_a^2(1+b)^2 - u_a^2). \tag{5.15}$$

Finally, by substituting (5.15) into (5.14), and combining this with (5.13), it follows that

$$a = \frac{b}{2}. \tag{5.16}$$

Thus, the fluid increases one-half of its velocity when reaching the disk, and

$$X_T = \rho A_p u_a^2(b + b^2/2) = \rho A_p u_a^2 2(a + a^2). \tag{5.17}$$

The velocity of advance can be estimated from the forward speed of the vessel, U as

$$u_a = (1-w)U, \tag{5.18}$$

where the *wake fraction* w usually takes values between 0.1 and 0.4 [66]. Because the forward speed of the vessel is assumed constant, the thrust can be equated from the hull resistant coefficient

$$X_T = (1-t)^{-1} X_{u|u|} U|U|, \tag{5.19}$$

where t is the so-called *thrust deduction number*, which takes values between 0.05 and 0.2 [66]. Then, for a given forward speed of the vessel, we can estimate the flow speed at the propeller as

$$u_p = \frac{1}{2}\left[(1-w)U + \sqrt{(1-w)^2U^2 + \frac{2(1-t)^{-1}X_{u|u|}U|U|}{\rho A_p}}\right]. \tag{5.20}$$

The radius of the wake at a location of x metres behind the propeller, $r(x)$—see Figure 5.10—can be estimated as [134]:

$$r(x) = r_p \frac{0.14\left(\frac{u_p}{2u_p-u_a}\right) + \left(\frac{x}{r_p}\right)^{1.5}}{0.14\left(\frac{u_p}{2u_p-u_a}\right)^{1.5} + \left(\frac{x}{r_p}\right)^{1.5}} \sqrt{\frac{u_p}{2u_p-u_a}}, \tag{5.21}$$

where r_p is the propeller diameter. Finally, if the centre of pressure of the rudder is located at the position x, then the average flow velocity over the rudder can be estimated as [134]:

$$u_r = u_p \left(\frac{r_p}{r(x)}\right)^2. \tag{5.22}$$

with u_p and $r(x)$ given above.

The reader should be aware that the simplified model for the interaction between rudder and propeller presented in this section, is only valid for ships sailing at a constant forward speed.

5.5.1 Fins

The case of fin stabilisers involves a more detailed analysis than that for the rudder because variations of the effective angle of attack due to the motion of the hull cannot be neglected in some conditions.

With the adopted positive convention shown in Figure 5.11, we have $\tau_{4\text{fins}} > 0$ whenever $\alpha_e > 0$ (*cf.* (5.7)). If we consider $\alpha_{\text{fl}} = 0$, positive mechanical angles of the fins will induce a negative roll moment: the positive mechanical angles have been defined using the right hand side convention for both fins. Similarly, if $\alpha = 0$, the flow angle induced by the combination of positive roll rate p and forward speed of the vessel U will induce a negative roll moment.

From this figure, it follows that the roll moment due to the hydrodynamic forces acting on the fins can be approximated by:

$$\tau_{4\text{fins}} \approx 2\, N\, r_f, \tag{5.23}$$

where N is the the resulting hydrodynamic force component normal to the fin, which is (*cf.* (5.9)) defined positive with positive angle convention for the fin angles, and r_f is the fin roll arm—see Figure 5.11.

In Expression (5.23), it has been assumed that both fins develop the same amount of roll moment, and that the magnitude of the forces producing this moment are approximated by the magnitude of the component normal to the fin. Experimental results indicate that the first assumption is not always

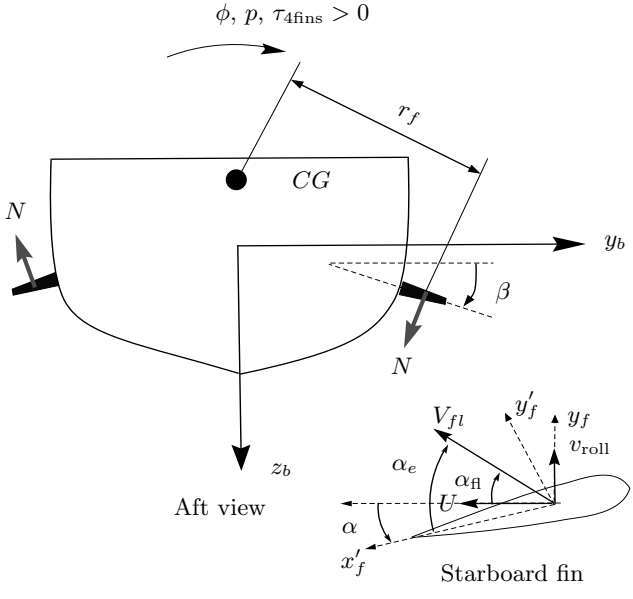

Fig. 5.11. Fin motion due to roll.

realistic due to the differences in flow velocity between the windward and leeward side of the vessel produced by the wave pattern [80]. This effects will be further discussed in Chapter 13. Using these approximations, we can obtain the following model for the forces and moments induced by the fins:

$$\begin{aligned}
\tau_{1\text{fins}} &\approx -T \\
\tau_{2\text{fins}} &\approx -N\, \sin(\beta) \\
\tau_{4\text{fins}} &\approx 2\, N\, r_f \\
\tau_{6\text{fins}} &\approx FCG\, N\, \sin(\beta),
\end{aligned} \tag{5.24}$$

were the angle β is fins tilt angle indicated in Figure 5.11, FCG is the longitudinal distance from the centre of pressure of the fins to the center of gravity (see Figure B.3). The forces T and N are the tangential and normal component of the hydrodynamic force generated by the fins (*cf.* (5.9)).

5.6 Hydraulic Machinery

Control surfaces are commanded by hydraulic machinery that implement the action demanded by the controller. The characteristics of this machinery are important since they can impose constraints on the control action. The mathematical model of the hydraulic machinery most commonly used in marine applications is the simplified model presented by van Amerongen [223]. Figure 5.12 presents a block diagram corresponding to this model, in which α_c is the control command and α_m is the mechanical angle of the fin or rudder. The model presented in Figure 5.12 captures the essential characteristics relevant to control system design:

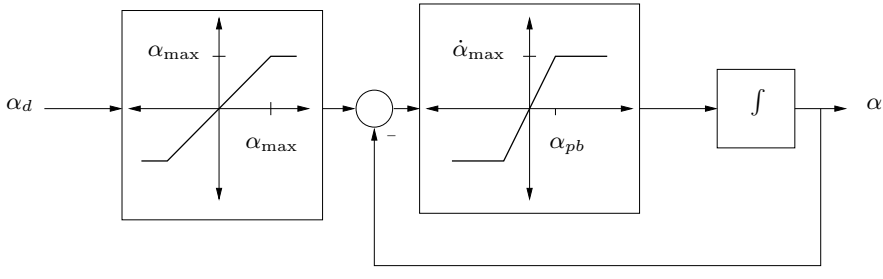

Fig. 5.12. Simplified block diagram of a hydraulic actuator model.

- Magnitude saturation: the foil motion is constrained to move within certain maximum angles, *i.e.* $-\alpha_{\max} \leq \alpha \leq \alpha_{\max}$.
- Slew rate saturation: The rate of rudder movement is limited by a maximum value $\dot{\alpha}_{\max}$.
- Time delay: the main servo is responsible for producing most of the delay between the desired rudder angle α_d and the actual rudder angle α. This delay is represented by a first order system with a time constant

$$t_r = \frac{\alpha_{pb}}{\dot{\alpha}_{\max}}$$

where α_{pb} is the so-called proportional band. Figure 5.13, shows the effect of rate limitations on the rudder response to a sinusoidal rudder command.

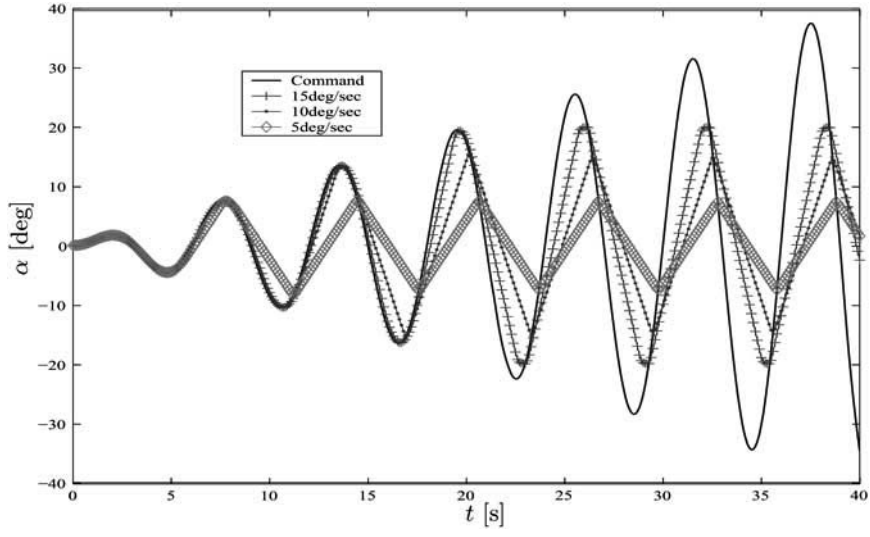

Fig. 5.13. Effect of rate limit on rudder response to a linearly growing sinusoidal command of period $7s$.

5.7 Part I Summary and Discussion

This first part of the book has introduced the models used for control system design. These include simplified nominal models, and also more complex calibration models, which can be used to test control strategies at preliminary stages before proceeding with physical model testing or full-scale trials. In Appendix B, a benchmark example is presented for which all the parameters of the models presented in this part are given.

The second part of the book provides an introduction to the particular ship motion control problem of roll stabilisation.

Part II

Introduction to Ship Roll Stabilisation

6

Ship Roll Stabilisation

This chapter provides an overview of the different techniques used to reduce the roll motion of ships.

6.1 Effects of Roll Motion on Ship Performance

Roll motion, in particular, affects ship performance in the following ways:

- Transverse accelerations due to roll induce interruptions in the tasks performed by the crew. This increases the amount of time required to complete the missions, and in some cases may even prevent the crew from performing tasks at all. This can render navy ships inoperable [152].

- Vertical accelerations induced by roll at locations away from the ship's centre line can contribute to the development of seasickness in the crew and passengers, which affects performance by reducing comfort.

- Roll accelerations may produce cargo damage, *e.g.* on soft loads such as fruit.

- Large roll angles limit the capability to handle equipment on board. This is important for naval vessels performing weapon operations, launching or recovering systems, and sonar operation.

6.2 Damping or Stabilising Systems?

There has been some controversy in the literature with regards to the use of the terms *roll stabilising* or *roll damping* systems. Some people argue that the roll motion of a ship is inherently stable, and suggests that *roll damping* is therefore more accurate. This choice, however, could be misleading because

these systems may do more than just modifying the damping. As discussed by Weinblum and St. Denis, [235], by referring to the equations of motion, one could distinguish three ways of reducing motion:

- Increase the damping,
- Increase the inertia (to decrease the roll natural frequency of the ship and avoid synchronization with the waves),
- Reduce the exciting moment.

Perhaps a more appropriate term to describe these systems could be *roll reduction* systems. Nevertheless, the industry (together with the vast majority of the literature) seems to have preferred *stabilisation* over *damping*, and a change now to *reduction* could lead to confusion. Therefore, in this book we will adopt the terms *ship roll stabilisation* and *stabiliser*, with the following definitions for them:

Definition 6.1 (Ship roll stabilisation—SRS). *Ship roll stabilisation refers to the reduction of the undesired ship roll motion induced by the waves.* ○ ○ ○

Definition 6.2 (Stabiliser or ship roll stabilisation system). *A stabiliser or ship roll stabilisation system is a stable feedback system used to reduce ship roll motion induced by the waves.* ○ ○ ○

Note that from a system dynamics perspective, *all* roll stabilisers can be described in terms of a feedback configuration, with the input-output causality depicted in Figure 6.1. Therefore, Definition 6.2 applies to both active and passive stabilisers.

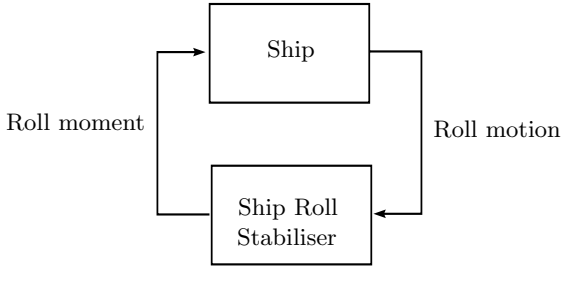

Fig. 6.1. Ship roll stabiliser.

Furthermore, since such a feedback system must be designed to be stable—whether the open-loop system is stable or not—the author believes that the use of the term *stabilising* provides an appropriate description.

6.3 Ship Roll Stabilisation Techniques

The first elements leading to good SRS are careful hull design and load distribution. It was shown by Froude, in his seminal paper *On the rolling of ships*, in 1861–[75, 76], that it is not the height of the waves, but the steepness (slope) what excites the rolling motion of a ship. He further commented that since short waves appear to be steeper than long waves, there is, then, no advantage in trying to reduce the natural roll period of the vessel. Instead, this period should be extended as much as possible so as to avoid synchronization with the wave excitation frequency. This can only be achieved by [77]:

- Increasing the moment of inertia,
- Reducing the transverse stability.

The first is entirely related to the distribution of the load on the ship, whereas the second also accounts for the shape of the hull. With regards to the hull shape and damping, significant increase in damping can be achieved by designing hulls with a small bilge radius, and with the appendages located as far as possible from the centre of gravity [93].

Despite good efforts to extend the natural period of the vessel, it is inevitable that wave loads will excite roll for some sailing conditions. In addition, the damping of the hull may not be sufficient to attenuate roll motion to the desired levels. For these reasons, the vessel is often equipped with roll reduction systems.

As commented by Chadwick [44] if one looks at the patent registers, there have been a large number of proposals from which only a few passed the stage of a prototype. Further, he makes the observation that all stabilisers depend on the motion of mass; thus, they can be classified according to three elementary properties:

1. Type of motion
   - **A (Acceleration)**. The reducing moment is produced by mass acceleration.
   - **D (Displacement)**. The reducing moment is produced by the action of gravity on a displaced mass.
2. Location
   - **I (Internal)**. Mass is internal to the ship.
   - **E (External)**. Mass is external to the ship.
3. Type of mass
   - **S (Solid)**. The mass is solid.
   - **F (Fluid)**. The mass is fluid.

Obviously, not all the combinations of the above are possible. By considering either fluid or solid mass, the elementary types that have resulted in full scale trials are as indicated in Table 6.1.

In the following, we provide an overview of the working principles of these devices and discuss their advantages and disadvantages.

Table 6.1. Types of stabiliser—adapted from [44].

Working principle	Example
AIS (Accel. of Internal Solid mass)	Gyroscopes
AEF (Accel. of External Fluid mass)	Bilge keels, fins, rudder
DIS (Disp. of Internal Solid mass)	Motion of weights
DIF (Disp. of Internal Fluid mass)	Anti-roll tanks

6.3.1 Gyroscopes

The gyroscope type of stabiliser consists of using the gyroscopic effects of a large rotating wheel to generate a reducing moment. The use of gyroscopic effects was proposed as a method to eliminate roll, rather than to reduce it. This method is not currently in use, but the interested reader can look into the references provided in Section 6.4—where we briefly discuss the history of SRS developments.

6.3.2 Bilge Keels

Bilge keels are the simplest form of stabiliser. These are long narrow keels mounted on the turn of the bilge. Figure 6.2 shows a conventional arrangement. The idea of using bilge keels was apparently put forward by Froude in the mid-19th century—see [236, 83, 78].

Bilge keels increase the hull damping by generating drag forces that act perpendicular to the keels and oppose the roll motion. In this way, the kinetic energy associated with roll is converted to fluid kinetic energy by viscous effects (shed vortices). The main advantages of bilge keels are the following:

- Relatively effective source of damping, especially at low speeds. The performance is in the range of 10–20% of roll angle reduction (RMS) [198].
- Low maintenance; no more than that normally done to the hull.
- No occupied space and no significant increase of ship dead weight.
- Low price and easy installation.

Some disadvantages of bilge keels are indicated as follows:

- Increase of hull resistance in calm water conditions (when roll reduction is not necessary.) Although this is alleviated by careful alignment with the hull streamlines, the increase of resistance in calm water can still be significant [198].

- Not all ships can be fitted with bilge keels. For example, they could be a potential problem for fishing vessels deploying nets, and are very easily damaged in ice-breakers.

For more details about performance and dimensions of bilge keels, see Ikeda, [111], and references therein.

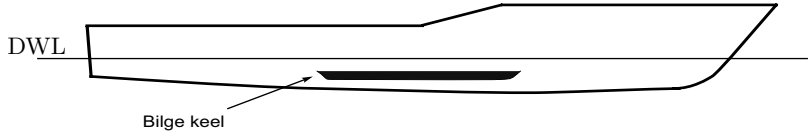

Fig. 6.2. Bilge keel arrangement.

6.3.3 Anti-rolling Tanks

The most widely used anti-roll tank is the U-tube tank; originally developed by Frahm in 1911 [70]. This type of tank is composed of two reservoirs, located one on port and one on starboard, connected at the bottom by a duct as shown in Figure 6.3. The principle of operation of anti-roll tanks is that as the ship rolls, the fluid inside the tank (usually water) moves with the same period the ship moves, but lagging a quarter of period behind the rolling of the vessel [45]. This way, the weight of the mass of fluid produces a moment that opposes the roll motion. This moment attains its maximum values when the ship passes through its vertical position.

Anti-roll tanks can be either passive or active. In passive tanks, the fluid flows freely from side to side. According to the density and viscosity of the fluid used, the tank is dimensioned so that the time required for most of the fluid to flow from side to side equals the natural roll period of the ship. Fine tuning can be achieved by adjusting the air that flows from one side to the other through the valve shown in Figure 6.3. This condition can only be attained at a single frequency—the tank natural frequency. Passive tanks are tuned to match the tank natural frequency with the roll natural frequency of the ship. Gradual performance degradation occurs if the frequency of roll motion departs from the tank natural frequency. This happens due to variations of the wave excitation frequency in different sea states. Figure 6.4 shows an example of roll response (roll amplitude/wave amplitude for a sinusoidal wave) with and without the tank. In this example, the roll resonant frequency is about 1 rad/s, and the tank is tuned for maximum performance at this frequency. The performance of the tank worsens at low excitation frequencies.

Active tanks operate in a similar manner to their passive counterparts, but they incorporate a control system which modifies the natural period of

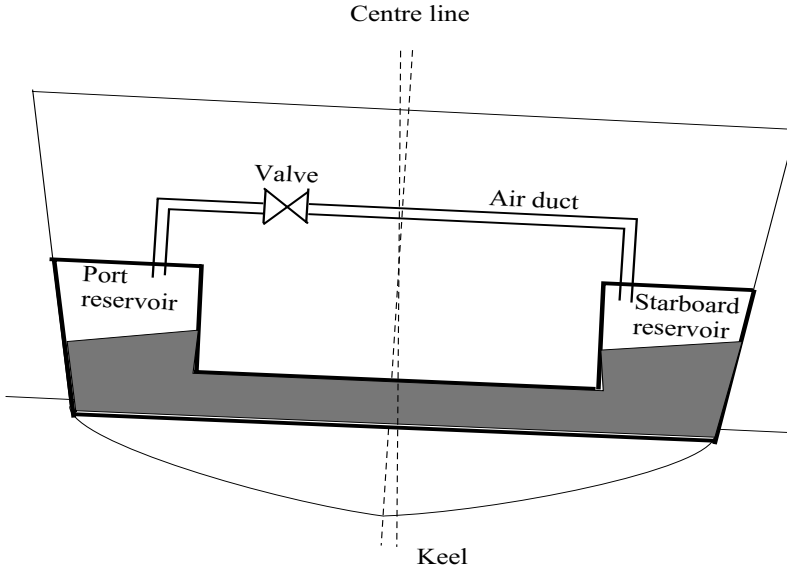

Fig. 6.3. Detail of a typical tank section, and transverse location on the hull.

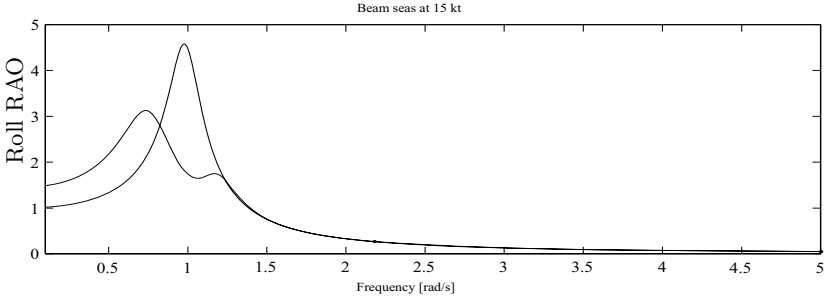

Fig. 6.4. Roll response in regular seas with—(thick) and without—(thin) passive anti-rolling tank. This figure has been reproduced from [172] with permission of ADI-limited, Australia.

the tank to match the actual ship roll period. This reduces the low frequency peak shown in Figure 6.4. As we have seen in Chapter 4, the frequency of roll motion is determined by a combination of wave excitation frequency and ship response according to the sailing conditions. Therefore, there are situations in which the roll period departs from the natural period. To improve the performance at low frequencies (see Figure 6.4), the control system continually senses the roll period and if necessary extends the tank period. This can be

done, for example, by adjusting the air flowing from one side to the other via a pneumatic valve in the air duct—see Figure 6.3—or by forcing the wave motion with a pump located in the lower duct.

The main advantages of anti-roll tanks are the following:

- Medium to high performance. This has been estimated to be in the range of 20–70% of roll reduction (RMS) [198].
- Performance is independent of the operation speed of the vessel. This makes them the preferred option for vessels that spend a large amount of time operating at low or zero speed, and require clean hulls for operations (*e.g.* fishing vessels).
- Low maintenance.
- Relative cost of these stabilisers is in the middle range.
- By incorporating appropriate additional features, the tank can also serve as an anti-heeling devise to compensate for uneven distribution of load.

Some disadvantages of anti-roll tanks are indicated as follows:

- Reduction of deadweight; estimated to be in the range of 1–4% of displacement [120]. This can be overcome by using reservoir water or fuel carried on board.
- Occupy large spaces.
- Affect the stability of the vessel due to free-surface effects. When a tank is not completely full and there is space for the water to move (free surface), there is a loss of transverse metacentric height due to the motion of the centre of gravity. This should be accounted for to avoid ship stability problems.

6.3.4 Active Fin Stabilisers

Fin stabilisers consist of a pair of hydrofoils mounted on rotatable stocks at the turn of the bilge located about amidships—see Figure 6.5. As the ship rolls, this motion is sensed via gyroscopes and fed back to the control system, which commands the actuator to modify the angle of incidence of the fins. Once there is an angle between the flow and the fin, hydrodynamic lift is generated, and a stabilising moment is obtained as a result of the generated lift and the location of the fins on the hull. As in any lifting device, the amount of lift, and hence the generated moment, depend on the vessel speed. At speeds higher than 10-15 knot, active fins are the most effective stabiliser.

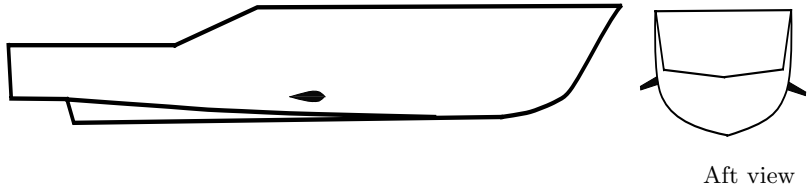

Fig. 6.5. Typical fin stabiliser arrangement.

The main advantages of fin stabilisers are their high performance; normally estimated in the range of 60–90% of roll reduction (RMS) [198], and the relatively easy control system design.

Some disadvantages of fin stabilisers are indicated as follows:

- Ineffective at low speeds.
- Costly maintenance.
- Need for control system with sensors and powerful hydraulic actuators.
- Easily damaged and with high risk of grounding when operating in shallow water or coming alongside other ships.
- Increased hull resistance when in use. Large-span fins are not usually viable (particularly if they are not retractable); thus, a small lift to drag ratio results from the usually low aspect ratio characteristics of the commonly employed fins. A rough estimate of speed loss due to fin activity is 10% [224].
- Increased resistance in calm water if they are not retractable. Retractable fins are more expensive and may require large spaces.
- Possibility of introducing underwater noise affecting sonar systems.
- Most expensive stabiliser.
- Highly nonlinear hydrodynamic effects (dynamic stall) may appear when operating in severe sea states and heavy rolling conditions [80]. This requires advanced control strategies to achieve high performance.

6.3.5 Rudder Roll Stabilisation RRS

Rudder roll stabilisation is a technique based on the fact that the rudder is located aft and also below the centre of gravity of the vessel, and thus the

rudder imparts not only yaw but also roll moment—see Figure 6.6. RRS is a extra feature of the course autopilot.

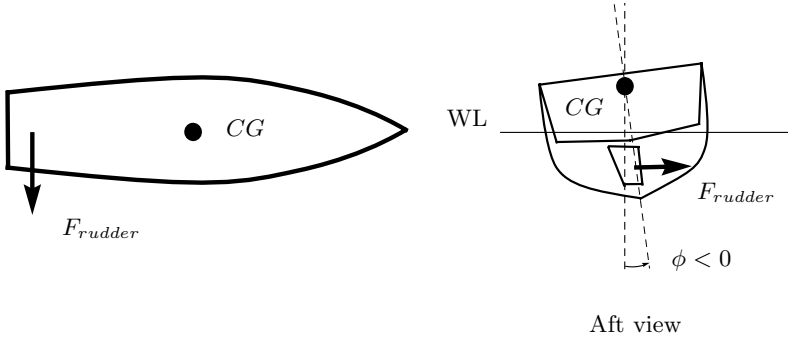

Fig. 6.6. Rudder-induced rolling moment.

Most of the drawbacks of conventional active fin stabilisers and anti-roll tanks are overcome by RRS. Provided the speed of the ship and the rudder rate are sufficiently high, this technique can be applied to different ship types: small and large naval vessels, patrol (coastguard) vessels, ferries and some Ro-Ro vessels [120]. The main advantages of RRS are the following:

- Medium to high performance. This can be in the range of 50-75% of roll reduction (RMS) [198].
- Relatively inexpensive.
- No resistance in calm water conditions.
- No large spaces required.
- Can be combined with other stabilisers to achieve higher performance.

Some disadvantages of RRS are indicated in the following:

- Ineffective at low speeds. Nevertheless, this can be higher than that of fins because the rudders are located in the race of the propellers; and thus, operate in higher speed flows than fins.
- Drag is produced when in use. Nevertheless, this can be less than the drag of fin stabilisers, provided ship turning is prevented [224].

- Rudder machinery up-grade may be needed to achieve high performance—faster rudder motion.

- Need sophisticated control systems to extend the good performance to different sailing conditions.

The latter observation has motivated a large amount of research since the first successful implementations were reported, which will be reviewed in Chapter 10.

6.4 A Note on the Early Days of Ship Roll Stabilisation

The undesirable effects of roll motion became more noticeable in the mid-19th century when significant changes were introduced to the design and development of ships. Sails were replaced by steam engines, wood was replaced by iron and, for warships, the arrangement was changed from broadside batteries to turrets [87]. The combination of these changes, in particular the dropping of sails, led to modifications of the transverse stability with the consequence of large roll motion.

The lead in research on roll stabilisation was first taken by British scientists. Indeed, William Froude (1810–1879) started studying the mechanisms that induced roll motion on ships before 1860 [236]. This was at the request of M. Brunel, a famous civil engineer of that time, who had been assigned the task of designing and constructing the *Great Eastern*[1] [75]. The work of Froude laid the foundations of our modern perception of roll motion: roll is the consequence of fluid pressure acting on the hull, and not of the impact of waves on the side of the ship, as once had been believed [45].

The first attempt to reduce roll motion was to fit bilge keels. It was Froude who stated the contribution of skin friction to roll damping and the importance of bilge keels [83]. According to Sir Wescott's memoir [236] observations made by Froude during the trial voyage of the *Great Eastern* led to the proposal of using bilge keels. For a list of more contemporary references on bilge keeps, see the recent paper of Ikeda [111].

What may also be regarded as a development of the bilge keel idea is the vertical plate keel, or longitudinal fin, which was tested in Denmark in the late 1880s [45]. Although this system reproduced the characteristics of bilge keels, the increase of draught was a clear disadvantage with respect to the latter.

According to the survey paper of Vasta *et al.*[230], Froude also installed water chambers in the upper part of a ship in 1874, but large free-surface

[1] Data of this ship can be found online in the *Ships of World: A Historical Encyclopedia*.

effects resulted in poor performance[2]. In 1878, the *Committee on the Inflexible*, in England, presented a study on damaged stability for the *HMS Inflexible*, in which they concluded that the free flow of the water within the damaged compartments contributed to an increase of righting power in excess of the values predicted by the stability curves. This happened only if the number of partially flooded compartments was low and the level of water appropriate [45, 87]. As a result of these experiments, the *HMS Inflexible* was permanently fitted with water chambers in 1880. Watt, in 1883–85—[232, 233], reported results obtained with water chambers mounted on the *HMS Inflexible*. This, together with the work of Froude, was probably the earliest attempt of using passive anti-rolling tanks.

Other early stabilisers also tried moving weights from side to side in the vessel and gyroscopes. Chalmers [45] provides an enjoyable set of historical notes on the development of these devices, but unfortunately no bibliographical references are made to the work thereby reviewed. As examples of moving-weight SRS, Chalmers reviews two attempts. The first, was the invention of Sir J. Thornycroft, which consisted of an 8 ton quadrant mounted on a vertical shaft which, when turned, moved the quadrant across from one side of the vessel to the other. The motion of the shaft was produced by a hydraulic system, and the valves of this hydraulic system were commanded by a pendulum and an electrical relay, and was proportional to a combination of the effective wave slope and roll angle [44]. *This seems to have been the first active SRS documented.* Full-scale experiments in 1891 gave peak roll reductions of 50% but, despite the good results, the idea was abandoned—perhaps, because of irregularities in the performance obtained due to poor accuracy of the mechanical feedback system—and never became a commercial product [44]. The second example reviewed by Chalmers was the proposal of Crémieu, from France, who suggested the use of a pendulum hanging from the underside of the upper deck, with it being partially submerged in a viscous fluid. Instead of using the original pendulum idea, experiments were performed using a four-wheeled truck which was free to move on curve rails inside a tank filled with lime water. Forced rolling in calm water yielded encouraging results, but a trip trial in waves proved the method to be inefficient and even dangerous.

The use of gyroscopic effects was then proposed as a method to eliminate roll rather than reducing it. Schlick was the first to propose use of the gyroscopic effects of large rotating wheels as a SRS in 1904 [197]. In 1907, White [238], described, on behalf of Schlick, the installation of a system for the ex-German torpedo-boat destroyer *See-Bar*. The Schlick gyroscope presented some problems in adjusting the precession moment according to the magnitude of the the waves, and although it worked well for the vessel used

[2]A similar comment referring to the work of Froude in 1874 is made by Battacharyya [28]. Unfortunately, bibliographic references to the reported work are mentioned neither in [230], nor in [28]. To date, the author has not been able to trace references to such work.

by Schlick, it did not perform as expected in other vessels—see [45] for details. The American company Sperry then developed a system that addressed the problem of the Schlick gyroscope by using an electrical motor commanded by switches and a small gyroscope to control the precession of the main gyroscope. In this, the velocity of precession was proportional to the roll rate of the vessel. Although the performance of these system was remarkable, up to 95% roll reduction, their high cost, the increase in weight and large stress produced on the hull masked their benefits and prevented further developments. For a thorough review of the theory and developments of these type stabilisers, see [45].

The work described above was followed by the development of the U-tank made by Frahm in 1911 [70]. This U-tank was found to be more effective than the free-surface tank previously used by Froude and Watt. The first vessel to be fitted with a Frahm tank was the cargo and passenger steamer *Ypiranga*, which ran between Hamburg, Mexico and Buenos Aires [45]. This type of anti-roll tank is still very much in use to date—see, for example, the work of the leading German company Intering (`http://www.intering.com/`).

Work on active anti-roll tanks started in the 1930s. For example, Minorski [151] used a pump to alter the natural flow in the tanks in 1934. The velocity of the fluid was varied according to the roll acceleration [44]. During the 1960s and 1970s there was significant research activity to better understand the performance of these stabilisers, see for example, [230, 87, 19, 234] and references therein. More complete passages on the history and the development of anti-roll tanks, which also includes contemporary references, can be found in [45, 230, 87, 82]. In particular, the paper of Vasta *et al.*[230], summarises the early development of stabilisers within the US Navy, which did not take place until the 1930s. This reports the use of tanks in different vessels, and provides a mathematical model of a U-tank based on the developments made at Stanford University in the early 1950s.

As commented by Bhattacharyya [28] significant adoption of active-fin stabilisers started after World War II. This was a consequence of the combined work of the Denny and the Brown Brothers companies in England, but the idea of using fin stabilisers was developed before the war. The first proposal for fin stabilisers was made by S. Motora of the Mitsubishi Nagasaki Shipyard in Japan, in 1923 [45]. This device was patented by Motora in the USA in 1925 [153]. By 1930, this had been applied successfully to three vessels: a passenger ship, a steamer, and a mine-sweeper. The fins were commanded by standard steering machinery, which was activated by a device which used a gyro. The maximum angle at which the first installed fins operated was 18 deg, and the time required to reach this angle was half a second. No attempt was made to control the angles gradually; the fins reached the maximum angle almost at once [45].

The first vessel of the Royal Navy equipped with fin stabilisers was the *HMS Bittern* in 1936—see [152]. The extensive work of the Denny and the Brown Bros. companies was reported in the paper of Allan, in 1945 [4]. The

work of Conolly in 1969 [52] provided a method to establish the number of fins required and the value of control gains to achieve a certain degree of roll stabilisation. During the 1970s, Lloyd [137, 140] and Carley and Duberley [43] contributed further towards a solid understanding of the performance and design of fin stabilisers.

The idea of using the rudder as a stabilisation device probably emerged from observations of ship roll behaviour under autopilot operation. Taggart [215] reported an unusual combination of circumstances occurring on the *American Resolute* (container ship) during a winter Atlantic crossing in 1967, which resulted in excessive ship rolling when automatic steering was used. From data observed during that trip and a model constructed from data of a summer crossing in 1968, it was concluded that the high roll motion observed, even in the absence of significant seaway, was the consequence of high yaw frequencies, which made the autopilot produce rudder activity close to the roll natural frequency of the ship. It was then suggested that the autopilot control system should be modified to avoid these effects; however, the fact that rudder motion could produce large roll could be used as anti-rolling device. This hypothesis was to be tested on the 1968 summer crossing, but calm seas hindered the attempt.

Motivated by the observations made by Taggart, van Gunsteren performed full-scale trials using the rudder as a stabiliser in 1972 aboard the motor yacht *M.S. Peggy* in Ijsselmeer (inner waters of The Netherlands). To the best of the author's knowledge, this was the first full-scale trial of a rudder stabiliser. This work was reported by in 1973 at the 3rd Symposium on Development of Interest to Yacht Architecture in Amsterdam, and then extended and presented at the International Ship Building Progress Journal in 1974—[229]. During these trials, a roll reduction of 43% DSA was obtained at a speed of 9 kt in beam seas.

Independently from the above work, Cowley and Lambert [54] presented a study of rudder roll stabilisation using analog computer simulations and model testing of a container ship in 1972. Subsequent sea trials following this work were reported in 1974–75 [53, 55], the latter with encouraging results. This work, obtained on commercial ships, motivated the exploration of rudder stabilisers in the naval environment in the United Kingdom. In 1975, Carley [42] and Lloyd [139] reported their studies, in which they analysed not only the benefits but also the complications associated with the control of rudder stabilisers. This work seems to have been the first rigorous attempt to analyse performance limitations of rudder stabilisers.

Although the idea of using the rudder as a roll stabilising mechanism ignited in the early 1970s, the performance obtained was, in general, poor. This was mainly because of the simple control strategies attempted, due to the limitations imposed by the analog computers. It was only in the 1980s that more advanced control algorithms, and digital computers made more successful experimental results possible: Baitis reported roll angle reductions of 50% in 1980—see [12]. After this, most of the successful implementations

were reported towards the end of the 1980s and beginning of the 1990s—see for example the work of van der Klught, [227], and Blanke *et al.*[34]. These were all within the naval environment.

Table 6.2. Summary of main ship roll stabiliser chronological developments– Adapted from [44].

Year	Device	Ship	Designer	Type
1870	Bilge keels	-	Froude (GBr)	Passive
1880	Tanks	*Inflexible*	Watt and Froude (GBr)	Passive
1891	Weight	*Cecile*	Thornycroft (GBr)	Active
1906	Gyro	*Sea-Bar*	Schlick (Ger)	Passive
1909	Weight	Steamer	Crémieu (Fra)	Passive
1910	U-tank	*Ypiranga*	Frahm (Ger)	Passive
1915	Gyro	*Conte di Savoia*	Sperry Company (USA)	Active
1924	Gyro (double wheel)	Destroyer	Fieux (Fra)	Passive
1924	Fins (variable angle)	*Matsu Maru*	Motora (Jap)	Active
1933	Fins (variable area)	*Aviso Estourdi*	Kefeli (Ita)	Active
1836	Fins (variable angle)	*HMS Bittern*	Denny-Brown (GBr)	Active
1939	U-tank	*Hamilton*	Minorsky (USA)	Active
1972	Rudder	*M.S. Peggy*	van Gunsteren (Ndl)	Active
1974	Rudder	*Manchester Concorde*	Cowley & Lambert (GBr)	Active

In this section has presented a brief review on the main developments of stabilisation concepts, and Table 6.2 summarises these developments. Through these, the technical feasibility of roll stabilisation has been amply demonstrated for over 100 years. Performance, however, can still fall short of expectations. As stated by Chadwick [44], this can be attributed to deficiencies in the control system due to lack of understanding of system dynamics and limited technology. It would then be fair to say that these, together with new developments in control, are the main reasons why after the last addition of rudder stabilisers in the 1970s, most of the work has shifted to developments in control system design rather than to the development of new stabilisation concepts.

7

Ship Motion Performance

Since the development of stabilisers began, several methods and figures have been used to quantify the performance of the stabiliser. This could create confusion when comparing systems from different manufacturers since differen methods yield different figures. In this section, we review the figures most commonly used to assess stabiliser performance. These figures are

- *Percentage Reduction of Roll at Resonance—RRR*
- *Percentage Reduction of Statistics of Roll—RSR*
- *Percentage Reduction of Probability of Roll Peak Occurrence—RRO*
- *Increase in Percentage of Time Operable—IPTO*

7.0.1 Reduction of Roll at Resonance—RRR

The roll motion of the ship can be described, in its most basic form, as a mass-spring-damper system. Indeed, the moment of inertia in roll is the mass component, the spring arises from the buoyancy and gravity forces which tend to restore the equilibrium position, and the damping arises from the interaction between the hull and the water. Since the damping is in general low, the response to wave excitation loads presents a resonant peak as was depicted in Figure 6.4 in Chapter 6.

Then, a common figure of performance consists in evaluating the roll reduction at the roll resonant frequency, ω_ϕ, for a sinusoidal wave excitation, with a wave encountering the ship from the beam:

$$RRR = 100 \left(1 - \frac{\bar{\phi}_s}{\bar{\phi}_u}\right)\Bigg|_{\omega_e=\omega_\phi}, \tag{7.1}$$

where $\bar{\phi}$ denotes the peak (or peak-to-peak) value of roll angle and the subscripts s and u stand for *stabilised* and *unstabilised* respectively.

This figure is a deterministic measure which turns out to overestimate the roll reduction obtained in a seaway, in which the waves have energy distributed

over a range of frequencies rather than at a single frequency. This effect, combined with the characteristics of the stabiliser feedback control system, results in smaller roll reduction than those predicted by (7.1). Although unrealistic, the *RRR* figure is very popular amongst stabiliser manufacturers because it shows a great performance for their systems.

7.0.2 Reduction of Statistics of Roll—RSR

Since the roll motion varies according to the sea state (wave heights, and wave periods) and sailing conditions (ship speed and heading), it is more appropriate to evaluate performance using statistics for a particular scenario. The *percentage reduction of statistics of roll* is defined as

$$RSR = 100\left(1 - \frac{S_s}{S_u}\right), \tag{7.2}$$

where the subscripts s and u stand for *stabilised* and *unstabilised* respectively, and S can be any of the following statistics of roll motion evaluated for a particular sea state and sailing conditions:

- Variance : $\mathbf{var}[\phi]$ or m_ϕ^0.
- Root Mean Square (RMS) value: $\phi_{RMS} = \sqrt{m_\phi^0}$.
- Single Significant Amplitude (SSA): $\phi_{SSA} = 2\sqrt{m_\phi^0}$.
- Double Significant Amplitude (DSA): $\phi_{DSA} = 4\sqrt{m_\phi^0}$ (also denoted by $\phi_{1/3}$).

The significant amplitude is the average of the highest one third of the peak or peak-to-peak values, and this seems to have been inherited from the equivalent concept of significant wave height, which is an estimate of the predictions made by observers looking at the surface of the ocean. We have reviewed these concepts quantitatively in Chapter 2.

In this context, the statistics can be evaluated as either the time average or the ensemble average. This allows one to use the frequency domain description to compute statistics using mathematical models and compare them with the statistics obtained from data of tank tests or full-scale sea trials.

One should be aware that the square-root relationship between the variance and the RMS value results in a higher reduction figure for variance than for RMS, SSA and DSA.

7.0.3 Reduction of Probability of Roll Peak Occurrence–RRO

A different way of thinking about roll reduction is by considering the reduction of occurrence of the event in which the roll exceeds a certain value [46]. As we have seen in Section 4.2, the roll motion of a ship can be described using a

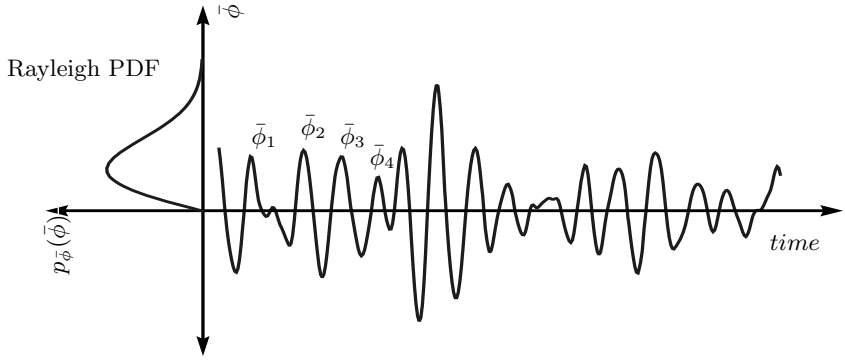

Fig. 7.1. Illustration of statistics of maxima of a narrow banded Gaussian process.

linear system to represent the hull response to the wave excitations, and these excitation be considered realisations of a narrow-banded Gaussian stochastic process—seakeeping assumption. Then, due to linearity, the roll motion itself can be considered a narrow-banded Gaussian stochastic process. For these type of processes, it can be shown that the probability of maxima is well approximated by a Rayleigh pdf —see [186, 182]. If we denote the maxima of a realization of roll angle by $\bar{\phi}_i$, as illustrated in Figure 7.1, then, the probability of exceeding certain value of roll angle $\phi^\star$ is given by

$$\mathbf{Pr}[\bar{\phi} > \phi^\star] = \int_{\phi^\star}^{\infty} \frac{\bar{\phi}}{m_\phi^0} \exp\left(-\frac{\bar{\phi}^2}{2m_\phi^0}\right) d\bar{\phi} = \exp\left(-\frac{(\phi^\star)^2}{2m_\phi^0}\right), \tag{7.3}$$

where the integrand is the so-called Rayleigh pdf. From this, for example, it is easy to see that roll angles exceeding twice the significant roll amplitudes ($2\phi_{SSA} = 4\sqrt{m_\phi^0}$) occur with probability 0.1, *i.e.* these are still quite probable.

By interpreting probability as frequency of occurrence, the values given by Equation (7.3) multiplied by 100 can be taken as the percentage of time in which the roll angle exceeds a given value during of the vessel's mission or time during which data are recorded. Then, the *Reduction of Probability of Roll Peak Occurrence–RRO* can be defined as

$$RRO(\phi^\star) = 100\left(1 - \frac{\mathbf{Pr}[\bar{\phi}_s > \phi^\star]}{\mathbf{Pr}[\bar{\phi}_u > \phi^\star]}\right) = 100[1 - \exp\left(-F\,(\phi^\star)^2\right)], \tag{7.4}$$

$$F = \frac{1}{(m_\phi^0)_s}\left(1 - \frac{(m_\phi^0)_s}{(m_\phi^0)_u}\right), \tag{7.5}$$

where $(m_\phi^0)_s$ corresponds to the variance of roll motion for the stabilised ship and $(m_\phi^0)_u$ to that of the unstabilised ship.

The above should be interpreted as follows: *for a given threshold angle $\phi^\star$, the probability of occurrence of maximum roll angles exceeding $\phi^\star$ is reduced by RRO%.* This figure can be particularly useful to estimate the advantages of incorporation a stabiliser in case of missions or machinery than can only be used if the roll angle does not exceed certain values. To illustrate the use of *RRO*, let us consider the data from sea trials of a motor yacht reported in [229]. From these data, the following statistics were obtained:

- $(m_\phi^0)_u = 46.25$ deg^2 unstabilised,
- $(m_\phi^0)_{sr} = 15.5$ deg^2 stabilised by rudder only,
- $(m_\phi^0)_{sf} = 5.5$ deg^2 stabilised by fins only.

In the upper plot of Figure 7.2, we can see the PDF of maxima fitted to the data obtained during the trial for the cases of no stabiliser active, rudder only and fins only. In the middle plot, we can see the probability of exceeding a maximum angle according to (7.3), which multiplied by 100 can be interpreted as the percentage of time the peak angles will be exceeded during the ship's mission. Finally, in the lower plot, we can see the *RRO* according to (7.4).

For this example, the $RSR = 42\%$ (RMS, SSA and DSA) for the case of rudder stabilisers and $RSR = 66\%$ (RMS, SSA and DSA) for fin stabiliser. From the last two plots it can be said, for example, that maximum roll angles exceeding $5deg$ occur with a probability of 0.58 (or 58% of the time) with no stabiliser, while only 0.19 (or 19% of the time) with rudder stabilisers, and 0.0123% (or 1.23% of the time) with fin stabilisers. Hence, the probability of occurence of roll peaks of $5deg$ is reduced by 67% for the case of rudder stabiliser, and 99% for the case of fin stabilisers.

As we can see the figures can be completely different, and the use of one method or the other ultimately depends on how the desired performance is specified. Although the *RRO* is a very useful index, it could be counter-intuitive if not interpreted properly. Indeed, from the lower plot in Figure 7.2, one could be led to think that as the threshold angles increase, the stabiliser performs better. However, one must also take into account that the events of exceeding high threshold angles will occur with very low probability and hence the calculated reduction becomes unreliable [46].

7.0.4 Increase in Percentage of Time Operable—IPTO

To address the problems mentioned above, a comprehensive assessment of the merit of a stabiliser can be obtained by using the increase in *Percentage of Time Operable* (*PTO*) resulting from the so-called seakeeping analysis. This index is interpreted as the percentage of time the ship remains fully operative according to prescribed requirements and all the expected sea states and sailing conditions.

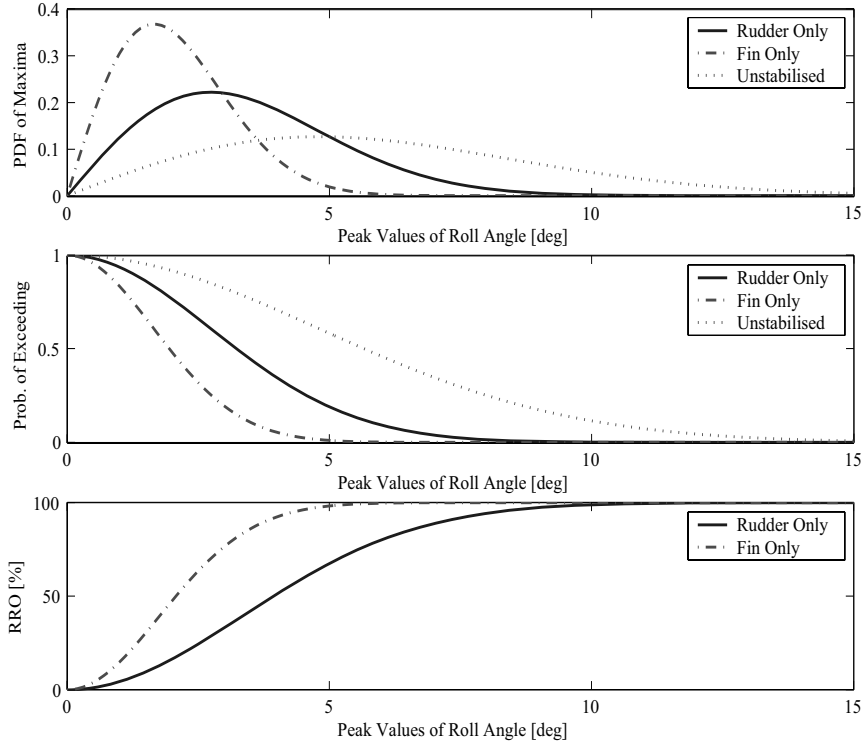

Fig. 7.2. Example of use of *RPO* for a motoryacht in irregular beam seas at 9kts. Example adapted from van Gunsteren [229].

To understand how the *PTO* is obtained, we need to describe briefly how the seakeeping analysis works. This analysis assesses or predicts how a vessel behaves in waves by calculating (or measuring) ship motion in different conditions and comparing the motion or motion-dependent indexes with levels that are deemed satisfactory for the particular missions. This can be separated into three steps:

1. Define the speed profile and the sea environment for each mission performed by the vessel. The speed profile is the set of speeds at which the mission is performed and their associated probabilities (interpreted as the percentage of time normally spent at each speed). The sea environment is defined by the long- and short-term statistics of the ocean waves (see Chapter 2).

2. Determine the statistics of the motion (*e.g.* roll, pitch and yaw angles and accelerations, vertical velocities and accelerations) for each combination of speed, heading and sea environment. These are determined via

numerical methods or from analysis of data recorded in sea trials.

3. Evaluate performance indexes (PI) and compare them with operability limits (OL) that are deemed satisfactory for the particular missions. For example, Table 7.1 shows some common performance indexes and their generic associated limits for a navy vessel in transit operations.

Table 7.1. Example of performance indexes and limits for a navy vessel in transit operations—adapted from [185] and published with permission of the Director of Navy Platform Systems (DNPS), Department of Defence, Australia. (The indices that have no limits associated are not considered of significant importance for this particular mission—however, these limits may significant for other missions.)

Performance Indexes (PI)	**Operability limits** (OL)
Motion sickness Incidence at the bridge	20% after 4 hours.
Motion induced interruptions at bridge	1 per minute.
Bow slamming	20 per hour.
Propeller emergence	90 per hour.
Deck wetness front deck	30 per hour.
Deck wetness quarter deck	30 per hour.
Vertical displacement	NA m SSA
Vertical acceleration	NA m/s^2 SSA
Lateral Force estimator	NA N/Kg SSA
Roll	NA deg SSA
Pitch	NA deg SSA
Yaw	NA deg SSA

The comparison between the values of the performance indexes and the limits established for the mission is often characterised by the PTO. For one mission, this can be obtained as indicated in the following steps:

1. The performance indexes (PI_n) (for example, as indicated in Table 7.1 *i.e.* PI_1—motion sickness index, PI_2—motion induced interruptions, etc.) are calculated using ship motion data for each combination of speed, heading, and sea environment.

2. For each combination of speed, heading, and sea state, a single parameter—Weighted Operability WO—is calculated as

$$WO = \sum_n c_n \, op(PI_n, OL_n),$$

where the coefficients c_n weigh the relative importance of the different indices for the particular mission, and the function $op(\cdot, \cdot)$ takes values in

[0, 1] depending on the value of PI_n with respect to its associated operability limit OL_n. Figure 7.3 shows two typical ways of defining $op(PI_n, OL_n)$.

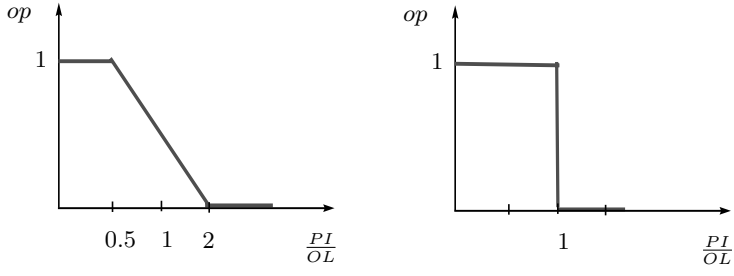

Fig. 7.3. Two examples of operability weighting function.

3. The PTO is then calculated as

$$PTO = 100 \sum_{i,j,k,m} \mathbf{Pr}\{speed_i\}\ \mathbf{Pr}\{heading_j\}\ \mathbf{Pr}\{T_k, \mathrm{H}_{1/3_m}\}\, WO_{i,j,k,m},$$

where $\mathbf{Pr}\{\cdot\}$ denotes probability, and $\mathbf{Pr}\{\cdot,\cdot\}$ joint probability. The parameters T_k and $\mathrm{H}_{1/3_m}$ are the various wave periods and significant wave heights.
The PTO can also be specified as a function of the significant wave height:

$$PTO(\mathrm{H}_{1/3}) = 100 \sum_{i,j,k,m} \mathbf{Pr}\{speed_i\}\ \mathbf{Pr}\{heading_j\}\ \mathbf{Pr}\{T_k|\, \mathrm{H}_{1/3_m}\}\, WO_{i,j,k,m},$$

where $\mathbf{Pr}\{\cdot|\cdot\}$ denotes conditional probability.

The improvement in operability due to the presence of the stabiliser can then be assessed via the increment in the PTO, *i.e.*

$$IPTO = (PTO_s - PTO_u). \tag{7.6}$$

Another way of assessing the improvement in the ability of the vessel to accomplish its mission due to the presence of the stabiliser is to compare the, so-called, *operability diagrams* for the stabilised and unstabilised vessel. Along with the PTO, it is also common to plot the criteria exceeding using a polar grid system. For example, Figure 7.4 shows the criteria plot or operability diagram for a naval vessel during an anti-submarine warfare mission presented by Crossland [56, 57]. On the left-hand side we can see the operability diagram

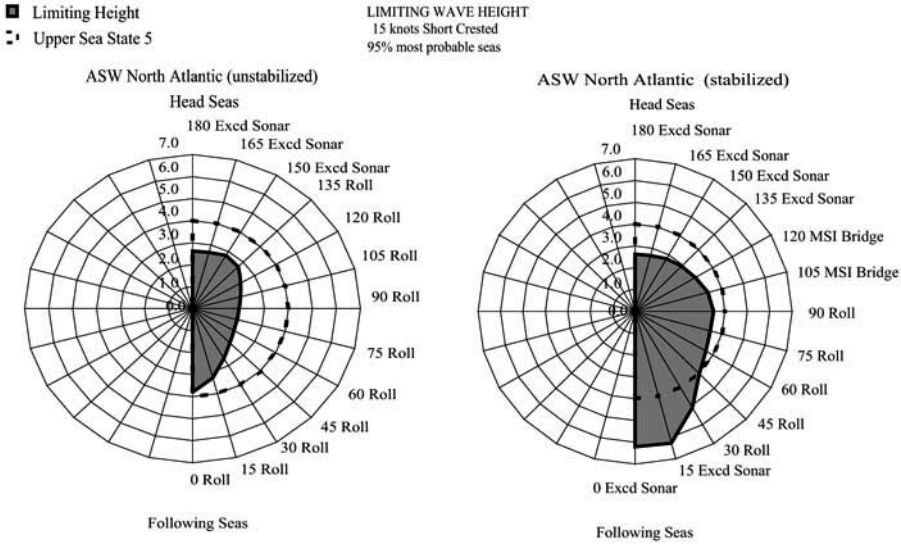

Fig. 7.4. Operability diagrams for a naval vessel performing an anti-submarine warfare mission in the North Atlantic—left plot unstabilised; right plot stabilized. Adapted from [56] and published with permission of the author, © Crown Copyright/MOD.

for the unstabilised case, while the stabilised case is on the right-hand side. The concentring circles represent different wave heights, while the radial lines represent the main direction of wave propagation with respect to the encounter angle. The shaded area lies on the combination of wave height and wave direction at which none of the performance indices exceeds its limit value. We can appreciate in this example that there is a significant increase in the maximum wave heights at which the vessel can perform the mission due to the stabiliser. This figure also shows information about the performance indexes that limit the operability for each heading. We can see that from following seas (0 deg) to bow seas (135 deg) high rolling angle is the main factor limiting the ability of this vessel to accomplish its mission.

The use of $IPTO$ represents an overall performance increment due to the stabiliser; and therefore, it is a key element to evaluate the cost-benefit of including it. For the example discussed above, Crossland reports a $IPTO = 14\%$, while Andrew *et al.*[5] reports a $IPTO = 20\%$. Baitis and Schmidt, [15], give the approximate rule of thumb that 40% of roll angle reduction RMS can result in a navy vessel being able to sustain its operability to one sea state higher.

Due to the large amount of computations required (typically between 1000 and 10,000 combinations of speed, heading and sea environment), the use of

this method to assess the performance has not been extensively reported in the literature, except for a few cases; namely, [5, 15, 16, 56, 135, 136].

7.1 Seakeeping Indices Affected by Roll

For the designer of a stabiliser control system, the seakeeping analysis has implications for the specifications of the control system. Indeed, since the performance of the ship is usually assessed via seakeeping performance indices, it is then natural to try to minimize the impact of roll on these indices.

Until the beginning of the 1980s, the only seakeeping criterion used to judge the rolling of the ship and the performance of its crew was the RMS value of roll angle [152]—typical limit for a warship was 6 deg RMS. A step towards improving this prediction was made by Baitis *et.al.* [16, 13] when they introduced the so-called *Lateral Force Estimator* (LFE) and *Motion Induced Interruption* (MII) performance indices.

The LFE is the lateral acceleration parallel to the deck. This, as an index to evaluate both crew and equipment performance, is more realistic than just the rolling angle. The roll angle is the same for the whole ship; however, the local accelerations vary from location to location, and the LFE accounts for this effect. For example, Sellars and Martin [198] refer to a case of the aircraft carrier *USS Midway* reported by Ricketts and Gale [188], in which only the value of rolling angle less than 5 deg SSA[1] was specified as a seakeeping criterion. Hull modifications made to this ship increased the transverse metacentric height and thus reduced the natural rolling period. The final ship design met the 5 deg SSA specification, but the ship became so stiffthat high lateral accelerations induced by roll motion resulted in unsafe handling of aircraft on the flying deck. Regarding human performance, the results reported by Monk [152] suggest that the ability of a crew performing tasks would be reduced by 50% due to lateral acceleration of 0.07g, while 25-30% by a roll angles of 6 deg RMS. This indicates that lateral accelerations can be more harmful than roll angles.

The MII as a human performance index is even more realistic than the LFE. This is because the MII index takes into account not only the lateral but also the apparent vertical accelerations. Another index commonly used in seakeeping affected by roll is the *Motion Sickness Incidence* (MSI). This is an indicator of the percentage of crew who would become sick as result of the exposure to ship motion. This index depends on vertical accelerations, and then roll becomes important for locations away from the centre line of the vessel. We next describe how to obtain the indices mentioned above and how roll affects them.

[1] Single Significant Amplitude: twice the RMS value.

7.1.1 Lateral Force Estimator—LFE

The *LFE* is the *apparent lateral force per unit mass* (acceleration) parallel to the deck in the athwartship direction at a particular location of interest. This index is often evaluated at locations that require manual work on deck or where equipment is stowed. Regarding operability limits, the seakeeping standard of the Royal Australian Navy [185], for example, requires LFE limits for some task with values varying from 0.05 g (on the flying deck for aircraft carriers) to 0.7 g (at the points for missile re-loading). In Faltinsen [63], values in the range of 0.03 g to 0.1 g are considered for more generic tasks.

To find the *LFE*, let us consider the following frames: h-frame, b-frame (both defined in Section 3.1), and a new body-fixed frame, the x-frame, fixed to the ship at the location of the center of gravity of a person (or a piece of equipment)—see Figure 7.5.

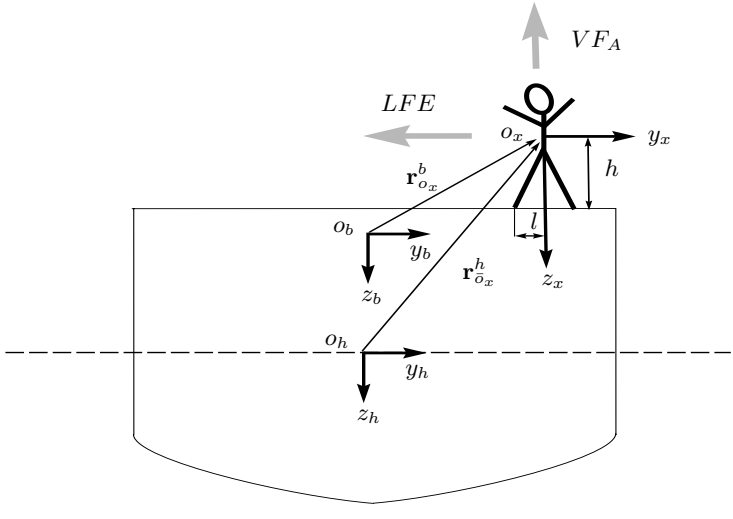

Fig. 7.5. Lateral force estimator and apparent lateral forces due to ship motion.

Let the velocity vector

$$\boldsymbol{\nu}^x \triangleq \begin{bmatrix} \mathbf{v}^x_{o_x} \\ \boldsymbol{\omega}^x_{nx} \end{bmatrix} \equiv [u^x, v^x, w^x, p^x, q^x, r^x]^\mathrm{T} \tag{7.7}$$

describe the linear velocity of the point o_x in the x-frame and relative angular velocity between the x- and the n-frame. Then, the *LFE* is the second component of the negative of the time derivative of $\boldsymbol{\nu}^x$, *i.e.*

$$LFE \triangleq (\dot{\boldsymbol{\nu}}^x - \mathbf{g}^x)_2, \tag{7.8}$$

where the notation $(\cdot)_i$ refers to the i-th component of the vector argument, and if we define $\mathbf{g} \triangleq [0, 0, g]^{\mathrm{T}}$ in the n-frame, then

$$\mathbf{g}^x = \mathbf{R}_n^x(\boldsymbol{\Theta}_{nx})\mathbf{g}. \tag{7.9}$$

The variables (7.7) can be obtained from the velocity vector $\boldsymbol{\nu}$ given in the b-frame:

$$\boldsymbol{\nu}^x = \mathbf{H}(\mathbf{r}_{o_x}^b)\boldsymbol{\nu}, \tag{7.10}$$

with the screw transformation $\mathbf{H}(\boldsymbol{\lambda})$ given in (3.30). Hence, the LFE can be computed from

$$\begin{aligned} LFE = (\mathbf{H}(\mathbf{r}_{o_x}^b)\dot{\boldsymbol{\nu}} - \mathbf{g}^x)_2 &= \dot{v} - z_{o_x}^b\dot{p} + x_{o_x}^b\dot{r} - [\cos(\theta)\sin(\phi)]g, \\ &\approx \dot{v} - z_{o_x}^b\dot{p} + x_{o_x}^b\dot{r} - \phi g \end{aligned} \tag{7.11}$$

Alternatively, the LFE is often computed using the seakeeping coordinates (3.7). Using a transformation similar to (3.38), we can express

$$\dot{\boldsymbol{\xi}} = \mathbf{J}_\delta^{-1}(\boldsymbol{\Theta}_{hx}, \mathbf{r}_{\bar{o}_h}^x)\delta\boldsymbol{\nu}^x. \tag{7.12}$$

If we expand the this kinematic transformation, consider small angles, assume a slender ship (so the components 1,3,5 can be decoupled from 2,4,6) and keep only the linear terms, we obtain

$$\dot{\xi}_1 \approx \delta u^x + z_{\bar{o}_h}^x\delta q^x - y_{\bar{o}_h}^x\delta r^x \tag{7.13}$$

$$\dot{\xi}_2 \approx \delta v^x + x_{\bar{o}_h}^x\delta r^x - z_{\bar{o}_h}^x\delta p + U\delta\psi \tag{7.14}$$

$$\dot{\xi}_3 \approx \delta w^x + y_{\bar{o}_h}^x\delta p^x - x_{\bar{o}_h}^x\delta q^x - U\delta\theta \tag{7.15}$$

$$\dot{\xi}_4 = \delta p^x \tag{7.16}$$

$$\dot{\xi}_5 = \delta q^x \tag{7.17}$$

$$\dot{\xi}_6 = \delta r^x. \tag{7.18}$$

By taking the time derivative, we obtain

$$\ddot{\xi}_1 = \dot{\delta u}^x + z_{\bar{o}_h}^x\dot{\delta q}^x - y_{\bar{o}_h}^x\dot{\delta r}^x \tag{7.19}$$

$$\ddot{\xi}_2 = \dot{\delta v}^x + x_{\bar{o}_h}^x\dot{\delta r} - z_{\bar{o}_h}^x\dot{\delta p}^x + U\delta r \tag{7.20}$$

$$\ddot{\xi}_3 = \dot{\delta w}^x + y_{\bar{o}_h}^x\dot{\delta p}^x - x_{\bar{o}_h}^x\dot{\delta q}^x - U\delta q^x \tag{7.21}$$

$$\ddot{\xi}_4 = \dot{\delta p}^x \tag{7.22}$$

$$\ddot{\xi}_5 = \dot{\delta q}^x \tag{7.23}$$

$$\ddot{\xi}_6 = \dot{\delta r}^x. \tag{7.24}$$

From (7.20), it follows that

$$LFE \approx \ddot{\xi}_2 + z^x_{\bar{o}_h}\ddot{\xi}_4 - x^x_{\bar{o}_h}\ddot{\xi}_6 - U\dot{\xi}_6 - \xi_4 g. \tag{7.25}$$

Expression (7.11) is convenient to calculate the LFE from measurements taken on board, because it is expressed in terms of the body-fixed coordinates. Expression (7.25), on the other hand, can be used to calculate the LFE response amplitude operator LFE-RAO using the MRAO, and then estimate the statics of the LFE by combining the LFE-RAO with the sea spectrum [94]. This is the approach used by standard seakeeping programs.

7.1.2 Motion-induced Interruptions–MII

A *motion-induced interruption* MII is an incident where ship motions cause a person, who is standing up, to loose balance resulting in stumble [13, 16]. This often results in interruptions of the tasks being performed by the person. These events can be predicted using the apparent accelerations normal and parallel to the deck given. The*apparent weight per unit of mass* W_A, is given by

$$W_A \triangleq (-\dot{\boldsymbol{\nu}}^x + \mathbf{g}^x)_3. \tag{7.26}$$

which is positive downwards in the persons-fixed x-frame—see Figure 7.6.

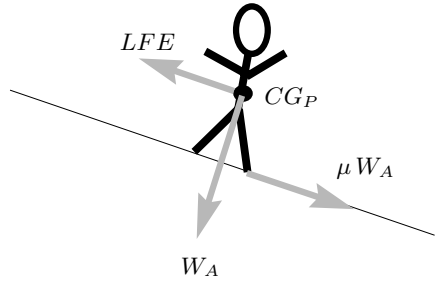

Fig. 7.6. Sliding moment to port due to apparent forces.

Therefore, the W_A can be calculated in terms of the body-fixed coordinates $\boldsymbol{\nu}$ as

$$\begin{aligned} W_A &= -\dot{w} - y^b_{o_x}\dot{p} + x^b_{o_x}\dot{q} + [\cos(\theta)\cos(\phi)]g, \\ &\approx -\dot{w} - y^b_{o_x}\dot{p} + x^b_{o_x}\dot{q} + g, \end{aligned} \tag{7.27}$$

Alternatively, the linear approximation in terms of the seakeeping coordinates $\delta\boldsymbol{\eta}$ is given by

$$W_A \approx -\ddot{\xi}_3 + y^x_{\bar{o}_h}\ddot{\xi}_4 - x^x_{\bar{o}_h}\ddot{\xi}_5 - U\dot{\xi}_5 + g. \tag{7.28}$$

The *conditions for sliding* are

$$\begin{aligned} LFE &> \mu\, W_A \quad \text{(slide to port)} \\ LFE &< -\mu\, W_A \quad \text{(slide to starboard)} \end{aligned} \tag{7.29}$$

where μ is the static friction coefficient. Typical values of μ are 0.2 for wet deck and 0.7 for dry deck.

By replacing the expressions for the LFE, *i.e.* either (7.11) or (7.25), and the expressions for the W_A, *i.e.* either (7.27) and (7.28), into the sliding conditions (7.29), we obtain an expression of the form

$$\begin{aligned} f_{sl.p} &> \mu\, g \quad \text{(slide to port)} \\ f_{sl.s} &< -\mu\, g \quad \text{(slide to starboard).} \end{aligned} \tag{7.30}$$

For example, using (7.11), and (7.27), in the port sliding condition of (7.29), we obtain

$$\dot{v} - z^b_{o_x}\dot{p} + x^b_{o_x}\dot{r} - \phi g > \mu(-\dot{w} - y^b_{o_x}\dot{p} + x^b_{o_x}\dot{q} + g), \tag{7.31}$$

from which it follows that the expression for $f_{sl.p}$ (as a function of b-frame coordinates) is

$$f_{sl.p} = \dot{v} - z^b_{o_x}\dot{p} + x^b_{o_x}\dot{r} - \phi g - \mu(-\dot{w} - y^b_{o_x}\dot{p} + x^b_{o_x}\dot{q}). \tag{7.32}$$

Similarly, the *conditions for tipping* is obtained by calculating the moments about the foot of a person standing facing towards the stern or the bow. Indeed, a person will tip to port if the moment due to the apparent lateral acceleration at person's center of gravity is greater than the moment due to the apparent weight [136]:

$$\begin{aligned} h\, LFE &> \ l\, W_A \quad \text{(tip to port)} \\ h\, LFE &< -l\, W_A \quad \text{(tip to starboard)}, \end{aligned} \tag{7.33}$$

where h represents the height of the persons center of gravity and l half of the persons stance—see Figure 7.5. Typical values are h=0.9 m and l=0.23 m [94]. The quotient l/h is called the *tipping coefficient*—which is often taken as 0.25. Then expressions similar to (7.30) can be obtained for tippling

$$\begin{aligned} f_{tip.p} &> \frac{l}{h} g \quad \text{(tip to port)} \\ f_{tip.s} &< -\frac{l}{h} g \quad \text{(tip to starboard).} \end{aligned} \tag{7.34}$$

If a magnitude x is Gaussian and narrow-banded, the number of times a threshold level L is exceeded during the period T_T is given by [94, 136]

$$M = \frac{T_T}{T_{z.x}} \exp\left[\frac{-L^2}{2\mathbf{var}[x]}\right], \tag{7.35}$$

The variable $T_z.x$ in (7.35) is the average zero-crossing period of the x, which is given by

$$T_{z.x} = 2\sqrt{\frac{\mathbf{var}[x]}{\mathbf{var}[\dot{x}]}}. \tag{7.36}$$

Using these results, the the *total number of motion induced interruptions per minute* can be estimated as

$$\begin{aligned} MII = &\frac{60}{T_{z.sl.p}} \exp\left[\frac{-(\mu g)^2}{2\,\mathbf{var}[f_{sl.p}]}\right] + \frac{60}{T_{z.sl.s}} \exp\left[\frac{-(\mu g)^2}{2\,\mathbf{var}[f_{sl.s}]}\right] \\ &+ \frac{60}{T_{z.tip.p}} \exp\left[\frac{-(lg/h)^2}{2\,\mathbf{var}[f_{tip.p}]}\right] + \frac{60}{T_{z.tip.s}} \exp\left[\frac{-(lg/h)^2}{2\,\mathbf{var}[f_{tip.s}]}\right] \end{aligned} \tag{7.37}$$

It should also be noted, as commented by Lloyd [136], that the theory considered above assumes that the person is a rigid body; hence, the person will not make any attempt to modify his or her position to prevent tipping or sliding. In practice, a person will modify his or her position so as to prevent these events. This, however, is also considered an MII, since attention from the task at hand must be diverted. Then, the MII index is a good estimator of crew performance.

7.1.3 Motion Sickness Incidence—MSI

Seasickness is believed to be caused by a combination of amplitude and frequency of vertical accelerations and the time of exposure [170]. The theories of motion sickness agree that the main contribution to this effect is sensory conflict triggered by either or both of the following effects [51]:

- Visual-inertial conflict. The motion perceived via visual stimulus is different from the motion perceived by the inner ear.

- Canal-otolith conflict. In the absence of visual stimulus, the motion perceived by the angular motion sensors (semicircular canals of the inner ear) is different from the motion perceived by the linear motion sensors (the otolith organs also in the inner ear: utricle and saccule)—see, for example, Chicago Dizziness and Balance (`http://www.dizziness-and-balance.com/cdb/index.htm`)

Here, we will refer to the work of Colwel [51]. In this work, a formula for prediction of initial motion sickness in the naval environment was presented, which extends the work of O'Halon and McCauley [169] and McCauley *et al.* [149] by considering a generic time of exposure:

$$MSI = 100\,\mathrm{erf}(z_a)\,\mathrm{erf}(z_t); \tag{7.38}$$

where

$$\mathrm{erf}(z) = \int_{-\infty}^{z} \exp(-\frac{1}{2}v^2)\,dv, \tag{7.39}$$

$$z_a = 2.128\,\log_{10}(a_{vert}) - 9.277\,\log_{10}(f) - 5.809\,\log_{10}(f)^2 - 1.851;$$

and

$$z_t = 1.134\,z_a + 1.989\,\log_{10}(T) - 2.904$$

In these formulae, a_{vert} is the RMS value of the vertical uni-modal acceleration expressed in units of g, f is the frequency in Hz, and T is the time of exposure in minutes. The MSI as defined above yields an estimate of the percentage of crew who will vomit after a exposure of T minutes to the given motion. The NATO seakeeping standard, STANAG [157], recommends a limit value of 20% after 4 hours for naval vessels.

The above formulae are valid for pure sinusoidal motion. The experiments reported in O'Halon and McCauley [169] and McCauley *et al.* [149] were performed using sinusoidal vertical motion. To apply the above to a more realistic ship environment, Lloyd [135, 136] recommends using the average magnitude of the vertical acceleration and the average frequency of the vertical displacement peaks, all given in the m-frame:

$$a_{vert} = 0.798\sqrt{\mathbf{var}[\ddot{\xi}_3]} \qquad f = \frac{2\pi}{\sqrt{\mathbf{var}[\ddot{\xi}_3]/\mathbf{var}[\dot{\xi}_3]}}. \tag{7.40}$$

There are other ways of specifying the MSI index as a function of the motion of the ship. We have only reviewed the method that we believe gives the most flexibility to calculate MSI. For other methods, see, for example, [67] and references therein.

7.2 Implications for Stabiliser Control System Design

The most important aspect of our discussion in this chapter is that, in regard to roll motion, not only the rolling angle but also the rolling acceleration are important for good ship performance, and also that these specifications may vary with the particular mission performed by the vessel.

The consequences of ignoring the specification of reducing acceleration in stabiliser control system design make the stabiliser unhelpful. As stated by

Warhust in [231] and also by Monk [152]: *"Lateral accelerations caused by roll-reducing devices may be more harmful to human performance than some greater amount of roll."* Surprisingly, this point seems to have been overlooked in the literature of control design for stabilisers. Except for a few cases—see, for example, [217, 216, 218, 212]—the majority of the work reported in the literature uses control strategies that seek only rolling angle reduction whereas accelerations get reduced in an indirect manner. It will then part be of our aim in this book to investigate the advantage of incorporating acceleration reduction as a *direct* control objective.

7.3 Part II Summary and Discussion

This part has introduced the particular problem of ship roll stabilisation. Different methods commonly employed to address this problem were discussed. The effect of roll on ship performance was also discussed and the methods used to assess such performance revisited. This provides essential information to specify objectives for the control system in agreement with the performance assessment methods—*the most important aspect of control system design.*

The third part of the book presents a study of performance limitations for ship roll stabilisers. This, together with the performance material presented in this chapter, and the models introduced in Part I, provides *all* the information necessary to define the control objectives and address the control design problem.

Part III

Performance Limitations in Feedback Control with Application to Ship Roll Stabilisers

8

Linear Performance Limitations

Since the first attempts to use the rudder as a stabiliser, it has been recognised that there are issues that can limit the achievable performance. Indeed, Carley [42] provided the first feasibility analysis on the use of rudders as roll stabilisers. In this study, he looked not only at the potential of the rudder to induce roll—as it had been done by others previously—but also at the consequences for the steering characteristics of the vessel. Carley investigated the issues related to the stability of the closed-loop system and the coupling between roll and heading and frequencies at which roll reduction could be achieved. This study, together with that of Lloyd [139] recognised that there are three main issues that can limit the performance:

- Non-minimum phase (NMP) dynamics.
- A trade-off between roll reduction and heading interference.
- Limited rudder motion.

The NMP dynamics appear in the rudder-to-roll response, and as a consequence there is a fundamental limitation in control system design: disturbance attenuation at some frequencies will result in amplification at other frequencies. This design limitation often affects the performance of typical feedback controllers which do not incorporate an extra feed-forward mechanism or alternatively adaptation to detect changes in the disturbance frequency. This limitation poses a trade-off between reducing the roll at some frequencies and roll amplification at others, which can be interpreted as a robustness issue related to the knowledge of the frequency of the wave induced motion—the disturbance. The second issue that can limit the performance is underactuation, *i.e.* there is one control action (rudder force) to achieve two objectives: roll reduction and low heading interference. The ability to achieve these objectives is related to the shape of the hull, the location of the rudder, and the frequencies at which the wave-induced roll has energy. Finally, the third issue is related to limits on the control action.

This chapter focuses on the first two issues, and analyses the fundamental performance limitations associated with the dynamics of the ship and the

characteristics of the disturbance. This analysis will be done within linear deterministic and linear stochastic frameworks. We will start by studying the problem as simple Single Input Single Output (SISO) feedback control system, and then extend our study to a Single Input Two Output (SITO) system. Through this studies, we will gain valuable insight into the main issues of RRS control design, and show how to obtain a benchmark to compare performance. The latter naturally leads to the question of applicability of rudder stabilisers for different types of ships, which will be also discussed in this chapter. In Chapter 9, we will incorporate the constraints associated with limited control action into the analysis.

8.1 Introduction to Fundamental Limitation in Feedback Control Systems

Performance limitation analysis is an important part of any control system design process. This analysis reveals, *a priori*, whether the control objectives are achievable or not and whether there are fundamental or unavoidable design trades-offs. These limitations and trade-offs, arise due to dynamic and structural characteristics of the feedback system, and are expressed in terms of functions that quantify system performance in various senses. Performance limitation analysis also has implications in determining applicability, *i.e.* in deciding whether a particular control structure or strategy is worth applying to a particular problem. In cases where the desired performance is unachievable, the result of this analysis may suggest how the system can be rearranged (by adding sensors and actuators, or even by re-designing the controlled system) so as to relax the trade-offs.

Performance limitation analysis generally yields results that can be classified into the following two groups:

- Limits on performance that hold for all possible designs in a given control architecture.
- The best achievable performance for a particular scenario.

The first group of results has evolved from the work of Bode during the 1940s [35]. This has become the foundation of the frequency-domain approach to the analysis of fundamental limitations in feedback control system design. The frequency domain approach has, since then, been thoroughly studied and extended by the work of various researchers, including Horowitz [108], Freudenberg and Looze [74], and others. The main idea behind this approach is that the closed-loop transfer functions of a linear feedback system (*e.g.* the sensitivity and complementary sensitivity functions) are analytic in the closed-right hand side of the complex plane if the system is closed-loop stable. This property, combined with interpolation constraints that must be satisfied at certain frequencies due to the structure of the feedback loop, leads to integral

relations, which can be used to quantify fundamental performance limitations and design trade-offs.

The second group of results is often chosen to be a special case that can be used as a benchmark against which other more realistic designs are compared. One of these methods—reviewed in a stochastic form in this chapter—relies on cheap limiting optimal control. The key idea is that the optimal controller will attain its best performance if the control effort is not penalized in the cost function to be minimised. Allowing arbitrarily large control signals is obviously impractical. However, the fact that, if under these conditions, the cost associated with the optimisation cannot be reduced to zero exposes the presence of fundamental limitations to any type of controller. This approach has been extensively studied for linear systems [128, 129, 71, 194, 184, 48] and has been extended to unconstrained nonlinear systems [201]. Also, a characterisation for stable-SISO systems tracking and rejecting step signals with input constraints can be found in [176, 177].

Whichever approach is used to study performance limitations, the knowledge of these limitations allows the designer to judge a potential design before going deep into it. This can save incurring expenses in terms of design time or effort.

To introduce the topic, let us consider a simple motivation example. Consider the linear feedback system shown in Figure 8.1, in which $G(s)$ is the transfer function of the *plant* or system to be controlled, and $C(s)$ is the transfer function of the controller.

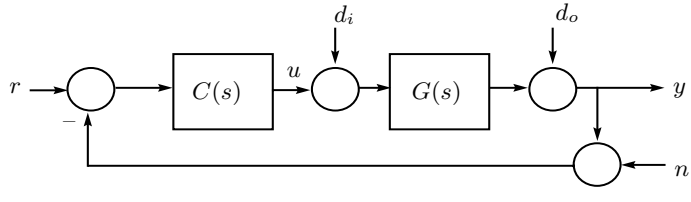

Fig. 8.1. Single-loop output feedback control system.

The scheme shown in Figure 8.1 can be taken as a simplified version of the block diagram of a control system of a stabiliser. Indeed, under linearity assumptions, we can consider, for the purpose of analysis, that the wave-induced motion is an output disturbance. Then, for fin stabilisers, we could have that

- r is the desired roll angle, *i.e.* zero.
- y is the roll angle ϕ and/or its time derivatives.
- d_o is the wave-induced motion in roll and its time derivatives.

- d_i accounts for unmodelled dynamics and other effects diminishing the control action such as local flows due to the wave-particle orbits.
- u is the desired mechanical angle of the fins.

The double objective of rudder stabilisers can be considered as a single-input two-output (SITO) problem as illustrated in Figure 8.2. In this case,

- $r = [0, \psi_d]^{\mathrm{T}}$ is the of vector desired roll and yaw angle .
- $y = [\phi, \psi]^{\mathrm{T}}$ is the vector of roll and yaw angles; this may also include their time derivatives.
- $d_o = [d_\phi, d_\psi]^{\mathrm{T}}$ is the wave-induced motion in roll (and yaw) and its time derivatives.
- d_i is similar to the case of fins, accounting for unmodelled dynamics and other effects diminishing the control action.
- $u = \alpha_d$ is the desired mechanical angle of the rudder.

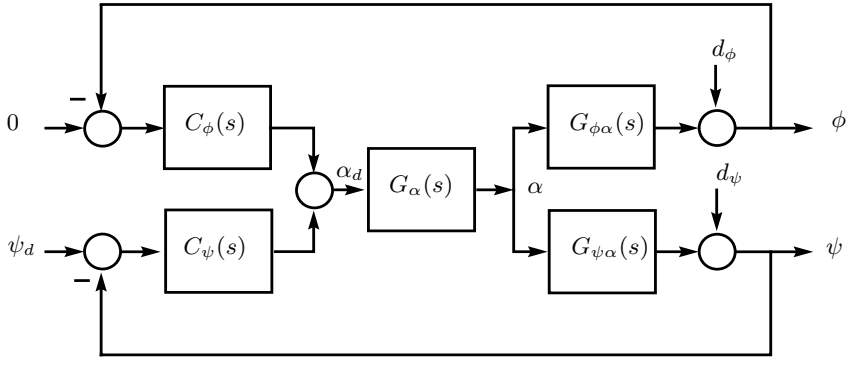

Fig. 8.2. Simplified rudder stabiliser control scheme

The transfer functions $C_\phi(s)$ and $C_\psi(s)$ represent the roll and yaw controllers respectively. The transfer function $G_\alpha(s)$ describes the dynamics of the steering machinery, *i.e.* it maps the desired rudder angle α_d into the actual rudder angle α. The transfer functions $G_{\phi\alpha}(s)$ and $G_{\psi\alpha}(s)$ map the actual rudder angle into the roll and yaw angles respectively.

For ease of exposition, let us introduce the topic of performance limitations using SISO systems. The same ideas, however, extend to the multivarible case, and as we will see, conclusions drawn from a SISO analysis are also relevant to rudder stabilisers.

One way of interpreting the effect of control is by analyzing the properties of the feedback structure depicted in Figure 8.1 in the frequency domain. Indeed, using the Laplace transform, we can establish the effect of the different magnitudes on the output of the system via

$$y(s) = T(s)r(s) + S(s)d_o(s) + S_i(s)d_i(s) + S_n(s)n(s). \tag{8.1}$$

For the feedback system shown in Figure 8.1, it follows that:

$$\begin{aligned} S(s) &= \frac{1}{1+G(s)C(s)} \qquad & T(s) &= \frac{G(s)C(s)}{1+G(s)C(s)} \\ S_i(s) &= \frac{G(s)}{1+G(s)C(s)} \qquad & S_n(s) &= \frac{-G(s)C(s)}{1+G(s)C(s)}. \end{aligned} \tag{8.2}$$

The transfer function $S(s)$ is called the *sensitivity* transfer function, and maps the output disturbance into the output. The function $T(s)$ is called the *complementary sensitivity* transfer function, and maps the reference into the output. The function $S_i(s)$ is called the *input sensitivity* transfer function and maps the input disturbance into the output. Finally, the function $S_n(s)$ is the transfer function that maps the measurement noise into the output.

Having defined the sensitivity functions, let us qualitatively discuss the *most* basic performance limitations that are associated with the feedback system through a simple example.

Example 4 (Perfect control and basic design trade-offs) *Perfect control would be achieved if the output y (variable of interest) followed the reference r as closely as possible for all frequencies in a desired range Ω (i.e., $\omega \in \Omega$) despite the disturbances present on the system; namely, d_o, d_i and n.*

This ambitious goal for the design of the controller $C(s)$ can be quantitatively stated by the following specifications in the frequency domain:

$$|S(j\omega)| \approx 0, \qquad |T(j\omega)| \approx 1, \qquad |S_i(j\omega)| \approx 0, \qquad |S_n(j\omega)| \approx 0 \qquad \forall \omega \in \Omega.$$

*However, from the definitions of the sensitivity functions (*cf. (8.2)*) it follows that it is impossible, in general, to satisfy such specifications. Indeed, from* (8.2)*, we have that*

$$S(s) + T(s) = 1, \qquad S_i(s) = G(s)S(s), \qquad S_n(s) = -T(s). \tag{8.3}$$

Therefore, for example, it is impossible to reduce the effect of the measurement noise on the output, and at the same time obtain a good tracking response (making y follow r) because $|S_n(j\omega)| = |T(j\omega)|$. This is a fundamental limitation *associated with the structure of the control system. This could be alleviated by pre-filtering the measurement. This is just one example of how to modify the system to relax the limitation.*

On the other hand, the algebraic constraint $S(s)+T(s) = 1$, indicates that if we reduce $|T(j\omega)|$ to avoid the influence of the noise n at some frequencies, then $|S(j\omega)|$ increases at these frequencies (at any frequency, either $|S(j\omega)|$

or $|T(j\omega)|$ must be greater or equal to 0.5), and both input and output disturbances may affect the output if they have enough energy at these frequencies. Furthermore, the ability to reject both disturbances depends on the frequency separation between $d_i(j\omega)$ and $d_o(j\omega)$ and the plant $G(j\omega)$. All these are examples of trade-offs *associated with the design.* ○ ○ ○

The above motivation example evidences the delicate interplay between the different parts of the control system, and the basic limitations and trade-offs the designer usually faces. Note that no particular characteristics of the plant (*e.g.* delays, unstable poles and non-minimum phase zeros) were mentioned. These characteristics and limited control action (constraints imposed by the actuators) can indeed aggravate the limitations and design trade-offs. For the case of stabiliser design for displacement ships, the non-minimum phase characteristic of the plant is one of the main effects imposing limitations on the performance of the control system.

8.2 Non-minimum Phase Dynamics in Ship Response

The term NMP is commonly utilized in control and electrical engineering to describe systems otherwise known as systems with inverse response. This characteristic is exhibited the system has unstable zero dynamics [112], which for a linear system results in zeros on the open right-hand side of the complex plane ($\mathbb{C}_+$). To illustrate the effect of a NMP zero on the response, consider a system $G(s)$, in Figure 8.1, with a positive real zero at $s = q$. Then the Laplace transform of the output response of the closed loop system to a positive step reference input is

$$Y(s) = T(s)\frac{1}{s}.$$

It follows from the definition of the Laplace transform that

$$Y(s) = \int_0^\infty e^{-st} y(t)dt = T(s)\frac{1}{s}. \tag{8.4}$$

Since the zero q is in the region of convergence of the above integral, and the zeros of $G(s)$ are also the zeros of the complementary sensitivity[1] $T(s)$, it follows that

$$\int_0^\infty e^{-qt} y(t)dt = T(q)\frac{1}{q} = 0. \tag{8.5}$$

The exponential term e^{-qt} in (8.5) is always positive for $t \in [0, \infty)$; therefore, this integral implies that the output $y(t)$ must change sign to balance the area under the curve of $e^{-qt}y(t)$. This is usually observed as an initial inverse

[1]The zeros cannot be moved by feedback and we assume no unstable pole-zero cancellation between the controller and the plant. Therefore the NMP also appears in the complementary sensitivity function.

response, *i.e.* if the final value of $y(t)$ due to the step input is positive, then the initial response will be negative and *vise versa*. It also follows from the integral (8.5) that the closer the zero is to the imaginary axis, the larger will be the initial inverse response. This is because there will be more positive area to compensate due to the exponential decaying at a slower rate with t when q becomes smaller.

The NMP characteristic of a physical dynamic system often arises from the interaction of opposite fast and slow dynamic effects. This can be seen in the following. Let us follow our simple example with one zero $s = q > 0$, and factorize the closed loop system as follows:

$$T(s) = \frac{N(s)(1 - q^{-1}s)}{D(s)} = \underbrace{\frac{N(s)}{D(s)}}_{T_1(s)} - \underbrace{\frac{N(s)q^{-1}s}{D(s)}}_{T_2(s)}. \tag{8.6}$$

In this expression, we see that the response of the system can be represented by the interaction of two systems; namely T_1 and T_2, whose responses oppose each other. Also, we can see that T_2 has an extra s in the numerator, which will result in a larger bandwidth for T_2 having a faster response than T_1.

In a displacement ship, the roll response to the rudder command generally presents NMP characteristics. Figure 8.3 shows a simulation example of roll response to a step-like change in rudder angle to make a port turn (left turn) in calm water. In this figure we can see the initial inverse response, which is due to the rudder-induced force Y_{rudder}. The roll response to this rudder command is fast because of the smaller moment of inertia and damping in roll with respect to that in yaw. Since the rudder also produces a yaw moment (the main function of the rudder), the ship will eventually start to turn. However, the dynamics associated with the yaw motion are usually slower than those of roll due to the larger moment of inertia and damping. Once there exists a rate of turn, a reaction force Y_{hyd} is induced due to hydrodynamic effects. This force is larger than that produced by the rudder and is the main force producing the turn [133]. Also, as depicted in Figure 8.3, this force produces a roll moment opposite and larger to that induced by the rudder. Figure 8.4 depicts the latter effect of the heel angle attained due to the rate of turn of a frigate performing a port turn similar to that shown in Figure 8.3.

The rest of the oscillations in the roll response depicted in Figure 8.4 appear due to a pair of complex conjugate poles on the rudder-to-roll response. These poles are attributed to the inertia, restoring forces and hydrodynamic damping associated with the roll motion.

From the linear manoeuvring model (low-frequency model) given in Section 4.3.4, we can find the rudder-to-roll and rudder-to-yaw transfer functions, which are of the form

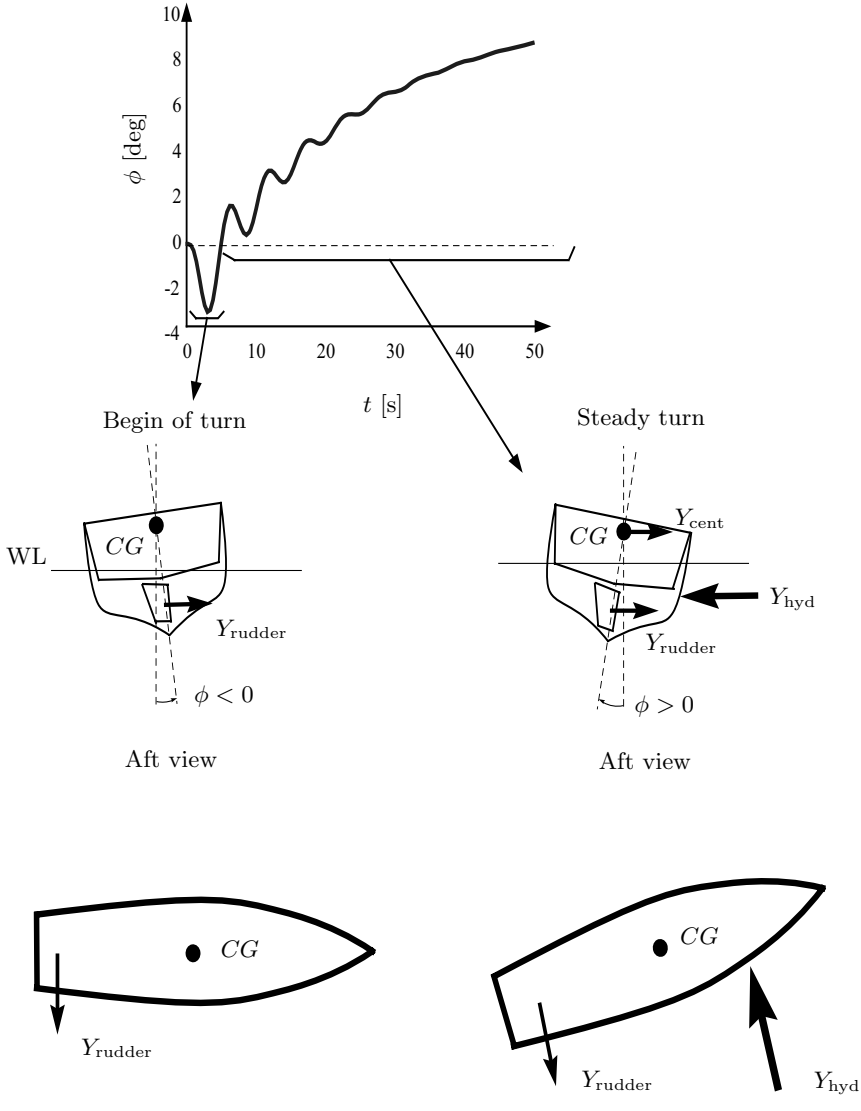

Fig. 8.3. Roll dynamics during a turn to port. From [173].

$$G_{\phi\alpha}(s) = \frac{K_{roll}(q_1 - s)(q_2 + s)}{(p_1 + s)(p_2 + s)(s^2 + 2\xi_\phi\omega_\phi s + \omega_\phi^2)}$$

$$G_{\psi\alpha}(s) = \frac{K_{yaw}(q_3 + s)(s^2 + 2\xi_q\omega_q s + \omega_q^2)}{s(p_1 + s)(p_2 + s)(s^2 + 2\xi_\phi\omega_\phi s + \omega_\phi^2)} \tag{8.7}$$

Fig. 8.4. Steady heel angle during a port turn of a Naval vessel. (©Crown Copyright/MOD. Reproduced with the permission of the Controller of Her Majesty's Stationery Office, United Kingdom.)

Figure 8.5 shows the frequency responses, and Figure 8.6 shows the poles and zeros of these transfer functions for the benchmark example at two speeds. From Figure 8.6, we see that the location of the NMP zero q_1 in (8.7) is affected by the speed. We can also see from this figure that the damping of the complex poles in the roll response increases with the speed.

If we isolate the roll from all other motion components, what is left is a second-order system (only the resonant poles in Figure 8.6). This second-order approximation is of the form

$$G_{\phi\alpha}(s) \approx \frac{\phi(s)}{\tau_{\alpha 4}(s)} = \frac{K_\tau \omega_\phi^2}{s^2 + 2\xi_\phi \omega_\phi s + \omega_\phi^2}, \tag{8.8}$$

where $\tau_{\alpha 4}(s)$ is the roll moment induced by the rudder and the non-dimensional damping coefficient ξ_ϕ is given by

$$\xi_\phi = \frac{K_p}{2\sqrt{\rho g \nabla GMt(I_{44} - K_{\dot{p}})}}, \tag{8.9}$$

and the *roll natural frequency* is

$$\omega_\phi = \sqrt{\frac{\rho g \nabla GMt}{I_{44} - K_{\dot{p}}}}, \tag{8.10}$$

and the low frequency gain is

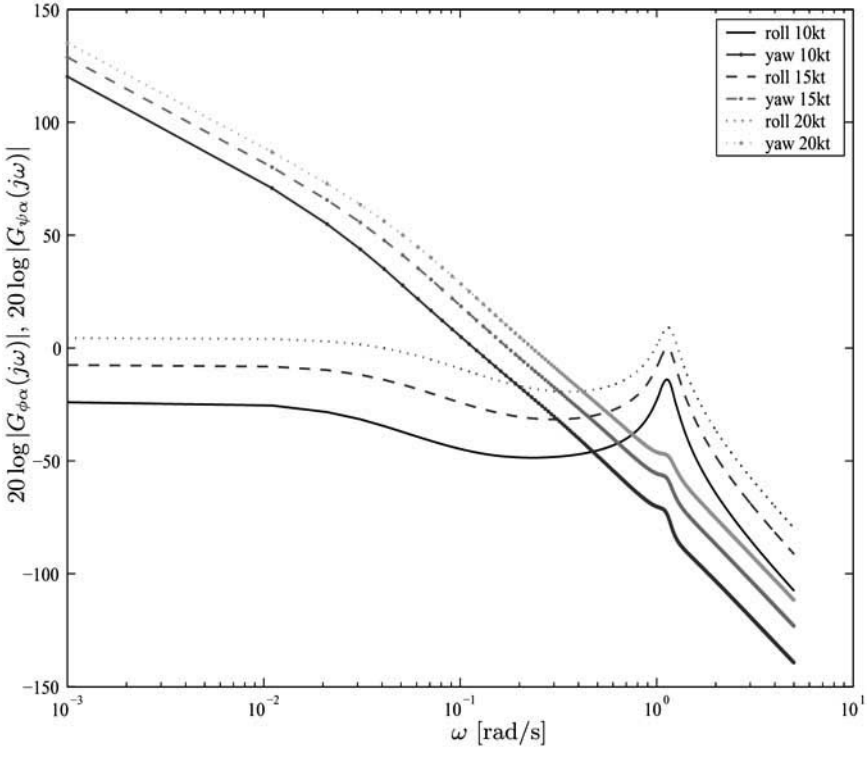

Fig. 8.5. Frequency response for the rudder-to-roll and rudder-to-yaw responses.

$$K_\tau = \frac{1}{\rho g \nabla GMt}. \tag{8.11}$$

The roll damping coefficient ξ_ϕ is typically between 0.1 and 0.2, and thus the response oscillates.

As we shall see in the rest of this chapter, the presence of NMP dynamics, *in general*, limits the performance of the control system. The behaviour of a particular ship depends on the location of the centre of gravityv(LCG,VCG—see Figure B.2), location of the rudder relative to the centre of gravity, and also the hydrodynamic characteristics of the hull, *i.e.* roll-sway-yaw couplings.

We will return to this when we specifically analyze the applicability of rudder stabilisers in a later section. We will next proceed with the introduction of the tools for such analysis.

8.3 Deterministic SISO Performance Limitations of RRS

To understand the basic limitations imposed by the NMP dynamics of the rudder-to-roll response, we will first study the problem as a simple Single In-

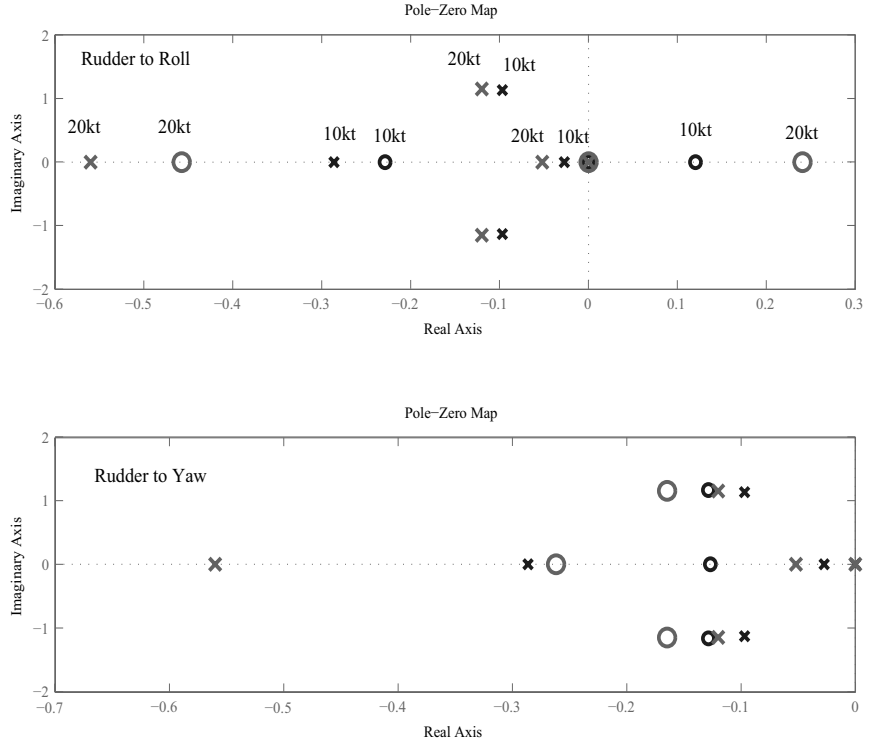

Fig. 8.6. Poles and zeros of the transfer function for the rudder-to-roll and rudder-to-yaw responses for two speeds: 20kt–big; 10kt–small.

put Single Output (SISO) control problem. Despite, the limited applicability, and simplistic view of a SISO rudder roll stabiliser (because the heading is ignored), the results of the analysis will serve to draw important conclusions valid for more realistic control objectives.

8.3.1 Sensitivity Integrals–Frequency Domain Approach

For SISO-NMP systems, we have the following integral constraint [74]:

Theorem 8.1 (Poisson Integral for Sensitivity Function—SISO Case). *Consider the feedback system shown in Figure 8.1, and let $S(s)$ be the sensitivity function defined in* (8.2)*. Assume the open loop system $L(s) = G(s)\,C(s)$ has a set of poles $\{p_i : i = 1, \ldots, np\} \in \mathbb{C}_+$ (open right hand side of the complex plane). Then $L(s)$ can be factorized as*

$$L(s) = \tilde{L}(s) B_S^{-1}(s),$$

where $\tilde{L}(s)$ is a proper rational transfer function with no poles in $\mathbb{C}_+$, and the all-pass factor or Blaschke product given by

$$B_S(s) = \prod_{i=1}^{np} \frac{p_i - s}{p_i + s}.$$

Provided the closed loop system is stable, then for each zero $q = \sigma_q + j\omega_q \in \mathbb{C}_+$ (open right hand side of the complex plane) of $L(s)$, the following integral constraint holds:

$$\int_{-\infty}^{\infty} \ln|S(j\omega)| \frac{\sigma_q}{\sigma_q^2 + (\omega_q - \omega)^2} d\omega = \pi \ln|B_S^{-1}(q)|. \tag{8.12}$$

Proof. See [89, 199] □

This result represents a weighted balance of area under the curve of $\ln|S(j\omega)|$. If, for simplicity, the open-loop system is stable, then the right-hand side of (8.12) is zero. This means that if the output disturbance is to be attenuated, *i.e.* $\ln|S(j\omega)| < 0$ (or equivalently $|S(j\omega)| < 1$) in a range of frequencies $\omega \in \Omega$, then there must be amplification of disturbances at frequencies outside Ω, *i.e.* for $\omega \notin \Omega$, $\ln|S(j\omega)| > 0$ (or $|S(j\omega)| > 1$) so the area balance is zero. Furthermore, due to the weighting factor in the above integral, this balance of area has to be achieved over a limited band of frequencies, which depend on the position of the MNP zeros. For example, Figure 8.7 shows the form of the weighting function for a real NMP zero. In the case of unstable systems, the trade off is worse because the right-hand side is positive.

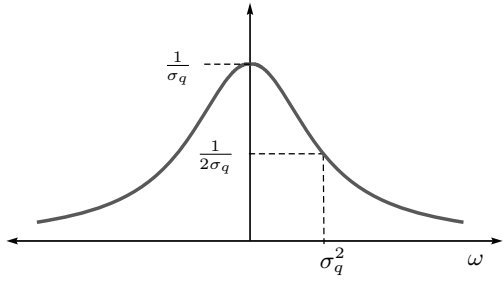

Fig. 8.7. Weighting function of the sensitivity integral constraint.

Let us see what implications the above result have in the design of a control system. Consider a stable system $G(s)$ with a real NMP zero q. Then, for an interval $[\omega_1, \omega_2]$ with $\omega_2 > \omega_1 > 0$, let us consider the integral of the weighting function, i.e.,

$$\begin{aligned}\Theta_q(\omega_1,\omega_2) &= \int_{\omega_1}^{\omega_2} \frac{q}{q^2+\omega^2}\, d\omega \\ &= \arctan\frac{\omega_2}{q} - \arctan\frac{\omega_1}{q}.\end{aligned} \tag{8.13}$$

Now, suppose that the feedback loop is to be designed to achieve

$$|S(j\omega)| \leq \alpha_1 < 1\,, \qquad \forall\omega \in \Omega_1 = [\omega_1,\omega_2]. \tag{8.14}$$

Dividing the range of integration in (8.12), and using the inequality (8.14) and also the fact that $|S(j\omega)| \leq \|S(j\omega)\|_\infty$ for all ω, we obtain that

$$\ln\alpha_1\ \Theta_q(\omega_1,\omega_2) + \ln\|S(j\omega)\|_\infty\,[\pi - \Theta_q(\omega_1,\omega_2)] \geq 0. \tag{8.15}$$

By exponentiating both sides of (8.15), it then follows that

$$\|S(j\omega)\|_\infty \geq \left(\frac{1}{\alpha_1}\right)^{\frac{\Theta_q(\omega_1,\omega_2)}{\pi-\Theta_q(\omega_1,\omega_2)}} \tag{8.16}$$

Thus, the right-hand side of (8.16) is a lower bound on the sensitivity peak. It is immediate from (8.16) that the lower bound on the sensitivity peak is strictly greater than one: this follows from the fact that $\alpha_1 < 1$ and $\Theta_q(\omega_1,\omega_2) < \pi$. Furthermore, the more the sensitivity is pushed down, i.e., the lower is α_1, and the bigger is the interval $[\omega_1,\omega_2]$, then the bigger $\|S(j\omega)\|_\infty$ will be at frequencies outside that interval.

Expression (8.16) can also be used to analyse the worst location of the interval $[\omega_1,\omega_2]$ of sensitivity reduction with respect to the NMP zero. This occurs at the logarithmic average of the frequencies ω_1 and ω_2, *i.e.*

$$q = \sqrt{\omega_1\ \omega_2}. \tag{8.17}$$

Expression (8.16) does not give any indication about the location of the $\|S(j\omega)\|_\infty$, *i.e.* the frequency at which this maximum is located. However, for robustness purposes and high-frequency noise rejection, it follows from (8.2) that it is necessary to constrain the complementary sensitivity $|T(j\omega)|$ at high frequency. This can be characterised by the following constraint:

$$|T(j\omega)| \leq \alpha_2 < 1 \qquad \forall\omega \in \Omega_3 = [-\infty,-\omega_3] \cup [\omega_3,\infty]. \tag{8.18}$$

Note that (8.18) implies $|S(j\omega)| \leq 1+\alpha_2$, $\forall\omega \in \Omega_3$. Therefore, using this additional information, and following a similar procedure as above, we obtain

$$\|S(j\omega)\|_\infty \geq \left(\frac{1}{\alpha_1}\right)^{\frac{\Gamma_q(\omega_2)-\Gamma_q(\omega_1)}{\Gamma_q(\omega_3)+\Gamma_q(\omega_1)-\Gamma_q(\omega_2)}} \times \left(\frac{1}{1+\alpha_2}\right)^{\frac{\pi-\Gamma_q(\omega_3)}{\Gamma_q(\omega_3)+\Gamma_q(\omega_1)-\Gamma_q(\omega_2)}} \tag{8.19}$$

where, $\Gamma_q(\omega_i) = \arctan \frac{\omega_i - \omega_q}{\sigma_q}$, for $i = 1, 2, 3$. From this last expression it is clear that the lower the bandwidth of $T(s)$ and the smaller α_2, the bigger the contribution to the lower bound on $\|S(j\omega)\|_\infty$, and more importantly, that the maximum sensitivity peak will be in the range of frequencies

$$\Omega_M = (0, \omega_1) \cup (\omega_2, \omega_3) \tag{8.20}$$

Figure 8.8 shows a schematic of the situation described above. This type of result is typical of classical linear controllers, PID and $\mathcal{H}_\infty$—see [199].

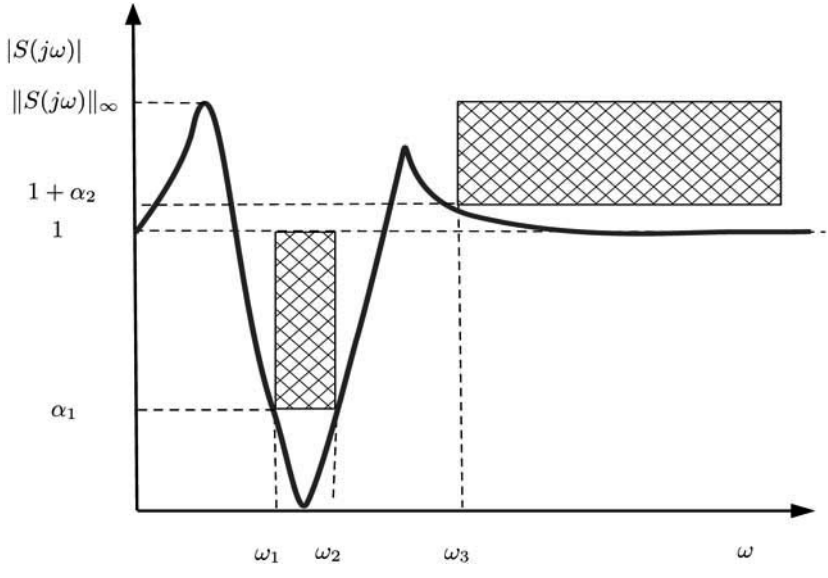

Fig. 8.8. Sensitivity trade-off.

Note that the results discussed above are very general; the only thing we have asked from the controller is to be stabilising, *i.e.* be designed such that the closed loop is stable.

The above description of the disturbance attenuation problem has been formulated from a deterministic point of view. The use of frequency response is particularly attractive to consider sinusoidal disturbances. *The result depicted in Figure 8.8 can be interpreted as a robustness trade-off with respect to the knowledge of the frequency of the disturbance.* Indeed, if the frequency of the disturbance were known exactly, the sensitivity could be reduced to zero (in theory because no input constraints or limits apply in the above analysis). For example, we could use the Internal Model Principle (see [89]) to design a controller that completely rejects that sinusoidal disturbance. However, if the

frequency of the disturbance is not known exactly or the disturbance energy is distributed over a range of frequencies, the reduction of the sensitivity should be considered over that range of frequencies. The price to pay for doing this is an increase of sensitivity outside this range of reduction, and the risk of disturbance amplification if the disturbance is indeed outside the reduction range.

The above discussion evidences limitations of controllers that seek large sensitivity reduction at a range of frequency when there is a NMP zero and uncertainty about the actual frequencies of the disturbance. From the above analysis, it follows that this becomes particularly critical when the reduction is sought close to the frequency of an MNP zero. We will next see how this affects the design of RRS.

8.3.2 Performance Trade-offs of Non-adaptive Feedback Controllers for RRS

If one designs a fixed controller for a rudder roll stabiliser, there is the risk that, for some sailing conditions and sea states, the disturbances have significant energy in the frequency ranges where roll is amplified. This is more likely to happen in quartering sailing conditions for which low encounter frequencies result—see Section 2.3. In Figure 8.8 this would mean having a disturbance with significant energy at frequencies below ω_1.

This limitations have been recognised since the first attempts to use rudder stabilisers were made—see [42, 139]. The analysis of performance limitations due to the NMP zero of rudder-based stabilisers using the Poisson integral formula, *cf.* (8.12), was first presented by Hearns and Blanke [100, 101].

In Chapter 4, we have shown examples of the Power Spectral Density (PSD) of wave-induced roll motion for the naval vessel benchmark used in this book—see Figures 4.9 and 4.10. A conservative design could be performed using a PID controller or $\mathcal{H}_\infty$ techniques by assuming that the PSD of roll has energy in the range of frequencies between $\omega_1 = 0.2$ rad/s and $\omega_2 = 2.5$ rad/s. For the ship sailing at 15 kt, the NMP zero of the roll response due to the rudder angle (8.7) is at $q_1 = 0.187$. Then using Equation (8.19), we can obtain a lower bound for $\|S(j\omega)\|_\infty$ that we can expect for some ω in Ω_M *cf.* (8.20) if we desire to reduce the sensitivity in the range $[\omega_1, \omega_2]$. Figure 8.9 shows the results. In this figure, we have fixed all the parameters save for the lower limit ω_1 and we have tried disturbance attenuations of 50% ($\alpha_1 = 0.5$) and 90% ($\alpha_1 = 0.1$). As expected, the closer ω_1 gets to the NMP zero and the more attenuation is sought in $[\omega_1, \omega_2]$, the bigger the $\|S(j\omega)\|_\infty$.

As shown in Chapter 4, the PSD of the wave-induced roll motion can shift in frequency, and due to the location of the sensitivity peaks, the low-frequency disturbances affect the performance the most. Low frequency wave-induced roll motion arises for two reasons:

- Changes in the sea state,

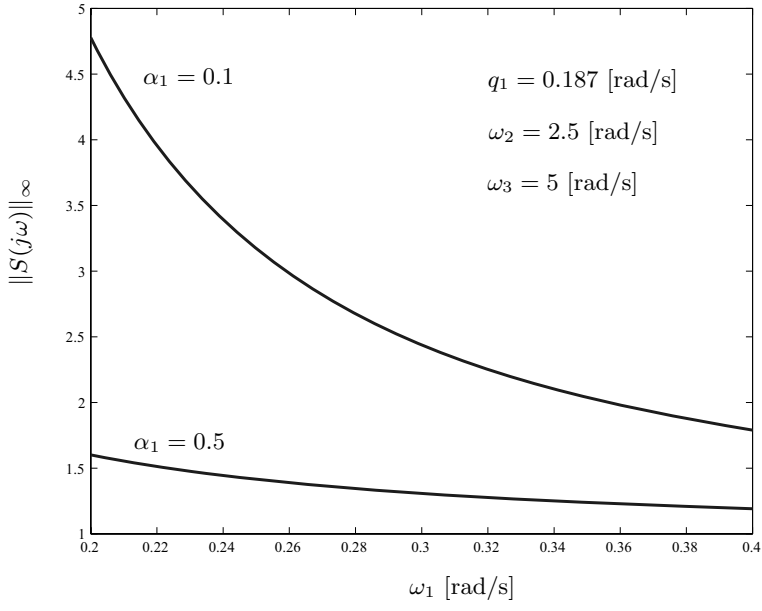

Fig. 8.9. Maximum sensitivity outside $[\omega_1, \omega_2]$ according to Expression (8.19).

- Changes in sailing conditions.

It is, then, very likely that, if the controller is designed to reject the disturbance at some fixed range of frequencies (usually about the roll natural frequency), then there will be cases (combinations of wave frequency, ship speed and heading) for which the power of the disturbances will be in the region of disturbance amplification. If this happens, Figure 8.9 shows how large that amplification can be for the chosen example according to (8.19).

It follows from the above discussion that controllers not adapted according to changes in the disturbance conditions for different sea states and sailing conditions can perform badly. Blanke *et al.* [32] discuss this problem for a particular ship, and they propose a solution in which the ship operator selects between different fixed rudder stabiliser controllers tuned to attenuate the disturbances at different ranges of wave periods, with a limit at low frequency, *i.e.* if the disturbances are at frequencies lower than this limit, then the roll controller is switched off and the autopilot corrects only heading deviations. In a subsequent chapter, we will present an alternative approach to avoid this issue based on an adaptive prediction of the disturbance (feed forward), and online optimisation.

As mentioned at the beginning of the section, the above analysis shows fundamental limitations and trade-offs related to what we can do with the sensitivity function when there is a NMP zero and sinusoidal disturbances. Notwithstanding the insight provided by these results, sinusoidal disturbances

are not the type of disturbance usually encountered for the problems being analysed in this book, and, therefore, in the next section we consider the problem from a stochastic point of view.

8.4 Stochastic SISO Performance Limitations of RRS

In the previous section, we discussed the implications of NMP dynamics from a deterministic point of view. In this section we take the stochastic approach.

8.4.1 Limiting Optimal Control Performance Limitations

An *optimal control problem* (OCP) is that of obtaining a control law $\mathbf{u}(\mathbf{x})$ belonging to a class of admissible controls $\mathcal{U}$ that minimizes a cost[2] associated with a system $\dot{\mathbf{x}} = \mathbf{f}(\mathbf{x}, \mathbf{u})$. The cost is usually a function of $\mathbf{x}$, $\mathbf{u}$, and $\boldsymbol{\lambda}$ (a vector of weighting parameters), *i.e.* $V(\mathbf{x}, \mathbf{u}, \boldsymbol{\lambda})$. The optimal control problem can then be posed as

$$\begin{aligned} \text{OCP}: \qquad & \min_{\mathbf{u}} V(\mathbf{x}, \mathbf{u}, \boldsymbol{\lambda}) \\ & \text{subject} \quad \text{to} \quad \mathbf{u} \in \mathcal{U} \quad \text{and} \quad \dot{\mathbf{x}} = \mathbf{f}(\mathbf{x}, \mathbf{u}). \end{aligned}$$

Then, we say that $\mathbf{u}^{\text{OPT}}$ is the optimal control if

$$V(\mathbf{x}, \mathbf{u}, \boldsymbol{\lambda}) \geq V(\mathbf{x}, \mathbf{u}^{\text{OPT}}, \boldsymbol{\lambda}) \quad \forall \quad \mathbf{u} \in \mathcal{U}\,.$$

We also denote the optimal control as

$$\mathbf{u}^{\text{OPT}} = \arg \min_{\mathbf{u} \in \mathcal{U}} V(\mathbf{x}, \mathbf{u}, \boldsymbol{\lambda}),$$

and the optimal cost

$$V^{\text{OPT}}(\mathbf{x}, \boldsymbol{\lambda}) = \min_{\mathbf{u} \in \mathcal{U}} V(\mathbf{x}, \mathbf{u}, \boldsymbol{\lambda}).$$

We say that an optimal control is a limiting optimal control if, in the limit as some of the components of $\boldsymbol{\lambda}$ tend to zero, the cost to be minimised $V(\mathbf{x}, \mathbf{u}, \boldsymbol{\lambda})$ becomes a function of either the state or the control action but not of both.

The use of optimal control to analyse performance limitations falls in the second type of results that this analysis yields. The results in the previous section showed that there are constraints and trade-offs associated with the dynamics of the plant that hold for every controller under the assumption that the closed loop is stable, and the architecture is that shown in Figure 8.1. In this section, we will analyse what is the *best* achievable performance. We do this using *cheap limiting optimal control*, or simply *cheap control*.

[2]The *cost* is a mathematical expression that characterises deviations from the desired performance or a desired outcome; hence, should be minimised.

Cheap Control is a case of limiting optimal control in which the weight of the control effort in the cost is (or tends to) zero. Since the control is cheap, there is no cost associated with using large control action—a high gain control. As previously mentioned, this setting is obviously unrealistic, but the fact that under these conditions the cost cannot be reduced to zero evidences fundamental limitations. Moreover, the cost obtained can be used as a benchmark to compare the value of the costs resulting from the application of other control strategies. Therefore, the result are a valuable tool for analysis. In this section, we are interested in the following control problem.

Problem 1 (Minimum Variance Cheap Control Problem SISO case) *For the SISO plant $G(s)$ and the control scheme shown in Figure 8.1, we seek the proper stabilising controller $C(s)$ that minimises*

$$V = \lim_{\epsilon \to 0} \mathbf{var}[y] + \epsilon \mathbf{var}[u]. \tag{8.21}$$

We assume that the only disturbance acting on the system is the output disturbance d_0, which is a Wide Sense Stationary (WSS) stochastic process. We further assume that d_0 has a power spectral density $\mathbf{S}_{dd}(\omega)$ that admits a rational approximation so it can be represented as filtered white noise n with constant PSD $\mathbf{S}_{nn}\, \forall \omega \in (-\infty, \infty)$, i.e.,

$$\mathbf{S}_{dd}(\omega) \approx |H(j\omega)|^2 \mathbf{S}_{nn}, \tag{8.22}$$

where the filter $H(s)$ is a rational stable transfer function. ∘ ∘ ∘

The problem defined above is one particular version of the so-called cheap optimal control problem. Note that as the weight ϵ in the control effort—hereby represented as the variance of the control signal—tends to zero, there is no penalty on how much control is used.

For stable plants with one NMP zero, we have the following result that quantifies the best achievable performance in terms of the cost (8.21).

Theorem 8.2. *Let $G(s)$ be a stable SISO plant with one NMP zero, say $q \in \mathbb{R}^+$. Then, the minimum value of the Cost* (8.21) *is*

$$\min V = 2q|H(q)|^2 \mathbf{S}_{nn} \tag{8.23}$$

or equivalently

$$\boxed{\mathbf{var}[y] \geq 2q|H(q)|^2 \mathbf{S}_{nn}} \tag{8.24}$$

∘ ∘ ∘

Proof. Since $G(s)$ is stable, we can use the following form of the Youla parameterization of all stabilising controllers [89]

$$C(s) = \frac{Q(s)}{1 - G(s)Q(s)}, \tag{8.25}$$

where $Q(s)$ is any stable, real, and rational transfer function. From this parameterisation, it follows that

$$S(s) = 1 - G(s)Q(s). \tag{8.26}$$

Using the Fourier transform pair between autocorrelation and the power spectral density, the variance of the output can be expressed as

$$\begin{aligned}\mathbf{var}[y] = \mathbf{R}_{yy}(0) &= \frac{1}{2\pi}\int_{-\infty}^{\infty}\mathbf{S}_{yy}(\omega)d\omega \\ &= \frac{1}{2\pi}\int_{-\infty}^{\infty}|H(j\omega)|^2|1-Q(\omega)G(j\omega)|^2\mathbf{S}_{nn}d\omega \\ &= \frac{\mathbf{S}_{nn}}{2\pi}\int_{-\infty}^{\infty}|H(j\omega)-Q(\omega)H(j\omega)G(j\omega)|^2d\omega \\ &= \mathbf{S}_{nn}\|H(j\omega)-Q(\omega)V(j\omega)\|_2^2,\end{aligned} \tag{8.27}$$

where in the last step we have made use of the $\mathcal{H}_2$ norm with

$$V(j\omega) = H(j\omega)G(j\omega). \tag{8.28}$$

Let us factorise $V(j\omega)$ as follows:

$$V(j\omega) = (H(j\omega)G_m(j\omega))\left(\frac{s-q}{s+q}\right) = V_m(j\omega)V_a(j\omega), \tag{8.29}$$

where $G_m(s)$ and consequently $V_m(s)$ have no poles or zeros in the closed right-hand side of the complex plane ($\overline{\mathbb{C}}_+$), and $V_a(s)$ is an all-pass term. Using this factorisation, expression (8.27) can be manipulated as follows:

$$\begin{aligned}\mathbf{var}[y] &= \mathbf{S}_{nn}\|V_a(j\omega)[V_a(j\omega)^{-1}H(j\omega)-Q(j\omega)V_m(j\omega)]\|_2^2 \\ &= \mathbf{S}_{nn}\|V_a(j\omega)^{-1}H(j\omega)-Q(j\omega)V_m(j\omega)\|_2^2 \\ &= \mathbf{S}_{nn}\|[V_a(j\omega)^{-1}H(j\omega)]_u+[V_a(j\omega)^{-1}H(j\omega)]_s-Q(j\omega)V_m(j\omega)\|_2^2,\end{aligned} \tag{8.30}$$

where we have used the fact that $|V_a(j\omega)| = 1$, and separated $V_a(j\omega)^{-1}W(j\omega)$ into its unstable and stable parts indicated by the subscripts u and s respectively.

Since $[V_a(j\omega)^{-1}H(j\omega)]_u \in \mathcal{H}_2^{\perp}$ and $[V_a(j\omega)^{-1}H(j\omega)]_s - Q(j\omega)V_m(j\omega) \in \mathcal{H}_2$, they are orthogonal. Then, we can express (8.30) as

$$\mathbf{var}[y] = \mathbf{S}_{nn}\|[V_a(j\omega)^{-1}H(j\omega)]_u\|_2^2+\mathbf{S}_{ww}\|[V_a(j\omega)^{-1}H(j\omega)]_s-Q(j\omega)V_m(j\omega)\|_2^2, \tag{8.31}$$

from which it follows that the $Q(s)$ that minimises the output variance is

$$Q(s)^{\text{OPT}} = V_m(s)^{-1}[V_a(j\omega)^{-1}H(j\omega)]_s, \tag{8.32}$$

and the minimum value of the output variance is

$$\min \mathbf{var}[y] = \mathbf{S}_{nn} \| [V_a(j\omega)^{-1} H(j\omega)]_u \|_2^2. \tag{8.33}$$

The final result follows from (8.33) noting that

$$\left[V_a(s)^{-1} H(s)\right]_u = \left[\left(\frac{s+\sigma_q}{s-\sigma_q}\right) H(s)\right]_u = \frac{\mathrm{Res}_q \left[\frac{s+\sigma_q}{s-\sigma_q} H(s)\right]}{s-\sigma_q} = \frac{2\sigma_q H(\sigma_q)}{s-\sigma_q}.$$

□

Note that $Q(s)^{\mathrm{OPT}}$ in (8.32) would be improper because $H(s)G(s)$ is usually strictly proper, and thus $V_m^{-1}(s)$ is improper. This is not a problem since we can always make a proper approximation by adding stable fast poles. This, however, implies that the second term in the right-hand side of (8.30) can be made arbitrarily small as the fast poles go to infinity, but it will not vanish. Therefore, in this case the "min" should be replaced by " inf" in Expression (8.23), and the inequality (8.24) holds strictly. Since we will use the result of this theorem as a performance benchmark rather than a tool for synthesizing the controller, this issue shall not be of concern.

The result given in Theorem 8.2 is a novel characterisation, in stochastic terms, of the trade-offs given in the previous sections using integrals on the sensitivity function. Indeed, in the deterministic framework, we have seen that the Poisson integral formula evidences a trade-off between sensitivity reduction at some frequencies and increase at others. We have also seen that this trade-off worsens when the sensitivity reduction is to be achieved at frequencies close to the NMP zero. The same effect is now quantified in the result of Theorem 8.2, in which the optimal controller tries to eliminate the effect of the disturbance over the output. However, the ability to do this is limited when the bulk of energy of the disturbance is concentrated close to the NMP zero (*i.e.* when the PSD or $|H(s)|$ has large values at $s = q$).

Finally, it is well known that a NMP zero close to the imaginary axis limits the performance of a regulator with step output disturbances [184] [48]. The result can be inferred from (8.24), since the disturbance has power at low frequency. However, it follows from (8.24) that a NMP zero at low frequency may not represent a difficulty in general.

8.4.2 Stochastic SISO Results and RRS

If (8.24) is used in the context of RRS, we could say that

$$\mathbf{E}[\phi^2] \geq 2q_1 \mathbf{S}_{\phi\phi}(-jq_1), \tag{8.34}$$

if the power spectrum of the roll wave-induced motion can be obtained by filtering white noise:

$$\mathbf{S}_{\phi\phi}(\omega) \approx |H(j\omega)|^2 \mathbf{S}_{\mathrm{nn}}, \tag{8.35}$$

where q_1 is the NMP zero of the rudder-to-roll response (8.7), and $\mathbf{S}_{\text{nn}}$ is the intensity of the noise that is filtered to obtain the distubance.

From (8.34), it follows that the closer the NMP zero is to the imaginary axis, the better are the chances for a rudder stabiliser to perform well. A NMP zero close to the imaginary axis will produce a large initial inverse response. This has already been discussed in Section 8.2, and the statement follows from Expression (8.5). The fact that a large initial inverse response is an indication of the potential for good performance of a rudder stabiliser has been discussed by Roberts [190, 189]. Therefore, the location of the NMP zero with respect to the imaginary axis gives a *definite* and *quantitative* interpretation for the statement appearing in the literature which says that for a rudder stabiliser to perform well there must be a frequency separation between the roll and yaw responses due to the rudder action. Indeed, if the zero is close to the imaginary axis, this means that there will be a delay in the development of the hydrodynamic roll moment acting on the hull that opposes that produced by the rudder.

However, (8.34) shows another important aspect: a NMP zero close to the imaginary axis does not *per se* guarantee good performance; there must also be a frequency separation between the NMP zero and the bulk of power of the wave induced roll motion in order to achieve good performance. This answers the question as to why RRS can have significantly different performance under different sailing conditions, with poor performance being particularly noticeable low encounter frequencies.

Also, it is common practice among stabiliser manufacturers to show the performance of their products for a beam sea condition with either regular seas or irregular seas with the wave energy concentrated at the resonant frequency. Both these approaches could be deceiving. Indeed, it is evident from Figure 8.8 that the performance at a single frequency, apart from being unrealistic, can be completely different from the response to a spectrum. From the Result (8.34), it follows that the beam sea performance for irregular seas could be deceiving as an indicator of performance in other sailing conditions. Before using the results of this section in a numerical example, we will consider the more realistic SITO case.

8.5 Optimal Roll Reduction *vs.* Yaw Interference Trade-off

8.5.1 SITO Control Problems in the Frequency Domain

The result of the previous section does not apply to normal operational conditions because the only control objective was to reduce roll regardless of how the heading of ship was affected. A more realistic study should also include the objective of small heading deviations. This leads to the study of Single Input Two Output (SITO) problems, in which there is only one actuator providing

the control action to achieve two control objectives. Therefore, in this section, it is our aim to find what *additional* implications the SITO nature of the plant brings to the control problem; and to obtain a quantitative characterisation of the performance in terms of the variances of both roll and yaw angles—we thus aim at obtaining an expression similar to (8.24).

A basic control structure of a RRS is shown in Figure 8.2. In conventional autopilot design, the measured yaw angle is usually filtered to avoid the control action trying to compensate for the first-order motions (oscillatory motions) induced by the waves—see Section 12.6. This way, the autopilot will react to low frequency disturbances produced by current and wind. Therefore, in our setting, we will consider only the roll disturbance d_ϕ and study the trade-off between roll reduction and yaw interference. Specifically, we will address the following problem:

Problem 2 (Minimum Variance Cheap Control Problem—SITO Case) *We consider the control scheme shown in Figure 8.2, in which*

- $G_{\phi\alpha}(s)$ *is a SISO stable transfer function with one NMP zero.*
- $G_{\psi\alpha}(s)$ *is a marginally stable SISO transfer function.*
- *The PSD* $\mathbf{S}_{d\phi d\phi}(\omega)$ *of the WSS stochastic disturbance* d_ϕ *admits a rational approximation, so it can be represented by filtered white noise,* i.e. $\mathbf{S}_{d\phi d\phi}(\omega) \approx |H(j\omega)|^2\mathbf{S}_{nn}$, *where* $\mathbf{S}_{nn}$ *is the constant PSD of the white noise* n.

Then we seek the controllers $C_\phi(s)$ *and* $C_\psi(s)$ *that minimise the following cost:*

$$V = \lambda \mathbf{var}[\phi] + (1-\lambda)\mathbf{var}[\delta\psi], \qquad \text{with} \quad \lambda \in [0,\, 1], \tag{8.36}$$

where $\delta\psi = \psi - \psi_d$ *is the deviation of the slowly varying yaw motion from the desired slowly varying yaw.*

By defining the cost in this way, the parameter λ *weighs the importance of minimizing the variance of one output over that of the other. Note that when* $\lambda = 1$, *the control objective puts a weight only on the roll, whereas for* $\lambda = 0$ *the control objective puts a weight only on the yaw deviations.* ∘ ∘ ∘

A question that we may first ask ourselves, is whether a multi-variable control design approach could bring any benefit to the frequency-domain constraint discussed in the previous sections for the SISO case, Section 8.12. Thus, before attempting to solve the problem defined above, it is worthwhile exploring whether the multi-variable approach can relax the deterministic integral constraint associated with the NMP zero.

It follows from Figure 8.2 that for multi-variable case, we have four sensitivity transfer functions, *i.e.*

$$\begin{bmatrix}\phi(s)\\ \psi(s)\end{bmatrix} = \begin{bmatrix}S_{\phi\phi}(s) & S_{\phi\psi}(s)\\ S_{\psi\phi}(s) & S_{\psi\psi}(s)\end{bmatrix}\begin{bmatrix}d_\phi(s)\\ d_\psi(s)\end{bmatrix}. \tag{8.37}$$

In the multi-variable case, the constraint imposed by the Poisson integral formula can be shared, in some cases, among the elements of the columns of the sensitivity matrix in (8.37). Indeed, in this case, not only the location of poles and zeros are of importance, but also their direction—see, for example, [199, 210]. This means that the integral constraint due to the NMP zero in $G_{\phi\alpha}(s)$ *may* be shared between $S_{\phi\phi}(s)$ (roll-to-roll sensitivity) and $S_{\psi\phi}(s)$ (roll-to-yaw sensitivity). Unfortunately, due to the rank deficiency of the plant for the SITO case being considered, the direction of the NMP zero associated with $G_{\phi\alpha}(s)$ is canonical, which means that the integral constraint only affects $S_{\phi\phi}(s)$—see [173]. In other words, *the trade-off associated with the roll sensitivity function cannot be alleviated by considering a multi-variable design approach.* Thus, the Poisson integral constraint of the SISO case holds

$$\int_{-\infty}^{\infty} \ln |S_{\phi\phi}(j\omega)| \frac{q_1}{q_1^2 + \omega^2} d\omega = 0, \tag{8.38}$$

where q_1 is the NMP associated with the rudder-to-roll response (8.7), and

$$S_{\phi\phi}(s) = \frac{1 + C_\psi(s)G_\psi}{1 + C_\psi(s)G_\psi + C_\phi(s)G_\phi}, \tag{8.39}$$

where

$$\begin{aligned} G_\phi &\triangleq G_{\phi\alpha}(s)G_\alpha(s), \\ G_\psi &\triangleq G_{\psi\alpha}(s)G_\alpha(s). \end{aligned} \tag{8.40}$$

Goodwin *et al.*[90] considered the frequency domain approach to study the SITO Problem 2. However, the solution obtained could not be expressed in a simple form as for the SISO case, *cf.* (8.24), and only numerical results could be obtained for different values of the parameter λ in Problem 2.

This provided the motivation to reconsider the problem in the time domain, which will lead to the same numerical results presented in [90], but it will also serve as basis for incorporating constraints on the control signal in the following chapter.

8.5.2 Limiting Stochastic LQR

Let us consider a state-space representation for a shaping filter $H(s)$ used to represent the output disturbance (wave-induced roll motion) as indicated in Problem 2:

$$\begin{aligned} \dot{\mathbf{x}}_\mathrm{w} &= \mathbf{A}_\mathrm{w}\mathbf{x}_\mathrm{w} + \mathbf{B}_\mathrm{w}\mathbf{w} \\ \mathbf{y}_\mathrm{w} &= \mathbf{C}_\mathrm{w}\mathbf{x}_w, \end{aligned} \tag{8.41}$$

where, $\mathbf{x}_\mathrm{w} = [\phi_\mathrm{w}, p_\mathrm{w}]^\mathrm{T}$, $\mathbf{y}_\mathrm{w} = [\phi_\mathrm{w}, 0]^\mathrm{T}$, and , and $\mathbf{w}$ is white noise. Also, let us consider a state-space representation for a model to describe the response due to the control action:

$$\begin{aligned}\dot{\mathbf{x}}_\mathrm{c} &= \mathbf{A}_\mathrm{c}\mathbf{x}_\mathrm{c} + \mathbf{B}_c u \\ \mathbf{y}_\mathrm{c} &= \mathbf{C}_\mathrm{c}\mathbf{x}_\mathrm{c},\end{aligned} \tag{8.42}$$

where $\mathbf{x}_c = [v_\mathrm{c}, p_\mathrm{c}, r_\mathrm{c}, \phi_\mathrm{c}, \psi_\mathrm{c}]^\mathrm{T}$, $\mathbf{y}_\mathrm{c} = [\phi_\mathrm{c}, \psi_\mathrm{c}]$ and $u = \alpha$.

The augmented open-loop system incorporating the disturbance model is

$$\begin{aligned}\dot{\mathbf{x}} &= \mathbf{A}\mathbf{x} + \mathbf{B}\mathbf{u} + \mathbf{W}\mathbf{w} \\ \mathbf{y} &= \mathbf{C}\mathbf{x}.\end{aligned} \tag{8.43}$$

where

$$\mathbf{x} = \begin{bmatrix}\mathbf{x}_\mathrm{c} \\ \mathbf{x}_\mathrm{w}\end{bmatrix} \quad \mathbf{A} = \begin{bmatrix}\mathbf{A}_\mathrm{c} & \mathbf{0} \\ \mathbf{0} & \mathbf{A}_\mathrm{w}\end{bmatrix} \quad \mathbf{B} = \begin{bmatrix}\mathbf{B}_\mathrm{c} \\ \mathbf{0}\end{bmatrix} \quad \mathbf{W} = \begin{bmatrix}\mathbf{0} \\ \mathbf{B}_\mathrm{w}\end{bmatrix} \quad \mathbf{C} = \begin{bmatrix}\mathbf{C}_\mathrm{c} & \mathbf{C}_\mathrm{w}\end{bmatrix} \tag{8.44}$$

where, $\mathbf{x} = [v_\mathrm{c}, p_\mathrm{c}, r_\mathrm{c}, \phi_\mathrm{c}, \psi_\mathrm{c}, \phi_\mathrm{w}, p_\mathrm{w}]^\mathrm{T}$, and $\mathbf{y} = [(\phi_\mathrm{c} + \phi_\mathrm{w}), \psi_\mathrm{c}]^\mathrm{T}$.

The problem of minimising the Cost (8.36), can be posed as a stochastic LQR problem [128]:

$$\begin{aligned}V &= \lim_{\varepsilon \to 0} \left\{\lambda \mathbf{var}[y_1] + (1-\lambda)\mathbf{var}[y_2 - \bar{y}_2] + \varepsilon \mathbf{var}[u]\right\} \\ &= \lim_{\varepsilon \to 0} \mathbf{E}\left[(\mathbf{y} - \bar{\mathbf{y}})^\mathrm{T}\mathbf{Q}(\mathbf{y} - \bar{\mathbf{y}}) + \varepsilon u^2\right] \\ &= \lim_{\substack{\varepsilon \to 0 \\ T \to \infty}} \frac{1}{T}\mathbf{E}\left[\int_0^T (\mathbf{y} - \bar{\mathbf{y}})^\mathrm{T}\mathbf{Q}(\mathbf{y} - \bar{\mathbf{y}}) + \varepsilon u^2 dt\right],\end{aligned} \tag{8.45}$$

where

$$\mathbf{Q} = \begin{bmatrix}\lambda & 0 \\ 0 & (1-\lambda)\end{bmatrix} \tag{8.46}$$

For a given $\varepsilon > 0$, the optimal linear solution that minimizes (8.45) is given by

$$u(t)^\mathrm{OPT} = \mathbf{K}(\varepsilon)\mathbf{x}(t); \qquad \mathbf{K}(\varepsilon) = -\varepsilon^{-1}\mathbf{B}^\mathrm{T}\mathbf{S}, \tag{8.47}$$

where S is the solution of the following associated Riccati equation

$$\mathbf{A}^\mathrm{T}\mathbf{S} + \mathbf{S}\mathbf{A} - (\mathbf{S}\mathbf{B})\varepsilon^{-1}(\mathbf{B}^\mathrm{T}\mathbf{S}) + \mathbf{C}^\mathrm{T}\mathbf{Q}\mathbf{C} = \mathbf{0}. \tag{8.48}$$

Figure 8.10 shows a block diagram of the LQR control scheme, in which we have separated the controller into a feedback component $\mathbf{K}_{fbk}$ and a feedforward component $\mathbf{K}_{ff}$, *i.e.* $\mathbf{K} = [\mathbf{K}_{fbk} \quad \mathbf{K}_{ff}]$.

To characterise the trade-off we are interested in, it is more convenient to evaluate $\mathbf{var}[y_1]$ and $\mathbf{var}[y_2]$ for a given λ rather than the total cost (8.45). To evaluate these, we can use the following property of the linear systems driven by white noise n:

Lemma 8.3 ([128]). *Consider the following stochastic differential equation*

$$\dot{\mathbf{x}} = \mathbf{A}\mathbf{x} + \mathbf{B}\mathbf{n},$$

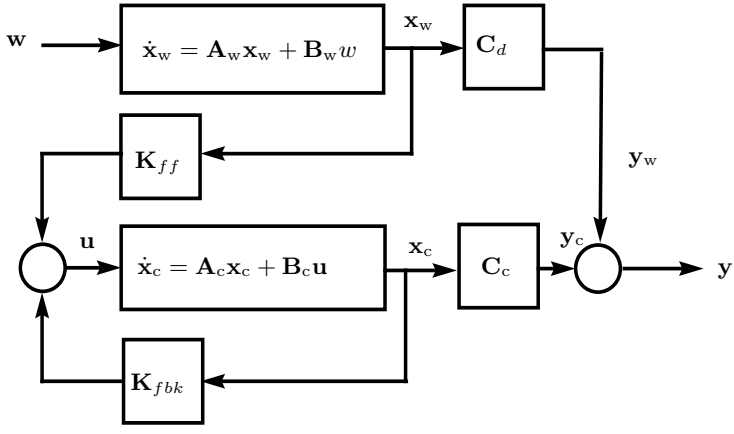

Fig. 8.10. State feedback regulator with disturbance model.

where $\mathbf{A}$ *and* $\mathbf{B}$ *have constant elements, and* $\mathbf{A}$ *is Hurwitz, and that the noise vector* $\mathbf{n}$ *is white with constant PSD matrix* $\mathbf{S}_{nn}$*. Then, the steady state covariance of the state vector* $\mathbf{x}$

$$\mathbf{C}_{\mathbf{xx}}^{\infty}[\tau] \triangleq \lim_{t\to\infty}\left(\mathop{\mathbf{E}}_{\mathbf{x}}[\mathbf{x}(t)\mathbf{x}(t+\tau)^{\mathrm{T}}] - \mathop{\mathbf{E}}_{\mathbf{x}}[\mathbf{x}(t)]\mathop{\mathbf{E}}_{\mathbf{x}}[\mathbf{x}(t+\tau)]\right).$$

is a constant non-negative definite matrix, which satisfies the following Lyapunov equation

$$0 = \mathbf{A}\mathbf{C}_{\mathbf{xx}}^{\infty}[0] + \mathbf{C}_{\mathbf{xx}}^{\infty}[0]\mathbf{A}^{\mathrm{T}} + \mathbf{B}\mathbf{S}_{nn}\mathbf{B}^{\mathrm{T}}, \tag{8.49}$$

where to simplify the notation, $\mathbf{C}_{\mathbf{xx}}^{\infty}[0]$ *will henceforth be denoted by* $\mathbf{C}_{\mathbf{xx}}^{\infty}$*.*

○ ○ ○

Direct application of Lemma 8.3 to the SITO closed-loop system resulting from using the law (8.47) yields

$$\mathbf{var}[y_1] = \mathbf{C}_1\mathbf{C}_{\mathbf{xx}}^{\infty}\mathbf{C}_1^{\mathrm{T}} \qquad \mathbf{var}[y_2] = \mathbf{C}_2\mathbf{C}_{\mathbf{xx}}^{\infty}\mathbf{C}_2^{\mathrm{T}} \qquad \mathbf{var}[u] = \mathbf{K}\mathbf{C}_{\mathbf{xx}}^{\infty}\mathbf{K}^{\mathrm{T}} \tag{8.50}$$

where $\mathbf{C}_{\mathbf{xx}}^{\infty}$ satisfies

$$0 = (\mathbf{A}+\mathbf{B}\mathbf{K})\mathbf{C}_{\mathbf{xx}}^{\infty} + \mathbf{C}_{\mathbf{xx}}^{\infty}(\mathbf{A}+\mathbf{B}\mathbf{K})^{\mathrm{T}} + \mathbf{W}\mathbf{S}_{nn}\mathbf{W}^{\mathrm{T}}, \tag{8.51}$$

and the matrices $\mathbf{C}_1$ and $\mathbf{C}_2$ are defined such $y_1 = \mathbf{C}_1\mathbf{x}$ and $y_2 = \mathbf{C}_2\mathbf{x}$.

To summarise, we can use the following procedure to obtain the trade-off for the SITO problem:

1. Choose $\lambda \in (0, 1]$ and small value for ε.
2. Generate the matrix $\mathbf{Q}$

$$\begin{bmatrix} \lambda & 0 \\ 0 & (1-\lambda) \end{bmatrix}$$

3. Solve the Riccati equation for $\mathbf{S}$ and evaluate the control gain $\mathbf{K}$ for the augmented system

$$\mathbf{0} = \mathbf{A}^{\mathrm{T}}\mathbf{P} + \mathbf{S}\mathbf{A} - (\mathbf{S}\mathbf{B})\varepsilon^{-1}(\mathbf{B}^{\mathrm{T}}\mathbf{P}) + \mathbf{C}^{\mathrm{T}}\mathbf{\Lambda}\mathbf{C}$$
$$\mathbf{K} = -\varepsilon^{-1}\mathbf{B}^{\mathrm{T}}\mathbf{P}$$

4. Solve the Lyapunov equation for the augmented state covariance in closed loop

$$0 = (\mathbf{A} + \mathbf{B}\mathbf{K})\mathbf{C}_{\mathbf{xx}}^{\infty} + \mathbf{C}_{\mathbf{xx}}^{\infty}(\mathbf{A} + \mathbf{B}\mathbf{K})^{\mathrm{T}} + \mathbf{W}\mathbf{S}_{nn}\mathbf{W}^{\mathrm{T}}.$$

5. Evaluate the variances of the output (and control)

$$\mathbf{var}[y_1] = \mathbf{C}_1\mathbf{C}_{\mathbf{xx}}^{\infty}\mathbf{C}_1^{\mathrm{T}} \quad \mathbf{var}[y_2] = \mathbf{C}_2\mathbf{C}_{\mathbf{xx}}^{\infty}\mathbf{C}_2^{\mathrm{T}} \quad \mathbf{var}[u] = \mathbf{K}\mathbf{C}_{\mathbf{xx}}^{\infty}\mathbf{K}^{\mathrm{T}}$$

By applying the algorithm described in Section 2.6, to the roll power spectral density, we can obtain the parameters of a shaping filter that for a particular sea state and sailing conditions. Using this with the approach described above, one can obtain the results shown in Figures 8.11 and 8.12. In these examples, we have used ITTC spectrum with a significant wave height of 4 m and a mean wave period of 7 s, and our example vessel (see Appendix B) sailing at a speed of 15 kt and relative heading with respect to the waves of 45 and 135 deg.

The results shown in Figures 8.11 and 8.12 are *the optimal unconstrained trade-offs between roll reduction and yaw interference for the sea state and particular sailing conditions considered (speed and heading).* Therefore, we can evaluate the price to paid—the increase in yaw RMS value—due to the desired roll reduction.

This is optimal because the cost minimised is related to the variances, which are the performance indices being assessed, and also because all the information available to calculate the controller is used: state feedback and full knowledge of the disturbance—no real controller will have access to this information. Therefore, we can expect other more realistic controllers to give performances on top of the curves shown in Figures 8.11 and 8.12. These plots can be used in two ways:

- To compare the performance of other designs.
- To see whether the required performance can be achieved in a particular sailing condition: *no realistic controller will achieve a performance below the graphs shown in Figures* 8.11 *and* 8.12

Table 8.1. Limiting achievable performance ($\lambda = 1$).

Enc Ang	roll open loop RMS	SISO lim RMS	LQR lim RMS	RR lim
χ =45 deg	6.65 deg	1.64 deg	1.7 deg	75.2%
χ=90 deg	12.7 deg	1.35 deg	1.38 deg	89.2%
χ =135 deg	5.9 deg	0.47 deg	0.66 deg	92.0%

The results regarding roll reduction are summarised in Table 8.1 for the limiting case, in which only roll reduction is considered. This table shows, the encounter angle, the open-loop RMS value of roll angle; the value according to the SISO case result (8.24), which corresponds to the case of $\lambda = 1$ in the stochastic LQR formulation of the problem, *cf.* (8.45); and the values obtained using the stochastic limiting LQR method with $\varepsilon = 10^{-7}$. Finally, in the fifth column, shows the roll reduction.

It is interesting to notice that although the sailing conditions considered for χ=45 and χ=135 deg present similar RMS values of roll angle in open loop, the case of quartering sea presents the worst performance in closed loop. This follows from (8.24) by noting that, for quartering seas, the PSD of the wave-induced roll motion has the bulk of its energy closer to the NMP zero, which is located at $q_1 = 0.187$ s^{-1}—compare Figures 8.11 and 8.12.

The above results are very conservative, and the roll reductions cannot be used to as an estimate of the roll reduction that one could obtain in a practical application. To have a less conservative bound on the performance, and thus be able to estimate performance for a ship in a practical situation we need to incorporate the constraints associated with the input. This will be the topic of the next chapter.

8.6 Comments on the Applicability of Rudder Stabilisers

Hearns and Blanke [100] have studied the variations in the location of the NMP zero, for variations in the values of some of the hydrodynamic derivatives and load condition for a particular vessel using a hydrodynamic model obtained from a PMM test. Their results are summarized in the following.

The increase of the following parameters brings the NMP zero closer to the imaginary axis (beneficial):

- GMt -transverse metacentric height.
- K_r - roll moment induced by rate of turn.
- K_{rudder} - roll moment induced by the rudder.
- Y_r - sway force induced by the rate of turn.
- Y_v - sway force induced by the sway velocity.
- N_r - yaw moment induced by the rate of turn.

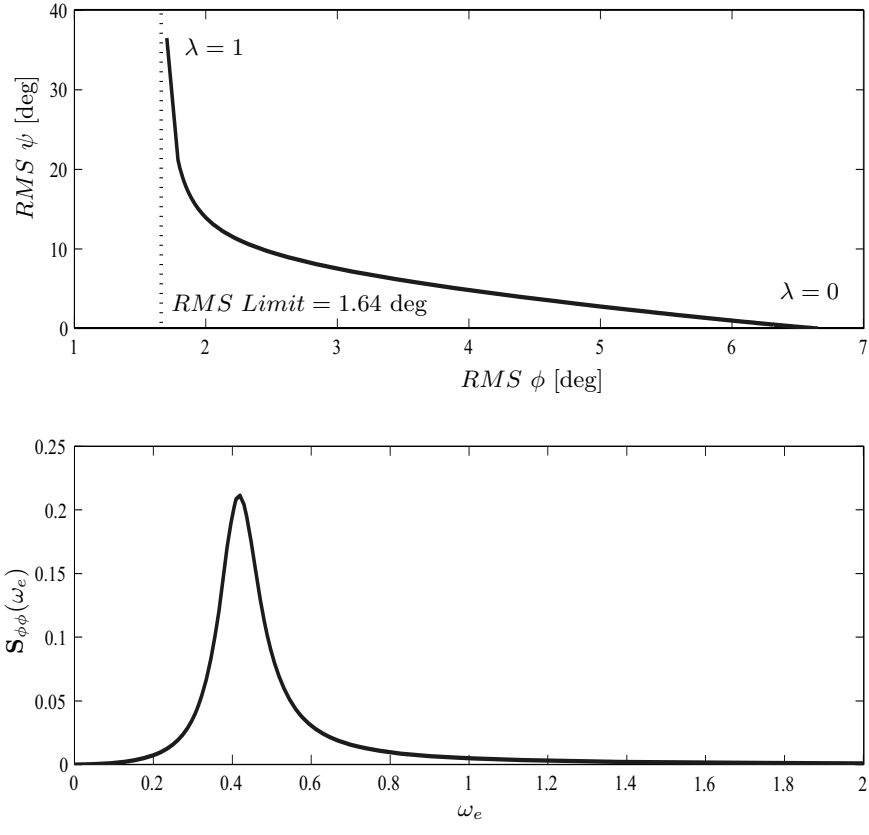

Fig. 8.11. Limiting optimal trade-off roll (deg RMS) vs yaw (deg RMS) for a rudder stabiliser. ITTC spectrum ($H_{1/3}$ =4 m, T = 7 s) and vessel sailing at 15 kt in quartering seas $\chi = 45$ deg.

The increase of the following parameters takes the NMP zero farther away from the imaginary axis (detrimental):

- K_v - roll moment induced by sway velocity.
- Y_{rudder} - sway force induced by the rudder.
- N_v - yaw moment induced by the sway velocity.
- N_{rudder} - yaw moment induced by the rudder.

Most of these parameters are related to the shape of the hull. The variations in GMt are related to the load condition and mass distribution on the hull. An increase of GMt will increase the roll natural frequency (8.10). However, from a seakeeping point of view, it has been recognised since the times of Froude [75] that there is no advantage in increasing the roll natural frequency because low-period waves are steeper than long period ones, and it is the wave slope

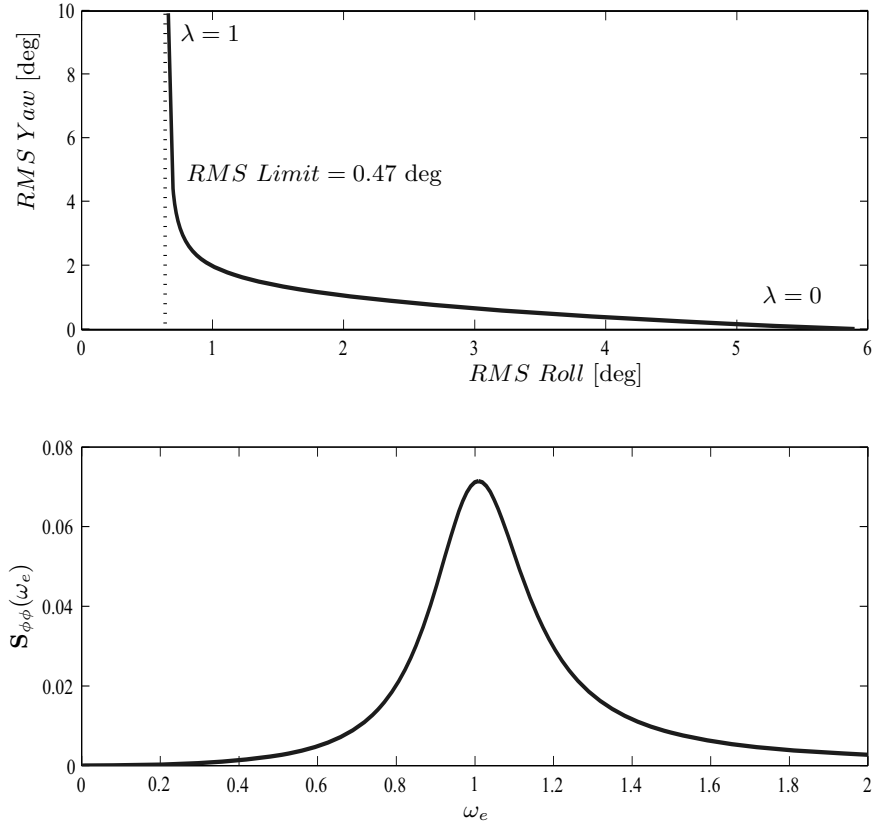

Fig. 8.12. Limiting optimal trade-off roll (deg RMS) vs yaw (deg RMS) for a rudder based stabiliser. ITTC spectrum ($H_{1/3}$ =4 m, T = 7 s) and vessel sailing at 15kts in bow seas $\chi = 135$ deg.

what excites roll motion. Also, an increase of GM_t would, in turn, increase the transverse accelerations and motion induced interruptions.

The only viable modification may then be the position of the rudder relative to CG. Indeed, it follows from all of the above that the larger the vertical distance from the centre of pressure of the rudder to the CG the better. This will induce a large roll moment. Similarly, the shorter the longitudinal distance from the center of pressure of the rudder to the CG the better. This would reduce the yaw moment; and hence delay the rate of turn: move the NMP zero close to the imaginary axis. The Danish navy vessel SF300, [34] uses to wing rudders for RRS, and a central rudder for the steering. The wing rudders are located forward from the central rudder, which makes them better for RRS purposes.

As commented by Cowley, [53], the ships best suited to the application of RRS are those with a small GMt, low damping, and long natural roll period

so the roll moments generated by the rudder are not limited by the rates of the steering machinery. The following criteria for applicability were discussed by van der Klugt, [228]:

- The rudder must be able to generate a considerable roll moment, at the roll natural frequency without affecting the yaw.
- The rudder speed must be sufficiently large.
- The aft of the ship should be able to withstand the large forces and moments generated by the rudder.

With regards to the steering machinery characteristics, a rule of thumb is to have a maximum rate such that [228]

$$\dot{\alpha}_{\max} \geq \alpha_{\max}\, \omega_\phi, \tag{8.52}$$

where $\alpha_{r\,\max}$ is the maximum rudder angle allowed for RRS, and ω_ϕ is the roll natural frequency. The maximum rudder angle can be taken as the rudder static stall angle. This is to specify the rudder machinery; in practice, the maximum angle will be set according to the speed of the vessel and can be limited to less than the stall angle.

The above criterium follows from considering a sinusoidal excitation

$$\alpha(t) = \alpha_{r\,\max} \sin(\omega_\phi t),$$

and taking its derivative

$$\dot{\alpha}(t) = \alpha_{r\,\max} \omega_\phi \cos(\omega_\phi t).$$

Another way of expressing this relationship, it by saying that for given maximum angle, the frequency that will be followed without distortion is

$$\omega_{\text{lin}} = \frac{\dot{\alpha}_{\max}}{\alpha_{\max}}.$$

In section 5.6, we saw that the rudder machinery can be modelled as a first order system, when operating linearly:

$$\frac{\alpha(s)}{\alpha_d(s)} = \frac{1}{1 + \tau_r\, s},$$

where $\alpha_d(s)$ is the angle commanded by the autopilot controller. As a rule of thumb, the pole of the steering machinery can be neglected if it is 5 times larger than the dominant poles of the system. van der Klugt, [228], proposes

$$\tau_r \leq \frac{1}{5\omega_\phi}.$$

The above gives an indication of the characteristics of the steering machinery. In the following chapter, we will show a method that can be used to assess the RRS performance based on these specifications. Hence, the method can be used to check the specifications of the steering machinery based on the desired performance.

8.7 NMP Dynamics in Fin Stabilizers

The problem of fin stabilisers, can be treated as SISO problem for the purpose of analysis. Since NMP dynamics can also appear in fin stabilisers, the results obtained for the SISO case provide insight into this effect.

Hull designs are constrained by many variables, and therefore it is common that fins end up located aft from the centre of gravity CG (LF < 0 *cf.* Figure B.3 in Appendix B). From the previous analysis it follows that when the fins are aft of the CG and there is an inclination between the fins and the water line ($\beta > 0$; in Figure 5.11), the fin induced sway force (*cf.* (5.24)) will induce a yaw moment in the same way as a rudder would. Therefore, NMP characteristics would arise in this case. *To avoid this, the fins should be located, if possible, forward and close to CG.*

Since the fins are conventionally located closer to the CG than the rudders, and the sway force induced by fins is smaller than that induced by rudders, the NMP zero appearing, if any, is located very close to the imaginary axis. Therefore, in most cases the NMP dynamics can be disregarded. Lloyd, [135], observed that for fins located aft from the CG, there is amplification in roll at low and at high frequencies, whereas for fins forward from the CG there is roll amplification only at high frequencies. Lloyd's conclusions are related to the typical sensitivity reduction for the case of NMP and MP zero using a fixed tuning controller.

In this chapter, we have presented a study of performance limitations related to the dynamics of the ship. We have analysed how these effects can affect the performance in different sailing conditions. Because the constraints on the magnitude and rate of the rudder angle were not considered in this analysis, the results give insight into the problem, but the performance figures are not practical—the bounds on performance are too conservative. In the following chapter, we incorporate constraints into the analysis.

9

Constrained Performance Limitations

In the previous chapter, we have seen that if we consider the problem of disturbance rejection for linear systems at a single frequency, there exist no limitations on the achievable closed-loop performance. In this context, good performance was associated with a reduced value for the magnitude of the sensitivity transfer function, and no limitations in the achievable performance refers to the fact that the effect of the disturbances on the output can be completely eliminated. This is accomplished by forcing the magnitude of the sensitivity function to be zero at the particular frequency of interest. We have also seen in Chapter 8 that this is not true, in general, when output disturbances have power distributed over a range of frequencies, rather than at a single frequency. In these cases, good performance can be associated with a reduced variance of the output of the closed-loop system, and eliminating the effect of the disturbance on the output is not always possible. Indeed, we have discussed situations in which the reduction of output variance is limited, and these limits hold regardless of how much power is available to implement the control action. These limitations are the consequence of the feedback structure and the dynamic characteristics of the plant, in particular non-minimum phase dynamics.

In this chapter, we analyze what additional limitations and design trade-offs arise due to limited control action (constraints) and actuator saturation effects. We proceed by first analysing the deterministic case for sinusoidal disturbances; and then we address the case of stochastic disturbances. Both cases are relevant to the problem of ship stabiliser design.

9.1 Input Constraints and Saturation Effects

Consider the control loop shown in Figure 9.1. Let us denote by u_d the *control command* or desired control demanded by the controller; and by u the actual *control action* delivered to the system by the actuator. We then say that the actuator saturates, or that saturation occurs, whenever the control

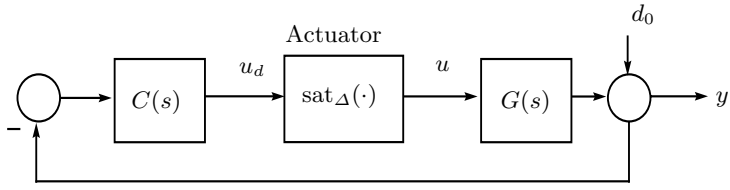

Fig. 9.1. Single control loop with saturation.

action differs significantly from the control command, *i.e.* $u \neq u_d$. Therefore, a saturation event implies that the actuator fails to deliver the commanded action due to limited power.

If the dynamics of the actuator are fast in comparison with the dynamics of the system, the effect of a saturating actuator can be modelled using the static function $\text{sat}_\Delta(\cdot)$ defined (for the scalar control case) as

$$\text{sat}_\Delta : \mathbb{R} \to \mathbb{R}, \quad \text{sat}_\Delta(x) = \begin{cases} \Delta & \text{if } x > \Delta, \\ x & \text{if } |x| \leq \Delta, \\ -\Delta & \text{if } x < \Delta. \end{cases}$$

If we consider the vector case, *i.e.* $\text{sat}_\Delta(\cdot) : \mathbb{R}^n \to \mathbb{R}^n$, the limits should be interpreted as holding component-wise unless otherwise indicated.

As depicted in Figure 9.1, the control action delivered to the plant $G(s)$ is given by

$$u = \text{sat}_\Delta(u_d).$$

Saturation usually occurs in situations where the control command is large and the control strategy ignores the fact that the actuator has limited power. This, in general, produces performance degradation. Control strategies that avoid saturation effects or limit degradation due to saturation are usually called *constrained control strategies* because the control command is *constrained* by design to avoid saturation. These strategies will be discussed in Chapter 11. This chapter will focus on quantifying the performance limitations associated with the fact that saturation can occur.

9.2 Input Constraints and Performance at a Single Frequency

Often the performance of a stabiliser is predicted for regular beam seas [198]. Although this situation is very restrictive (and can be highly unrealistic), such estimates can be interpreted as a rough indicator of the actual performance. They may also be used to compare different designs and/or to help

to dimension the actuator. For this reason, we incorporate, in this section, an analysis of performance for the case of sinusoidal disturbances and discuss the implications of having an actuator with limited power or limited authority.

9.2.1 Magnitude Limitations

Let us assume that the output disturbance d_0 in Figure 9.1 is a sinusoid of known frequency ω_0 *i.e.*

$$d_0(t) = \bar{d}_0 \cos(\omega_0 t),$$

and that the control signal is constrained in magnitude to avoid saturation effects, *i.e.*

$$|u(t)| \leq \Delta, \qquad \text{for all} \quad t. \tag{9.1}$$

Under these assumptions, and further assuming that the closed-loop system is operating linearly, then the performance in terms of disturbance rejection can be quantified in the frequency domain. Indeed, when the SISO control loop of Figure 9.1 is operating linearly, we have

$$U(s) = -\frac{T(s)}{G(s)} D_0(s), \tag{9.2}$$

where $U(s)$ and $D_0(s)$ are the Laplace transform pairs of $u(t)$ and $d_0(t)$ respectively, and $T(s)$ is the complementary sensitivity function—see Section 8.1. Note that since $u_d(t) = u(t)$.

Because the system is operating linearly, the signal $u(t)$ will be sinusoidal:

$$u(t) = \bar{u} \cos[\omega_0 t + \epsilon(\omega_0)],$$

where the amplitude $\bar{u}$ is given by

$$\bar{u} = \left| \frac{T(j\omega_0)}{G(j\omega_0)} \right| \bar{d}_0. \tag{9.3}$$

Using the relationship between the sensitivity and complementary sensitivity functions (*cf.* Section 8.1), we can write

$$|S(s)| + |T(s)| \geq 1, \tag{9.4}$$

which holds for all s in the region of convergence of both $S(s)$ and $T(s)$. Using (9.2), we obtain

$$|S(j\omega_0)| \geq 1 - \frac{|G(j\omega_0)|}{\bar{d}_0} \bar{u}. \tag{9.5}$$

Provided $G(s)$ has no poles at $\pm j\omega_0$, the best we can do to reject the disturbance is to make $|S(j\omega_0)| = 0$. This can be achieved using the Internal Model Principle (IMP)—see, for example, [89]. Obviously this analysis holds as long as the system remains linear. When the constraint (9.1) is to be satisfied, the

value of the control given by (9.3) will not always be feasible for any size of $d_0(t)$, and saturation can occur. Then, we can use (9.3) to determine, for instance, which value of $\bar{d_0}$ would result in saturation effects, and also what implications this may have on the performance if we are to avoid saturation by reducing the control command such that the system remains linear.

The amplitude $\bar{d_0}^*$ of the largest disturbance that we can possibly reject completely without saturating the actuator can be determined from (9.3) and the constraint (9.1) as

$$\bar{d_0}^* = |G(j\omega_0)|\,\Delta. \tag{9.6}$$

Using (9.5) and (9.6) we could also say that if the controller is adjusted such that saturation never occurs for $\bar{d_0} \leq \bar{d_0}^*$, then

$$\begin{aligned} |S(j\omega_0)| &= 0 && \text{if} \quad \bar{d_0} \leq \bar{d_0}^* \\ |S(j\omega_0)| &> 1 - \frac{|G(j\omega_0)|}{\bar{d_0}}\Delta && \text{if} \quad \bar{d_0} > \bar{d_0}^*. \end{aligned}$$

If the performance is measured as the percentage of reduction of the output amplitude of the closed-loop system with respect to that of the open loop system, then we can express the performance by

$$R_{\%} = 100\,\frac{\bar{d_0} - \bar{y}}{\bar{d_0}} = 100\,(1 - |S(j\omega_0)|),$$

where $\bar{y}$ is the steady-state amplitude of the output. Finally, we obtain that

$$\begin{aligned} R_{\%} &= 100 && \text{if} \quad \bar{d_0} \leq \bar{d_0}^* \\ R_{\%} &< 100\,\frac{|G(j\omega_0)|}{\bar{d_0}}\Delta && \text{if} \quad \bar{d_0} > \bar{d_0}^*. \end{aligned} \tag{9.7}$$

Expression (9.7) shows an explicit relationship between the performance of the closed-loop system and the magnitude constraint.

In the next section, we consider a similar analysis for the case in which the control input is constrained in rate.

9.2.2 Rate Limitations

Let us consider now the following constraint:

$$|\dot{u}(t)| < \Delta_v.$$

Under similar assumptions as in the case of a magnitude constraint, we have that the amplitude $\bar{d_0}^{**}$ of the largest output disturbance that we can possibly reject completely without saturating the actuator in rate is

$$\bar{d_0}^{**} = \left| \frac{G(j\omega_0)}{\omega_0} \right| \Delta_v. \tag{9.8}$$

Proceeding in a similar manner as in the magnitude limitation case, we obtain

$$\begin{aligned} |S(j\omega_0)| &= 0 && \text{if} \quad \bar{d_0} \leq \bar{d_0}^{**} \\ |S(j\omega_0)| &> 1 - \frac{|G(j\omega_0)|}{\omega_0 \bar{d_0}} \Delta_v && \text{if} \quad \bar{d_0} > \bar{d_0}^{**}. \end{aligned}$$

Then, using the same measure of performance as in the case of magnitude constraints, we obtain

$$\begin{aligned} R_{\%} &= 100 && \text{if} \quad \bar{d_0} \leq \bar{d_0}^{**} \\ R_{\%} &< 100 \, \frac{|G(j\omega_0)|}{\omega_0 \bar{d_0}} \Delta_v && \text{if} \quad \bar{d_0} > \bar{d_0}^{**}. \end{aligned} \tag{9.9}$$

Expressions (9.7) and (9.9) quantify how avoiding saturation of the actuator, in either magnitude or rate, can affect the performance in cases for which the output disturbances are characterised by a sinusoid.

9.3 Application to Rudder-Based Stabilizers

Let us consider the following particular choice of the elements involved in the analysis presented above, where

- $G(s)$ is the roll response due to the control action (rudder angle).
- Δ is the limit on the maximum rudder angle.
- $\bar{d_0}$ is the roll disturbance calculated for a particular wave height and the roll response operator of the ship.

Table 9.1 shows some results assuming a rudder-based stabiliser for the naval vessel example (see Appendix B) sailing at 15 kt in beam seas. The constraint on the rudder angle is 25 deg, and the rudder rate 12 deg/s and the roll disturbance corresponds to a wave height of 4m with periods T ranging from 4 to 10 s.

This analysis could only be applied to ships with highly resonant roll response to wave excitations—very narrow-banded motion RAO. Under this condition, it could be argued that the ship would often roll at frequencies very close to the ship's natural frequency [133]. Therefore, the assumption of sinusoidal disturbances may approximately hold even for some irregular sea conditions. For ships that do not possess such a narrow-band roll response, it is necessary to analyse the problem at a range of frequencies, rather than at a single frequency. A method which can be applied to these cases is considered in the following section.

Table 9.1. Performance degradation due to magnitude constraints on the rudder angle for regular beam seas. The roll disturbances correspond to a wave height 4m, and the constraint in the maximum rudder angle is of 25 deg and rudder rate 12 deg/s.

T [s]	$\bar{d}_0^*$ Roll [deg]	$\bar{d}_0$ Roll [deg]	RR %
4	5.53	16.75	33
5	17.4	23.7	73.5
6	21.2	39.7	53.4
7	12.2	36.5	33.4
8	9.2	18.7	49.3
10	7.1	7.7	91.2

9.4 Stochastic Approach: Variance Constraints

In Chapter 8, we analyzed the best performance for the regulator problem using stochastic limiting LQR. We obtained an upper bound for the performance of a closed loop system subject to stochastic disturbances, for a SISO and SITO NMP system. In this section, we will be particularly interested in studying the same problems but subject to constraints on the input.

Our approach is based on the methods to tune LQR control strategies proposed by Skelton, [209]. These methods are consistent with the work presented in Chapter 8; and therefore, represent a straightforward extension of those results for the case of constrained systems. Specifically, one of these methods addresses the, so-called, Input Variance Constrained (IVC) control problem.

This problem seeks the state-feedback stabilizing controller that minimizes the steady state expected value of a quadratic form of the output subject to variance constraints of the components of the input vector. This problems considers soft constraints rather than hard constraints[1] because the constraints are imposed on the statistics of the input variables. However, by careful choice of the limit, we can evaluate the price to be paid for avoiding hard constraints with certain probability. This is particularly simple if the constrained variables can be assumed to be narrow-banded and Gaussian stochastic processes.

9.4.1 IVC Optimal Control Problem Formulation

We will begin this section by defining the following optimal control problem:

Definition 9.1 (IVC Problem). *Consider the linear time-invariant system*

$$\begin{aligned} \dot{\mathbf{x}} &= \mathbf{A}\mathbf{x} + \mathbf{B}\mathbf{u} + \mathbf{W}\mathbf{w} \\ \mathbf{y} &= \mathbf{C}\mathbf{x}, \end{aligned} \tag{9.10}$$

[1] A soft constraint is a constraint that can be violated temporarily, whereas a hard constraint cannot be violated—see Section 11.1.

where $\mathbf{x} \in \mathbb{R}^n$, $\mathbf{u} \in \mathbb{R}^m$, $\mathbf{y} \in \mathbb{R}^p$, *and* $\mathbf{w} \in \mathbb{R}^q$ *is a zero mean Gaussian white stochastic process with constant power spectral density matrix* $\mathbf{S}_{\mathrm{ww}}$. *Assume that the pair* $(\mathbf{A}, \mathbf{B})$ *is stabilisable.*

Given a matrix $\mathbf{Q} = \mathrm{diag}(\lambda_1, \ldots, \lambda_p)$, *we seek the stabilizing state feedback controller* $\mathbf{u} = K\mathbf{x}$, (i.e. $\mathbf{A}+\mathbf{BK}$ *is Hurwitz) that minimizes a weighted output variance, i.e.,*

$$\mathbf{K}^{\mathrm{OPT}} = \arg \min_{\mathbf{K}} \lim_{t \to \infty} \mathbf{E}[\mathbf{y}(t)^{\mathrm{T}} \mathbf{Q} \mathbf{y}(t)] \tag{9.11}$$

subject to the constraints

$$\begin{aligned} \dot{\mathbf{x}} &= \mathbf{A}\mathbf{x} + \mathbf{B}\mathbf{u} + \mathbf{W}\mathbf{w}, \\ \mathbf{y} &= \mathbf{C}\mathbf{x}, \\ \mathbf{u} &= \mathbf{K}\mathbf{x}, \\ \lim_{t \to \infty} \mathbf{E}[u_i^2(t)] &\leq \gamma_i^2, \qquad \text{for} \quad i = 1, 2, \ldots, m, \end{aligned} \tag{9.12}$$

where u_i *are the components of the control vector* $\mathbf{u}$. ∘ ∘ ∘

The IVC problem is always feasible since any specified bound on input energy or input variance ($\mathbf{var}[u_i] =< \gamma_i^2$) is achievable because no performance bound is demanded on the cost (9.11) (we simply minimize this cost without any constraint upon it.) An approximate solution for the IVC problem can be obtained using the following algorithm:

Given a set of small numbers $\{\epsilon_i : i = 1, \ldots, m\}$, and the diagonal matrix $\mathbf{R} = \text{diag}(1/\gamma_1^2, \ldots, 1/\gamma_m^2)$, then

1. solve the following Riccati equation for S:

$$\mathbf{0} = \mathbf{SA} + \mathbf{A}^{\mathrm{T}}\mathbf{S} - \mathbf{SBR}^{-1}\mathbf{B}^{\mathrm{T}}\mathbf{S} + \mathbf{C}^{\mathrm{T}}\mathbf{QC}$$

2. Evaluate

$$\mathbf{K} = \begin{bmatrix} \mathbf{K}_1 \ \mathbf{K}_2 \vdots \mathbf{K}_m \end{bmatrix}^{\mathrm{T}} = -\mathbf{R}^{-1}\mathbf{B}^{\mathrm{T}}S.$$

3. Solve the following Lyapunov equation for $\mathbf{C}_{\mathbf{xx}}^{\infty}$ (the closed-loop steady-state covariance of $\mathbf{x}$):

$$\mathbf{0} = \mathbf{C}_{\mathbf{xx}}^{\infty}(\mathbf{A} + \mathbf{BK})^{\mathrm{T}} + (\mathbf{A} + \mathbf{BK})\mathbf{C}_{\mathbf{xx}}^{\infty} + \mathbf{WS}_{\mathbf{ww}}\mathbf{W}^{\mathrm{T}}.$$

4. If

$$|\mathbf{K}_i\mathbf{C}_{\mathbf{xx}}^{\infty}\mathbf{K}_i^{\mathrm{T}} - \gamma_i^2| \leq \epsilon_i \qquad \text{for all} \quad i = 1, 2, \ldots, m, \qquad \text{STOP.}$$

Otherwise, update the diagonal elements of R according to

$$R_{ii} \leftarrow \frac{K_i\mathbf{C}_{\mathbf{xx}}^{\infty}K_i^{\mathrm{T}}}{\gamma_i^2}R_{ii} \qquad \text{for} \quad i = 1, 2, \ldots, m,$$

and go back to 1.

The algorithm given above solves an equivalent LQR problem, in which $\mathbf{Q}$ is given and the weighing matrix $\mathbf{R}$ is varied such that the variance of the input is adjusted to be close within the specified tolerance to the constraint. See [209] and [243] for further details.

Note that if the output has zero mean, then

$$\begin{aligned} \mathbf{E}[\mathbf{y}(t)^{\mathrm{T}}\mathbf{Q}\mathbf{y}(t)] &= \mathbf{tr}(\mathbf{QC}_{\mathbf{yy}}^{\infty}[0]) \\ &= \sum_{i=1}^{p} \lambda_i \mathbf{var}[y_i]. \end{aligned} \tag{9.13}$$

Consequently, the IVC problem defined above can be used to solve a constrained version of the SISO and SITO problems presented in Chapter 8 provided the system given by (9.10), is the augmented system to incorporate the plant and the disturbance model–see section 8.5.2. We will illustrate the use of the above ideas via an example.

For the case of rate constraints, we can use the same algorithm by augmenting the state with integrators. Let us define a set of variables $\mathbf{v}$, such that

$$\dot{\mathbf{v}} = \mathbf{u}. \tag{9.14}$$

Then, we can augment the system as follows:

$$\begin{aligned}\dot{\mathbf{x}} &= \mathbf{A}\mathbf{x} + \mathbf{B}\mathbf{v} + \mathbf{W}\mathbf{w},\\ \dot{\mathbf{v}} &= \mathbf{u},\end{aligned} \tag{9.15}$$

and consider the IVC problem for the augmented system, where γ_i are now rate variance constraint.

9.4.2 IVC Application to RRS

Let us consider a sea state described by the ITTC spectrum with a significant wave height of 4 m and a mean wave period of 7 s. For the case of magnitude constraints on the rudder angle, the static stall angle can be used as an absolute constraint—however, as the speed increases smaller angles should be considered. The maximum rudder mechanical angle is larger than the stall angle, and by preventing the rudder mechanical angle from exceeding the static stall angle, it is likely that the rudder will not stall in unsteady operating conditions (normal conditions in RRS). Then, the constraint on the variance of the rudder can be chosen such that saturation does not occur all of the time. Under this assumption, the rudder command generated by the controller can be assumed Gaussian; and therefore, the distribution of maxima of rudder angle can be approximated by a Rayleigh distribution—see Section 7.0.3. The Rayleigh probability density function is parameterised by the standard deviation $\sqrt{m_0}$, which in our case is the value γ_u we use in the IVC problem. Thus, the value γ_u can be determined based on the probability of exceeding the absolute constraints, which can be interpreted as the percentage of time the actuator will saturate.

For example, using the Rayleigh distribution, we have that to avoid exceeding a rudder angle of 25 deg with probability 0.75, we should have a standard deviation of 15 deg. The choice of 0.75 for the probability ensures that the bound is not very conservative.

We then consider the cheap stochastic LQR problem described in Chapter 8, and also the IVC problem presented above for the same case, *i.e.* we seek to minimize

$$V = \lambda \mathbf{var}[\phi] + (1-\lambda)\mathbf{var}[\delta\psi],$$

where ϕ is the roll angle and $\delta\psi$ the slowly-varying yaw deviations from the desired yaw. The parameter λ takes values in the interval $[0, 1]$, and the rudder angle α is subject to the constraint

$$\mathbf{var}[\alpha] \leq \gamma_u^2,$$

with

$$\gamma_u = \begin{cases} \infty & \text{unconstrained case} \\ 15\text{deg} & \text{constrained case} \end{cases}$$

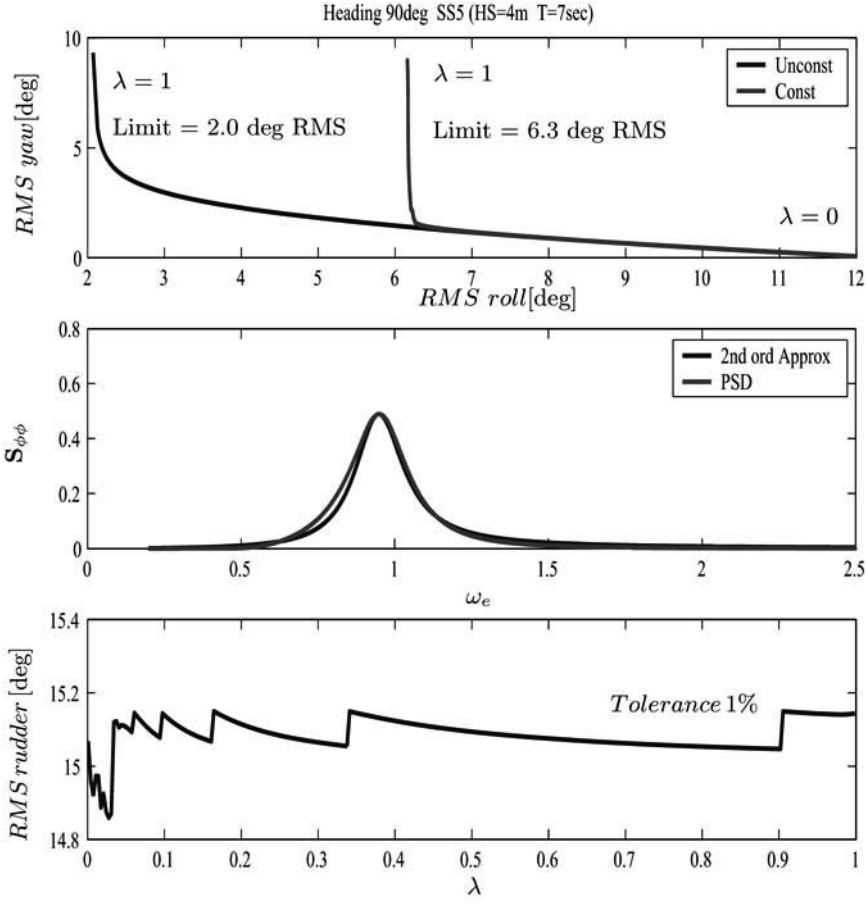

Fig. 9.2. Limiting optimal trade-off roll (deg RMS) vs yaw (deg RMS) for a rudder based stabiliser. ITTC spectrum (Hs =4m, T=7sec) and vessel sailing at 15kts in beam seas $\chi = 90deg$.

Figure 9.2 shows the solutions obtained for beam seas. In the first plot of Figure 9.2, we see the trade off between roll reduction and yaw interference for constrained and unconstrained cases. The axes of this plot correspond to RMS values of the respective quantities. The second plot of this figure presents the second order approximation and the roll PSD obtained from the wave spectrum and the roll RO. The third plot shows the RMS value of the rudder angle obtained from the IVC algorithm for the different values of λ.

We can see that for this particular example, the limitations imposed by the constraints on the rudder angle are more significant than those arising from the dynamics. Therefore, in these conditions the performance limitations associated with roll reduction can be entirely attributed to the limited moment

produced by the rudder. With regards to trade-off between roll reduction and yaw interference, we can see that by exceeding a particular value of λ there is not gain in roll reduction and and only a significant increase in yaw. This value of λ depends on the particular sailing condition, and can be obtained using an adaptive mechanism in a practical implementation.

Figure 9.3 shows similar results for the case of a bow-sea sailing condition. Here again, the limits imposed by the constraints are predominant. Finally, Figure 9.4 shows the results obtained for quartering seas. In this case, we can see that the limitations imposed by the dynamics of the system become more dominant, and the addition of constraints does not affect the performance significantly. This is because for the sailing condition in following seas, the limitations imposed by the NMP dynamics become more apparent due to the low frequency content of the disturbance. As we will see in Chapter 12, these effects are reflected in the simulation results.

Table 9.2. Performance degradation due to magnitude constraints on the rudder angle in irregular seas. The roll disturbances correspond to a wave height 4 m for SS5 and 2.5 m for SS4. The mean wave period is 7 s for SS5 and 9.5 s for SS4. The constraint in the maximum RMS value for the rudder angle is of 15 deg. loop

Sailing Cond	Roll OL	Roll CL unc	Roll CL con	RR unc	RR con
90 deg, Hs=4, T=7	12.4 deg	1.38 deg	6.5 deg	83%	47 %
135 deg, Hs=4, T=9.5	4.1 deg	0.6 deg	1.45 deg	85%	65 %
45 deg, Hs=2.5, T=7.5	3.64 deg	1.33 deg	1.6 deg	63%	56 %

Table 9.2 summarises the results for the case of maximum roll reduction ($\lambda = 1$). The first column of Table 9.2 shows the open-loop (OL) RMS value of the roll angle for the adopted sailing condition. The second and third columns indicate the closed-loop RMS value of the roll angle for the unconstrained and constrained cases respectively. Finally, the last two columns show the performance; hereby measured through the percentage of RMS roll reduction in closed loop with respect to that in open loop.

From these results, we could say that *constraints imposed by the limited power of the rudder are the main factor limiting the performance for sailing conditions in bow and beam seas. However, in following seas, the dynamic behaviour of the vessel plays a very important role.*

Finally, it should be noted that the above figures have been obtained without considering the rate limits on the rudder motion imposed by the hydraulic machinery. The effect of the rate limit is to attenuate the control action. Therefore, the expected roll reduction can, indeed, be worse that that predicted above. However, if one compare the results of Table 9.2, with those for the unconstrained case shown in Table 8.1, we can see that the results of the IVC problem can be used as a performance estimator. This could be a

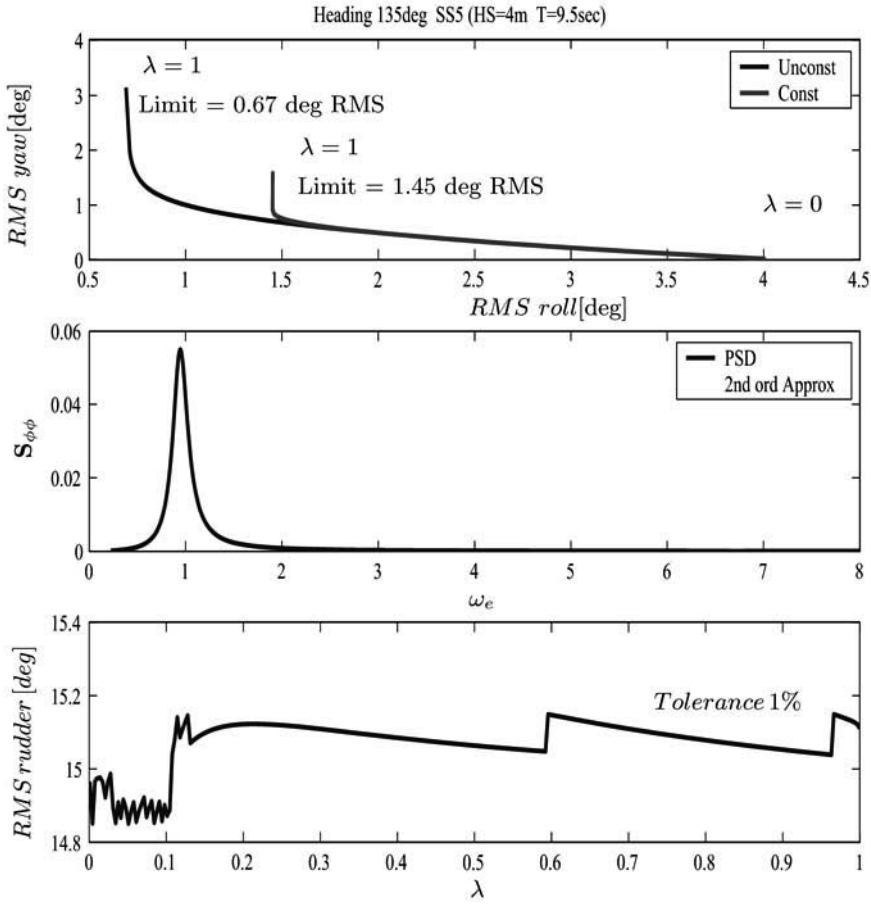

Fig. 9.3. Limiting optimal trade-off roll (deg RMS) vs yaw (deg RMS) for a rudder based stabiliser. ITTC spectrum (Hs =4m, T=9.5sec) and vessel sailing at 15kts in bow seas $\chi = 135deg$.

significant advantage because of the simplicity of the IVC algorithm and that of the models used.

The IVC problem for the case of input rate constraints can be treated via state augmentation as already commented, and the decision about using magnitude and rate constraints for the analysis can be made based on the modal frequency of the disturbance psd.

9.5 Part III Summary and Discussion

This part of the book described issues associated with the dynamic characteristics of ships that may limit the achievable performance of the control

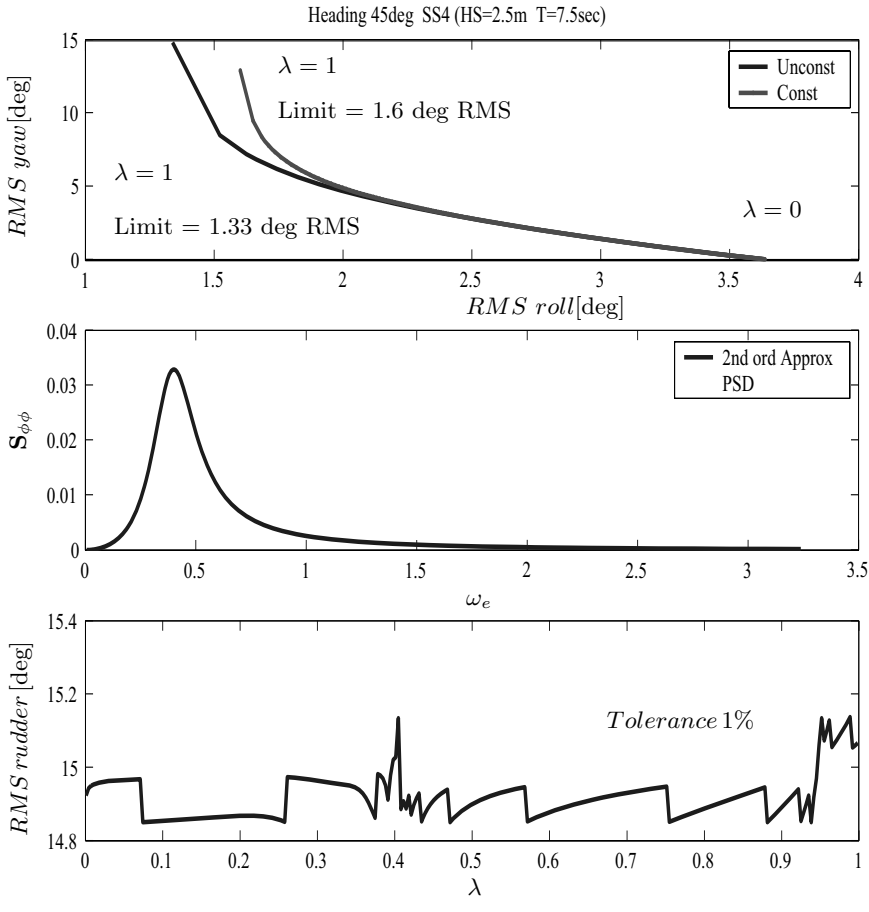

Fig. 9.4. Limiting optimal trade-off roll (deg RMS) vs yaw (deg RMS) for a rudder based stabiliser. ITTC spectrum (Hs =2.5m, T=7.5sec) and vessel sailing at 15kts in quartering seas $\chi = 45deg$.

system—the understanding of these issues is believed to be essential for designing a good control strategy. If one knows the plant well, then it is simple to chose the appropriate control strategy and perform the tuning of the controller.

Using simple models, it was shown that both the dynamics of the ship and the constraints on the control action play different roles under different conditions, and that it is difficult, in general, to predict the overall performance based on the results of only some sailing conditions.

The main aim of this part was to provide the designer with insight on how the different aspects of the problem relate. As a result of this, we have also presented a simple method that can be used to obtain an indication of the

potential roll reduction to be expected—provided a simple linear model of the ship and disturbances are available.

Part IV

Control System Design for Autopilot with Rudder Roll Stabilisation and Fin Stabilisers

10

Previous Research in Control of Rudder Roll Stabilisation and Fin Stabilisers

This chapter presents a modest review and a discussion of *some* of the previous research in control system design for RRS, fin and combined rudder-fin stabilisers. The review is organised in chronological order and separated according to the problem being addressed: rudder stabiliser and fin-rudder stabiliser.

10.1 Rudder Roll Stabilisation in the 1970s

As mentioned in Section 6.4, it is believed that the idea of using the rudder as a stabilisation device emerged from observations of unusual ship roll behavior under autopilot operation. Taggart [215] reported one example observed during a winter Trans Atlantic voyage of a high-speed container ship in 1967. During this trip the characteristics of the autopilot were tested under different conditions, and it was observed that under certain circumstances, the rudder induced significant roll motion. Taggart planned to test the idea of using the rudder for simultaneous course keeping and roll reduction during the following summer crossing, but his attempt was frustrated by calm seas. Motivated by these observations, van Gunsteren performed full-scale trials using a rudder as a stabiliser in 1972 aboard the motor yacht *M.S. Peggy* in The Netherlands [229]. The controller used was proportional to roll rate and also to yaw angle and rate. During the trials, a roll reduction of 43% DSA[1] was obtained.

In 1972, Cowley and Lambert [54] presented a study of rudder roll stabilisation. They used an analog computer model and a scale model of a fast container ship to test the hypothesis that a rudder could be used as a stabilising device. The controller used consisted of an autopilot and a roll feedback loop. The autopilot was a phase-lead compensator designed without considering the effect of roll motion. The roll loop was added after the autopilot was

[1] Double significant amplitude, *i.e.* 2 $\phi_{1/3}$, where $\phi_{1/3}$ is the average of the largest one-third roll amplitudes.

designed; this consisted of a simple gain feedback loop. Roll angle was used as a feedback signal, but this produced large changes in the heading response at low frequencies; the use of roll rate gave better results. In the scale-model tests, the model was constrained in yaw and sway, and a moving weight was used to simulate an irregular beam sea. The roll reductions obtained were of 20 and 30% DSA. The continuation of this work was reported by Cowley [53] in 1974. In this, a free-running scale model was used first, and then full-scale sea trials. Model tests in irregular quartering seas gave a roll reduction of 50% DSA. Sea trials on a container ship gave reductions of 20% in moderate seas. The results of further full scale trials were reported in 1975 by Cowley and Lambert [55]. The data were taken from seven Transatlantic voyages of a container ship fitted with a rudder stabilisation system. The average roll reduction was of 40% DSA.

Motivated by the results of Cowley and Lambert described above, and the recommendations made by Carley and Duberley [43] for an integrated rudder and fin control system to improve fin performance, the use of rudder stabilisers was further explored within the naval environment in the United Kingdom. The first of these results were reported by Carley [42] and Lloyd [139]. It would be fair to say that neither of them envisaged a successful application of RRS for navy vessels. Indeed, Carley provided the first feasibility analysis on the use of rudder as a stabiliser. This was a theoretical study based on models obtained from data of sea trials. In this study, he not only looked at the potential of the rudder to induce roll, but also the consequences for the steering characteristics of the vessel. The transfer functions from rudder to roll and to heading, $G_{\phi\alpha}(s)$ and $G_{\psi\alpha}(s)$, were estimated using system identification techniques, and the following type of controllers was used:

$$C_\psi(s) = K_1 \frac{1 + aT_1 s}{1 + T_1 s} + \frac{1}{T_3 s}, \qquad C_\phi(s) = K_2 \frac{s(1 + T_1 s)}{s^2 + 2\xi\omega_\phi s + \omega_\phi^2},$$

where ω_ϕ in the roll controller is the natural roll frequency of the vessel and the last term of the heading controller (autopilot) is an optional weather-helm term.

Using the above controllers, Carley investigated issues related to the stability of the closed-loop system and the coupling between roll and heading and frequencies at which roll reduction could be achieved. This was done using the sensitivity transfer functions $S_{\psi\phi}(s) = \psi(s)/d_\phi(s)$ and $S_{\phi\psi}(s) = \phi(s)/d_\psi(s)$—see Section 8.5.1. This study recognised the limitation imposed on the control system design due to the non-minimum phase characteristics of the rudder-to-roll response with the possibility of roll amplification at low encounter frequencies, and the trade-off between roll reduction and heading interference.

Lloyd [139] presented data from trials of a frigate, which show that forced roll induced by rudders (in calm water) is similar in magnitude to that induced by fins. He also presented a mathematical model, and simulation results for rudder stabilisation that compared the roll power spectral densities for the stabilised and unstabilised ship. The controllers used were similar to those

used by Carley, as shown above. The highest roll reduction obtained was 40%, and this was for a simulated sailing condition of 60 deg encounter angle (quartering seas). The work was concluded with remarks similar to those made by Carley regarding the limitations due to the roll amplification at low frequencies. Lloyd also made the important observation that a RRS may result in broach-to conditions.

The research on RRS in US also started in the mid 1970s. In 1974, the David Taylor Naval Ship Research and Development Center (DTNSRDC) started investigations on the use of rudder stabilisers for the US Navy (USN). In 1975, it was concluded that not all the classes had the necessary rudder-induced roll moment necessary for achieving good performance [16]. At this time, US Coast Guard (USCG) *Hamilton* cutter class was undergoing trials to improve the helicopter-vessel interaction. These trials showed that roll stabilisation was an important factor in performance and safety of helicopter landing and take-off. Since anti-roll tanks and fin stabilisers were not an economically viable alternative, a joint USN-USCG RRS program was started in 1975.

Two prototype vessels from the USCG *Hamilton* class went for trials with a RRS in 1979. The results of these trials were reported in 1980 by Baitis [12] and in 1983 by Baitis *et al.*[16]. These trials went further with regards to the evaluation of ship performance under RRS; they assessed not only the roll reduction and heading interference, but also the increase in ship operability with different controllers. The roll reductions reported were between 31 and 49% for beam seas, about 22% in bow seas and 28% in quartering seas. The control scheme used a roll-rate gain loop which was added to the manual control provided by the helmsman. The addition of a roll-angle gain loop was also attempted and it proved to increase performance only in quartering seas. It was concluded that unless the controller could alter the loop signals used for feedback, it was best to use roll-rate feedback. This work also evaluated the limitations imposed by the rudder rate. Tests with the original rudder rate of 4.7 deg/s and a modified 21 deg/s were performed. It was shown that the limited authority of the rudder machinery, leading to the rudder inability to follow the commanded angle, provided significant degradation in performance; and hence, constrained control should be used. The comment was also made that adaptivity with respect to sailing conditions was desirable.

The above has been the literature most cited since the 1970s. It can be argued that the limited performance obtained in these works was the result of the simple control strategies used. As we shall see in the next section, the introduction of digital computers in the 1980s allowed tracking the problem using a multi-variable control framework and adaptation, with a significant improvement in performance. This was already envisaged, however, throughout the work reported in the 1970s.

10.2 Rudder Roll Stabilisation in the 1980s

During the 1980s, there was a significant contribution to the problem of RRS. Almost 25 years have passed, and still most of the citations made in the contemporary literature regarding RRS implementations refer to the work of the 1980s. This was the work of different research groups which targeted the development in different countries: The Netherlands, Denmark, Sweden and the USA.

Work in The Netherlands

One of the most significant contributions to the developments of RRS was done by Dutch researchers. This was the result of a cooperative project between Delft University and the Royal Netherlands Navy, which started in 1981. This research evolved from computer simulations, to scale-model trials and finally to full scale trials performed in 1983. Most of the work has been reported by van der Klugt in his doctoral thesis [228], and also by van Amerongen *et al.*[225].

The control design was made using LQG techniques without considering the limitations imposed by the actuators, and then the design was modified so as to deal with these nonlinearities. The state vector considered was $\mathbf{x} = [v', p, r, \phi, \psi]^{\mathrm{T}}$, where v' is the sway velocity due to the rudder action only.

Three methods were tested to avoid saturation of the steering machinery:

- Gain scheduling
- Automatic Gain Control (AGC)
- Adaptive criterion

The hill-climbing technique was used to compute the sets of gains for different frequencies and intensities of the wave-induced forces. These gain sets were then used in a gain scheduling control scheme. The characteristics of the disturbance were estimated using Kalman filters and this was used to change the gains. This control approach performed well in simulations, but its performance fell short of expectations during full-scale trials. In addition, it did not guarantee that saturation of the steering machinery would not occur.

The second method used AGC to limit the action demanded from the steering machinery. This AGC system would reduce the control command to ensure that saturation never occurs (the philosophy is similar to that of antiwind-up use in PID controllers). The main advantage of this is the prevention of phase lag induced by rate limitations, which could lead to closed-loop stability problems. Figure 10.1 shows a block diagram of the AGC proposed by van Amerongen *et al.* The output of the controller, α_c, is affected by a gain which is adjusted according to the commanded rate. The output of the AGC, α_d, is the demand to the steering machinery. When $|\dot{\alpha}_c|$ is larger than $\dot{\alpha}_{max}$, the gain is reduced and takes values less than 1. When the condition is reversed, the memory function brings the gain slowly back to 1—this reduces

the phase lag. Figure 10.2 shows a simulation result which compares the output of the steering machinery with and without AGC. The memory function reduces the phase lag to minimum, and the parameter $a < 1$ determines the rate of change of the gain.

Laudval and Fossen [131] proposed an improvement for the above AGC mechanism, which they called time-varying gain reduction (TGR). In this proposal, rather than reducing the values of the gain instantaneously when there is a difference between the maximum rate allowed and the current demanded rate, the gain is reduced when commanded action and delivered action are different. Also, the decision about gain reduction is taken based on the behaviour over a time interval. This produces a smoother variation of the gains, and better roll reduction in comparison to the AGC.

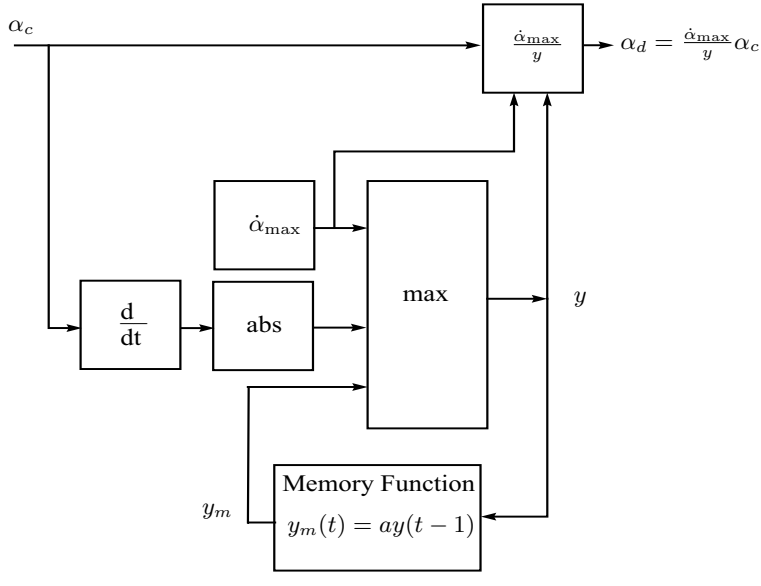

Fig. 10.1. Automatic gain control of Van Amerongen *et al.*[225] to avoid saturation of steering machinery.

The AGC action can be thought of as a reduction of all the feedback gains simultaneously, and thus it is not necessarily the best solution.

The final proposal of the Dutch group was an adaptive scheme to change the weighting coefficients in the cost function used for the LQG problem. By applying appropriate filtering, a frequency separation was obtained, and total rudder angle was separated into two components: $\alpha_c = \alpha_\phi + \alpha_\psi$. These two components were obtained by solving two LQG problems; *i.e.* the total cost was of the form

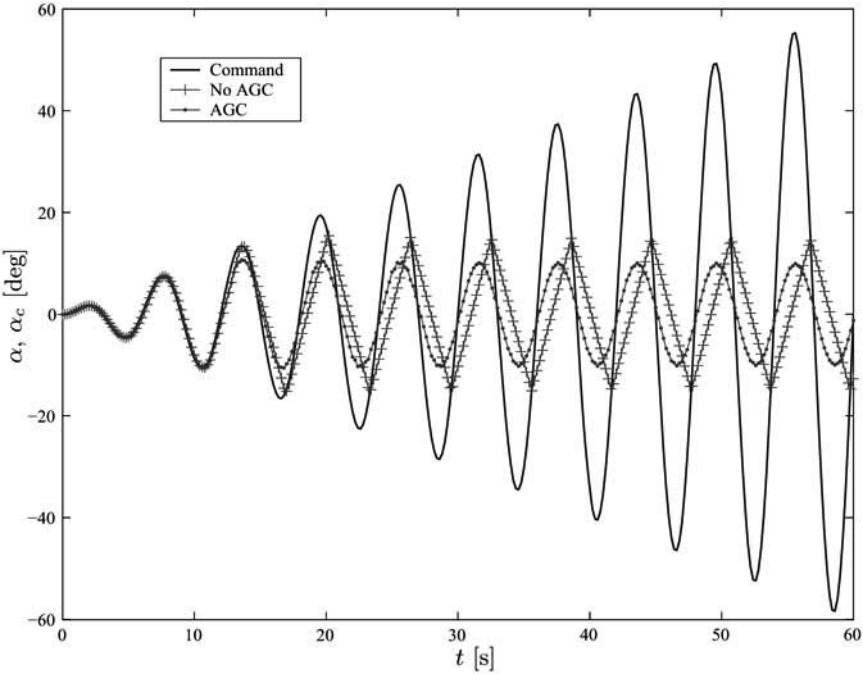

Fig. 10.2. Automatic gain control effect on rudder response to a linearly growing sinusoidal command of period 7 s.

$$J = \lambda_\phi J_\phi + J_\psi,$$

where

$$J_\phi = q_p \mathbf{var}[p] + q_\phi \mathbf{var}[\phi] + \mathbf{var}[\alpha_\phi],$$

and

$$J_\psi = q_\psi \mathbf{var}[\delta\psi] + \mathbf{var}[\alpha_\psi],$$

with the variances interpreted as

$$\mathbf{var}[y] = \mathbf{E}[y^2] \approx \lim_{T\to\infty} \frac{1}{T} \int_0^T y^2(t)\, dt.$$

The parameters q_i were fixed, and the parameter λ_ϕ, was adapted online based on speed, maximum rudder angle allowed, max rudder rate, max heading deviations, *etc.* This adaptation is done slowly, and once a new λ_ϕ is obtained, the Ricatti equations associated with the LQR problem are solved online using a state-space representation based on the innovations. The control law was of the of the form

$$\alpha_c = \mathbf{K}_\phi \cdot [v', p, \phi]^{\mathrm{T}} + \mathbf{K}_\psi \cdot [r, \delta\psi]^{\mathrm{T}}.$$

Full-scale trials with the gain scheduling scheme combined with the AGC gave roll reductions of up to 65% for conditions in which the encounter frequency was close to the roll natural frequency. However, at higher and low encounter frequencies, the performance deteriorated as expected—see Chapters 8 and 9.

Work in Denmark

The Royal Danish Navy introduced RRS on the SF300 vessels, which are relatively fast monohull patrol vessels. These vessels have three rudders and three propellers, and the two wing rudders are used for RRS. The development was a collaboration between the Navy and a private shipyard. The results of some tests were presented by Blanke *et al.*in 1989, [34].

The controllers were designed using LQG techniques considering a single multi-variable system. Investigation into the possibility of decoupling the roll from the yaw for control design led to the conclusion that this was not viable for these vessels. An adjustment was introduced for the operator to decide on roll reduction vs. heading interference. On the one extreme, the control objective was only to keep the course, while on the other, it was only to reduce the roll—similar to the approach used in our study performance limitations in Chapter 8, *cf.* (8.45).

It was noticed that when sailing at low speeds, the control command could saturate the steering machinery, leading to phase lags between the desired rudder angle and that achieved—which decreased the performance. To address this issue, an AGC mechanism was used. Regarding filtering, the yaw signal was filtered with a nonlinear high-gain observer to eliminate the wave frequency so only the low-frequency components were used as a heading feedback signal for the autopilot. For the roll angle and rate signals, the filtering was kept to a minimum to avoid delays which could affect the performance.

The performance reported during initial tests for moderate sea states was in the range of 50–60% for beam and quartering seas and between 35–40% for quartering seas. However, further work on these vessels was reported by Blanke *et al.*in 2000 [32], due to the lower performance recorded during operations. The SF300 is a multi-role naval vessel; and as such, significant variations in the loading conditions can be expected for the different missions performed by the vessel. This, in addition to a motion spectra different than those anticipated during the control system design, resulted in a performance lower than expected. Experience from data collected on operations in inner Danish waters showed that the wave spectra can have a significant spreading and more energy at low frequency than the idealised spectra commonly used for design in naval architecture—see Section 2.5. The controller design was then reassessed.

This time, the $\mathcal{H}_\infty$ approach was taken. The desired rudder angle was separated into two components $\alpha_d = \alpha_\phi + \alpha_\psi$, where

$$\alpha_\phi = k_r\, u_{rel} \frac{s^2 + 2\xi_z\omega_z s + \omega_z^2}{s^2 + 2\xi_p\omega_p s + \omega_p^2}(\tau_p p(s) + \tilde{\phi}(s)),$$

where $\tilde{\phi}$ was the high-pass filtered roll angle. The autopilot control was nonlinear with appropriate gain scheduling according to the speed of the vessel and the thrust of the propulsion devices:

$$\alpha_\psi = f(r, \delta\psi, u),$$

see [32] for further details.

The control design objective was to achieve 50% reduction in most sailing conditions and for the speed envelope of the operations performed by the vessels. Because of the widely varying conditions, the controller could be switched manually according to the wave period estimated by the operator: 8 s, 10 s, 12 s and 15 s. A sketch of the roll sensitivity functions is shown in Figure 10.3.

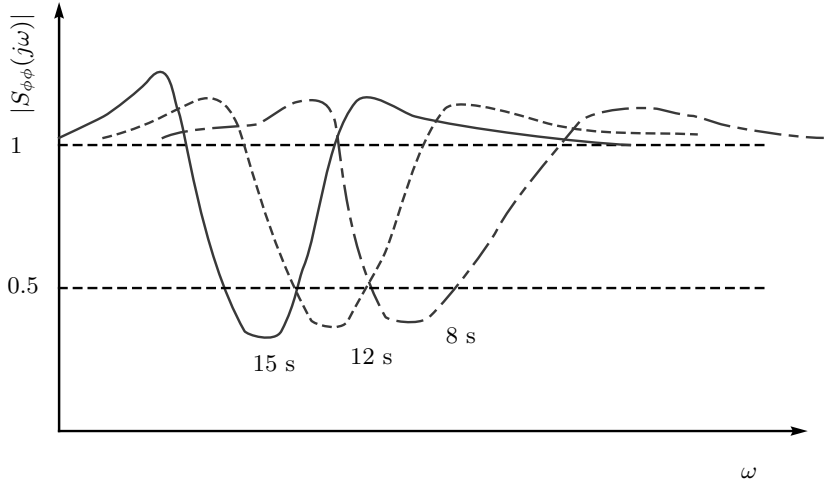

Fig. 10.3. Sketch of sensitivity functions of selective controllers switched according to the prevailing wave period. Blanke *et al.*—see [32].

If the wave period exceeded 20 s, the stabiliser was switched off—in these conditions, the roll reduction *vs.* heading interference was too big for this particular ship. A self-tuning procedure was also used to determine the location of the complex poles of the roll controller. This auto-tuning was run in calm water.

Work in Sweden

Källström *et al.*[120], reported the implementation of RRS on ships of the Royal Swedish Navy (RSN). The system evolved into a commercial product

called ROLL-NIX. This system was designed for use on straight courses; it switched off automatically when major manoeuvring was required, and back on when the vessel resumed a steady course. This ensured no interference with manoeuvring in situations requiring rapid course changes.

The control algorithm was based on LQG, and incorporated adaptation mechanisms to cope with different weather conditions. During 1987, two types of vessels from the RSN were fitted with ROLL-NIX. These were a fast attack craft (35 m long, 170 m^3 of displacement) and mine layers (100 m long, 3300 m^3). The performance of the attack craft was in the range of 45–60% for beam and quartering seas in weather conditions of 4, 5 and 6 Beaufort scale at a speed of 27 kt. The results on the mine layer *HMS Carlskrona* was in the range of 40–45% for beam and quartering seas in weather conditions of 4 Beaufort scale at the speed of 16 kt.

Work the USA

As already mentioned, the work on RRS in the USA started during the 1970s, and the first generation of analog controllers gave roll reduction in the range of 30–40% for the coast-guard WECH *Hamilton* class cutters—see [16]. A second generation of digital controllers was introduced in 1987, and gave performances of up to 70% of roll reduction using a modified steering machinery system [15]. From 1977 to 1986, the only vessels operating with RRS in the USA were the coast-guard cutters. After this, the US Navy renewed its interest in RRS and tests were extended in destroyers; some results were reported by Baitis and Schmidt in 1989 [15]. The signal from the rudder stabiliser controller was added to the signal generated by the autopilot or by manual steering. Roll reductions of 40% RMS were obtained for the destroyers. From the results obtained with these vessels, it was concluded that a good rule of thumb is that 40% of roll reduction could allow the vessel to sustain the operational capacity at one sea state higher—see [15]. The use of RRS within the US Navy has grown since and nowadays several classes are equipped with these systems—see [244].

10.3 Rudder Roll Stabilisation in the 1990s

During the 1990s, there was significant research activity on the theoretical aspects of the problem. In particular, the robustness properties of the controller and adaptive techniques gained much attention. Several different control techniques were proposed, but only a few full-scale implementations were reported.

Blanke and Christensen [33] studied the sensitivity of the performance of LQ control to variations in the coupling coefficients of the equations of motion. They used a linear model based on the hydrodynamic data estimated during the design stage of the SF300 vessels—this is the model presented

in Section 4.3.4. Using a simple multi-variable LQ controller, they defined a nominal design, and analysed the changes in performance due to changes in the following parameters of the model: U—speed; K_p—roll moment due to roll rate; N_p—yaw moment due to roll rate; and VCG—vertical centre of gravity. It was found that small changes in these parameters can modify the dynamic response of a vessel significantly. Further work based on sea trials of sister ships with modifications in the appendages and different load conditions was reported by Blanke in 1996 [31]. It was found that the influence of the linear roll damping coefficient N_p was quite significant—and this parameter changed with the location of the bilge keels. In this work, a model for structured uncertainty was also proposed.

Källström and Schultz [117], and Källström *et al.*[150], described further the merits of ROLL-NIX and its adaptive properties. In these works, it was mentioned that a prediction mechanism is used in ROLL-NIX to produce a rudder action based on predictions of the roll angle, and that this improves the roll reduction significantly—unfortunately, there is not much detail available on the actual control strategy because of commercial issues. Zhow *et al.*[242], proposed the use of recursive prediction error methods to identify the rudder to motion response and combine this with an LQG controller. Katebi *et al.*[122], also proposed the use of LQG. Hearns and Blanke [100, 101] proposed the use of Quantitative Feedback Theory to design cascade SISO controllers for roll and yaw which targeted the problem of uncertainty in the model. Stoustrup *et al.*[214, 205] specified the control system requirements in the frequency domain, and adopted $\mathcal{H}_\infty$ optimisation. They compared the performance of $\mathcal{H}_\infty$ controller with that of an LQ controller, and found that for the former, the roll angle amplification at low frequencies is less than that for the LQ controller. Yang and Blanke, [240] incorporated the uncertainty models—proposed by Blanke in [31]—into the robust control design framework, and used μ-synthesis. Laudval and Fossen [130] took the nonlinear approach and proposed the use of sliding mode control. This is, perhaps, the only reference in the literature that uses a nonlinear model for the design. The main reason for the adoption of linear models is that RRS is mostly used in course-keeping operations, and thus, only small deviations from the steady-state course should be expected.

A stochastic approach based on autoregressive models was proposed by Oda, *et al.*[167, 164], and Sasaki *et al.*[196]. Full-scale implementations were reported by Oda *et al.*[165, 166]. A multi-variable autoregressive model was first identified from data collected in calm water, and then an LQ optimal control problem was solved to obtain the control gains. The modelling and control design of this approach fall into the framework of Generalised Predictive Control (GPC), which can be reduced to a LQG problem—see [29]. In order to avoid the saturation of the steering machinery, the cost function minimised included a term that penalised the rate of rudder motion.

10.4 Rudder Roll Stabilisation from 2000 to 2004

Blanke *et al.*[32], presented the continuation of work on the SF300 vessels, which used different controllers manually switched according to the wave period observed by the operator. This allowed the control system to cope with sea spectra that are broader and have more low-frequency content than those normally used in preliminary control and ship design—more comments on this work were made in Section 10.2.

Perez, *et al.*[179], proposed the use of constrained model predictive control (MPC) as a natural extension for the successful implementations reported in the 1980s [228, 225, 34]. In this approach, the constraints on the magnitude and rate of the rudder are incorporated *ab initio* into the design, while the benefits of quadratic cost (LQ control) that captures the performance of the system in terms of the variances of roll, yaw and rudder angle is preserved. The proposed method also used an optimal predictor—a shaping filter which represents the wave induced roll model. This filter is used to predict future roll angles and roll rates, and can be thought of as a feed-forward mechanism—thus, the control action is decided upon current and future (predicted) values of the disturbance. In [179], the parameters of the predictor filter were assumed known, but this assumption was removed in [178], where a quasi-adaptive method was proposed. With this method the estimation of the parameters of the predictor is performed in open loop before switching the controller on—a quasi-adaptive strategy. This extension allows the control strategy to be adaptive with respect to changes in the sea state, and sailing conditions (speed and heading). A shortcoming of this approach, however, is that it requires opening the loop to re-estimate the parameters of the wave-induced roll model. This method will be presented and extended to avoid the mentioned problem in Chapter 12.

Tzeng *et al.*[221], proposed the use of Internal Model Control—see, for example, [89]. In this approach, the shape of a desired roll sensitivity transfer function is selected, and then this is approximated by designing a controller using the Youla parameterisation of all stabilising controllers—see, for example, [89]. The design of roll and heading controllers was done independently, and the control commands were added together. To avoid saturating the steering machinery, an anti-windup scheme was used to reduce the output of the controller if there is a difference between the the rudder command and the actual rudder angle—the philosophy is similar to that of the AGC scheme proposed in [228, 225, 131].

In conventional autopilot design, the measured yaw angle and yaw rate are filtered to remove the wave-frequency components and leave only the low-frequency content for use as feedback signal for the autopilot to generate corrections—we will further discuss this in Section 12.6. This way, losses in terms of resistance and wear of the actuator are minimised because the autopilot does not correct the heading at every single wave [30]. Nicolau and Ceanga [161], proposed a roll damping system that uses only raw measurements of yaw

angle for the autopilot, and corrects the rudder command generated such that those commands that tend to increase the roll are eliminated. The system has a fuzzy analyser that, according to certain rules, modifies the command generated by the autopilot based on measurements of roll angle and roll rate. The roll reductions reported were about 15%.

10.5 Work on Fin and Combined Rudder and Fin Stabiliser Control

From the control system design point of view, the problem of control of fin stabilisers is relatively simpler than that of rudders stabilisers. The main reason for this is that the design can be performed by decoupling the roll from the other equations of motion; and, in general, the non-minimum phase dynamics do not affect the design—NMP dynamics appear only if the fins are located aft from LCG, see Section 8.7.

Because of this, classical PID and $\mathcal{H}_\infty$ types of controllers usually perform well [104, 103, 105, 102, 123], and most of the early literature on fin stabilisation focused strongly on the hydrodynamic aspects of the fins, fin size and location rather than control design [4, 52, 138, 14, 140, 59]. This research continues to date due to tendency of fins to develop dynamic stall conditions in moderate to severe sea states [80]. This latter work has motivated the control strategy proposed in Chapter 13.

As mentioned above, the traditional approach for the design of fin stabilisers consists of using the decoupled roll motion equations. Despite this, Carley and Duberley, [43], observed in 1972 that the cross-coupling between roll, sway and yaw often reduces the performance of the fins, and therefore if the system as a whole is to operate optimally, and integrated control for rudder and fin should be considered. This way, the autopilot action does not counteract the action of the fins with regards to roll. This together with the developments of RRS has motivated a wealth of research into the combined rudder-fin stabilisation.

The work on control of combined fin-rudder stabilisers has reported the use of PID controllers [102, 56, 219, 57], LQG controllers [119, 202] and H_∞ [95, 206, 205, 207, 191, 57, 219]. Tzeng and Wu, [222], however, proposed the use of internal model control based on the decoupled roll model. Perez and Goodwin [175, 178], proposed the use of constrained MPC as a natular extension of their work on RRS. This work reviewed in Chapter 13.

10.6 Main Issues Reported in Previous Work

From the review provided in this chapter, it follows that the main issues subject to research interest since the first implementations were reported are the following:

- Mechanisms to deal with input constraints,
- Adaptive methods to address changing in the sea states,
- Robustness issues regarding changes in ship dynamic response due to speed and load variations.

In the final chapters of this book, we propose a solution that addresses most of these issues in a unified framework. Indeed, our proposal allows one to incorporate input and output or state constraints. We also use an adaptive method to update the part of the controller which uses a disturbance model according to the sea state and sailing conditions. Robust and adaptive design to address changes in the ship dynamic behaviour due to speed and load condition changes can be addressed in a gain scheduling like formulation. The Next chapter provides the background material for the development of the proposed solution.

11

Constrained Control via Optimisation

When the performance of a controlled physical system is to be maximised, dealing with actuator saturation and, perhaps, constraint violation often becomes unavoidable. As introduced in Chapter 9 (Section 9.1), actuator saturation occurs when the actuator fails to deliver the commanded action, *i.e.* when the control action differs from the control command. This effect appears when the control strategy does not contemplate the fact that actuators have limited authority, and the consequences are, in general, a degradation of the closed-loop performance, a reduction of the lifespan of the actuator and, in some cases, stability problems. For example, in the case of RRS, if we look at the effect of rate constraints imposed by the rudder machinery on the rudder angle shown in Figure 5.13, it follows that the peaks of rudder angle could be significantly delayed with respect to the peaks of the commanded angle. This can cause the rudder moment to be more in phase with the motion rather than out of phase, and thus create stability problems—roll amplification, rather than reduction.

Apart from actuator saturation, most controlled systems are required to operate at the limits of their capabilities so as to maximise performance. This is reflected in specifications that require quantities of the system (states, inputs, outputs or combinations of these) to be within certain limits, and often as close as possible to those limits. If all these limits are to be satisfied, then the control command typically needs to be constrained: a *constrained control strategy* should be applied. Constrained control has a long history in practice [22] and it has gained a great deal of attention from the research community during the past three decades [147, 109, 141].

This chapter provides an introduction to the topic of constrained control. In particular, we will concentrate on model predictive control (MPC) strategies. It could be inferred from the development of the book thus far, that we are ultimately aiming at formulating a constrained control problem within a stochastic framework.

11.1 Constraint Classification

Constraints, in the context of this chapter, are expressed in terms of *limits* on the magnitude of the quantities and signals involved in the control system and/or their time derivatives or time differences. Within this framework, we can first classify constraints into two groups: *hard* and *soft* . Hard constraints are those limits imposed by either physical characteristics of the system to be controlled or safety reasons. Hence, hard constraints must never be exceeded. Soft constraints, on the other hand, may be exceeded, temporarily, without any consequences other than poor performance.

A second classification of constraints refers to what type of quantity or signal in the system is constrained. If constraints are imposed so as not to saturate the actuators, the constraints are normally called *input constraints*. If the constraints are imposed on a state or output variables, the constraints are called *state* or *output constraints* respectively.

11.2 Different Approaches to Constrained Control Problems

The strategies to deal with constrained control problems can be broadly classified into four categories, which we call [91]:

- Serendipitous,
- Cautious,
- Remedial,
- Tactical.

In the *serendipitous* case, large control action is allowed despite the constraints and operative conditions near and/or on the constraints. This strategy simply ignores the constraints in the design; perhaps because operating conditions near or on the constraints are seldom encountered, or because these situations do not degrade the performance—a rather exceptional situation.

In the *cautious* case, the control action is reduced such that situations in which the system operates close to the constraints are always avoided. This implies that the design can be considered in a linear framework. The price to be paid for this is, often, poor performance for not exploiting the full potential of the control action. An example of this approach can be the control strategy presented by Oda *et al.*[165, 166] in which a high weighting is used to penalise the control in the cost of the associated optimal control problem to ensure that saturation does not occur. Another example is the use of the IVC technique presented in Chapter 9 to design LQG controllers, in which the problem can be formulated such that saturation occurs with a certain (low) probability.

In the *remedial* case, the design is initially performed without considering the constraints, and usually within a linear framework. Then, special features are added to ensure that the constraint requirements are met. Examples of

these strategies are AGC—(automatic gain control) and the classic methods of anti-wind-up. The latter strategies have long been used in practice due to their simplicity [22, 125, 61, 171].

Finally, in the *tactical* case, the constraints are included into the control design *ab initio*, and operating conditions on, or near, the constraints are contemplated. As a consequence, these strategies generally accomplish the best performance and yield very profitable results. The most widely adopted of these strategies are the, so-called, model predictive control (MPC) or model-based predictive control strategies.

In the sequel, we will discuss the underlying ideas of MPC and its heuristics. This strategy results from a special implementation of the solution of a discrete-time sequential-decision problem. We will henceforth focus on discrete-time problems.

11.3 Finite-horizon Sequential-decision Problems

Sequential-decision problems are characterised by three elements: a *dynamic system*, *a set of constraints* and a *cost* to be minimised [24]. A general form for the *dynamic system* can be represented by

$$\mathbf{x}_{k+1} = \mathbf{f}(\mathbf{x}_k, \mathbf{u}_k). \tag{11.1}$$

The variable $\mathbf{x}_k$ is the value of the state at the instant t_k. The variable $\mathbf{u}_k$ is the control action at the instant t_k. The control here is the *decision variable* to be selected at the time or stage k. Finally, the function $f(\cdot, \cdot)$ specifies the transition or evolution of the system under the decisions made at the different stages.

The *set of constraints* is usually specified by the two sets in which the state and the control should take values:

$$\mathbf{x}_k \in \mathcal{X}_k \qquad \mathbf{u}_k \in \mathcal{U}_k. \tag{11.2}$$

The *cost* is a mathematical expression that characterises deviations from the desired performance or a desired outcome; and hence, should be minimised. Further, the cost is assumed to be additive in the sense that the cost incurred at stage k is $g_k(\mathbf{x}_k, \mathbf{u}_k)$, and it accumulates over future stages, *i.e.* the total cost is of the form

$$g_T(\mathbf{x}_N) + \sum_{k=0}^{N-1} g_k(\mathbf{x}_k, \mathbf{u}_k), \tag{11.3}$$

where $g_T(\mathbf{x}_N)$ is a terminal cost incurred at the end of the optimisation horizon N.

The optimisation is performed over the control moves $\mathbf{u}_0, \ldots, \mathbf{u}_{N-1}$, and each of these control moves is selected with knowledge of the state $\mathbf{x}_k$ (as we shall see this can be relaxed). In this class of problems, decisions must

be made at several stages—the present stage, $k = i$ for $i \in \{0, \ldots, N-1\}$ and future stages, $k = N-i, \ldots, N$. Consequently, if the total cost is to be minimised, then one must balance the desire of minimising the cost associated with the current decision against the desire to avoid high costs in the future [25].

There are two alternatives to solve the class of problems described above [26]:

1. Open loop,
2. Closed loop.

In the open-loop minimisation, all the control values or control moves are selected at once at the initial stage $k = 0$, *i.e.* the solution is of the form

$$\mathbf{U}^{\mathrm{OPT}} = \{\mathbf{u}_0^{\mathrm{OPT}}, \ldots, \mathbf{u}_{N-1}^{\mathrm{OPT}}\}.$$

The closed-loop minimisation, by contrast, seeks the optimal control policy (a sequence of functions)

$$\boldsymbol{\Pi}_N^{\mathrm{OPT}} = \{\boldsymbol{\pi}_0^{\mathrm{OPT}}(\cdot), \ldots, \boldsymbol{\pi}_{N-1}^{\mathrm{OPT}}(\cdot)\},$$

such that $\mathbf{u}_k = \boldsymbol{\pi}_k^{\mathrm{OPT}}(\mathbf{x}_k)$ for each possible value of $\mathbf{x}_k$.

For deterministic problems with state measurements (complete state information), the above two options lead to the same values of the optimal controls; their implementation, however, is different. The preference for implementing one method or the other may depend on different factors that we will comment on later in Section 11.7. When uncertainty is present, however, the difference between the two approaches may be significant. This is because the information contributed by the measurements up to the stage k can be used to determine the control action at this stage [26, 24].

11.4 Infinite Horizons and Receding-horizon Implementation

To solve practical problems which require control over a long period of time, one would have to consider a sequential-decision optimal control problem over an infinitely long future horizon. In these cases and for the problem considered here, the only viable option is to search for the optimal control policy rather than the sequence of control values. As it occurs, whenever this problem has a solution, the elements (functions) of the optimal policy are all the same (stationary policy). One particular example is the case of unconstrained linear systems with quadratic cost—known as LQR control.

For a more general class of problems, however, the solution may not be easy to find. An approach to deal with these problems, in an approximate manner, is to consider a finite-horizon problem and implement a *Receding-Horizon* (RH) feedback strategy based on the solution of the finite-horizon problem.

This type of solution can be implemented in two different ways depending on the approach used to solve the associated finite-horizon problem. Indeed, one way of implementing a RH solution is to obtain the control policy $\mathbf{\Pi}_N^{\text{OPT}}$ solution for a finite-horizon problem and then use the first element of the solution sequence as feedback control law, *i.e.*

$$\mathbf{u}_k = \boldsymbol{\mathcal{K}}_N(\mathbf{x}_k) = \boldsymbol{\pi}_0^{\text{OPT}}(\mathbf{x}_k), \qquad \text{for} \quad k = 0, 1, \ldots$$

We will refer to this implementation as *the explicit RH implementation*. The subscript N indicates that the control law has been obtained by solving a problem of horizon N. In this case, the feedback control law implemented, $\mathcal{K}_N(\cdot)$, takes into account N future actions from the current stage, and it is implicitly assumed that the influence of the actual decision on those beyond N future stages is summarised by an appropriately chosen terminal cost. Therefore, by using a large horizon for the associated finite-horizon problem one can hope to obtain a reasonable approximation to an infinite-horizon problem. For further details about RH control and also for the continuous time formulation, see, for example, [47] and references therein.

The other alternative for the implementation would be to select the sequence of control values that solves an open-loop minimisation based on the current information, and apply the first control move to the plant. Then, repeat the optimisation once new information is available (measurements). This process continues indefinitely. In this case, the feedback control law $\boldsymbol{\mathcal{K}}_N(\cdot)$ is implicitly defined, *i.e.* only its value is known for the given value of the state $\mathbf{x}_k$. Thus, we will refer to this implementations as *the implicit RH implementation*.

The main difference between these two implementations is that the implicit case uses online optimization to evaluate a function $\boldsymbol{\mathcal{K}}_N(\cdot)$. The main advantage of the implicit RH-implementation is that it often can be used in problems for which the (offline) computation of the control policy is difficult or even impossible—constrained control problems, generally, fall into these kind of problems. This method, however, poses an implementation problem since the length of the horizon cannot be chosen arbitrarily large. This is limited by the computer power and sampling period requirements, *i.e.* large horizons are only viable provided the optimisation problem can be solved in time before the next control should be updated.

11.5 Model Predictive Control

To date, the heuristics of model predictive control used in most practical applications consist of an implicit RH implementation of the solution of a finite-horizon open-loop sequential-decision problem. However, in some cases, the explicit receding horizon implementation can be used; this is the case of constrained LQ-control—See comments in Section 11.7.

The most important feature of MPC is its ability to handle multi-variable constrained control problems with different types of constraints for which offline computations of a control law are in general impossible to obtain. Because of this, MPC has become an indispensable tool in industrial control engineering and the method of choice for advanced control applications [141]. Numerous surveys about MPC have appeared in the literature—see, for example, [49, 81, 154, 183, 147, 141].

The key elements of an MPC algorithm (in a deterministic framework) can be summarised as follows:

- A model for *predicting* the future response of the system over a prediction horizon N (number of samples or sample periods) given the initial state $\mathbf{x}_0 = \mathbf{x}$
$$\mathbf{x}_{k+1} = \mathbf{f}(\mathbf{x}_k, \mathbf{u}_k) \qquad \text{for} \quad k = 0, \ldots, N-1.$$
- Sets of state and input constraints
$$\mathbf{x}_k \in \mathcal{X}_k \qquad \mathbf{u}_k \in \mathcal{U}_k.$$
- A cost function
$$g_T(\mathbf{x}_N) + \sum_{k=0}^{N-1} g(\mathbf{x}_k, \mathbf{u}_k).$$
- An algorithm for solving, online, the associated optimal problem of minimising the cost subject to the constraints and obtain the sequence of control moves[1].
$$\mathbf{U}^{\text{OPT}} = \{\mathbf{u}_0^{\text{OPT}}, \ldots, \mathbf{u}_{N-1}^{\text{OPT}}\}.$$

With all the above ingredients, the following steps are envisaged to calculate the control at each stage k (sampling instant) for the RH implementation:

1. Measure the state $\mathbf{x}_k$ of the system, and use this state to initialise the open-loop optimisation problem: $\mathbf{x}_0 = \mathbf{x}_k$.
2. Solve the open-loop finite-horizon optimisation problem using $\mathbf{x}_0$ to obtain
$$\mathbf{U}^{\text{OPT}} = \{\mathbf{u}_0^{\text{OPT}}, \ldots, \mathbf{u}_{N-1}^{\text{OPT}}\}.$$
3. Apply the first element of the control sequence as the current control action $\mathbf{u}_k = \mathbf{u}_0^{\text{OPT}}$.

The above steps are then repeated indefinitely at all subsequent stages (sampling instants).

[1] In this book, we assume that the controlled system and its model are time invariant. Therefore, at each stage, the optimisation problem can be considered starting from 0 and extending until $N-1$.

11.6 Constrained Linear Systems

As a model for the plant or system to be controlled, we consider the following discrete-time and time-invariant linear system, given in a state-space form

$$\mathbf{x}_{k+1} = \mathbf{A}\mathbf{x}_k + \mathbf{B}\mathbf{u}_k. \tag{11.4}$$

We assume that $\mathbf{x}_k \in \mathbb{R}^n$ is available to implement the control (perfect state information), and the control move $\mathbf{u}_k \in \mathcal{U} \subset \mathbb{R}^m$ for all k. The set $\mathcal{U}$ is a convex and compact set that represents the constraints on the input. We further assume that the pair $(\mathbf{A}, \mathbf{B})$ is stabilisable.

As already mentioned, most MPC strategies or algorithms solve the associated finite-horizon problem numerically at each sampling time. This procedure can be performed because of the deterministic nature of the problem. Indeed, given the initial state $\mathbf{x}_0 = \mathbf{x}$, the future states of the system up to N can be obtained as a function of the sequence of control moves $\mathbf{U}_N$ by projecting the Model (11.1) forwards in time. Using this, the problem is transformed into the problem of minimizing a quadratic function with respect to the sequence $\mathbf{U}_N$ subject to the constraints $\mathbf{u}_k \in \mathcal{U}$ on each element of $\mathbf{u}_k$ in the sequence $\mathbf{U}_N$. To show this we first need to define the finite-horizon problem utilized in this formulation.

Definition 11.1 (Finite-horizon Optimal Control Problem (Sequence Solution)). *Given an initial state $\mathbf{x}_0 = \mathbf{x}$, the problem considered is that of finding the optimal sequence of control values*

$$\mathbf{U}_N^{\mathrm{OPT}} = \{\mathbf{u}_0^{\mathrm{OPT}}, \mathbf{u}_1^{\mathrm{OPT}}, \ldots, \mathbf{u}_{N-1}^{\mathrm{OPT}}\}, \tag{11.5}$$

such that

$$\mathbf{U}_N^{\mathrm{OPT}} = \arg \min_{\mathbf{U}_N \in \overline{\mathbf{U}}_N} V_N(\mathbf{x}, \mathbf{U}_N); \tag{11.6}$$

subject to

$$\mathbf{x}_{k+1} = \mathbf{A}\mathbf{x}_k + \mathbf{B}\mathbf{u}_k, \quad \text{for} \quad k = 0, \ldots, N-1 \tag{11.7}$$

$$\mathbf{x}_0 = \mathbf{x}. \tag{11.8}$$

where $\overline{\mathbf{U}}_N$ denotes the set of all admissible N-sequences of control values in which $\mathbf{u}_i \in \mathcal{U}$ for $i = 0, \ldots, N-1$, and the scalar positive real value cost function V_N over a finite horizon N is given by

$$V_N(\mathbf{x}, \mathbf{U}_N) = g_T(\mathbf{x}_N) + \sum_{k=0}^{N-1} g(\mathbf{x}_k, \mathbf{u}_k)\,, \tag{11.9}$$

with

$$\begin{aligned} g_T(\mathbf{x}_N) &= \mathbf{x}_N^{\mathrm{T}} \mathbf{S} \mathbf{x}_N \\ g(\mathbf{x}_k, \mathbf{u}_k) &= \mathbf{x}_k^{\mathrm{T}} \mathbf{Q} \mathbf{x}_k + \mathbf{u}_k^{\mathrm{T}}(\mathbf{x}_k) \mathbf{R} \mathbf{u}_k(\mathbf{x}_k)\,, \end{aligned} \tag{11.10}$$

and $\mathbf{S}, \mathbf{R} > 0$, $\mathbf{Q} \geq 0$.

Further, the resulting ***optimal cost*** *is denoted by* $V_N^{\mathrm{OPT}}(\mathbf{x})$, i.e.

$$V_N^{\mathrm{OPT}}(\mathbf{x}) = \min_{\mathbf{U}_N \in \overline{\mathbf{U}}_N} V_N(\mathbf{x}, \mathbf{U}_N), \tag{11.11}$$

The solution of the above problem can be found as follows. By defining the vectors

$$\mathbf{X} = \begin{bmatrix} \mathbf{x}_1 \\ \mathbf{x}_2 \\ \vdots \\ \mathbf{x}_N \end{bmatrix} \quad \text{and} \quad \mathbf{U} = \begin{bmatrix} \mathbf{u}_0 \\ \mathbf{u}_1 \\ \vdots \\ \mathbf{u}_{N-1} \end{bmatrix}, \tag{11.12}$$

the response of the system over the horizon N can be expressed as a linear combination of the initial state $\mathbf{x}_0$ and the vector $\mathbf{U}$

$$\mathbf{X} = \boldsymbol{\mathcal{A}}\mathbf{x}_0 + \boldsymbol{\mathcal{B}}\mathbf{U}, \tag{11.13}$$

with

$$\boldsymbol{\mathcal{A}} = \begin{bmatrix} \mathbf{A} \\ \mathbf{A}^2 \\ \vdots \\ \mathbf{A}^N \end{bmatrix}, \qquad \boldsymbol{\mathcal{B}} = \begin{bmatrix} \mathbf{B} & \mathbf{0} & \cdots & \mathbf{0} \\ \mathbf{AB} & \mathbf{B} & \cdots & \mathbf{0} \\ \vdots & \vdots & \ddots & \vdots \\ \mathbf{A}^{N-1}\mathbf{B} & \mathbf{A}^{N-2}\mathbf{B} & \cdots & \mathbf{B} \end{bmatrix}. \tag{11.14}$$

The Cost (11.9) can then be expressed as

$$V_N(\mathbf{x}_0, U) = \mathbf{x}_0^{\mathrm{T}}\mathbf{Q}\mathbf{x}_0 + \mathbf{X}^{\mathrm{T}}\boldsymbol{\mathcal{Q}}\mathbf{X} + \mathbf{U}^{\mathrm{T}}\boldsymbol{\mathcal{R}}\mathbf{U}, \tag{11.15}$$

where

$$\boldsymbol{\mathcal{Q}} = \mathrm{diag}\{\mathbf{Q}, \ldots, \mathbf{Q}, \mathbf{S}\}, \tag{11.16}$$

$$\boldsymbol{\mathcal{R}} = \mathrm{diag}\{\mathbf{R}, \ldots, \mathbf{R}\}. \tag{11.17}$$

By substituting (11.13) into (11.15) we obtain

$$\boxed{V_N(\mathbf{x}_0, \mathbf{U}) = \mathbf{x}_0^{\mathrm{T}}\,\mathbf{Y}\,\mathbf{x}_0 + \frac{1}{2}\mathbf{U}^{\mathrm{T}}\,\mathbf{H}\,\mathbf{U} + \mathbf{U}^{\mathrm{T}}\,\mathbf{F}\,\mathbf{x}_0 \quad ,} \tag{11.18}$$

where

$$\mathbf{Y} = \mathbf{Q} + \boldsymbol{\mathcal{A}}^{\mathrm{T}}\,\boldsymbol{\mathcal{Q}}\,\boldsymbol{\mathcal{A}}, \tag{11.19}$$

$$\mathbf{H} = 2(\boldsymbol{\mathcal{R}} + \boldsymbol{\mathcal{B}}^{\mathrm{T}}\,\boldsymbol{\mathcal{Q}}\,\boldsymbol{\mathcal{B}}), \tag{11.20}$$

$$\mathbf{F} = 2\boldsymbol{\mathcal{A}}^{\mathrm{T}}\,\boldsymbol{\mathcal{Q}}\,\boldsymbol{\mathcal{B}}. \tag{11.21}$$

The different types of constraints on the inputs $\mathbf{u}_k$ and constraints on the some outputs, *e.g.* $\mathbf{y}_k = \mathbf{C}\mathbf{x}_k$, can be expressed as a linear inequality on $\mathbf{U}$. For example, consider the following input and output constraints:

$$\mathbf{u}_{\min} \leq \mathbf{u}_k \leq \mathbf{u}_{\max}; \quad k = 0, 1, \ldots, N-1 \tag{11.22}$$

$$\mathbf{y}_{\min} \leq \mathbf{y}_k \leq \mathbf{y}_{\max}; \quad k = 1, 2, \ldots, N-1 \tag{11.23}$$

$$\Delta\mathbf{u}_{\min} \leq \mathbf{u}_k - \mathbf{u}_{k-1} \leq \Delta\mathbf{u}_{\max}; \quad k = 0, 1, \ldots, N-1. \tag{11.24}$$

These can be taken into the following form

$$\boxed{\mathbf{LU} \leq \mathbf{M}.} \tag{11.25}$$

As an illustration for the single-input single-output case, $\mathbf{L}$ and $\mathbf{K}$ take the following form:

$$\mathbf{L} = \begin{bmatrix} \mathbf{I} \\ -\mathbf{I} \\ \mathbf{D} \\ -\mathbf{D} \\ \mathbf{W} \\ -\mathbf{W} \end{bmatrix} \quad \mathbf{K} = \begin{bmatrix} \overline{\mathbf{U}}_{\max} \\ \overline{\mathbf{U}}_{\min} \\ \overline{\mathbf{Y}}_{\max} \\ \overline{\mathbf{Y}}_{\min} \\ \overline{\mathbf{V}}_{\max} \\ \overline{\mathbf{V}}_{\min} \end{bmatrix} \tag{11.26}$$

where $\mathbf{I}$ is the $N \times N$ identity matrix and $\mathbf{W}$ is the following $N \times N$ matrix

$$\mathbf{W} = \begin{bmatrix} \mathbf{I} & \mathbf{0} & \cdots & \mathbf{0} \\ -\mathbf{I} & \mathbf{I} & & \mathbf{0} \\ \vdots & \ddots & \ddots & \vdots \\ \mathbf{0} & \cdots & -\mathbf{I} & \mathbf{I} \end{bmatrix}. \tag{11.27}$$

The matrix $\mathbf{D}$ is the following $N \times N$ matrix:

$$\mathbf{D} = \begin{bmatrix} \mathbf{CB} & \mathbf{0} & \cdots & \cdots & \mathbf{0} \\ \mathbf{CAB} & \mathbf{CB} & \cdots & \cdots & \mathbf{0} \\ \vdots & \ddots & \ddots & \ddots & \vdots \\ \mathbf{CA}^{N-1}\mathbf{B} & \cdots & \cdots & \mathbf{CAB} & \mathbf{CB} \end{bmatrix} \tag{11.28}$$

and

$$\overline{\mathbf{U}}_{\max} = \begin{bmatrix} \mathbf{u}_{\max} \\ \vdots \\ \mathbf{u}_{\max} \end{bmatrix} \qquad \overline{\mathbf{U}}_{\min} = \begin{bmatrix} -\mathbf{u}_{\min} \\ \vdots \\ -\mathbf{u}_{\min} \end{bmatrix} \tag{11.29}$$

$$\overline{\mathbf{V}}_{\max} = \begin{bmatrix} \mathbf{u}_{-1} + \Delta\mathbf{u}_{\max} \\ \Delta\mathbf{u}_{\max} \\ \vdots \\ \Delta\mathbf{u}_{\max} \end{bmatrix} \qquad \overline{\mathbf{V}}_{\min} = \begin{bmatrix} -\mathbf{u}_{-1} - \Delta\mathbf{u}_{\min} \\ -\Delta\mathbf{u}_{\min} \\ \vdots \\ -\Delta\mathbf{u}_{\min} \end{bmatrix} \tag{11.30}$$

$$\overline{\mathbf{Y}}_{\max} = \begin{bmatrix} \mathbf{y}_{\max} - \mathbf{CAx}_0 \\ \vdots \\ \vdots \\ \mathbf{y}_{\max} - \mathbf{CA}^{N-1}\mathbf{x}_0 \end{bmatrix} \qquad \overline{Y}_{\min} = \begin{bmatrix} -\mathbf{y}_{\min} + \mathbf{CAx}_0 \\ \vdots \\ \vdots \\ -\mathbf{y}_{\min} + \mathbf{CA}^{N-1}\mathbf{x}_0 \end{bmatrix} \tag{11.31}$$

and $\mathbf{u}_{\max}$, $\mathbf{u}_{\min}$, $\Delta\mathbf{u}_{\max}$, $\Delta\mathbf{u}_{\min}$, $\mathbf{y}_{\max}$, $\mathbf{y}_{\min}$ are the upper and lower limits on $\mathbf{u}_k$, $(\mathbf{u}_k - \mathbf{u}_{k-1})$ and $\mathbf{y}_k$ respectively.

The optimal solution is then given by the following quadratic programme (QP) [36, 27]:

$$\begin{aligned} \mathbf{U}^{\mathrm{OPT}} = \arg\min_{\mathbf{U}} \frac{1}{2}\mathbf{U}^{\mathrm{T}}\mathbf{H}\mathbf{U} + \mathbf{U}^{\mathrm{T}}\mathbf{F}\mathbf{x}_0 \\ \text{s.t.} \quad \mathbf{L}\mathbf{U} \leq \mathbf{M}. \end{aligned} \tag{11.32}$$

The formulation presented in this section for deterministic linear systems with quadratic costs and polytopic type of constraint sets results in a quadratic programme, and can be referred to as a QP-based MPC or QP-MPC. This is to distinguish it from other formulations of MPC in which the cost is modified such that it increases unboundedly when $\mathbf{U}$ approaches the constraints, and using this modified cost, an unconstrained minimisation is required. This formulation will not be considered here; however, the reader is referred to, for example, [141] and [239].

11.7 Explicit and Implicit Implementations of QP-MPC

To date, most practical implementations of MPC use the implicit RH, which requires solving the optimisation problem online. However, for MPC formulations resulting in a QP, the explicit solution is also available [21, 20, 113, 200]. In this case, the solution is piece-wise affine and defined over a partition of the state space:

$$\mathbf{u}_k^{\mathrm{OPT}} = \mathcal{K}_N(\mathbf{x}_k) = \begin{cases} \mathbf{G}_0\,\mathbf{x}_k + \mathbf{h}_0 & \text{if } \mathbf{x}_k \in \mathcal{X}_0, \\ \mathbf{G}_1\,\mathbf{x}_k + \mathbf{h}_1 & \text{if } \mathbf{x}_k \in \mathcal{X}_1, \\ \quad\vdots & \quad\vdots \\ \mathbf{G}_L\,\mathbf{x}_k + \mathbf{h}_L & \text{if } \mathbf{x}_k \in \mathcal{X}_L, \end{cases} \tag{11.33}$$

where L depends on the length of horizon N and the type of constraints being considered. This solution has contributed significantly to the understanding of the underlying structure of MPC for the class of problems considered.

In principle, it would seem that the explicit implementation requires less online computation because the control law is determined offline and the online part consists only of evaluating the correct expression. However, a look-up table mechanism needs to be implemented online to find in which region $\mathcal{X}_i$ $(i = 0, 1, \ldots, L)$ the measured state $\mathbf{x}_k$ is, and thus evaluate the correct expression in (11.33). The computational advantage of this over solving a QP online has not been yet established in general.

If online tuning is required or some type of adaptation is needed, the implicit implementation is preferred because the offline part of the explicit implementation $(\mathbf{G}_i, \mathbf{h}_i, \mathcal{X}_i)$ needs to be recomputed every time a part of the model, the parameters of the cost or the constraints change—and this may require a long time (with respect to the sampling period). In addition, the implicit implementation allows tightening the constraints online. Therefore, it provides a simple way to achieve control reconfiguration in the case faults. As discussed in [141], if, for example, one actuator fails, one could set the constraint of the signal associated with the failing actuator to zero and solve the optimisation problem with this new constraint.

Although the above argument seems to indicate that the implicit implementation is preferable, the benefits of the explicit implementation cannot be ruled out for some particular applications. For a further discussion see [91].

11.8 Stability of Model Predictive Control

An important property of any control law is whether closed-loop stability can be ensured. Because "optimality" does not, by itself, guarantee stability, the latter needs to be independently established [121] [193]. In this regard, it is interesting to note, however, that the absence of a formal proof of stability for MPC has not historically hindered its use in practical applications. Indeed, constrained MPC has been used in industry for more than three decades, yet formal proofs of stability have appeared only in recent times.

A great deal of the MPC literature has focused on establishing sufficient conditions for stability. This has evolved, essentially, into a number of different proposals for model predictive control, with their specific properties and ingredients to guarantee stability of the algorithms. Mayne *et al.*[147] and Mayne [148] have recently presented the state of the art in this area of on going research activity. These works distill the common ingredients that characterise the different forms of stability proofs for MPC reported in the literature.

In this section, we review the elements of the problem that allow one to establish stability of the RH implementation using the classical proof prototype [147].

A standard technique to analyse MPC stability, proposed originally in [47] and later generalised in [124], is to use the value function of the finite-horizon optimal control problem as a Lyapunov function for the closed-loop system.

The elements of the optimal control problem that affect closed-loop stability are:

- The terminal cost $g_T(\cdot)$.
- A terminal constraint set $\mathcal{X}_T$.
- A local stabilising controller $\boldsymbol{\mathcal{K}}_T(\mathbf{x})$ that gives positive invariance of $\mathcal{X}_T$, *i.e.* for any state $\mathbf{x}$ in $\mathcal{X}_T$, the successor state $\mathbf{x}^+ = \mathbf{f}(\mathbf{x}, \boldsymbol{\mathcal{K}}_T(\mathbf{x}))$ is also in $\mathcal{X}_T$.

It has been shown in [147] that the following conditions are sufficient for stability:

1. $\mathcal{X}_T$ is closed, $0 \in \mathcal{X}_T$ and $\mathcal{X}_T \subset \mathcal{X}$ (the state constraints $\mathcal{X}$ are satisfied in $\mathcal{X}_T$).
2. $\boldsymbol{\mathcal{K}}_T(\mathbf{x}) \in \mathcal{U}$ for all $\mathbf{x} \in \mathcal{X}_T$ (input constraints are satisfied in $\mathcal{X}_T$).
3. $g_T(\cdot)$ is a local Lyanpunov function for all $\mathbf{x} \in \mathcal{X}_T$.

How to arrive to these conditions is indicated in the following.

Consider the time-invariant discrete-time system $\mathbf{x}^+ = \mathbf{f}(\mathbf{x}, \mathbf{u})$, which satisfies $\mathbf{f}(0, 0) = 0$ with the associated cost

$$V_N(\mathbf{x}, \mathbf{U}) = g_T(\mathbf{x}_N) + \sum_{k=0}^{N-1} g(\mathbf{x}_k, \mathbf{u}_k), \tag{11.34}$$

where $g(\cdot, \cdot) \geq 0$. Under regularity assumptions, the value function $V_N^{\mathrm{OPT}}(\cdot) = \min_{\mathbf{U} \in \overline{\mathbf{U}}} V_N(\mathbf{x}, \mathbf{U})$ is positive definite and proper: $V_N^{\mathrm{OPT}}(\mathbf{x}) \to \infty$ when $\|\mathbf{x}\| \to \infty$. Therefore, it can be used as a Lyapunov function candidate.

Recall that at event k, the measurement of the state assumes a value, say $\mathbf{x}$, and then MPC solves for the sequence of control values

$$\mathbf{U}^{\mathrm{OPT}}(\mathbf{x}) = \{\mathbf{u}_0^{\mathrm{OPT}}(\mathbf{x}), \ldots, \mathbf{u}_{N-1}^{\mathrm{OPT}}(\mathbf{x})\}.$$

Let us assume that $\mathbf{x} \in \mathcal{X}_N$, where $\mathcal{X}_N$ is the set of all the states that can be steered to $\mathcal{X}_T$ by application of admissible control sequences of the form $\mathbf{U} = \{\mathbf{u}_0, \ldots, \mathbf{u}_{N-1}\}$. The MPC controller $\mathbf{u} = \boldsymbol{\mathcal{K}}_N(\mathbf{x}) = \mathbf{u}_0^{\mathrm{OPT}}(\mathbf{x})$ steers the initial state to the successor $\mathbf{x}^+ = \mathbf{f}(\mathbf{x}, \boldsymbol{\mathcal{K}}_N(\mathbf{x}))$. Now we seek a feasible, though not necessarily optimal, sequence $\mathbf{U}^*$, such that $V_N(\mathbf{x}^+, \mathbf{U}^*)$ is an upper bound for $V_N^{\mathrm{OPT}}(\mathbf{x}^+)$.

Since $\{\mathbf{u}_0^{\mathrm{OPT}}(\mathbf{x}), \ldots, \mathbf{u}_{N-1}^{\mathrm{OPT}}(\mathbf{x})\}$ is feasible, and the final state $\mathbf{x}_N$ obtained by application of such sequence lies in $\mathcal{X}_T$ (because $\mathbf{x} \in \mathcal{X}_N$), then the shortened sequence $\{\mathbf{u}_1^{\mathrm{OPT}}(\mathbf{x}), \ldots, \mathbf{u}_{N-1}^{\mathrm{OPT}}(\mathbf{x})\}$ would steer $\mathbf{x}^+$ to the same final state $\mathbf{x}_N \in \mathcal{X}_T$. If conditions 1 and 2 above are satisfied, then, the following is a feasible sequence for the problem starting at $\mathbf{x}^+$:

$$\mathbf{U}^* = \{\mathbf{u}_1^{\mathrm{OPT}}(\mathbf{x}), \ldots, \mathbf{u}_{N-1}^{\mathrm{OPT}}(\mathbf{x}), \boldsymbol{\mathcal{K}}_T(\mathbf{x}_N)\}.$$

Then, it follows that

$$\begin{aligned} V_N(\mathbf{x}^+, \mathbf{U}^*) = V_N^{\mathrm{OPT}}(\mathbf{x}) - g(\mathbf{x}, \boldsymbol{\mathcal{K}}_N(\mathbf{x})) \\ - g_T(x_N) + g(\mathbf{x}_N, \boldsymbol{\mathcal{K}}_T(\mathbf{x}_N)) + g_T(f(x_N, \boldsymbol{\mathcal{K}}_T(\mathbf{x}_N))). \end{aligned}$$

This cost, which is an upper bound of $V_N^{\mathrm{OPT}}(\mathbf{x}^+)$, satisfies

$$V_N^{\mathrm{OPT}}(\mathbf{x}^+) \leq V_N(\mathbf{x}^+, \mathbf{U}^*) \leq V_N^{\mathrm{OPT}}(\mathbf{x}) - g(\mathbf{x}, \mathcal{K}_N(\mathbf{x}))$$

provided that

$$g_T(f(x_N, \boldsymbol{\mathcal{K}}_T(\mathbf{x}_N))) - g_T(x_N) + g(\mathbf{x}_N, \boldsymbol{\mathcal{K}}_T(\mathbf{x}_N)) \leq 0 \forall \quad \mathbf{x} \in \mathcal{X}_T.$$

The latter yields the condition 3, and then stability follows from Luapunov arguments with domain of attraction $\mathcal{X}_N$:

$$V_N^{\text{OPT}}(\mathbf{x}^+) - V_N^{\text{OPT}}(\mathbf{x}) \leq -g(\mathbf{x}, \boldsymbol{\mathcal{K}}_N(\mathbf{x})).$$

For linear systems, the terminal cost function is typically chosen to be the value function of the infinite-horizon unconstrained optimal control problem (LQR), *i.e.* $g_T(\mathbf{x}) = \mathbf{x}^{\text{T}}\mathbf{S}\mathbf{x}$ where $\mathbf{S}$ is the solution of the associated algebraic Riccati equation; and the terminal constraint set is chosen to be the maximal output admissible set [85] for the closed-loop system using the control law $\boldsymbol{\mathcal{K}}_T(x) = -\mathbf{K}x$. The bigger the terminal set is, the easier it is to steer the state into that set. Recent results reported in [60] found a terminal set larger than the output admissible set, with a different choice for $\boldsymbol{\mathcal{K}}_T(x)$ which guarantees the stabilising properties of MPC.

Note that in the material presented in this section, it has been implicitly assumed that the model describes the behaviour of the plant perfectly. In practice, of course, the satisfaction of the above conditions does not necessarily guarantee stability: as stated by many authors including Mayne *et al.*[147], a framework to analyse robust stability is still a missing link in MPC. In addition, Wills [239] comments that, from observations of industrial experiments and simulations, the inclusion of a terminal constraint set can have undesirable effects on the dynamic behaviour of the control action. In contrast, the inclusion of a terminal cost term seems to have a beneficial effect on the closed-loop dynamics. For a further discussion on stability of MPC see [91].

11.9 Constrained Control of Uncertain Systems

When controlling physical systems, the constrained control problem often becomes more involved because of the presence of uncertainty. In this context, uncertainty can be classified according to three sources:

- Incomplete state information to implement the control (output feedback),
- Unmodelled dynamics,
- Disturbances.

In control problems for uncertain systems, there are predominantly two approaches to model uncertainty [24]: via a stochastic description or via a set-membership description. The stochastic approach describes uncertainty in terms of probability distributions associated with the uncertain quantities (disturbances, initial conditions, parameters, *etc.*). The alternative set-membership approach describes uncertainty only in terms of some information regarding the sets in which the uncertain quantities take values.

Within the framework of MPC, the set-membership description of uncertainty has been advocated in the literature—see, for example, [204, 132]. The

stochastic approach, however, fits more naturally into the class of problems described in this book.

Although there has been an effort to address the problem of constrained control of uncertain systems with a stochastic uncertainty description, it is still not fully resolved within the framework of MPC—see [173, 180]. When there is incomplete state information, an observer-based strategy that seems natural for control in the presence of stochastic disturbances is the one that uses the so-called *Certainty Equivalence* (CE) Principle. Specifically, CE consists of estimating the state and then using these estimates as if they were the true state in the control law that would result if the problem were formulated as a deterministic problem (no uncertainty). This strategy is motivated by the case of unconstrained control problems for linear systems with quadratic cost, for which CE is optimal [8, 26]. The use of CE in RH leads to certainty equivalent MPC (CE-MPC) and, due to its simplicity, this strategy has been advocated in the literature [154] and reported in a number of applications [6, 143].

Notwithstanding the widespread use of CE-MPC in different industrial applications, it must be stressed that CE-MPC generally results in a suboptimal control strategy. Two factors can be highlighted that render CE-MPC suboptimal: (1) the state estimate is assumed to be the true current state, and (2) the stochastic behaviour of the system is neglected over the prediction horizon.

CE-MPC, then, consists in estimating the state $\hat{\mathbf{x}}$, based on information of past inputs and outputs, and subsequently use this estimate as if it were the true state in formulation described in the previous section. This estimate is often obtained from a Kalman Filter algorithm, see Appendix A. The steps to find the control then reduce to the following:

1. Obtain the estimate of the state $\hat{\mathbf{x}}_k$ of the system using the measurement $\mathbf{y}_k$ and the past control move $\mathbf{u}_{k-1}$, and use this estimate to initialise the open-loop optimisation problem: $\mathbf{x}_0 = \hat{\mathbf{x}}_k$.
2. Solve the open-loop finite-horizon optimisation problem using $\mathbf{x}_0$ to obtain
$$\mathbf{U}^{\text{OPT}} = \{\mathbf{u}_0^{\text{OPT}}, \ldots, \mathbf{u}_{N-1}^{\text{OPT}}\}.$$
3. Apply the first element of the control sequence as the current control action $\mathbf{u}_k = \mathbf{u}_0^{\text{OPT}}$.

The above steps are then repeated indefinitely at all subsequent stages (sampling instants). We will further describe this approach in the next chapters for the specific problems of constrained control of rudder and fin stabilisers.

12

Control System Design for Autopilots with Rudder Roll Stabilisation

This chapter presents a control system design of autopilots with rudder roll stabilisation. First, the basic functions of contemporary autopilots are commented and their influence on control design discussed. Then, the challenges for control design are reviewed, and the control problem is stated. Finally, a solution is proposed and the performance evaluated via numerical simulations.

12.1 Overview of Autopilot Functions and their Influence on Control Design

Contemporary autopilot systems incorporate sophisticated functions and different operation modes. As discussed in Chapter 1, a ship motion control system consists of a guidance system, a control system, and a navigation system—see Figure 1.1.

The common operation modes handled by the guidance system for autopilots are indicated in the following [86]:

- **Manual mode**. In this mode, the autopilot is in standby, and the command of the actuators is generated manually.
- **Heading mode**. In this mode, only the heading-to-steer angle ψ_d (the desired heading[1]) is provided for the ship to follow, and the autopilot controller corrects the actual heading. This mode requires only heading measurements from a gyro or a compass.
- **Course mode**. In this mode, the system seeks to keep a constant course. The heading-to-steer angle is determined from the course-to-steer angle γ_d (the desired course) and an estimation of the drift angle β. The drift angle is calculated using the estimations sway and surge velocities in the body-fixed frame. These estimations are provided by an observer.

[1] For a definition of heading, course, and drift angles see Section 3.3.4.

- **Waypoint mode**. In this mode, the system seeks to bring the vessel to a desired waypoint. The actual position and estimated drift angle are used to calculate the heading-to-steer angle, and the guidance system will generate a trajectory that compensates for cross-track error in order to reach a given waypoint. This mode is selected for one waypoint at a time and does not facilitate turning and switching between active tracks. This mode requires heading measurement, position measurement and a one-track route (line between two waypoints). The waypoint mode seeks to bring the vessel to a fixed point in space, whereas the course mode only seeks to keep a constant course. An autopilot in a waypoint mode constantly updates its course in order to reach the waypoint. A vessel in course mode, on the other hand, constantly updates the heading to stay on the given course; *i.e.* the cross-track error is not corrected.
- **Route mode**. In this mode, the vessel follows a specified route (usually a piece-wise rectilinear path defined by using the waypoints as vertices—see [67] for details). At each time, there is only one active track (the line between the two active waypoints), and when the ship reaches the proximity of the end waypoint of the active track, a new track becomes active leading to the next waypoint in the path. The cross-track error for the active path is constantly minimized. The route model is the only mode that provides a trajectory for switching between active tracks. This trajectory is usually an arc of a circle. The route mode requires heading measurements, position measurements, speed measurements and a navigational aid for administration of waypoints.

In all these modes, the navigation system uses different methods and information to define, at each time instant, the heading-to-steer angle ψ_d, which is the reference sent to the controller (see Figure 1.1). In some cases, the reference computing algorithms of the navigation system will also generate $\dot{\psi}_d$, and $\ddot{\psi}_d$ via appropriate filtering. This provides more information and thus influence on the control system design. We will leave our discussion about the guidance system here, for this has been comprehensively covered in [67], and will concentrate on the control system design.

In addition, to the guidance system modes, the controller of contemporary autopilots also provides the following functions, which influence the control system design:

- Manual and automatic control tuning
- Manual and automatic constrained adjustment
- Rudder roll stabilisation function
- Integrated rudder and fin control
- Fault detection and diagnosis

These functions, together with the reference provided by the guidance system and the measurement provided by the navigation system, have a significant influence on the control architecture used. The design of autopilots with rudder

roll stabilisation and the integrated fin-rudder control have been the subject of ongoing research for over 30 years. This is a consequence of the significant bearing the control strategy has on ship performance and also the complexity associated with the control design. This is discussed in the next section.

12.2 RRS: A Challenging Control Problem

Using the rudder for simultaneous course keeping and roll reduction is not a simple task. As we have seen in Chapters 8 and 9, the ability to accomplish this depends on the following factors:

- Dynamic characteristics of the ship,
- Sea state,
- Sailing conditions (speed and encounter angle),
- Type of control system.

The control system must then be designed so as to best deal with the following issues:

- **Under-actuated system**. There is one control action (rudder moments) to achieve two control objectives: *roll reduction* and *low heading interference*. A key fact for the successful application of this technique is that the dynamics associated with the rudder-induced roll motion are faster than the dynamics associated with the rudder-induced yaw motion. This depends on the shape of the hull and the location of the rudder and the center of gravity of the ship. The difference in dynamic response between roll and yaw is characterized by the location of a Non-Minimum Phase zero (NMP) associated with the rudder to roll response—see Chapter 8. The closer the NMP zero to the imaginary axis, the faster the roll response to the rudder with respect to the response in yaw; and thus, the better the potential for roll reduction without much heading interference.
- **Uncertainty**. There are three sources of uncertainty associated with the control design. First, there is incomplete state information available to implement the control law. Although, complete measurement of the state is possible, the necessary sensors can be very expensive. Second, there are disturbances from the environment (wave-induced motion) which, in principle, cannot be known *a priori*. Third, in the case of model-based control (like MPC), there is uncertainty associated with the accuracy of the model used to predict the response to the rudder action.
- **Disturbance rejection with a non-minimum phase system**. As discussed in Chapter 8, the NMP zero in the rudder-to-roll response imposes fundamental limitations and trade-offs regarding disturbance rejection and achievable roll reduction at different frequency bands. The energy of the disturbance shifts in frequency according to the sea state and sailing conditions. Because of these changes, there could be significant roll amplifi-

cation if the controller is not adapted to the changes in the disturbance characteristics.

- **Input constraints**. The rudder action demanded by the controller should satisfy *rate* and *magnitude* constraints. Rate constraints are associated with safety and reliability. By imposing rate constraints on the rudder command, we ensure an adequate lifespan of the hydraulic actuators and avoid their saturation. Rate saturation reduces the control action and introduces phase lags which could lead to closed-loop stability problems—see Figure 10.2. Magnitude constraints are associated with performance and economy. Large rudder angles may result in flow separation (loss of actuation and poor performance). Also, it is convenient to reduce the maximum rudder action at higher speeds in order to reduce the mechanical loads on the rudder and the steering machinery. The controller should allow for the constraints to be changed either manually or automatically in a prescribed manner.
- **Output constraints**. Since the rudder affects the ship heading, it may be desirable, in some cases, to include constraints on the maximum heading deviations allowed when the rudder is also used to reduce roll.
- **Unstable plant**. The response of yaw to rudder action is marginally unstable: there is an integrator. Indeed, if the rudder is offset from its central position with a step-like command, then there will be a ramp-like increase in the heading angle. Some vessels are directionally unstable, requiring permanent rudder offset to keep the heading.
- **Coordination with other stabilisers**. Rudder roll stabilisation can be used as a sole stabiliser or together with fin stabilisers. The latter calls for coordination in the control system such that rudder and fin action do not counteract each other. Also, depending on the particular operation, it is desirable to be able to change the amount of roll produced by each device.

From all of the issues mentioned above, it is evident that the problem of rudder roll stabilisation of ships is a challenging one and, as such, the chosen control strategy plays an important role in achieving high performance.

12.3 Control System Architecture

The proposed architecture for the control system of an autopilot with RRS is shown in Figure 12.1. In this scheme, we can distinguish three different parts:

- Parameter estimation,
- Wave Filtering
- Controller.

The above order is in agreement with the causality of the signals processing performed while the control is in operation. Indeed, the parameters of the models are estimated, if necessary, and then the measured signals (representing the physical magnitudes) are filtered to be used by the controller to

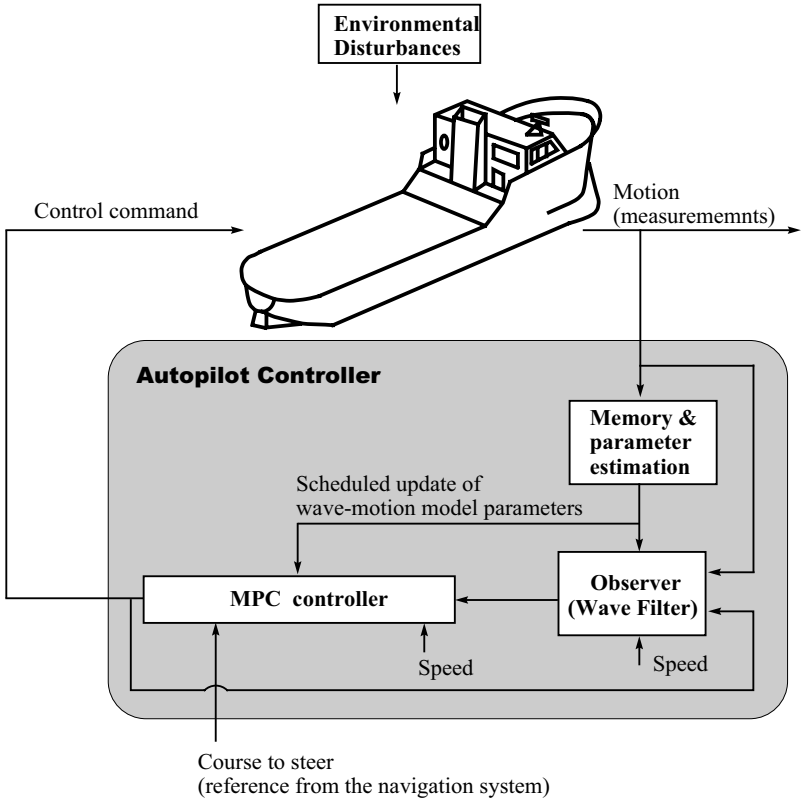

Fig. 12.1. Proposed control system architecture for autopilot with RRS design.

generate the control command. The design process, however, may not follow the above order. The sections of this chapter will take the reader through the following design steps:

- Define a control design model,
- Design appropriate filters,
- Estimate parameters,
- State the assumptions for control design,
- Propose the control strategy, and
- Test the performance of the proposed scheme.

12.4 Control Design Models

In Chapter 4, we presented both high-fidelity and control-design models. In this chapter, we will use the control design models for observer and controller

design and high-fidelity models for testing. For control design purposes we will use a motion superposition type of model, *i.e.* the total motion of the vessel will be considered as the superposition of the motion induced by the waves and the motion induced by the controller. As we will see, this leads to a simple strategy to adapt the controller to changes in the sea state.

12.4.1 Control to Motion Model

To model the response of the vessel to the control action, we can use the linear low-frequency model presented in Section 4.3.4, together with the linear forces and moments induced by the rudder given in Section 4.3:

$$\begin{aligned} \mathbf{M}^b\dot{\boldsymbol{\nu}} &= \mathbf{D}^b(U)\boldsymbol{\nu} + \mathbf{G}^b\boldsymbol{\eta} + \boldsymbol{\tau}_c^b \\ \dot{\boldsymbol{\eta}} &= \boldsymbol{\nu}, \end{aligned} \tag{12.1}$$

where

$$\boldsymbol{\nu} = \begin{bmatrix} v, \, p, \, r \end{bmatrix}^{\mathrm{T}} \quad \text{and} \quad \boldsymbol{\eta} = \begin{bmatrix} \phi, \, \psi \end{bmatrix}^{\mathrm{T}} \tag{12.2}$$

are given in the body-fixed frame. The control vector $\boldsymbol{\tau}_c^b$ are the forces and moments generated by the rudder motion and U is the average forward speed of the vessel.

Alternatively, we can use the unified model for slow manoeuvering in a seaway *cf.* (4.81):

$$\begin{aligned} \mathbf{M}^b\dot{\boldsymbol{\nu}} &= \mathbf{D}^b(U)\boldsymbol{\nu} + \mathbf{C}_r^b\boldsymbol{\mu} + \mathbf{G}^b\boldsymbol{\eta} + \boldsymbol{\tau}_c^b \\ \dot{\boldsymbol{\mu}} &= \mathbf{A}_r^b\boldsymbol{\mu} + \mathbf{B}_r^b\boldsymbol{\nu}, \\ \dot{\boldsymbol{\eta}} &= \boldsymbol{\nu}, \end{aligned} \tag{12.3}$$

where the matrices $\mathbf{M}^b$ and $\mathbf{D}^b(U)$ in (12.3) are different to those in (12.1), and states $\boldsymbol{\mu}$ represent the fluid memory effects. The model (12.1) is a low frequency model, and the model (12.3) captures both the low frequency effects and the fluid memory effects associated with the motion of the ship at the wave frequencies.

For the design of an autopilot with RRS, 45 states may need to be considered for $\boldsymbol{\mu}$ in order to approximate the retardation functions for the horizontal motions: sway, roll, and yaw. Although the number of additional states in (12.3) may seem large, it still remains relatively low if we compare these models to those employed in process control applications.

The control designs presented in this chapter are based on optimal control, and since the states $\boldsymbol{\mu}$ are not involved in the cost, these designs can be applied to both models (12.1) and (12.3). Nevertheless, since the use of (12.3) for control design is the subject of current research (and it has not been tested in practical designs), we will continue this chapter using (12.1). Note, however, that the methods are equally applicable to (12.3).

Let us define the following state and control variables

$$\mathbf{x}^{\mathrm{c}} \triangleq \left[v^{\mathrm{c}},\, p^{\mathrm{c}},\, r^{\mathrm{c}},\, \phi^{\mathrm{c}},\, \psi^{\mathrm{c}}\right]^{\mathrm{T}}, \quad \mathbf{u} \triangleq \alpha, \tag{12.4}$$

where the superscript c in the variables indicates *control-induced* motion. Using these variables, the state-space representation of (12.1) becomes

$$\dot{\mathbf{x}}^{\mathrm{c}} = [\mathbf{M}_{\mathrm{sys}}^{-1}\mathbf{F}(U)]\,\mathbf{x}^{\mathrm{c}} + [\mathbf{M}_{\mathrm{sys}}^{-1}\mathbf{H}(U)]\,\mathbf{u}, \tag{12.5}$$

with

$$\mathbf{M}_{\mathrm{sys}} \triangleq \begin{bmatrix} (m - Y_{\dot{v}}) & -(mz_G + Y_{\dot{p}}) & (mx_G - Y_{\dot{r}}) & 0 & 0 \\ -(mz_G + K_{\dot{v}}) & (I_{xx} - K_{\dot{p}}) & -K_{\dot{r}} & 0 & 0 \\ (mx_G - N_{\dot{v}}) & -N_{\dot{p}} & (I_{zz} - N_{\dot{r}}) & 0 & 0 \\ 0 & 0 & 0 & 1 & 0 \\ 0 & 0 & 0 & 0 & 1 \end{bmatrix} \tag{12.6}$$

$$F(U) \triangleq \begin{bmatrix} Y_{|u|v}|U| & 0 & (Y_{ur} - m)U & Y_{\phi uu}U^2 & 0 \\ K_{|u|v}|U| & K_p + K_{|u|p}|U| & (K_{ur} + mz_G)U & K_{\phi uu}U^2 - \rho g \nabla G M t & 0 \\ N_{|u|v}|U| & N_p + N_{|u|p}|U| & N_{|u|r}|U| - mx_G U & N_{\phi u|u|}U|U| & 0 \\ 0 & 1 & 0 & 0 & 0 \\ 0 & 0 & 1 & 0 & 0 \end{bmatrix}, \textit{and} \tag{12.7}$$

$$H(U) \triangleq \begin{bmatrix} 1 \\ -r_r \\ -LCG \\ 0 \\ 0 \end{bmatrix} \frac{1}{2}\rho\, u_r(U)^2 A_r \left(\frac{\partial C_L}{\partial \alpha}\right)\Bigg|_{\alpha=0} \tag{12.8}$$

The parameter A_r is the area of the rudder, C_L is the lift coefficient and $u_r(U)$ is the flow speed over the rudder, which depends on the average speed of the vessel—see (5.22). For the definition of LCG and rudder roll lever arm r_r, see Figure 5.9.

The parameters of the model presented above are given in Appendix B for the benchmark example. It should be mentioned that for different vessels, the structure of $F(U)$ may change. Recall from Section 4.3.2 that the parameters in $F(U)$ correspond to a series expansion for the hydrodynamic forces, and the numerical values are estimated using data from scale-model tests or from computational methods based on theoretical approaches—see, for example, [11, 18, 23]. An alternative approach consists of using system identification techniques. System identification for ship steering models will not be addressed in this book, and the interested reader is referred to [118, 30, 227, 241, 98].

Therefore, *our first assumption for control design is that the parameters of the above model are known for a set of different speeds*—usually a set of speeds with increments of 5 kt is sufficient. In Figure 12.1, this has been explicitly

accounted for by indicating the speed dependency of the blocks using models which require parameter value updating if the speed changes.

From the continuous-time linear time-invariant model (12.5), a discrete-time model can be obtained:

$$\mathbf{x}^{\mathrm{c}}_{k+1} = \mathbf{\Phi}_{\mathrm{c}}\mathbf{x}^{\mathrm{c}}_{k} + \mathbf{\Gamma}_{\mathrm{c}}\mathbf{u}_k, \tag{12.9}$$

$$\mathbf{x}^{c}_{k} = \left[v^{\mathrm{c}}_k,\, p^{\mathrm{c}}_k,\, r^{\mathrm{c}}_k,\, \phi^{\mathrm{c}}_k,\, \psi^{\mathrm{c}}_k\right]^{\mathrm{T}} \qquad \text{and} \quad \mathbf{u}_k = \alpha_k. \tag{12.10}$$

The notation $\mathbf{x}^{c}_{k}$ refers to the value of the variable $\mathbf{x}^{\mathrm{c}}(t)$ evaluated at the time instant $t = t_0 + kT_s$, where T_s is the sampling period, and $k \in \mathbb{Z}$ describes the different discrete time events.

The matrices $\mathbf{\Phi}_{\mathrm{c}}$ and $\mathbf{\Gamma}_{\mathrm{c}}$ can be obtained from the matrices of the continuous time model by using, for example, the zero-order hold method—see, [72]:

$$\mathbf{\Phi}_{\mathrm{c}} = \exp([\mathbf{M}^{-1}_{\mathrm{sys}}\mathbf{F}(U)]T_s) \approx \mathbf{I} + [\mathbf{M}^{-1}_{\mathrm{sys}}\mathbf{F}(U)]T_s \tag{12.11}$$

$$\mathbf{\Gamma}_{\mathrm{c}} = \int_0^{T_s} [\mathbf{M}^{-1}_{\mathrm{sys}}\mathbf{H}(U)] \exp([\mathbf{M}^{-1}_{\mathrm{sys}}\mathbf{H}(U)]\tau)\, d\tau \approx [\mathbf{M}^{-1}_{\mathrm{sys}}\mathbf{H}(U)]T_s. \tag{12.12}$$

12.4.2 Wave-induced Motion Model

Under a motion superposition assumption, the measurements taken at discrete-time intervals could be expressed as

$$\mathbf{y}_k = \begin{bmatrix} v_k \\ p_k \\ r_k \\ \phi_k \\ \psi_k \end{bmatrix} = \begin{bmatrix} v^{\mathrm{c}}_k + v^{\mathrm{w}}_k \\ p^{\mathrm{c}}_k + p^{\mathrm{w}}_k \\ r^{\mathrm{c}}_k + r^{\mathrm{w}}_k \\ \phi^{\mathrm{c}}_k + \phi^{\mathrm{w}}_k \\ \psi^{\mathrm{c}}_k + \psi^{\mathrm{w}}_k \end{bmatrix} + \mathbf{n}_k, \tag{12.13}$$

where the superscript w stands for *wave-induced motion* (oscillatory motion), and $\mathbf{n}_k$ represents the noise introduced by the measurement system.

It is worth emphasizing, that the above is just a *conceptual model* used for filtering and control system design. Note also that in some cases not all the measurements indicated above will be available. This has implications for the wave filter design, which we will discuss in the next section.

Observations of time series of ship motion induced by waves—see, for example, Figures 4.11 and 4.12—indicate that the data are correlated; and therefore, the time series can be modelled as filtered white noise—spectral factorisation [8]. The filters commonly adopted for autopilot design applications are of second order [66, 67]:

$$\begin{bmatrix}\dot{\phi}^{\mathrm{w}}\\ \dot{p}^{\mathrm{w}}\end{bmatrix} = \begin{bmatrix}0 & 1\\ -\omega_\phi^2 & -2\zeta_\phi\omega_\phi\end{bmatrix} \begin{bmatrix}\phi^{\mathrm{w}}\\ p^{\mathrm{w}}\end{bmatrix} + \begin{bmatrix}\upsilon_{1\phi}\\ \upsilon_{2\phi}\end{bmatrix},$$

$$\begin{bmatrix}\dot{v}^{\mathrm{w}}\\ \ddot{v}^{\mathrm{w}}\end{bmatrix} = \begin{bmatrix}0 & 1\\ -\omega_v^2 & -2\zeta_v\omega_v\end{bmatrix} \begin{bmatrix}v^{\mathrm{w}}\\ \dot{v}^{\mathrm{w}}\end{bmatrix} + \begin{bmatrix}\upsilon_{1v}\\ \upsilon_{2v}\end{bmatrix}, \tag{12.14}$$

$$\begin{bmatrix}\dot{\psi}^{\mathrm{w}}\\ \dot{r}^{\mathrm{w}}\end{bmatrix} = \begin{bmatrix}0 & 1\\ -\omega_\psi^2 & -2\zeta_\psi\omega_\psi\end{bmatrix} \begin{bmatrix}\psi^{\mathrm{w}}\\ r^{w}\end{bmatrix} + \begin{bmatrix}\upsilon_{1\psi}\\ \upsilon_{2\psi}\end{bmatrix},$$

where υ_{ij} are independent white noise processes, and ω_j are the modal frequencies of the power spectral density of motion. Therefore, these depend on the sea state and sailing conditions. The intensity of the noises and the damping coefficients ζ_j must be estimated online to reflect the actual sailing conditions of the vessel. We will address this in Section 12.5.

Using a zero-order hold method, the models take the following form in discrete time:

$$\begin{bmatrix}\phi^{\mathrm{w}}_{k+1}\\ p^{\mathrm{w}}_{k+1}\end{bmatrix} = \underbrace{\begin{bmatrix}1 & T_s\\ -\omega_\phi^2 T_s & 1-2\zeta_\phi\omega_\phi T_s\end{bmatrix}}_{\mathbf{\Phi}^{\mathrm{w}}_{\phi}} \begin{bmatrix}\phi^{\mathrm{w}}_{k}\\ p^{\mathrm{w}}_{k}\end{bmatrix} + \begin{bmatrix}\upsilon_{1\phi}\\ \upsilon_{2\phi}\end{bmatrix},$$

$$\begin{bmatrix}v^{\mathrm{w}}_{k+1}\\ \delta v^{\mathrm{w}}_{k+1}\end{bmatrix} = \underbrace{\begin{bmatrix}1 & T_s\\ -\omega_v^2 T_s & 1-2\zeta_v\omega_v T_s\end{bmatrix}}_{\mathbf{\Phi}^{\mathrm{w}}_{v}} \begin{bmatrix}v^{\mathrm{w}}_{k}\\ \delta v^{\mathrm{w}}_{k}\end{bmatrix} + \begin{bmatrix}\upsilon_{1v}\\ \upsilon_{2v}\end{bmatrix}, \tag{12.15}$$

$$\begin{bmatrix}\psi^{\mathrm{w}}_{k+1}\\ r^{\mathrm{w}}_{k+1}\end{bmatrix} = \underbrace{\begin{bmatrix}1 & T_s\\ -\omega_\psi^2 T_s & 1-2\zeta_\psi\omega_\psi T_s\end{bmatrix}}_{\mathbf{\Phi}^{\mathrm{w}}_{\psi}} \begin{bmatrix}\psi^{\mathrm{w}}_{k}\\ r^{\mathrm{w}}_{k}\end{bmatrix} + \begin{bmatrix}\upsilon_{1\psi}\\ \upsilon_{2\psi}\end{bmatrix},$$

where υ_{ij} are sequences of independent identically distributed Gaussian random variables. In the next section, we will see a method to estimate the parameters of the above models from measured data.

12.5 Disturbance Parameter Estimation and Forecasting

In the previous section, we have adopted models for the wave-induced motion of the vessel. In this section we a discuss a mechanism for eastimating the parameters of the models (12.15).

In dynamic positioning operations, it is common practice to fix the damping coefficients in (12.15) to the value of 0.1, and estimate the natural frequencies ω_ϕ, ω_v and ω_ψ online. Then, one can use gain scheduling to account

for the uncertainty in the intensity of the noises—the sea state. Alternatively, one can use an adaptive wave filter to estimate both parameters and states. For details of these approaches, see [66, 67] and references therein. Here, we will take a slightly different approach.

The models given in (12.15) can be written in the following general form:

$$\begin{bmatrix} x_{1,k+1} \\ x_{2,k+1} \end{bmatrix} = \begin{bmatrix} \theta_{11} & \theta_{12} \\ \theta_{21} & \theta_{22} \end{bmatrix} \begin{bmatrix} x_{1,k} \\ x_{2,k} \end{bmatrix} + \begin{bmatrix} v1_k \\ v2_k \end{bmatrix}, \tag{12.16}$$

where θ_{ij} are the unknown parameters. By defining the vector

$$\boldsymbol{\theta} \triangleq \left[\theta_{11}, \theta_{12}, \theta_{21}, \theta_{22}\right]^{\mathrm{T}}, \tag{12.17}$$

we can reorganise the above model in the following way:

$$\begin{bmatrix} x_{1,k+1} \\ x_{2,k+1} \end{bmatrix} = \begin{bmatrix} x_{1,k} & x_{2,k} & 0 & 0 \\ 0 & 0 & x_{1,k} & x_{2,k} \end{bmatrix} \boldsymbol{\theta} + \begin{bmatrix} v1_k \\ v2_k \end{bmatrix}. \tag{12.18}$$

If we measure the variables $x_{1,k}$ and $x_{2,k}$, and we assume that the parameters are slowly varying, *i.e.* $\dot{\boldsymbol{\theta}} \approx \mathbf{0}$, then we can write the following dynamic model:

$$\begin{aligned} \boldsymbol{\theta}_{k+1} &= \boldsymbol{\theta}_k, \\ \begin{bmatrix} x_{1,k} \\ x_{2,k} \end{bmatrix} &= \begin{bmatrix} x_{1,k-1} & x_{2,k-1} & 0 & 0 \\ 0 & 0 & x_{1,k-1} & x_{2,k-1} \end{bmatrix} \boldsymbol{\theta}_k + \begin{bmatrix} v1_k \\ v2_k \end{bmatrix}. \end{aligned} \tag{12.19}$$

System (12.19) is in a form to which we can apply a Kalman Filter[2] to estimate $\widehat{\theta}_{k|k}$ from the measurements. Indeed, the first equation in (12.19) is the state equation and second the measurement equation. The Kalman Filter algorithm for the parameter estimation becomes:

Prediction:

$$\begin{aligned} \widehat{\boldsymbol{\theta}}_{k|k-1} &= \widehat{\boldsymbol{\theta}}_{k-1|k-1} \\ \boldsymbol{\Sigma}_{k|k-1} &= \boldsymbol{\Sigma}_{k-1|k-1} + \mathbf{R}_\theta. \end{aligned} \tag{12.20}$$

Measurement update:

$$\begin{aligned} \widehat{\boldsymbol{\theta}}_{k|k} &= \widehat{\boldsymbol{\theta}}_{k|k-1} + \mathbf{L}_k(\mathbf{y}_k - \mathbf{C}_k\widehat{\boldsymbol{\theta}}_{k|k-1}), \\ \mathbf{L}_k &= \boldsymbol{\Sigma}_{k|k-1}\mathbf{C}_k^{\mathrm{T}}(\mathbf{C}_k\,\boldsymbol{\Sigma}_{k|k-1}\mathbf{C}_k^{\mathrm{T}} + \mathbf{R}_{\mathrm{v}})^{-1}, \\ \boldsymbol{\Sigma}_{k|k} &= (\mathbf{I} - \mathbf{L}_k\mathbf{C}_k)\boldsymbol{\Sigma}_{k|k-1}, \end{aligned} \tag{12.21}$$

where

$$\begin{aligned} \mathbf{y}_k &= \begin{bmatrix} x_{1,k} \\ x_{2,k} \end{bmatrix} \\ \mathbf{C}_k &= \begin{bmatrix} x_{1,k-1} & x_{2,k-1} & 0 & 0 \\ 0 & 0 & x_{1,k-1} & x_{2,k-1} \end{bmatrix}, \end{aligned} \tag{12.22}$$

[2] see Appendix A.

and the matrices $\mathbf{R}_\theta$ and $\mathbf{R}_\mathrm{v}$ are the tuning parameters of the estimator. This method is a recursive implementation of the least-squares estimation method—see, for example, [88, 10].

Once the parameters are obtained, the quality of the model can be assessed according to its performance for forecasting. The optimal N-step ahead predictor for the system (12.16) takes the following form [88, 10, 37]:

$$\begin{bmatrix} \check{x}_{1,k+N|k} \\ \check{x}_{2,k+N|k} \end{bmatrix} = \begin{bmatrix} \theta_{11} & \theta_{12} \\ \theta_{21} & \theta_{22} \end{bmatrix}^N \quad \begin{bmatrix} x_{1,k} \\ x_{2,k} \end{bmatrix}, \tag{12.23}$$

where $\check{x}_{1,k+N|k}$ is the prediction of variable x_1 at the time instant $k+N$ given its value at the instant k. It should be mentioned that the larger the prediction horizon, the bigger the uncertainty of the prediction. Thus, the uncertainty grows with N—see, for example, [88, 37] for further details.

As an example of parameter estimation, consider the results shown in Figure 12.2 corresponding to the roll model for the benchmark example. This figure shows the evolution of the parameters during the estimation period, in which roll angle and roll rate measurements are taken. For this example, the following tuning parameters were used:

$$\mathbf{R}_\theta = 1 \times 10^{-6}\mathbf{I}_{4\times 4}, \quad \mathbf{R}_\mathrm{v} = 1 \times 10^{-4}\mathbf{I}_{2\times 2}, \quad \mathbf{\Sigma}_{0|0} = \mathbf{I}_{4\times 4}. \tag{12.24}$$

After the parameters are estimated, the optimal predictor given in (12.23) was used for forecasting the roll angle and the roll rate; this is shown in Figure 12.3. Similar results are shown in Figure 12.4 for the same sea state but sailing in bow seas.

The natural roll period of the benchmark example vessel is about 7 s, by sampling with T_s=0.25 s, we have about 28 samples per roll oscillation period—a rule of thumb in digital control is to sample between 10 and 20 times during the period or during the fastest time constant [72]. In Figures 12.3 and 12.4, the horizons are $N = 5$ and 10 means predictions at 1.25 and 2.5 s ahead. The latter is longer than a quarter of the roll oscillation—which seems to be a good prediction horizon for predictive control purposes. Similar results can be obtained for the yaw and sway models.

Regarding the measurements of the states of the models in (12.15), it follows from the conceptual model (12.13) that when the rudder activity is only reserved to correct the slowly varying heading deviations, *e.g.* under manual control or only with the autopilot function on, the measurements can be considered as the wave-induced motion part in (12.13). Therefore, these measurements can be used to run the parameter estimation filter before switching on the RRS function of the autopilot.

Unless there is a significant change in speed or heading, the parameters of the models depend only on the sea state. As discussed in Chapter 2, *cf.* Section 2.4, the sea state can be considered stationary only for short periods of

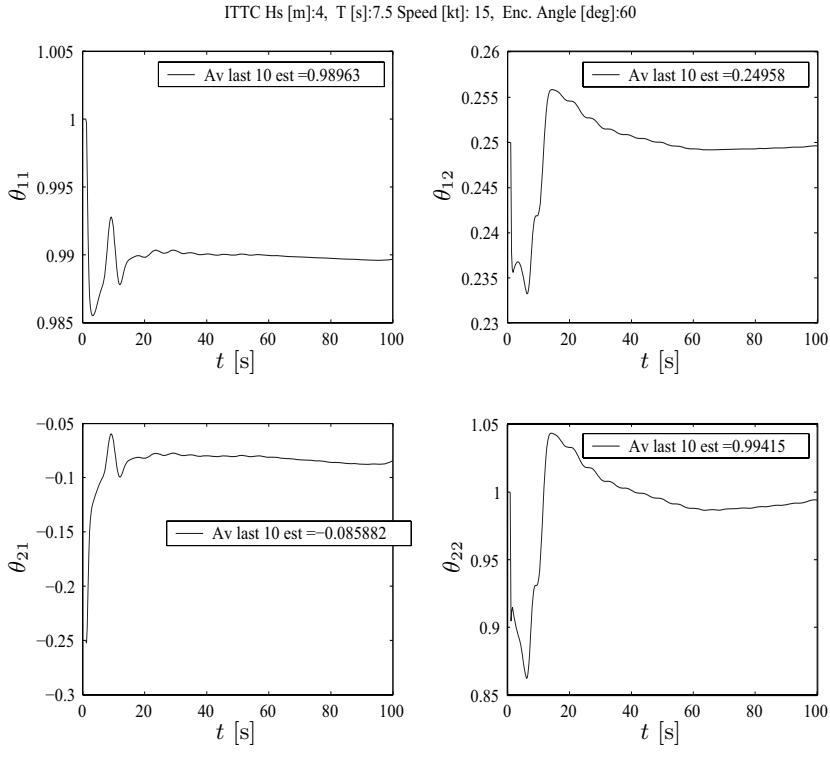

Fig. 12.2. Estimated parameters for Roll model in quartering seas seas

time—usually about 20 min. Therefore, the parameters can be updated regularly every few minutes or whenever there is a change in speed and encounter angle.

Once the RRS function is on, the rudder-induced motion will affect the motion induced by the waves—the essence of the stabiliser. However, the closed-oop measurements can still be used to estimate the parameters of the shaping filters, with minor losses in performance. This way we can obtain a fully adaptive observer—and if the roll model is used in the controller to predict roll motion, then we can also obtain an adaptive controller. This is the approach taken in the following sections.

Finally, in the case of sway velocity, the measurements of the state of the model (12.15) will rarely be available. In this case good results are still obtained if we take $\mathbf{\Phi}_v^{\mathrm{w}} = \mathbf{\Phi}_\psi^{\mathrm{w}}$. Indeed, this was the approach used to obtain the parameters of for simulation results of the wave filter discussed in the next section.

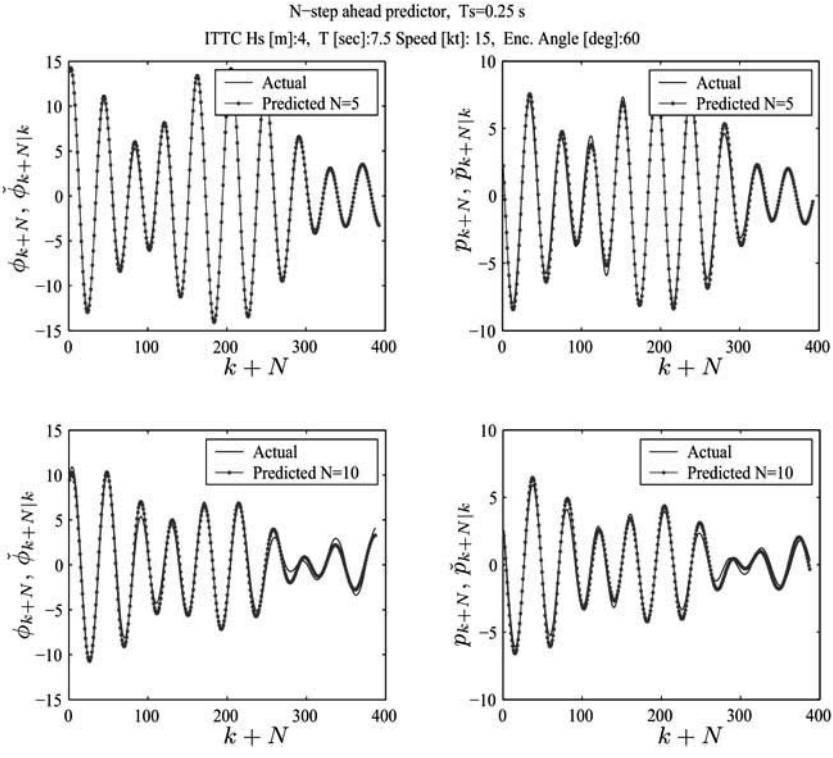

Fig. 12.3. Roll angle and roll rate predictions in quartering seas

12.6 Observer Design: State Estimation and Wave Filtering

The objective of the autopilot controller is to correct the deviations of the slowly-varying heading from the desired heading:

$$\bar{\psi}_k - \psi_k^{\mathrm{d}} \approx 0.$$

The angle ψ_k^{d} is the heading-to-steer angle generated by the guidance system (see Section 12.1), and the slowly-varying heading of the ship has two components:

$$\bar{\psi}_k = \psi_k^{\mathrm{c}} + \psi_k^{\mathrm{b}}. \tag{12.25}$$

The angle ψ_k^{c} is the yaw due to the control action, and ψ_k^{b} is a bias term induced by slowly-varying disturbances like wind and current. The reason for correcting only the slowly-varying yaw is to avoid the autopilot demanding control action with every wave—which would increase the wear of the actuators and induce speed losses [30].

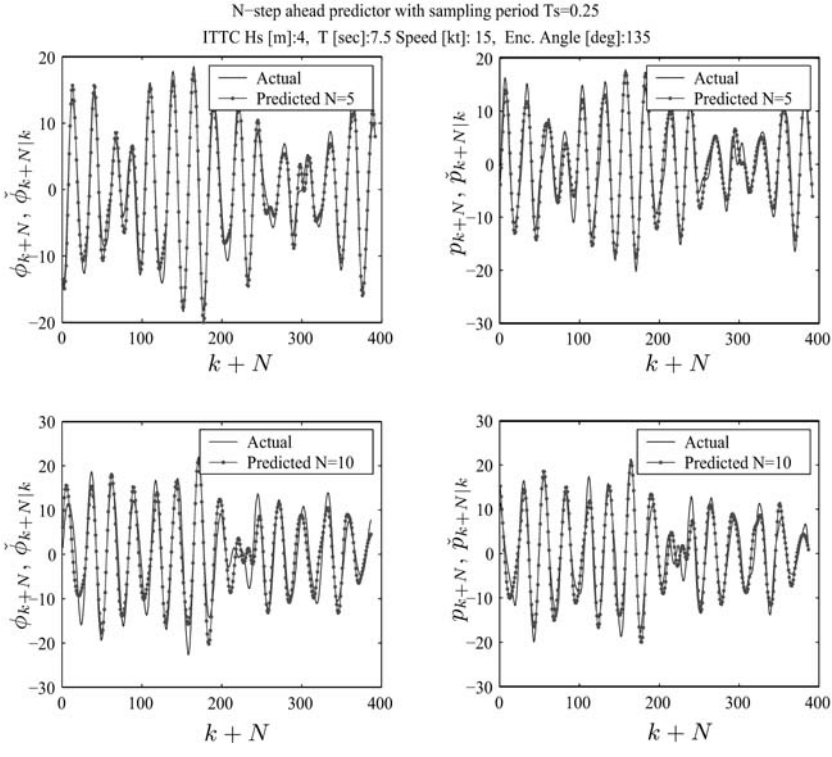

Fig. 12.4. Roll angle and roll rate predictions in bow seas

The measured yaw angle contains both the slowly-varying yaw and the wave-induced yaw:

$$\psi_k = \psi_k^{\mathrm{c}} + \psi_k^{\mathrm{b}} + \psi_k^{\mathrm{w}}. \tag{12.26}$$

Therefore, the wave-frequency motion must be removed (filtered) from the measurements of yaw and yaw rate, and only the slowly-varying components be used for feedback. The filter that performs this task is, thus, called a *wave filter*.

Several techniques have been applied for wave filtering in autopilot design [66, 67]:

- Dead band techniques,
- Low pass and notch filters in cascade configuration, and
- Observers (Kalman Filter, Nonlinear, Passivity-based and Adaptive)

The advantages of using observers over other filtering techniques are smaller phase lags and the fact that an observer can also be used to integrate measurements from different devices and estimate magnitudes that are not measured. In this book, we will follow an observer-based wave filter design.

Therefore, for state-feedback control design of a conventional autopilot, we can use an observer to estimate the following signals:

$$\hat{\mathbf{x}}_k = \left[\hat{r}^{\mathrm{c}}_k, \hat{\bar{\psi}}_k\right]^{\mathrm{T}}, \tag{12.27}$$

with $\bar{\psi}$ given in (12.25).

For an autopilot with RRS we need to incorporate into (12.27) the total roll angle, *i.e.* the wave induced-motion and the control-induced motion, and the control-induced sway, which gives the NMP dynamics in the rudder to roll response. Therefore, for an autopilot with RRS, we can use the following feedback signals to implement a state-feedback control[3]:

$$\hat{\mathbf{x}}_k = \left[\hat{v}^{\mathrm{c}}_k, \hat{p}^{\mathrm{c}}_k, \hat{r}^{\mathrm{c}}_k, \hat{\psi}^{\mathrm{c}}_k, \hat{p}^{\mathrm{w}}_k, \hat{\phi}^{\mathrm{w}}_k, \hat{\psi}^{\mathrm{b}}_k\right]^{\mathrm{T}}. \tag{12.28}$$

In order to obtain these estimates from the measurements (12.13), we define the following augmented state vector:

$$\mathbf{z}_k \triangleq \left[v^{\mathrm{c}}_k, p^{\mathrm{c}}_k, r^{\mathrm{c}}_k, \phi^{\mathrm{c}}_k, \bar{\psi}_k, \phi^{\mathrm{w}}_k p^{\mathrm{w}}_k, \psi^{\mathrm{w}}_k, r^{\mathrm{w}}_k, v^{\mathrm{w}}_k, \delta v^{\mathrm{w}}_k, r^{\mathrm{b}}_k,\right]^{\mathrm{T}}. \tag{12.29}$$

In the above state, we have included the bias in the yaw rate rather than in the yaw angle, and use $\bar{\psi}_k$ as a state variable. The bias can be either in the yaw rate, as indicated above, or in the yaw angle. The equation update for this bias is

$$r^{\mathrm{b}}_{k+1} = r^{\mathrm{b}}_k + \mathrm{w}_{12}. \tag{12.30}$$

With the state vector (12.29), the following augmented model can be considered:

$$\begin{aligned} \mathbf{z}_{k+1} &= \mathbf{\Phi}_z \mathbf{z}_k + \mathbf{\Gamma}_z \mathbf{u}_k + \mathbf{w}_k \\ \mathbf{y}_k &= \mathbf{C}_z \mathbf{z}_k + \mathbf{n}_k, \end{aligned} \tag{12.31}$$

where $\mathbf{w}_k$ and $\mathbf{n}_k$ are vectors of independent identically distributed Gaussian variables with covariance matrices $\mathbf{R}_w$ and $\mathbf{R}_n$. The matrices of the model are

$$\mathbf{\Phi}_z = \begin{bmatrix} \mathbf{\Phi}_c & \mathbf{0} & \mathbf{0} & \mathbf{0} & 0 \\ \mathbf{0} & \mathbf{\Phi}^{\mathrm{w}}_{\phi} & \mathbf{0} & \mathbf{0} & 0 \\ \mathbf{0} & \mathbf{0} & \mathbf{\Phi}^{\mathrm{w}}_{\psi} & \mathbf{0} & 0 \\ \mathbf{0} & \mathbf{0} & \mathbf{0} & \mathbf{\Phi}^{\mathrm{w}}_{v} & 0 \\ \mathbf{0} & \mathbf{0} & \mathbf{0} & \mathbf{0} & 1 \end{bmatrix} \qquad \mathbf{\Gamma}_z = \begin{bmatrix} \mathbf{\Gamma}_c \\ \mathbf{0} \\ \mathbf{0} \\ \mathbf{0} \end{bmatrix}, \tag{12.32}$$

and the matrix $\mathbf{C}_z$ depends on the measurements (12.13).

Using this model we can design an observer, to estimate $\hat{\mathbf{z}}_k$, given the measurements (12.13). This observer takes the following form:

[3]The feedback signal depends on the type of controller used. Here, we will use a state-feedback controller based on the material presented in Chapter 11. Different types of controllers may require different feedback signals, which determine both the number of states and the structure of the observer.

Prediction:

$$\hat{\mathbf{z}}_{k|k-1} = \mathbf{\Phi}_z \hat{\mathbf{z}}_{k-1|k-1} + \mathbf{\Gamma}_z \mathbf{u}_{k-1}, \qquad \hat{\mathbf{z}}_{0|0} = \mathbf{z}_0, \tag{12.33}$$

Measurement Update:

$$\hat{\mathbf{z}}_{k|k} = \hat{\mathbf{z}}_{k|k-1} + \mathbf{L}(\mathbf{y}_{k|k} - \mathbf{C}_z \hat{\mathbf{z}}_{k|k-1}) \tag{12.34}$$

There are different ways of designing the observer gain L in (12.34). One of these consists in using Kalman Filtering techniques—see Appendix A. With this approach, the observer equations become:

Prediction:

$$\begin{aligned} \hat{\mathbf{z}}_{k|k-1} &= \mathbf{\Phi}_z \, \hat{\mathbf{z}}_{k-1|k-1} + \mathbf{\Gamma}_z \, \mathbf{u}_{k-1} \\ \mathbf{\Sigma}_{k|k-1} &= \mathbf{\Phi}_z \, \mathbf{\Sigma}_{k-1|k-1} \, \mathbf{\Phi}_z^{\mathrm{T}} + \mathbf{R}_{\mathrm{w}}. \end{aligned} \tag{12.35}$$

Measurement update:

$$\begin{aligned} \hat{\mathbf{z}}_{k|k} &= \hat{\mathbf{z}}_{k|k-1} + \mathbf{L}_k(\mathbf{y}_k - \mathbf{C}_z \hat{\mathbf{z}}_{k|k-1}), \\ \mathbf{L}_k &= \mathbf{\Sigma}_{k|k-1} \mathbf{C}_z^{\mathrm{T}} (\mathbf{C}_z \, \mathbf{\Sigma}_{k|k-1} \mathbf{C}_z^{\mathrm{T}} + \mathbf{R}_{\mathrm{n}})^{-1}, \\ \mathbf{\Sigma}_{k|k} &= (\mathbf{I}_n - \mathbf{L}_k \mathbf{C}_z) \mathbf{\Sigma}_{k|k-1}, \end{aligned} \tag{12.36}$$

The matrix $\mathbf{\Sigma}_{k|k}$ is the covariance of the estimation error, and the matrices $\mathbf{R}_{\mathrm{w}}$, and $\mathbf{R}_{\mathrm{n}}$ are the covariance matrices of the state and measurement noises respectively. In practice, these matrices are chosen to be diagonal, and their elements are the parameters used to tune the observer—see Appendix A.

As an example, consider the simulation results shown in Figure 12.5. For this simulation, the motion of the ship due to the rudder motion was simulated using a nonlinear model and the wave-induced motion using the sum of sinusoids with random phases—seakeeping models. The observer has been designed without sway velocity measurements, and the following matrices and initial conditions were used in the observer:

$$\begin{aligned} \mathbf{R}_{\mathrm{w}} &= \mathrm{diag}(\left[10^{-5}\ 10^{-5}, 10^{-5}, 10^{-5}, 10^{-5}, 1, 1, 1, 1, 1, 1, 10^{-5}\right]), \\ \mathbf{R}_{\mathrm{n}} &= 10^{-1}\mathbf{I}_{4\times 4}, \\ \mathbf{\Sigma}_{0|0} &= \mathbf{I}_{12\times 12}, \\ \hat{\mathbf{z}}_{0|0} &= \left[0, \cdots, 0\right]^{\mathrm{T}}. \end{aligned}$$

The variance of the state noise in the first 5 state variables has been taken low—these are the variables describing the motion due to the control action. For the other variables, the variances were taken to be higher; these describe the noises driving the shaping filters that model the wave-induced motion.

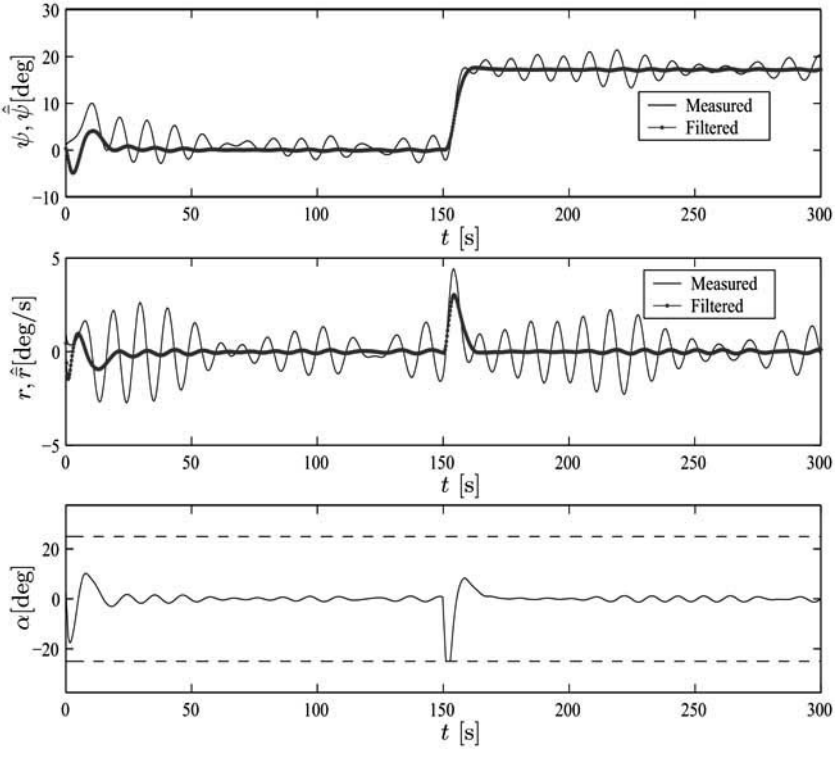

Fig. 12.5. Kalman filter-based wave filter and autopilot performance.

12.7 Autopilot Control System Design

After having considered the problems of parameter estimation and filtering, we are now ready to state the control design problem, and the assumptions that lead to our proposed solution.

12.8 Autopilot Control Problem and Assumptions for the Design

The basic control objectives for the particular motion control problem being addressed are as follows:

1. Minimise the roll motion: roll angle and accelerations;
2. Produce low interference with yaw;
3. Satisfy input constraints.

In a discrete-time framework, all the above objectives can be captured by the following optimal control problem.

Definition 12.1 (Output-feedback Input-Constrained Control Problem). *Find the feedback control command* $\mathbf{u}_k = \mathcal{K}(\mathbf{y}_k)$*, that minimises the following cost:*

$$V = \lim_{N\to\infty} \frac{1}{N}\, \mathbf{E}\{\sum_{k=0}^{N} (\mathbf{y}_k - \mathbf{y}_k^d)^{\mathrm{T}} \mathbf{Q} (\mathbf{y}_k - \mathbf{y}_k^d) + (\mathbf{y}_{k+1} - \mathbf{y}_k)^{\mathrm{T}} \mathbf{P} (\mathbf{y}_{k+1} - \mathbf{y}_k) + \mathbf{u}_k^{\mathrm{T}} \mathbf{R} \mathbf{u}_k\}, \quad (12.37)$$

subject to the system

$$\begin{aligned} \mathbf{x}_{k+1} &= \mathbf{\Phi}\mathbf{x}_k + \mathbf{\Phi}\mathbf{u}_k + \mathbf{w}_k, \\ \mathbf{y}_k &= \mathbf{C}\mathbf{x}_k + \mathbf{n}_k, \end{aligned}$$

and the following constraints

$$|\mathbf{u}_k| \le \mathbf{u}_{\max} \qquad \text{and} \qquad |\mathbf{u}_{k+1} - \mathbf{u}_k| \le \Delta\mathbf{u}_{\max} \qquad |\mathbf{D}\mathbf{y}_k| \le \mathbf{y}_{\max}.$$

∘ ∘ ∘

Under the assumption that the estimates given in (12.28) are available to to design the autopilot controller, we can then formulate the control problem using the following state variables

$$\mathbf{x}_k = \left[v_k^{\mathrm{c}},\, p_k^{\mathrm{c}},\, r_k^{\mathrm{c}},\, \bar{\phi}_k,\, \psi_k^{\mathrm{c}},\, p_k^{\mathrm{w}},\, \phi_k^{\mathrm{w}},\, r_k^{\mathrm{b}}\right]^{\mathrm{T}}. \quad (12.38)$$

The control will be the rudder angle

$$\mathbf{u}_k \triangleq \alpha_k, \quad (12.39)$$

and output variables

$$\mathbf{y}_k = \left[v_k^{\mathrm{c}},\, (p_k^{c} + p_k^{\mathrm{w}}),\, r_k^{\mathrm{c}},\, (\phi_k^{\mathrm{c}} + \phi_k^{\mathrm{w}}),\, \bar{\psi}_k\right]^{\mathrm{T}}. \quad (12.40)$$

The desired output is will be

$$\mathbf{y}_k^d = [0, 0, 0, 0, \psi^d], \quad (12.41)$$

or

$$\mathbf{y}_k^d = [0, 0, r_k^d, 0, \psi_k^d] \quad (12.42)$$

if the guidance system provides also a desired yaw rate—see Section 12.1.

The matrices $\mathbf{Q}$ and $\mathbf{P}$ in the cost can be chosen as

$$\begin{aligned} \mathbf{Q} &= \mathrm{diag}\left(\left[0,\, 0,\, q_r,\, q_\phi,\, q_\psi\right]\right), \\ \mathbf{P} &= \mathrm{diag}\left(\left[0,\, q_p,\, 0,\, 0,\, 0,\, \right]\right), \\ \mathbf{R} &= q_\alpha. \end{aligned} \quad (12.43)$$

With these, the cost (12.37) becomes

$$V = \lim_{N\to\infty} \frac{1}{N}\,\mathbf{E}\left\{\sum_{k=0}^{N}\left[q_\phi \phi_k^2 + q_p(p_{k+1}-p_k)^2\right] + q_\psi \Delta\psi_k^2 + q_r \Delta r_k^2 + q_\alpha \alpha_k^2\right\}, \tag{12.44}$$

with $\Delta\psi_k \triangleq \bar{\psi}_k - \psi_k^{\mathrm{d}}$ and $\Delta r_k \triangleq \bar{r}_k - r_k^{\mathrm{d}}$. This cost can be interpreted as follows

$$V \propto q_\phi \mathbf{var}[\phi] + q_p \mathbf{var}[\dot{p}] + q_r \mathbf{var}[\Delta r] + q_\psi \mathbf{var}[\Delta\psi] + q_\alpha \mathbf{var}[\alpha].$$

To simplify the tuning, we will choose the parameters in the cost above such that (12.37) becomes

$$V = \lim_{N\to\infty} \frac{1}{N}\,\mathbf{E}\left\{\sum_{k=0}^{N}\lambda\left[\phi_k^2 + \gamma_p(p_{k+1}-p_k)^2\right] + (1-\lambda)[\gamma_r \Delta r_k^2 + \gamma_\psi \Delta\psi_k^2 + \gamma_\alpha \alpha_k^2]\right\}. \tag{12.45}$$

The cost (12.45) is a discrete-time version of the one proposed by [228]; however, it incorporates an extra term which weights the roll accelerations via the difference $(p_{k+1} - p_k)$. The scalar parameter $\lambda \in [0,\, 1)$ represents a trade-off between the objectives of roll reduction and yaw interference, and this can be varied on-line. Hence, there is a single parameter that can be varied by the operator according to the different mission or particular scenario in which the ship is operating, or by an adaptive scheme. The parameter γ_p will be used to investigate the benefits of penalising roll accelerations.

When λ=0, the above cost reduces to the classical cost used for optimal autopilot design:

$$V = \lim_{N\to\infty} \frac{1}{N}\,\mathbf{E}\left\{\sum_{k=0}^{N}\gamma_r \Delta r_k^2 + \gamma_\psi \Delta\psi_k^2 + \gamma_\alpha \alpha_k^2\right\}. \tag{12.46}$$

This type of cost function was first used for autopilot design by Koyama [126] with the following special choice for the parameters

$$\gamma_r = 0, \quad \gamma_\psi = 0.0076, \quad \gamma_r = \frac{\gamma}{0.0076}. \tag{12.47}$$

where γ takes values between 8 and 10. With this particular choice of parameters, the value of the cost represents the percentage of speed loss. Norrbin [162] proposed minimising a similar cost, but with a different value for γ= 0.1. Therefore, one can choose $0.1 < \gamma < 10$ according to the severity of sea state, where the low value that allows more rudder activity should be used in

lower sea states [67]. van Amerongen and van Nauta Lemke [226] proposed incorporating a penalty on the yaw rate, *i.e.* $\gamma_r \neq 0$. If the roll and sway motions are not considered, the model of the ship can be reduced to the so-called Nomoto model, and the optimal solution reduces to a PD controller, *i.e.* a term proportional to the heading error, and a term proportional to the heading rate error—see [67] for details.

We next show how the above problem can be shaped into the MPC framework.

12.9 A Model Predictive Control Solution

As discussed in Chapter 11, Problem 12.1 is not easy to solve due to the constraints, but we can approximate its solution using a receding horizon approximation based on the certainty equivalent solution of a finite-horizon problem. Therefore, we *propose* as a solution for the autopilot control system design the use of *Certainty Equivalent Model Predictive Control with implicit receding-horizon implementation*. The following state-feedback finite-horizon optimal control problem will then be considered.

Definition 12.2 (Finite-horizon optimal control problem). *Given the initial condition for the augmented state* $\check{\mathbf{x}}_0$ *we seek the sequence of control moves*

$$\check{\mathbf{U}}^{\text{OPT}} = \{\check{\mathbf{u}}_0^{\text{OPT}}(\check{\mathbf{x}}_0), \ldots, \check{\mathbf{u}}_{N-1}^{\text{OPT}}(\check{\mathbf{x}}_0)\}; \tag{12.48}$$

which minimises the following cost

$$J_N(\check{\mathbf{x}}_0, \mathbf{U}) = \check{\mathbf{x}}_N^{\mathrm{T}} \check{\mathbf{S}}\, \check{\mathbf{x}}_N + \sum_{j=0}^{N-1} \check{\mathbf{x}}_j^{\mathrm{T}} \check{\mathbf{Q}}\, \check{\mathbf{x}}_j + \check{\mathbf{u}}_j^{\mathrm{T}} \check{\mathbf{R}}\, \check{\mathbf{u}}_j + 2\, \check{\mathbf{u}}_j^{\mathrm{T}} \check{\mathbf{T}}\, \check{\mathbf{x}}_j, \tag{12.49}$$

subject to

$$\begin{aligned} \check{\mathbf{x}}_{j+1} &= \boldsymbol{\Phi} \check{\mathbf{x}}_j + \boldsymbol{\Gamma} \check{\mathbf{u}}_j, \\ \check{\mathbf{y}}_j &= \mathbf{C} \check{\mathbf{x}}_j, \end{aligned} \tag{12.50}$$

and the constraints

$$|\check{\mathbf{u}}_k| \leq \mathbf{u}_{\max} \qquad \text{and} \qquad |\check{\mathbf{u}}_{k+1} - \check{\mathbf{u}}_k| \leq \Delta \mathbf{u}_{\max} \qquad |\mathbf{D}\check{\mathbf{y}}_k| \leq \mathbf{y}_{\max}. \tag{12.51}$$

The notation $\check{\mathbf{x}}$ *is used here to distinguish the predicted state—predicted using* (12.50)*—from the true state* $\mathbf{x}$.

The matrices in the cost are given by

$$\begin{aligned} \check{\mathbf{Q}} &= (\boldsymbol{\Phi} - \mathbf{I})^{\mathrm{T}} (\mathbf{C}^{\mathrm{T}} \mathbf{P} \mathbf{C})(\boldsymbol{\Phi} - \mathbf{I}) + \mathbf{C}^{\mathrm{T}} \mathbf{Q} \mathbf{C} \\ \check{\mathbf{R}} &= \boldsymbol{\Gamma}^{\mathrm{T}} (\mathbf{C}^{\mathrm{T}} \mathbf{P} \mathbf{C}) \boldsymbol{\Gamma} + \mathbf{R} \\ \check{\mathbf{T}} &= \boldsymbol{\Gamma}^{\mathrm{T}} (\mathbf{C}^{\mathrm{T}} \mathbf{P} \mathbf{C})(\boldsymbol{\Phi} - \mathbf{I}). \end{aligned} \tag{12.52}$$

The matrices $\mathbf{Q}$, $\mathbf{P}$, *and* $\mathbf{R}$ *are the parameters defining the cost* (12.45), *which can be taken as in* (12.43). *The matrices* $\mathbf{\Phi}$, $\mathbf{\Gamma}$ *describe the augmented system:*

$$\mathbf{\Phi} = \begin{bmatrix} \mathbf{\Phi}_{\mathrm{c}} & \mathbf{0} \\ \mathbf{0} & \mathbf{\Phi}_{\phi}^{\mathrm{w}} \end{bmatrix} \quad \mathbf{\Gamma} = \begin{bmatrix} \mathbf{\Gamma}_{\mathrm{c}} \\ \mathbf{0} \end{bmatrix}. \tag{12.53}$$

The final element to complete the definition of the problem is the matrix $\check{\mathbf{S}}$. *This matrix is taken as the solution of the following discrete-time algebraic Riccati equation:*

$$\check{\mathbf{S}} = \mathbf{\Phi}^{\mathrm{T}}\check{\mathbf{S}}\mathbf{\Phi} + \check{\mathbf{Q}} - \mathbf{K}^{\mathrm{T}}\bar{\mathbf{R}}\mathbf{K}\,. \tag{12.54}$$

with

$$\mathbf{K} = \bar{\mathbf{R}}^{-1}\mathbf{\Gamma}^{\mathrm{T}}\check{\mathbf{S}}\mathbf{\Phi}\,, \qquad \bar{\mathbf{R}} = \check{\mathbf{R}} + \mathbf{\Gamma}^{\mathrm{T}}\check{\mathbf{S}}\mathbf{B}. \tag{12.55}$$

○ ○ ○

The cross terms in the cost (12.49), that were not considered in Chapter 11, appear due to the terms in the cost penalising the difference $p_{k+1} - p_k$. This cross term only affects the matrices that define the quadratic programme . The solution of the above problem is given by

$$\begin{aligned} \check{\mathbf{U}}^{\mathrm{OPT}} = &\arg\min_{\check{\mathbf{U}}} \frac{1}{2}\check{\mathbf{U}}^{\mathrm{T}}(\mathbf{H}_1 + \mathbf{H}_2)\check{\mathbf{U}} + \check{\mathbf{U}}^{\mathrm{T}}(\mathbf{F}_1 + \mathbf{F}_2)\check{\mathbf{x}}_0 \\ &\text{s.t.} \quad \mathbf{L}\check{\mathbf{U}} \leq \mathbf{M}, \end{aligned} \tag{12.56}$$

where

$$\mathbf{H}_1 = 2(\boldsymbol{\mathcal{R}} + \boldsymbol{\mathcal{B}}^{\mathrm{T}}\,\boldsymbol{\mathcal{Q}}\,\boldsymbol{\mathcal{B}}) \qquad \mathbf{H}_2 = 4\,\boldsymbol{\mathcal{T}}\,\overline{\boldsymbol{\mathcal{B}}}, \tag{12.57}$$

$$\mathbf{F}_1 = 2\boldsymbol{\mathcal{A}}^{\mathrm{T}}\,\boldsymbol{\mathcal{Q}}\,\boldsymbol{\mathcal{B}} \qquad \mathbf{F}_2 = 2\,\boldsymbol{\mathcal{T}}\,\overline{\boldsymbol{\mathcal{A}}}, \tag{12.58}$$

$$\boldsymbol{\mathcal{Q}} = \mathrm{diag}\{\check{\mathbf{Q}}, \ldots, \check{\mathbf{Q}}, \check{\mathbf{S}}\}\,, \tag{12.59}$$

$$\boldsymbol{\mathcal{R}} = \mathrm{diag}\{\check{\mathbf{R}}, \ldots, \check{\mathbf{R}}\} \tag{12.60}$$

$$\boldsymbol{\mathcal{T}} = \mathrm{diag}\{\check{\mathbf{T}}, \ldots, \check{\mathbf{T}}\}, \tag{12.61}$$

and

$$\boldsymbol{\mathcal{A}} = \begin{bmatrix} \mathbf{A} \\ \mathbf{\Phi}^2 \\ \vdots \\ \mathbf{\Phi}^N \end{bmatrix}, \qquad \overline{\boldsymbol{\mathcal{A}}} = \begin{bmatrix} \mathbf{I} \\ \mathbf{\Phi} \\ \vdots \\ \mathbf{\Phi}^{N-1} \end{bmatrix}, \tag{12.62}$$

$$\boldsymbol{\mathcal{B}} = \begin{bmatrix} \mathbf{\Gamma} & \mathbf{0} & \cdots & \mathbf{0} \\ \mathbf{\Phi\Gamma} & \mathbf{\Gamma} & \cdots & \mathbf{0} \\ \vdots & \vdots & \ddots & \vdots \\ \mathbf{\Phi}^{N-1}\mathbf{\Gamma} & \mathbf{\Phi}^{N-2}\mathbf{\Gamma} & \cdots & \mathbf{\Gamma} \end{bmatrix} \quad \overline{\boldsymbol{\mathcal{B}}} = \begin{bmatrix} \mathbf{0} & \mathbf{0} & \cdots & \mathbf{0} \\ \mathbf{\Gamma} & \mathbf{0} & \cdots & \mathbf{0} \\ \vdots & \vdots & \ddots & \vdots \\ \mathbf{\Phi}^{N-2}\mathbf{\Gamma} & \mathbf{\Phi}^{N-3}\mathbf{\Gamma} & \cdots & \mathbf{0} \end{bmatrix}. \tag{12.63}$$

The matrices $\mathbf{L}$ and $\mathbf{M}$ that define the constraints are given in (11.26), but without considering the output constraints, *i.e.* for the case of symmetric constraints these become

$$\mathbf{L} = \begin{bmatrix} \mathbf{I} \\ -\mathbf{I} \\ \mathbf{W} \\ -\mathbf{W} \end{bmatrix}; \quad \mathbf{K} = \begin{bmatrix} \overline{\mathbf{M}}_{\text{mag}} \\ \overline{\mathbf{M}}_{\text{mag}} \\ \overline{\mathbf{M}}_{\text{rate}} \\ \overline{\mathbf{M}}_{\text{rate}} \end{bmatrix} \tag{12.64}$$

where $\mathbf{I}$ is the $N \times N$ identity matrix and W is the following $N \times N$ matrix

$$\mathbf{W} = \begin{bmatrix} 1 & \cdots & & 0 \\ -1 & 1 & & 0 \\ \vdots & \ddots & \ddots & \vdots \\ 0 & \cdots & -1 & 1 \end{bmatrix}, \tag{12.65}$$

and

$$\overline{\mathbf{M}}_{\text{mag}} = \begin{bmatrix} \mathbf{u}_{\max} \\ \vdots \\ \mathbf{u}_{\max} \end{bmatrix}; \qquad \overline{\mathbf{M}}_{\text{rate}} = \begin{bmatrix} \mathbf{u}_{-1} + \Delta\mathbf{u}_{\max} \\ \Delta\mathbf{u}_{\max} \\ \vdots \\ \Delta\mathbf{u}_{\max} \end{bmatrix}, \tag{12.66}$$

where $\mathbf{u}_{-1}$ is the previously applied control.

The above problem will then be solved on-line, and the implicit receding horizon feedback control law will be implemented, *i.e.*

$$\mathbf{u}_k = \mathcal{K}_N(\check{\mathbf{x}}_0) = \check{\mathbf{u}}_0^{\text{OPT}}(\check{\mathbf{x}}_0). \tag{12.67}$$

The initial condition for solving the above problem is provided by the observer, *i.e.* $\check{\mathbf{x}}_0 = \hat{\mathbf{x}}_{k|k}$,

To summarize the proposed control strategy, the following steps are envisaged at each sampling instant:

1. Given the new measurements, update the state estimate $\hat{\mathbf{x}}_{k|k}$.
2. Using the initial condition $\check{\mathbf{x}}_0 = \hat{\mathbf{x}}_{k|k}$, solve the quadratic programme, *cf.* (12.56) to obtain the sequence of controls $\check{\mathbf{U}}^{\text{OPT}}$.
3. Update the control command $\mathbf{u}_k = \check{\mathbf{u}}_0^{\text{OPT}}(\check{\mathbf{x}}_0)$.

12.10 Performance of Model Predictive RRS

In this section, we will present simulation results to assess the performance of the RRS function of an autopilot designed according to the strategy proposed in the previous section. We will use the benchmark example vessel given in Appendix B.

We have selected the speed of 15 kt for the simulations, because this is the nominal speed of the vessel and also the speed at which this vessel perform its missions most of the time. The performance will be assessed for the following scenarios:

- **Case A**: Beam seas (χ =90 deg), H_s =2.5 m (Top SS4), T =7.5 s,
- **Case B**: Quartering seas (χ =45 deg), H_s =4 m (Top SS5), T =8.5 s, and
- **Case C**: Bow seas (χ =135 deg), H_s = 4 m (Top SS5), T = 9.5 s.

The control action will be updated with a sampling rate of 0.25 s. Finally, the maximum rudder angle will be limited to 22 deg, and maximum rudder rate will be limited to 20 deg/s.

We will assess the performance via

1. percentage of reduction in roll angle variance and RMS value,
2. yaw angle RMS value induced by the rudder, and
3. percentage of reduction of Motion Induced Interruptions (MII).

To evaluate the MII (see Section 7.1), we will consider a location at 7 meters above the centre of gravity such that we can neglect the effect of vertical motion on the MII. This location coincides with the rear part of the bridge of the benchmark vessel.

12.10.1 Choosing the Prediction Horizon

Different prediction horizons were tested. As expected, for short prediction horizons (N=1, and N=2), the performance was poorer than for longer horizons (N=5 and N=10). For a horizon of 10 sample periods, an improvement of 10% in roll reduction was obtained with respect to that of N=1. For horizons longer than 10 samples, there was no significant improvement. Therefore, this is the horizon adopted to reduce the size of the optimisation problem, which was solved using the MATLAB® QP-solver.

12.10.2 Penalising Roll Acceleration in the Cost

We performed several tests to assess the effect of the simple tuning parameter λ and also the effect of incorporating a penalty for roll acceleration in the cost (12.45). Table 12.1 shows the results for the sailing condition χ=90 deg (beam seas), Hs=2.5 m, T=7.5 s, and the set of parameters λ =0.5 and 0.9, and γ_p=0 and 1. The figures shown in this table are the average of the results of 10 realisations simulated for each case—total of 40 simulations.

As we can see, penalising accelerations has a small effect in the roll performance but a greater effect on acceleration, and more importantly, on the reduction of MII for a low value of λ. With a high value of λ, the improvement for penalizing accelerations is not significant.

From the above results, it follows that an improvement in roll acceleration performance can be obtained by penalising accelerations in the cost. However,

Table 12.1. Performance at low and high gain ($\lambda = 0.5$ and $\lambda = 0.9$) with and without roll acceleration penalty.

χ=90,Hs=2.5m,T=7.5s	$\lambda = 0.5$ $\gamma_p = 0$	$\lambda = 0.5$ $\gamma_p = 1$
Roll red %	29.8	34.0
Roll Acc Red %	27.6	31.7
MII red %	51.8	60.2
Yaw rms	0.35	0.41
Rudder rms	4.50	5.12
χ=90,Hs=2.5m,T=7.5s	$\lambda = 0.9$ $\gamma_p = 0$	$\lambda = 0.9$ $\gamma_p = 1$
Roll red %	64.0	63.94
Roll Acc Red %	59.7	60.9
MII red %	99.0	99.2
Yaw rms	0.92	1.02
Rudder rms	10.5	10.7

the improvement is only small in some cases. Despite this, performance is never worse with respect to the MII, which seems to indicate that incorporating a roll acceleration penalty is beneficial.

We next present the time series of some of our simulation results, and discuss the particular cases.

12.10.3 Case A: Beam Seas at the Top of Sea State 4

The data corresponding to this case are shown in Table 12.2. This table presents the particular parameters used for the controller, the sea state and sailing conditions, and the performance in terms of roll angle reduction, roll acceleration reduction and MII reduction. The time series corresponding to this case are shown in Figure 12.6.

This case is close to the worst condition the ship can experience with regard to roll motion for the assumed sea state. The encounter frequency is close to the natural roll frequency, which is approximately 1 rad/s. Therefore, the roll excitation due to the waves is close to resonance. Notwithstanding this, we can still observe good performance. We can see from the time series that the rudder angle satisfies the constraints and is permanently at the limit of its operative conditions in both rate and magnitude.

Results over 20 different realisations, indicate roll reductions of the order of 60-65% for roll RMS values. A significant improvement is achieved, however, in regard to MII: 90–95% reduction.

Table 12.2. Rudder roll stabilization simulation report for beam seas at the top of Sea State 4–SS4.

MPC parameters	Symbol	Value	Unit
Prediction horizon	N	10	samples
Sampling time	T_s	0.25	sec
Rudder magnitude constraint	$\Delta\mathbf{u}_{max}$	22	deg
Rudder rate constraint	$\mathbf{u}_{max}$	20	deg/sec
Tuning	$\lambda, \gamma_p, \gamma_\alpha$	0.95, 1, 1	–
Sailing Conditions	**Symbol**	**Value**	**Unit**
Wave spectrum	$\mathbf{S}_{\zeta\zeta}(\omega)$	ITTC	$m^2 sec$
Significant wave height	$\mathrm{H}_{1/3}$	2.5	m
Average Wave period	T	7.5	sec
Encounter angle	χ	90	deg
RRS Performance	**Symbol**	**Value**	**Unit**
Heading deviation (RMS)	$\Delta\psi$	3.6	deg
Rudder angle (RMS)	α	15.15	deg
Roll Angle—Autopilot only (RMS)	ϕ	8.13	deg
Roll Angle—Autopilot + RRS (RMS)	ϕ	2.89	deg
Reduction Angle (RMS)	RR	**64.38**	%
Roll Acceleration—Autopilot only (RMS)	$\ddot{\phi}$	7.22	deg/sec^2
Roll Acceleration—Autopilot + RRS (RMS)	$\ddot{\phi}$	2.94	deg/sec^2
Reduction Acceleration (RMS)	RR	**59.24**	%
MII—Autopilot only	MII	5.02	per min
MII—Autopilot + RR	MII	0.057	per min
Reduction MII	RR	**98.85**	%

12.10.4 Case B: Quartering Seas at the Top of Sea State 5

Table 12.3 shows the result obtained for this case, and Figure 12.7 depicts the corresponding time series.

As expected, the performance in quartering seas decreases significantly due to the low encounter frequency of the disturbance and the interference with yaw. As discussed in Chapter 9, the fundamental limitations associated with the NMP zero of the rudder-to-roll response and the underactuated nature of the system swamp the limitations due to the constraints imposed by the limited authority of the rudder. Note from Figure 12.7 that the rudder angle is far away from the constraints.

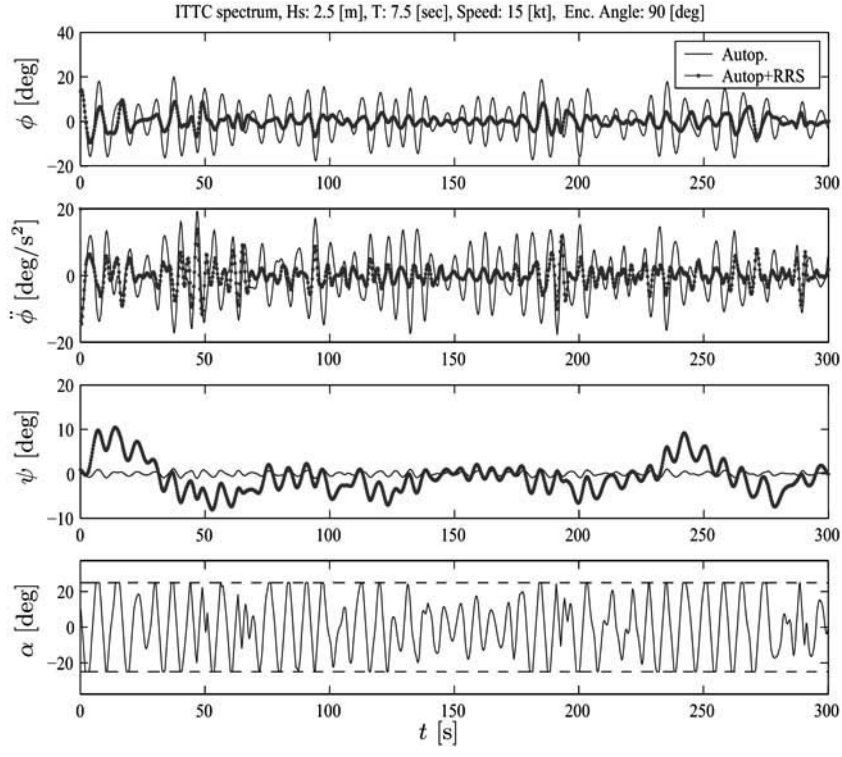

Fig. 12.6. Case A. Simulation for SS4 in beam seas and high gain (λ=0.9, γ_p=1). Angles are given in degrees, and the roll acceleration in deg/sec^2.

12.10.5 Case C: Bow Seas at the Top of Sea State 5

Table 12.4 shows the result obtained for this case, and Figure 12.8 depicts the corresponding time series.

This case presents good performance. If we compare the RMS of roll in open loop with that of Case B, we can see that these are similar. However, due to the higher encounter frequency, the interference with the heading is smaller, and thus the roll reduction is significantly better, and limited only by the rate constraints of the rudder motion.

12.10.6 The Role of Adaptation

Table 12.5 shows how the adaptation of parameters of the roll wave-induced model used in the controller influence the performance for a particular example. In this example, the relative heading with respect to the waves was changed from quartering to beam seas, *i.e.* χ: 45 →90 deg, and also from beam to bow seas, *i.e.* χ: 90 → 135 deg. The second column of Table 12.5

Table 12.3. Rudder roll stabilization simulation report for quatering seas at the top of Sea State 5—SS5.

MPC parameters	Symbol	Value	Unit
Prediction horizon	N	10	samples
Sampling time	T_s	0.25	sec
Rudder magnitude constraint	$\Delta\mathbf{u}_{max}$	22	deg
Rudder rate constraint	$\mathbf{u}_{max}$	20	deg/sec
Tuning	$\lambda, \gamma_p, \gamma_\alpha$	0.95, 1, 1	–
Sailing Conditions	**Symbol**	**Value**	**Unit**
Wave spectrum	$\mathbf{S}_{\zeta\zeta}(\omega)$	ITTC	$m^2 sec$
Significant wave height	$\mathrm{H}_{1/3}$	4	m
Average Wave period	T	7.5	sec
Encounter angle	χ	45	deg
RRS Performance	**Symbol**	**Value**	**Unit**
Heading deviation (RMS)	$\Delta\psi$	5.0	deg
Rudder angle (RMS)	α	7.42	deg
Roll Angle—Autopilot only (RMS)	ϕ	3.68	deg
Roll Angle—Autopilot + RRS (RMS)	ϕ	2.19	deg
Reduction Angle (RMS)	RR	**40.33**	%
Roll Acceleration—Autopilot only (RMS)	$\ddot{\phi}$	0.65	deg/sec^2
Roll Acceleration—Autopilot + RRS (RMS)	$\ddot{\phi}$	0.42	deg/sec^2
Reduction Acceleration (RMS)	RR	**34.7**	%
MII—Autopilot only	MII	0.0	per min
MII—Autopilot + RR	MII	0.0	per min
Reduction MII	RR	—	%

shows the performance of the RRS after the change in heading for the cases in which the parameters of the wave roll motion model were not adapted, and kept the values used in the condition prior to the change. The third column shows the result after letting the parameters be updated to the new condition. The parameters were updated using closed-loop measurements.

For the change of heading from quartering seas to beam seas, there is a significant improvement in performance when adapting the parameters. This is because, for this example, the change in encounter frequency is large, requiring a significant update of the parameters. For the change of heading from beam to bow seas, the increase in performance is not as large, due to the relatively small changes in the parameters of the model.

Although, we have considered only a simple case to illustrate the role of adaptation, one should bear in mind that changes in speed as well as sea state can lead to important variations in the characteristics of roll motion (power spectrum); and therefore, adaptation plays a significant role in the proposed strategy.

It should also be mentioned that the use of a model to predict the disturbance over the prediction horizon can be considered as a feed-forward term.

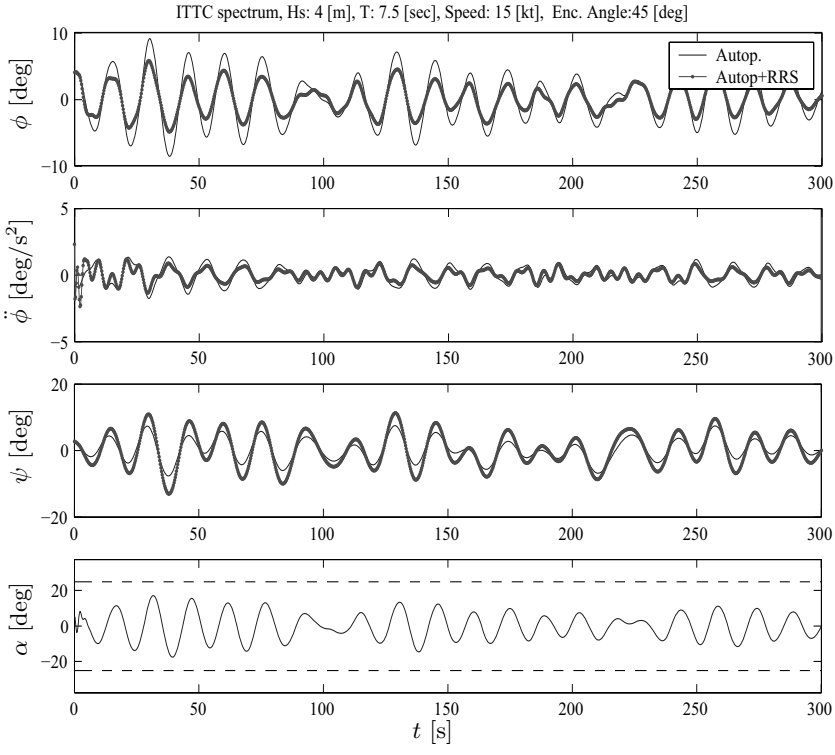

Fig. 12.7. Case B. Simulation for SS5 in quartering seas and high gain (λ=0.9, γ_p=1). Angles are given in degrees, and the roll acceleration in deg/sec^2.

By augmenting the model to incorporate the wave-induced roll motion and using the observer to estimate the states of this model, the control scheme is similar to that shown in Figure 8.10. This, together with the adaptation of the parameters of the disturbance model ensure that the roll amplifications characteristic of classical controllers (PID and $\mathcal{H}_\infty$) will not occur.

12.10.7 A Comment About the Simulation Results

The simulations shown above illustrate some of the most relevant situations. Note that in all the cases, the parameters of the controller are fixed for all the simulations. The only part of the controller that changed with each sailing condition was the model for the disturbance, which was estimated from closed loop measurements.

The three cases for which we have shown the time series illustrate the different possibilities with respect to constraint handling and performance limitations. Indeed, in Case A, the encounter frequency is high enough so that

Table 12.4. Rudder roll stabilization simulation report for bow seas at the top of Sea State 5—SS5.

MPC parameters	Symbol	Value	Unit
Prediction horizon	N	10	samples
Sampling time	T_s	0.25	sec
Rudder magnitude constraint	$\Delta\mathbf{u}_{max}$	22	deg
Rudder rate constraint	$\mathbf{u}_{max}$	20	deg/sec
Tuning	$\lambda, \gamma_p, \gamma_\alpha$	0.95, 1, 1	–
Sailing Conditions	**Symbol**	**Value**	**Unit**
Wave spectrum	$\mathbf{S}_{\zeta\zeta}(\omega)$	ITTC	$m^2 sec$
Significant wave height	$\mathrm{H}_{1/3}$	4	m
Average Wave period	T	9.5	sec
Encounter angle	χ	135	deg
RRS Performance	**Symbol**	**Value**	**Unit**
Heading deviation (RMS)	$\Delta\psi$	1.72	deg
Rudder angle (RMS)	α	10.85	deg
Roll Angle—Autopilot only (RMS)	ϕ	6.53	deg
Roll Angle—Autopilot + RRS (RMS)	ϕ	2.54	deg
Reduction Angle (RMS)	RR	**61.0**	%
Roll Acceleration—Autopilot only (RMS)	$\ddot{\phi}$	6.12	deg/sec^2
Roll Acceleration—Autopilot + RRS (RMS)	$\ddot{\phi}$	2.89	deg/sec^2
Reduction Acceleration (RMS)	RR	**52.7**	%
MII—Autopilot only	MII	4.84	per min
MII—Autopilot + RR	MII	0.04	per min
Reduction MII	RR	**99**	%

Table 12.5. Performance after a change in course from quartering to beam seas and from beam to bow seas with no adaptation (NA) and after adapting the disturbance predictor (A).

ITTC, Hs=2.5m,T=7.5s	45→90NA	45→90A
Roll red %	41.5	65.2
Roll Acc Red %	36.0	60.6
MII red %	81.2	99.1
Yaw rms	0.70	0.86
Rudder rms	6.2	10.1
ITTC, Hs=2.5m,T=7.5s	**90→135NA**	**90→135A**
Roll red %	62.0	66. 4
Roll Acc Red %	46.7	56.6
MII red %	100	100
Yaw rms	0.33	0.4
Rudder rms	4.2	5.2

limitations due to the coupling between roll and the steering characteristics are not significant, but sufficiently low so as to enable the controller to use the

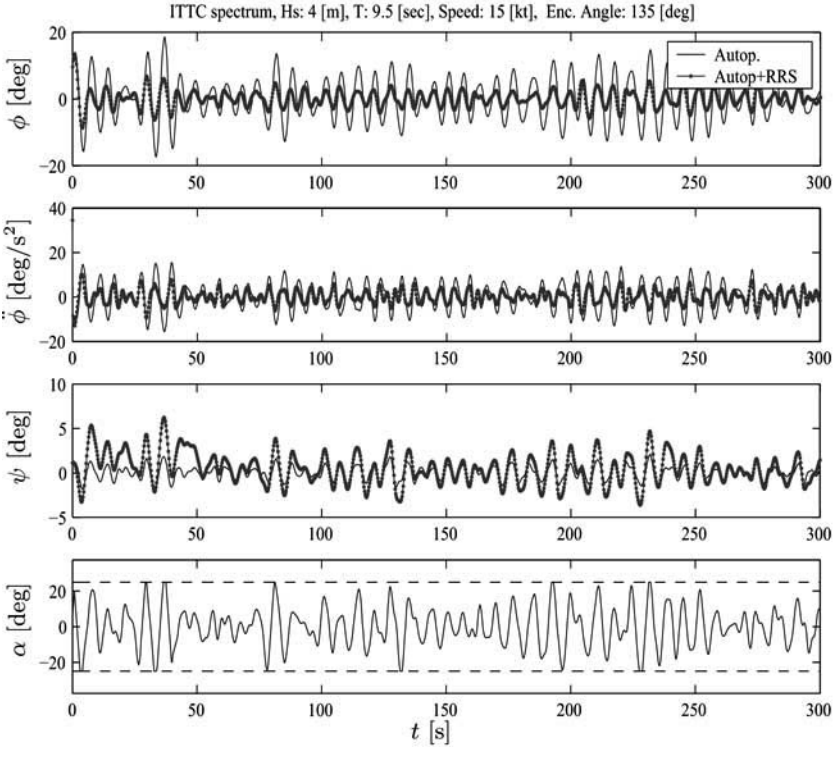

Fig. 12.8. Case C. Simulation for SS5 in bow seas and high gain control (λ=0.9, γ_p=1.) Angles are given in degrees, and the roll acceleration in deg/sec^2.

full speed of the rudder. The controller limits the maximum angle. In Case B, the encounter frequency is low, and the limitation due to the interaction between roll and the steering characteristics of the vessel are the dominant limiting factor. Note that the rudder angle does not reach the constraints in either magnitude or rate. Finally, in Case C, the encounter frequency is high and the main limitation is the constraint in rudder rate to avoid the saturation of the steering machinery.

These simulations illustrate the performance of MPC as a possible solution to handle the constrained control problem of rudder-based stabilizers. The results obtained in the simulations are in agreement with the performance expected and the changes in performance due to changing sailing conditions according to the study of fundamental limitations performed in Chapter 8 and 9.

13

Constrained Control of Fin Stabilisers

This chapter addresses the control system design of fin stabilisers. The particular problem of dynamic stall is discussed and a constrained control design solution is proposed.

13.1 Performance and Control of Rudder and Fins

The performance of fin stabilisers is usually superior to that of RRS mainly because of two main reasons:

- Fins have more capacity than rudders to produce roll. The roll arm of stabiliser fins is usually larger than that of rudders due to the location of the fins on the hull, *i.e.* $r_f > r_r$—see Figures 5.9 and 5.11. Therefore, small fins can produce a significant roll moment.

- There is, in general, a small coupling between the roll and yaw motion produced by the fins, due to the location of the fins in the hull.

Because of the small coupling with the steering, the design of controllers for fin stabilisers can be performed under the assumption that the roll motion is decoupled from the other components of motion—this simplifies the design and results in effective classical controllers like PID and $\mathcal{H}_\infty$. If the fins are located either far aft or ahead of the centre of gravity, however, there will be a coupling with the steering, which can reduce the performance of the fins. This problem has long been recognised in fin stabiliser design [43] and has two consequences.

If the fins are located aft from the centre of gravity, they also produce a yaw moment similar to that produced by the rudder. In this case, there will be a non-minimum phase zero in the fin-to-roll response, and the usual control design trade-off for classical controllers holds: reducing the roll at frequencies close to the vessel's roll natural frequency will result in amplifications of roll at high and low frequencies—see Chapter 8. This zero, however, is usually

located closer to the imaginary axis than it is for rudders. Therefore, only sailing conditions resulting very low encounter frequency will usually produce problems [135, 136].

The other consequence of the coupling with the steering is that, if there is no appropriate wave filtering for the autopilot, it can happen that fins and rudder act against each other and the effectiveness of the fins is reduced [43]. One solution to this problem consists of selecting the location of the fins so as to minimise the coupling with the heading. This may not always be feasible because ship designs are constrained by many factors, which may have higher priority than the location of the fins. A second solution is to design an integrated rudder and fin stabiliser control system. The latter improves the performance of both the autopilot and the fins, even when the potential of the rudder to reduce roll is low.

From the control point of view, another advantage of fins (apart from using only the decoupled roll model for design) is that, because of their size, small and fast hydraulic machinery can be used to command them. Therefore, limitations due to fin rate motion are not as critical as for RRS—stability issues due to slow actuator dynamics are seldom a problem. Magnitude constraints, however, can be more complex to handle than in the case of rudder stabilisers. Fins have a large arm with respect to the centre of gravity of the ship, which is advantageous for producing roll moments; however, this long arm results in the local flow velocities induced by large roll motion affecting the performance. This can result in dynamic stall conditions—see Section 5.3 in Chapter 5. As we will see, when this happens, and the control design does not for this, large performance degradation can result. This problem can be addressed using a special characteristic of MPC: a combination of input and output constraints.

13.2 A Model for Fin Stabilizer Control Design

The decoupled linear equations of motion for roll in the body-fixed frame are

$$\begin{aligned} I_{44}\dot{p} + Dp + G\phi &= \tau^b_{4\text{fins}} + \tau^b_{4\text{w}}, \\ \dot{\phi} &= p, \end{aligned} \tag{13.1}$$

where τ^b_{fins} is the roll moment generated by the fins, and $\tau^b_{4\text{w}}$ the roll moment generated by the waves. The inertia $I_{\phi\phi} = I_{xx} - K_{\dot{p}}$ is the total roll inertia, and damping coefficient D is an equivalent linear damping, which accounts for potential and viscous effects, which for roll are the main source of damping. This equivalent damping can be obtained using energy-based or stochastic linearisation:

$$D = \arg\min_{D_{\text{L}}} \mathbf{E}\{(D_{\text{NL}}(p) - D_{\text{L}}\, p)^2\}, \tag{13.2}$$

where $D_{\mathrm{NL}}(p)$ is the nonlinear damping usually of the form $D_{\mathrm{NL}}(p) = K_p p + K_{|u|p} U p + K_{p|p|} p|p|$. For details on statistical linearisation of roll damping see [182, 192].

The total roll moment generated by the fins, which is the control action, can be expressed as (see (5.11))

$$\tau^b_{\mathrm{fins}} = 2K_\alpha \alpha_e, \qquad K_\alpha \triangleq \frac{1}{2}\rho\, r_f V_{fl}^2 A_f \left.\frac{\partial C_L}{\partial \alpha_e}\right|_{\alpha_e=0}, \tag{13.3}$$

where ρ is the water density, r_f is the fin moment arm, V_{fl} is the relative speed between the fins and the flow (which will be approximated as the forward speed of the vessel, *i.e.* ($V_{fl} \approx U$), A_f is the area of the fins, C_L is the lift coefficient, and α_e the effective angle of attack between the fins and the fluid velocity. The effective angle of attack can be defined using the magnitudes depicted in Figure 5.5:

$$\alpha_e = -\alpha_{fl} - \alpha, \tag{13.4}$$

with

$$\alpha_{fl} = \arctan\left(\frac{v_{\mathrm{roll}}}{U}\right) = \arctan\left(\frac{r_f\, p}{U}\right) \approx \frac{r_f}{U} p. \tag{13.5}$$

where α is the mechanical angle of the fins (control command), and α_{fl} is the angle induced by the combination of roll rate and forward speed of the vessel. With the adopted positive convention, we have $\tau_{\mathrm{fins}} > 0$ whenever $\alpha_e > 0$. If we consider $\alpha_{fl} = 0$, positive mechanical angles of the fins will induce a negative roll moment: the positive mechanical angles have been defined using the right hand side convention for both fins. Similarly, if $\alpha = 0$, the flow angle induced by the combination of positive roll rate p and forward speed of the vessel U will induce a negative roll moment. The roll moment induced by the fins can then be expressed as

$$\tau^b_{4\mathrm{fins}} = 2K_\alpha \left(-\frac{r_f}{U} p - \alpha\right). \tag{13.6}$$

To design the control system, we will assume an output disturbance, *i.e.* instead of considering the wave excitation moment, τ^b_{w} as a disturbance, *cf.* (13.1), we will consider the motion induced by this moment as a disturbance. Under this assumption, the model describing the control-induced motion is given by

$$\begin{bmatrix} \dot{\phi}^{\mathrm{c}} \\ \dot{p}^{\mathrm{c}} \end{bmatrix} = \begin{bmatrix} 0 & 1 \\ I_{44}^{-1} G & I_{44}^{-1} D - K_\alpha \frac{r_f}{U} \end{bmatrix} \begin{bmatrix} \phi^{\mathrm{c}} \\ p^{\mathrm{c}} \end{bmatrix} - \begin{bmatrix} 0 & K_\alpha \\ 0 & K_\alpha \end{bmatrix} \begin{bmatrix} \alpha^{\mathrm{sf}} \\ \alpha^{\mathrm{pf}} \end{bmatrix}, \tag{13.7}$$

where α^{sf} and α^{pf} are the starboard and port fin mechanical angles respectively. It is common practice to design the control assuming only one control input, and then command one fin out of phase with respect to the other. Nevertheless, the experimental work of [80] shows that as the sea state becomes severe, the flow of the windward fin is often affected by the waves more than

the flow of the leeward fin. Hence, it will be convenient to consider the angle of starboard and port fins as two separate control commands when constraints are incorporated into the design. The super-script c in the variables of (13.7) indicates control-induced motion.

Using the zero-order hold method, a discrete-time equivalent system can be obtained for (13.7):

$$\mathbf{x}^{\mathrm{c}}_{k+1} = \mathbf{\Phi}_{\mathrm{c}}\mathbf{x}^{\mathrm{c}}_{k} + \mathbf{\Gamma}_{\mathrm{c}}\mathbf{u}_k, \tag{13.8}$$

where

$$\mathbf{x}^{\mathrm{c}}_{k} = \begin{bmatrix} \phi^{\mathrm{c}}_k \\ p^{\mathrm{c}}_k \end{bmatrix} \qquad \text{and} \quad \mathbf{u}_k = \begin{bmatrix} \alpha^{\mathrm{fs}}_k \\ \alpha^{\mathrm{fp}}_k \end{bmatrix}. \tag{13.9}$$

By combining this model with the wave-induced roll model given in (12.15) (*cf.* Section 12.4.2) we obtain an augmented model, which can be used for stabiliser control system design

$$\begin{aligned} \mathbf{x}_{k+1} &= \mathbf{\Phi}\mathbf{x}_k + \mathbf{\Gamma}\mathbf{u}_k + \mathbf{w}_k, \\ \mathbf{y}_k &= \mathbf{C}\mathbf{x}_k + \mathbf{n}_k, \end{aligned} \tag{13.10}$$

where the augmented state is

$$\mathbf{x}_k = [\phi^{\mathrm{c}}_k,\, p^{\mathrm{c}}_k,\, \phi^{\mathrm{w}}_k,\, p^{\mathrm{w}}_k]^{\mathrm{T}}, \tag{13.11}$$

$$\begin{aligned} \mathbf{y}_k &= [(\phi^{\mathrm{c}}_k + \phi^{\mathrm{w}}_k),\, (p^{\mathrm{c}}_k + p^{\mathrm{w}}_k)]^{\mathrm{T}}, \\ &\triangleq [\phi_k,\, p_k]^{\mathrm{T}}, \end{aligned} \tag{13.12}$$

and

$$\mathbf{\Phi} = \begin{bmatrix} \mathbf{\Phi}_{\mathrm{c}} & \mathbf{0} \\ \mathbf{0} & \mathbf{\Phi}^{\mathrm{w}}_{\phi} \end{bmatrix}, \quad \mathbf{\Gamma} = \begin{bmatrix} \mathbf{\Gamma}_{\mathrm{c}} \\ \mathbf{0} \end{bmatrix}, \quad \mathbf{C} = \begin{bmatrix} 1\,0\,1\,0 \\ 0\,1\,0\,1 \end{bmatrix} \tag{13.13}$$

To this model, we can apply the same Kalman filtering techniques for state estimation used in Chapter 12—See also Appendix A. The parameters of wave-induced roll part of the model can be estimated as discussed in Section 12.5.

13.3 Output Constraints to avoid Dynamic Stall

As discussed in Section 5.3, stabiliser fins normally operate in unsteady conditions. From the control system design perspective, these effects can be neglected altogether in *most* cases, and the design can be performed using the steady hydrodynamic characteristic of the fins, *i.e.* the steady lift *vs.* angle of attack characteristic discussed in Section 5.2. The steady characteristics describe the behaviour of the fin accurately when the motion of the ship and the action demanded by the controller result in a quasi-steady motion of the fins.

In severe sea states, however, the motion of the hull and the water particle orbits close to the fin can induce a large effective angle of attack even for small mechanical angles of the fin. This produces flow separation and loss of control

action. Unlike commonly encountered actuators found in control applications, when the flow separation occurs under unsteady condition a severe hysteric behaviour develops and the control action is lost until the effective angle of attack is reduced and the flow reattaches—see Figure 5.7.

Recent experimental results aimed at investigating operational limits of fin stabilizers reported in [80] indicate that the degradation roll reduction due to the development of dynamic stall can be severe. Indeed, Figure 13.1 depicts a record of roll motion in such a situation for a scale model of a ferry.

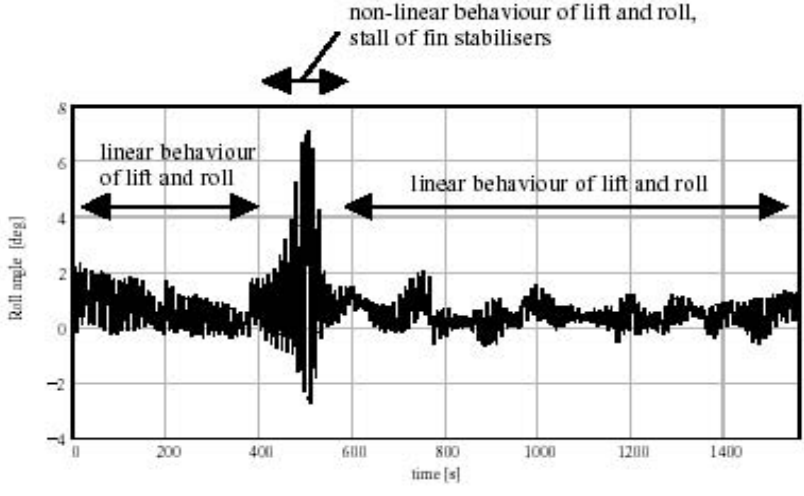

Fig. 13.1. Roll motion under fin dynamic stall of a 1:40 model of a 180m fast ferry at 35kts in quartering irregular seas. Experiments performed at MARIN-Maritime Research Institute Netherlands. Courtesy of MARIN.

From the results reported in [80], it also follows that even during the unsteady operation of fins, stall can be prevented provided the effective angle of attack is not taken beyond the steady-flow stall angle. This indicates that a constraint on the effective angle of attack could prevent the development of dynamic stallling conditions. Therefore, we will consider the control design subject to the following constraint:

$$\begin{bmatrix} 0 & \frac{-rf}{U} \\ 0 & \frac{-rf}{U} \end{bmatrix} \begin{bmatrix} \phi \\ p \end{bmatrix} - \begin{bmatrix} \alpha_k^{\mathrm{fs}} \\ \alpha_k^{\mathrm{fp}} \end{bmatrix} < \begin{bmatrix} \alpha_{\mathrm{s}} \\ \alpha_{\mathrm{p}} \end{bmatrix}, \tag{13.14}$$

where $\alpha_{\mathrm{s}}, \alpha_{\mathrm{p}} \leq \alpha_{\mathrm{stall}}$—the steady flow stall angle. The reason for taking the constraint α_{s} and α_{p} to be less than the steady-flow stall angle is that there is uncertainty associated with the influence of the orbital particle velocity on the effective angle of attack, due to the waves moving relative to the hull.

13.4 A MPC Fin-Stabiliser Controller

Similarly to the problem of RRS, we can pose the constrained control problem for fin stabilisers as follows:

Definition 13.1 (Output-Feedback Constrained Control Problem for Fins). *Find the feedback control command* $\mathbf{u}_k = \mathcal{K}(\mathbf{y}_k)$*, that minimizes the following cost:*

$$V = \lim_{N\to\infty} \frac{1}{N} \mathbf{E}\left\{ \sum_{k=0}^{N} \mathbf{y}_k^{\mathrm{T}} \mathbf{Q} \mathbf{y}_k + \mathbf{u}_k^{\mathrm{T}} \mathbf{R} \mathbf{u}_k \right\}, \tag{13.15}$$

subject to the system (13.10)*:*

$$\begin{aligned} \mathbf{x}_{k+1} &= \mathbf{\Phi}\mathbf{x}_k + \mathbf{\Gamma}\mathbf{u}_k + \mathbf{w}_k, \\ \mathbf{y}_k &= \mathbf{C}\mathbf{x}_k + \mathbf{n}_k, \end{aligned}$$

with the given initial conditions $\mathbf{x}_0$*, and previous control command* $\mathbf{u}_{-1}$*, and also subject to the following constraints*

$$|\mathbf{u}_k| \le \mathbf{u}_{\max} \qquad \text{and} \qquad |\check{\mathbf{u}}_k - \check{\mathbf{u}}_{k-1}| \le \mathbf{\Delta}_u \qquad |\mathbf{N}\mathbf{y}_k - \mathbf{u}_k| \le \mathbf{\Delta}_{yu}, \tag{13.16}$$

where

$$\mathbf{u}_{\max} = \begin{bmatrix} \alpha_{\max} \\ \alpha_{\max} \end{bmatrix}, \ \mathbf{\Delta}_u = \begin{bmatrix} \Delta_u \\ \Delta_u \end{bmatrix}, \ \mathbf{N} = \begin{bmatrix} 0 & \frac{-rf}{U} \\ 0 & \frac{-rf}{U} \end{bmatrix}, \text{ and } \mathbf{\Delta}_{yu} = \begin{bmatrix} \alpha_{\mathrm{s}} \\ \alpha_{\mathrm{p}} \end{bmatrix}, \tag{13.17}$$

with $\alpha_{\max}$ *being the maximum mechanical angle allowed to the fins,* Δ_u *the maximum fin rate allowed by the hydraulic machinery commanding the fins,* U *the forward speed of the vessel and* $\alpha_{\mathrm{s}}, \alpha_{\mathrm{p}} \le \alpha_{\mathrm{stall}}$*.* ○ ○ ○

If the matrices $\mathbf{Q}$ and $\mathbf{R}$ in (13.15) are chosen

$$\mathbf{Q} = \begin{bmatrix} q_\phi & 0 \\ 0 & q_p \end{bmatrix} \qquad \mathbf{R} = \begin{bmatrix} q_{sf} & 0 \\ 0 & q_{pf} \end{bmatrix}, \tag{13.18}$$

Then the cost function can be interpreted as

$$V \propto q_\phi \mathbf{var}[\phi] + q_p \mathbf{var}[\dot{p}] + q_{sf} \mathbf{var}[\alpha^{\mathrm{fs}}] + q_{pf} \mathbf{var}[\alpha^{\mathrm{fp}}].$$

The solution of the above problem can be approximated using CE-MPC. Thus, we first consider the following finite-horizon optimal control problem (under the assumption that there is full-state information):

Definition 13.2 (Finite-Horizon optimal control problem). *Given the initial condition for the augmented state* $\check{\mathbf{x}}_0$ *we seek the vector of control commands*

$$\check{\mathbf{U}}^{\mathrm{OPT}} = [\check{\mathbf{u}}_0^{\mathrm{OPT}}(\check{\mathbf{x}}_0), \ldots, \check{\mathbf{u}}_{N-1}^{\mathrm{OPT}}(\check{\mathbf{x}}_0)]^{\mathrm{T}}; \tag{13.19}$$

that minimizes the following cost

$$J_N(\check{\mathbf{x}}_0, \mathbf{U}) = \check{\mathbf{x}}_N^{\mathrm{T}}\, \check{\mathbf{S}}\, \check{\mathbf{x}}_N + \sum_{j=0}^{N-1} \check{\mathbf{x}}_j^{\mathrm{T}}\, \check{\mathbf{Q}}\, \check{\mathbf{x}}_j + \check{\mathbf{u}}_j^{\mathrm{T}}\, \check{\mathbf{R}}\, \check{\mathbf{u}}_j, \tag{13.20}$$

subject to

$$\check{\mathbf{x}}_{j+1} = \mathbf{\Phi}\check{\mathbf{x}}_j + \mathbf{\Gamma}\check{\mathbf{u}}_j, \qquad \check{\mathbf{x}}_{j=0} = \check{\mathbf{x}}_0,$$

and

$$|\check{\mathbf{u}}_j| \leq \mathbf{u}_{\max} \qquad \text{and} \qquad |\check{\mathbf{u}}_j - \check{\mathbf{u}}_{j-1}| \leq \mathbf{\Delta}_u \qquad |\mathbf{N}\check{\mathbf{y}}_j - \check{\mathbf{u}}_j| \leq \mathbf{\Delta}_{yu}, \tag{13.21}$$

○ ○ ○

The solution of the above problem reduces to the following quadratic programme:

$$\begin{aligned} \check{\mathbf{U}}^{\mathrm{OPT}} = &\arg\min_{\check{\mathbf{U}}} \frac{1}{2}\check{\mathbf{U}}^{\mathrm{T}}\mathbf{H}\check{\mathbf{U}} + \check{\mathbf{U}}^{\mathrm{T}}\mathbf{F}\check{\mathbf{x}}_0 \\ &\text{s.t.} \quad \mathbf{L}\check{\mathbf{U}} \leq \mathbf{M}, \end{aligned} \tag{13.22}$$

where

$$\mathbf{H} = 2(\boldsymbol{\mathcal{R}} + \boldsymbol{\mathcal{B}}^{\mathrm{T}}\, \boldsymbol{\mathcal{Q}}\, \boldsymbol{\mathcal{B}}), \tag{13.23}$$

$$\mathbf{F} = 2\boldsymbol{\mathcal{A}}^{\mathrm{T}}\, \boldsymbol{\mathcal{Q}}\, \boldsymbol{\mathcal{B}}, \tag{13.24}$$

$$\boldsymbol{\mathcal{Q}} = \mathrm{diag}\{\check{\mathbf{Q}}, \ldots, \check{\mathbf{Q}}, \check{\mathbf{S}}\}\,, \tag{13.25}$$

$$\boldsymbol{\mathcal{R}} = \mathrm{diag}\{\check{\mathbf{R}}, \ldots, \check{\mathbf{R}}\}, \tag{13.26}$$

and

$$\mathbf{\Phi} = \begin{bmatrix} \mathbf{\Phi} \\ \mathbf{\Phi}^2 \\ \vdots \\ \mathbf{\Phi}^N \end{bmatrix}, \qquad \mathcal{B} = \begin{bmatrix} \mathbf{\Gamma} & \mathbf{0} & \cdots & \mathbf{0} \\ \mathbf{\Phi\Gamma} & \mathbf{\Gamma} & \cdots & \mathbf{0} \\ \vdots & \vdots & \ddots & \vdots \\ \mathbf{\Phi}^{N-1}\mathbf{\Gamma} & \mathbf{\Phi}^{N-2}\mathbf{\Gamma} & \cdots & \mathbf{\Gamma} \end{bmatrix}. \tag{13.27}$$

The constraints are given by

$$\mathbf{L} = \begin{bmatrix} \mathcal{I} \\ -\mathcal{I} \\ \mathcal{N} \\ -\mathcal{N} \\ \mathcal{W} \\ -\mathcal{W} \end{bmatrix}; \quad \mathbf{K} = \begin{bmatrix} \overline{\mathbf{U}} \\ -\overline{\mathbf{U}} \\ \overline{\mathbf{Y}} \\ -\overline{\mathbf{Y}} \\ \overline{\mathbf{V}} \\ -\overline{\mathbf{V}}. \end{bmatrix} \tag{13.28}$$

where

$$\mathcal{I} = \begin{bmatrix} \mathbf{I}_{2\times 2} & \cdots & & \mathbf{0} \\ \mathbf{0} & \mathbf{I}_{2\times 2} & & \mathbf{0} \\ \vdots & \ddots & \ddots & \vdots \\ \mathbf{0} & \cdots & \mathbf{0} & \mathbf{I}_{2\times 2} \end{bmatrix} \quad \mathcal{W} = \begin{bmatrix} \mathbf{I}_{2\times 2} & \cdots & & \mathbf{0} \\ -\mathbf{I}_{2\times 2} & \mathbf{I}_{2\times 2} & & \mathbf{0} \\ \vdots & \ddots & \ddots & \vdots \\ \mathbf{0} & \cdots & -\mathbf{I}_{2\times 2} & \mathbf{I}_{2\times 2} \end{bmatrix}, \tag{13.29}$$

$$\mathcal{N} = \begin{bmatrix} -\mathbf{I}_{2\times 2} & \mathbf{0} & \cdots & \cdots & \mathbf{0} \\ \mathbf{NC\Gamma} & -\mathbf{I}_{2\times 2} & \cdots & \cdots & \mathbf{0} \\ \mathbf{NC\Phi\Gamma} & \mathbf{NC\Gamma} & -\mathbf{I}_{2\times 2} & \cdots & \mathbf{0} \\ \vdots & \ddots & \ddots & \ddots & \vdots \\ (\mathbf{NC\Phi}^{N-2}\mathbf{\Gamma}) & (\mathbf{NC\Phi}^{N-3}\mathbf{\Gamma}) & \cdots & \mathbf{NC\Gamma} & -\mathbf{I}_{2\times 2} \end{bmatrix}, \tag{13.30}$$

and

$$\overline{\mathbf{U}} = \begin{bmatrix} \mathbf{u}_{\max} \\ \vdots \\ \mathbf{u}_{\max} \end{bmatrix}; \ \overline{\mathbf{V}} = \begin{bmatrix} \mathbf{u}_{-1} + \mathbf{\Delta}_u \\ \mathbf{\Delta}_u \\ \vdots \\ \mathbf{\Delta}_u \end{bmatrix}; \ \overline{\mathbf{Y}} = \begin{bmatrix} \mathbf{\Delta}_{yu} - \mathbf{NCx}_0 \\ \mathbf{\Delta}_{yu} - \mathbf{NC\Phi x}_0 \\ \vdots \\ \mathbf{\Delta}_{yu} - \mathbf{NC\Phi}^{N-1}\mathbf{x}_0 \end{bmatrix} \tag{13.31}$$

Because the state (13.11) is not available to implement the control, we use the estimate provided by the Kalman filter—certainty equivalent solution. By doing so, the following steps are taken at each sampling instant:

1. Take measurements $\mathbf{y}_k$.
2. Update the state estimate $\hat{\mathbf{x}}_{k|k}$ using the measured output and the previous control.
3. Using the initial condition $\check{\mathbf{x}}_0 = \hat{\mathbf{x}}_{k|k}$, solve the quadratic programme (13.22) to obtain the sequence of controls $\check{\mathbf{U}}^{\text{OPT}}$.
4. Update the control command $\mathbf{u}_k = \check{\mathbf{u}}_0$.

These steps implicitly define the following control law

$$\mathbf{u}_k = \mathcal{K}_N(\hat{\mathbf{x}}_{k|k}). \tag{13.32}$$

13.5 Numerical Simulations

To simulate the unsteady hydrodynamic characteristic of the fins, we can use a piecewise-linear approximation with memory implemented using Petri nets. Figure 13.2 shows this type of model excited with a sinusoidal effective angle of attack. The first two plots (top) depict the linear behaviour of the fin when $\alpha_e < \alpha_{stall}$, *i.e.*

$$C_L \approx \left.\frac{\partial CL}{\partial \alpha_e}\right|_{\alpha_e=0} \alpha_e \tag{13.33}$$

The second set of plots depicts the effect of a minor excess of the stall angle. The third set of plots depicts a major excess. This model captures the effect

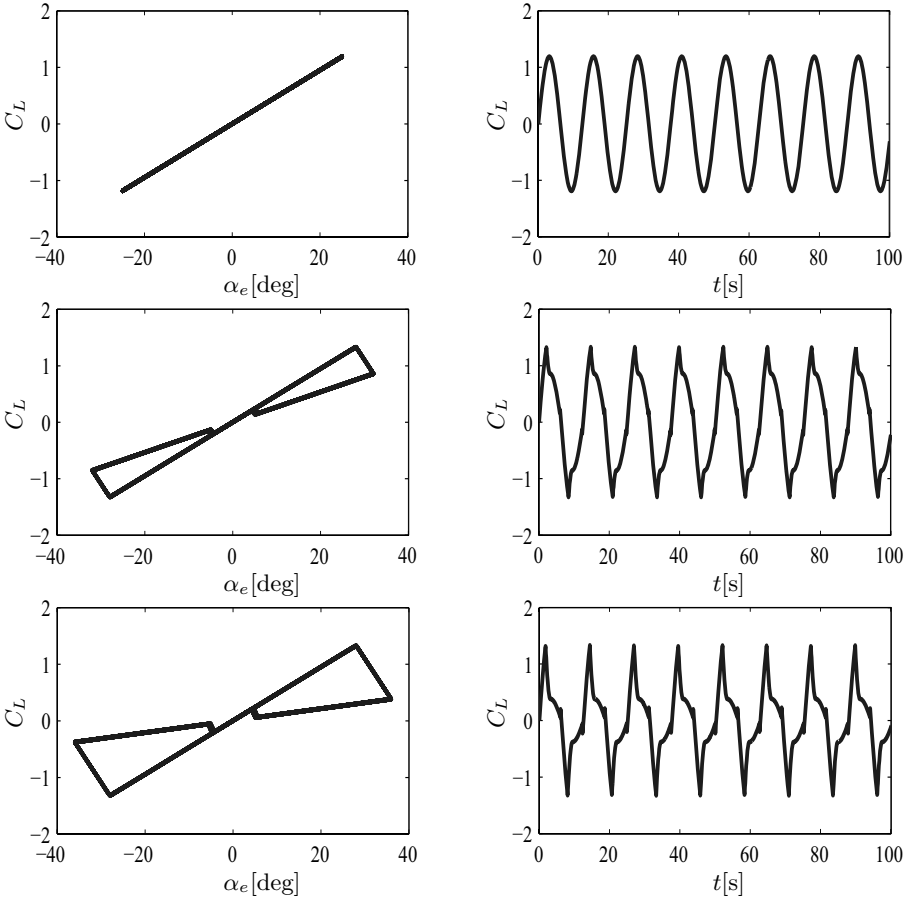

Fig. 13.2. Model for unsteady hydrodynamic characteristic of a foil for a sinusoidal variations of the angle of attack. The top plots (left and right), show the case for no stall. The two middle plots show minor stall, while the bottom plots show major dynamic stall conditions.

of hysteresis, which depends on how much the stall angle has been exceeded. The effects depicted compare well with the experimental results shown in Figure 5.7.

Several scenarios were tested for the vessel sailing at 15 kt, and a sea environment described by the ITTC spectrum parameterized with wave height of 4 m. The controller parameters used in the simulations are shown in Table 13.5. The first set of simulations were performed with a magnitude constraint for the mechanical angle of the fins of 25 deg and maximum rate of 25 deg/s, without any constraint on the effective angle of attach—*i.e.* the usual design situation. We found that, for the benchmark example vessel, with the adopted

sea state, the fins stalled in beam seas only for wave periods of 6 and 7 s—near resonant roll condition.

Table 13.1. MPC parameters used in the simulations.

MPC parameters	Value
Prediction horizon	12 samples
Sampling time	0.25 s
Fin magnitude constraint	25 deg
Fin rate constraint	12 deg/s
Tuning	q_p= 2; q_ϕ= 10; $q_{sf} = q_{pf}$= 0.1

For an average wave period of 7 s, the performance obtained is shown in Figure (13.3). In the first two plots of this figure we can see the roll angle and the roll rate in open and closed loop conditions. The third and fourth plots show the mechanical angle of attack and the effective angle of attack respectively. Finally, the last plot shows the generated lift.

From Figure (13.3), we can appreciate that the effect of dynamic stall on the performance is significant. As stated by Galliarde in [80], when dynamic stall occurs, the ship behaves as if it were in open loop for a few roll periods. This effect is evident in Figure (13.3). The stall is usually triggered by a high wave, and it extends for a few cycles depending on the size of the waves that follow the triggering wave. Since the controller is not informed about the loss of actuation, once the stall starts, the controller demands larger and larger mechanical angles until it reaches the mechanical limits. This, in turn, contributes further to the loss of actuation and may even eliminate the control action—see the time series of the lift in Figure (13.3). In addition, higher waves and thus high roll usually occur in groups. Therefore, this situation contributes to extending the period in which the control action is lost.

Figure 13.4, shows a simulation with the same time series for comparison but with a controller that constrains not only the mechanical angle of the fin but also the effective angle of attack. The improvement is significant. Figure 13.5 shows the lift vs. effective angle of attack of the model for the two cases simulated.

Note also that by incorporating a constraint on the effective angle of attack, rather than reducing the whole control action (cautious approach), the control remains fully capable when there is no risk of dynamic stall. The main issue from the ship performance point of view in these conditions, however, is that the bursts of high roll motion that appear as a consequence of dynamic stall are almost impossible to predict by the crew. This interrupts the tasks performed by the crew and increases the amount of time required for the ship to accomplish its mission. The author recalls a discussion with a naval officer from the Royal Australian Navy who preferred to switch the fin stabilizers off whenever these conditions appeared. The officer argued that it was easier for

the crew to work with higher but predictable roll angles rather than reduced roll angles with occasional bursts of high roll motion.

As already mentioned, from a practical point of view, it is be necessary to constrain the estimated effective angle of attack to take values even smaller than the static stall angle to account for the uncertainty associated with the true effective angle of attack. This can be inferred from the results depicted in Figure 13.5.

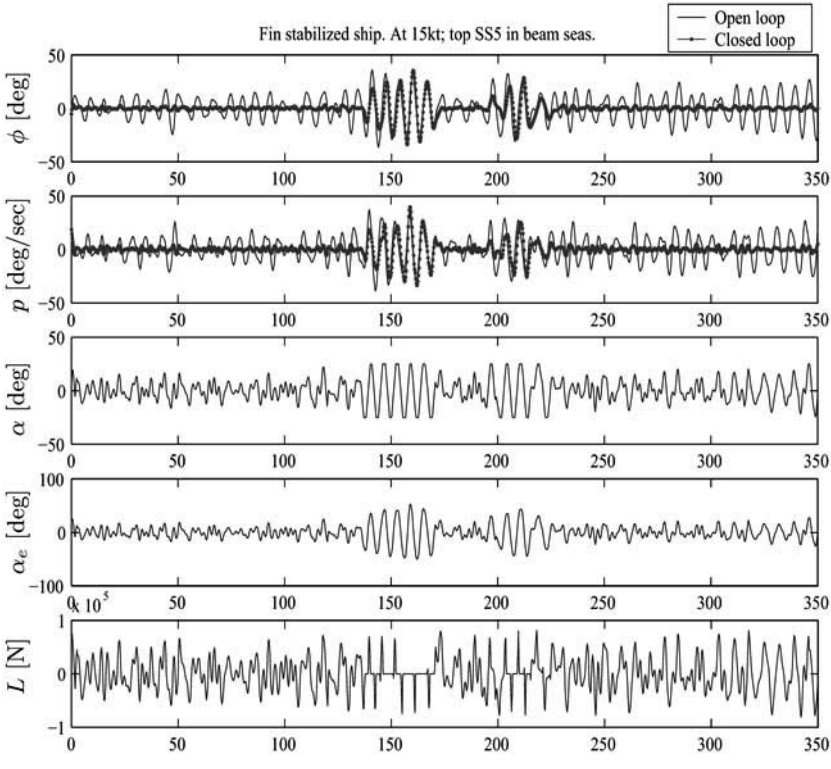

Fig. 13.3. Simulation in Beam seas Top SS5 average wave period 7 sec. No effective angle of attack constraint.

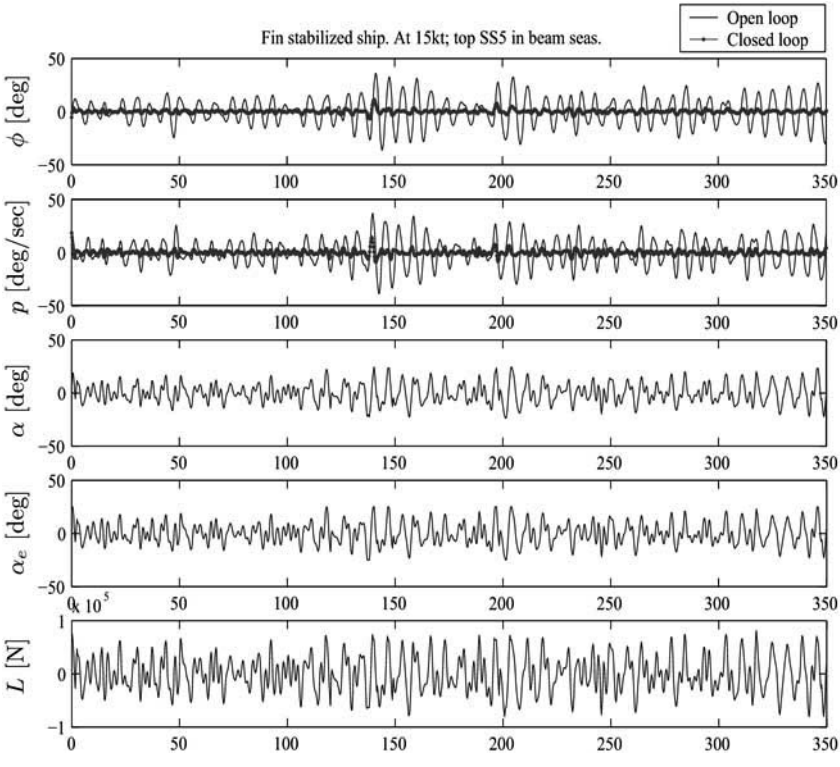

Fig. 13.4. Simulation in Beam seas Top SS5 average wave period 7 sec. With effective angle of attack constraint.

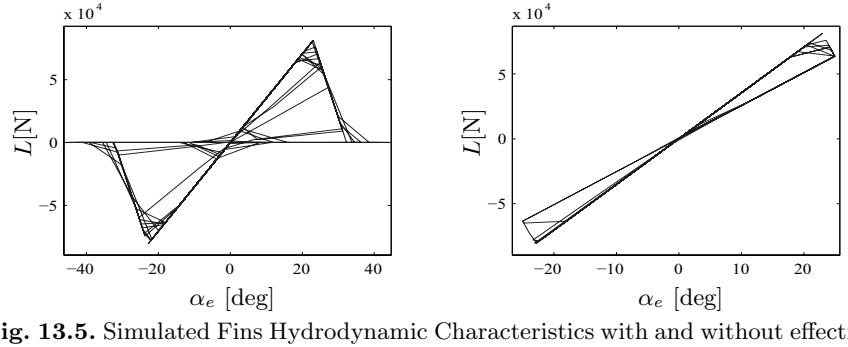

Fig. 13.5. Simulated Fins Hydrodynamic Characteristics with and without effective angle of attack constraint.

13.6 Integrated Control of Rudder and Fins

The extension of the proposed solutions to the integrated control of rudders and fins is trivial. Indeed, the problem is similar to Problem 12.1, but with the state vector

$$\mathbf{x}_k \triangleq \left[v_k^{\mathrm{c}},\, p_k^{\mathrm{c}},\, r_k^{\mathrm{c}},\, \phi_k^{\mathrm{c}},\, \bar{\psi}_k,\, p_k^{\mathrm{w}},\, \phi_k^{\mathrm{w}},\, r_k^{\mathrm{b}}\right]^{\mathrm{T}}, \tag{13.34}$$

and the control

$$\mathbf{u}_k \triangleq \begin{bmatrix} \alpha_k^{\mathrm{rud}} \\ \alpha_k^{\mathrm{fs}} \\ \alpha_k^{\mathrm{fp}} \end{bmatrix}, \tag{13.35}$$

and their respective constraints. The cost function for combined rudder and fin control can be chosen as

$$\begin{aligned} V = &\sum_{k=0}^{N} \lambda\,[\phi_k^2 + \gamma_p (p_{k+1} - p_k)^2] \\ &+ (1-\lambda)[\gamma_r \Delta r_k^2 + \gamma_\psi \Delta \psi_k^2 + \gamma_{\mathrm{rud}} (\alpha_k^{\mathrm{rud}})^2 + \gamma_{fs} (\alpha_k^{\mathrm{fs}})^2 + \gamma_{\mathrm{pf}} (\alpha_k^{\mathrm{fp}})^2]. \end{aligned} \tag{13.36}$$

13.7 Summary and Discussion

After studying the mathematical models, performance assessment methods and fundamental performance limitations during the first three parts of the book, all the key ingredients for the control system design were presented. This final part of the book, then, addressed the control system design.

The results obtained via numerical simulations forecast a successful application of MPC to the problem of control system design of rudder and fin stabilizers. The proposed solution provides the designer with a systematic framework to address the multivariable nature of these problems and the different type of constraints that may be required in different scenarios (sailing conditions and type of stabilizers.) Furthermore, with recent advances in both optimization science and computational speed (DSP technology), the problems addressed in this book present no complications regarding computational issues associated with the real-time implementation of MPC. Save for minor improvements, the material presented in this book covers most of the design stages prior to dealing with specific implementation issues.

Finally, the order in which the material was presented provides a systematic approach to control system design—this is not limited to the problems addressed in this book.

A

Observers and Kalman Filtering

Observers are commonly used in ship motion control systems to perform several tasks: filter first-order wave induced motion, estimate magnitudes that are not measured, assist in fault detection, *etc.* This appendix summarises the concept of state estimation using observers, and in particular the so-called Kalman Filter. This material provides enough background for the reader to follow the topics of the book, and references to the literature are included for in-depth discussions of this important topic.

A.1 State Estimation via Observers

Let us assume that we can describe the plant or system to be controlled by

$$\begin{aligned} \dot{\mathbf{x}}(t) &= \mathbf{A}\mathbf{x}(t) + \mathbf{B}\mathbf{u}(t), \\ \mathbf{y}(t) &= \mathbf{C}\mathbf{x}(t), \end{aligned} \tag{A.1}$$

An *observer*, is a dynamic system that provides an estimate of the state of the plant, $\hat{\mathbf{x}}(t)$, based on input and output measurements, *i.e.* $\mathbf{u}(t)$ and $\mathbf{y}(t)$. This can be achieved by copying the dynamics of the plant and incorporating a feedback from the difference between the plant output and the output generated using the the estimates of the state. That is, the observer is of the type

$$\begin{aligned} \dot{\hat{\mathbf{x}}}(t) &= \mathbf{A}\hat{\mathbf{x}}(t) + \mathbf{B}\mathbf{u}(t) + \mathbf{L}(\mathbf{y}(t) - \hat{\mathbf{y}}(t)), \\ \hat{\mathbf{y}}(t) &= \mathbf{C}\hat{\mathbf{x}}(t). \end{aligned} \tag{A.2}$$

The dynamics of the *estimation error*, defined as $\mathbf{e}(t) \triangleq \mathbf{x}(t) - \hat{\mathbf{x}}$, satisfy

$$\dot{\mathbf{e}}(t) = (\mathbf{A} - \mathbf{L}\mathbf{C})\mathbf{e}(t), \tag{A.3}$$

which shows that if $\mathbf{L}$ is designed such that the above equation is stable, then the estimation error tends to zero whatever the initial condition. If the pair $(\mathbf{A}, \mathbf{C})$ is observable, *i.e.* if the information contained in $\mathbf{y}(t)$ is rich enough to estimate the state–see [89], then $\mathbf{L}$ can be designed to locate the eigenvalues of $(\mathbf{A} - \mathbf{LC})$ anywhere in the complex plane, and thus define the rate of convergence of the estimate. See, for example, [89] for details on how to design $\mathbf{L}$ via pole placement.

We can apply the same concept for a discrete-time type of system:

$$\begin{aligned} \hat{\mathbf{x}}_{k+1|k} &= \mathbf{A}\hat{\mathbf{x}}_{k|k-1} + \mathbf{B}\mathbf{u}_k + \mathbf{L}(\mathbf{y}_k - \hat{\mathbf{y}}_{k|k-1}), \\ \hat{\mathbf{y}}_{k|k-1} &= \mathbf{C}\hat{\mathbf{x}}_{k|k-1}, \end{aligned} \tag{A.4}$$

where the error $\mathbf{e}_{k|k-1} \triangleq \mathbf{x}_k - \hat{\mathbf{x}}_{k|k-1}$ satisfies

$$\mathbf{e}_{k+1|k} = (\mathbf{A} - \mathbf{LC})\mathbf{e}_{k|k-1}. \tag{A.5}$$

The notation $\hat{\mathbf{x}}_{k+1|k}$ indicates that the estimate of the state at the stage $k+1$ has been obtained using the information up to the stage k, *i.e.* $I^k = \{\mathbf{u}_k, \mathbf{y}_k, \mathbf{u}_{k-1}, \mathbf{y}_{k-1}, ...\mathbf{y}_0\}$. Therefore, this type of observer is called a *predictor observer*.

A discrete-time observer that uses the information of the most current measurement is called a *current observer*. This can be implemented as

$$\begin{aligned} \hat{\mathbf{x}}_{k|k} &= \hat{\mathbf{x}}_{k|k-1} + \mathbf{L}_c(\mathbf{y}_k - \hat{\mathbf{y}}_{k|k-1}), \\ \hat{\mathbf{x}}_{k+1|k} &= \mathbf{A}\hat{\mathbf{x}}_{k|k} + \mathbf{B}\mathbf{u}_k, \\ \hat{\mathbf{y}}_{k|k-1} &= \mathbf{C}\hat{\mathbf{x}}_{k|k-1}. \end{aligned} \tag{A.6}$$

By eliminating $\hat{\mathbf{x}}_{k|k}$, in the above equations, we obtain

$$\hat{\mathbf{x}}_{k+1|k} = (\mathbf{A} - \mathbf{LC})\hat{\mathbf{x}}_{k|k-1} + \mathbf{B}\mathbf{u}_k, \tag{A.7}$$

with $\mathbf{L} = \mathbf{A}\mathbf{L}_c$, from which we can recover the estimation error equation (A.5) and design $\mathbf{L}_c$ such that the estimation error converges to zero. Current observers have, in general, a better performance than predictor observers.

A.2 Kalman Filtering

The Kalman filter is a special type of observer that accounts for the presence of process disturbances and measurement noise, and the gain $\mathbf{L}$ is determined using statistical information.

Consider the time-varying system

$$\begin{aligned} \mathbf{x}_{k+1} &= \mathbf{A}_k\mathbf{x}_k + \mathbf{B}_k\mathbf{u}_k + \mathbf{w}_k, \\ \mathbf{y}_k &= \mathbf{C}_k\mathbf{x}_k + \mathbf{n}_k. \end{aligned} \tag{A.8}$$

The state disturbance $\mathbf{w}_k$ and the measurement noise $\mathbf{n}_k$ are uncorrelated sequences of zero-mean identically distributed Gaussian vectors with finite covariance:

$$\mathbf{E}[\mathbf{w}_k] = 0, \quad \mathbf{E}[\mathbf{n}_k] = 0, \quad \mathbf{E}[\mathbf{w}_k \mathbf{n}_j^{\mathrm{T}}] = \mathbf{0}.$$
$$\mathbf{E}[\mathbf{w}_k \mathbf{w}_j^{\mathrm{T}}] = \begin{cases} \mathbf{C_{ww}} & k = j \\ \mathbf{0} & k \neq j \end{cases}, \quad \mathbf{E}[\mathbf{n}_k \mathbf{n}_j^{\mathrm{T}}] = \begin{cases} \mathbf{C_{nn}} & k = j \\ \mathbf{0} & k \neq j \end{cases}.$$

Let us start by assuming that at the stage k, we have and estimate of the state based on prior information (*a priori estimate*): $\hat{\mathbf{x}}_{k|k-1}$. We also define the *a priori estimation error*,

$$\mathbf{e}_{k|k-1} \triangleq \mathbf{x}_k - \hat{\mathbf{x}}_{k|k-1},$$

which we assume to have a zero mean with known covariance:

$$\boldsymbol{\Sigma}_{k|k-1} = \mathbf{E}[\mathbf{e}_{k|k-1} \mathbf{e}_{k|k-1}^{\mathrm{T}}] = \mathbf{E}[(\mathbf{x}_k - \hat{\mathbf{x}}_{k|k-1})(\mathbf{x}_k - \hat{\mathbf{x}}_{k|k-1})^{\mathrm{T}}].$$

Based on newly available information $\mathbf{y}_k$, let us consider the following estimation update:

$$\hat{\mathbf{x}}_{k|k} = \hat{\mathbf{x}}_{k|k-1} + \mathbf{L}_k(\mathbf{y}_k - \mathbf{C}\hat{\mathbf{x}}_{k|k-1}). \tag{A.9}$$

Using this *a posteriori* update we can define the *a posteriori* estimation error $\mathbf{e}_{k|k} \triangleq \mathbf{x}_k - \hat{\mathbf{x}}_{k|k}$ with covariance:

$$\begin{aligned} \boldsymbol{\Sigma}_{k|k} &= \mathbf{E}[\mathbf{e}_{k|k} \mathbf{e}_{k|k}^{\mathrm{T}}] = \mathbf{E}[(\mathbf{x}_k - \hat{\mathbf{x}}_{k|k})(\mathbf{x}_k - \hat{\mathbf{x}}_{k|k})^{\mathrm{T}}] \\ &= \mathbf{E}\{[(\mathbf{x}_k - \hat{\mathbf{x}}_{k|k-1}) - \mathbf{L}_k(\mathbf{y}_k - \mathbf{C}\hat{\mathbf{x}}_{k|k-1})] \\ &\quad [(\mathbf{x}_k - \hat{\mathbf{x}}_{k|k-1}) - \mathbf{L}_k(\mathbf{y}_k - \mathbf{C}\hat{\mathbf{x}}_{k|k-1})]^{\mathrm{T}}\}. \end{aligned}$$

Taking the expectation, and noticing that $(\mathbf{x}_k - \hat{\mathbf{x}}_{k|k-1})$ is uncorrelated with the measurement noise, we obtain:

$$\boldsymbol{\Sigma}_{k|k} = (\mathbf{I} - \mathbf{L}_k \mathbf{C}_k) \boldsymbol{\Sigma}_{k|k-1} (\mathbf{I} - \mathbf{L}_k \mathbf{C}_k)^{\mathrm{T}} + \mathbf{L}_k \mathbf{C_{nn}} \mathbf{L}_k^{\mathrm{T}} \tag{A.10}$$

This formula is valid for any value of the gain $\mathbf{L}_k$. Now we seek the *optimal gain (Kalman Gain)*:

$$\mathbf{L}_k^{\mathrm{OPT}} = \arg\min_{\mathbf{L}_k} \mathrm{trace}(\boldsymbol{\Sigma}_{k|k}),$$

That is, the gain that minimizes the sum of the variance of the components of the estimation error:

$$\mathrm{trace}(\boldsymbol{\Sigma}_{k|k}) = \mathbf{var}[e_{1,k|k}] + \mathbf{var}[e_{2,k|k}] + \cdots + \mathbf{var}[e_{n,k|k}].$$

After manipulating (A.10), taking its derivative with respect to $\mathbf{L}$, and equating it to zero, we find–see [40] for details:

$$\mathbf{L}_k^{\text{OPT}} = \boldsymbol{\Sigma}_{k|k-1}\mathbf{C}_k^{\text{T}}(\mathbf{C}_k\boldsymbol{\Sigma}_{k|k-1}\mathbf{C}_k^{\text{T}} + \mathbf{C}_{\mathbf{nn}})^{-1},$$

and

$$\boldsymbol{\Sigma}_{k|k}^{\text{OPT}} = (\mathbf{I} - \mathbf{L}_k^{\text{OPT}}\mathbf{C}_k)\boldsymbol{\Sigma}_{k|k-1}.$$

The current optimal estimate $\hat{\mathbf{x}}_{k|k}^{\text{OPT}}$, is then obtained by using $\mathbf{L}_k^{\text{OPT}}$ in (A.9). This estimate can be projected in time using the model of the system. Indeed, since the process noise $\mathbf{w}_k$ is uncorrelated, the *optimal one-step-ahead prediction* is obtain from

$$\hat{\mathbf{x}}_{k+1|k}^{\text{OPT}} = \mathbf{A}_k\,\hat{\mathbf{x}}_{k|k}^{\text{OPT}} + \mathbf{B}_k\mathbf{u}_k.$$

Also,

$$\begin{aligned}\mathbf{e}_{k+1|k}^{\text{OPT}} &= \mathbf{x}_{k+1} - \hat{\mathbf{x}}_{k+1|k}^{\text{OPT}} = (\mathbf{A}_k\,\hat{\mathbf{x}}_{k|k}^{\text{OPT}} + \mathbf{w}_k) - \mathbf{A}_k\hat{\mathbf{x}}_{k|k}^{\text{OPT}},\\ &= \mathbf{A}_k\,\mathbf{e}_{k|k}^{\text{OPT}} + \mathbf{w}_k,\end{aligned}$$

and then,

$$\boldsymbol{\Sigma}_{k+1|k}^{\text{OPT}} = \mathbf{E}[\mathbf{e}_{k+1|k}^{\text{OPT}}(\mathbf{e}_{k+1|k}^{\text{OPT}})^{\text{T}}] = \mathbf{A}_k\boldsymbol{\Sigma}_{k+1|k}^{\text{OPT}}\mathbf{A}_k^{\text{T}} + \mathbf{C}_{\mathbf{ww}}.$$

Therefore, the Kalman Filter takes the form:

Measurement Update (initial conditions $k = 0, \hat{\mathbf{x}}_{0|-}, \boldsymbol{\Sigma}_{0|-}$):

$$\begin{aligned}\mathbf{L}_k &= \boldsymbol{\Sigma}_{k|k-1}\mathbf{C}_k^{\text{T}}(\mathbf{C}_k\boldsymbol{\Sigma}_{k|k-1}\mathbf{C}_k^{\text{T}} + \mathbf{C}_{\mathbf{nn}})^{-1},\\ \hat{\mathbf{x}}_{k|k} &= \hat{\mathbf{x}}_{k|k-1} + \mathbf{L}_k(\mathbf{y}_k - \mathbf{C}\hat{\mathbf{x}}_{k|k-1}),\\ \boldsymbol{\Sigma}_{k|k} &= (\mathbf{I} - \mathbf{L}_k^{\text{OPT}}\mathbf{C}_k)\boldsymbol{\Sigma}_{k|k-1}.\end{aligned} \tag{A.11}$$

Prediction:

$$\begin{aligned}\hat{\mathbf{x}}_{k+1|k} &= \mathbf{A}_k\,\hat{\mathbf{x}}_{k|k} + \mathbf{B}_k\mathbf{u}_k,\\ \boldsymbol{\Sigma}_{k+1|k} &= \mathbf{A}_k\boldsymbol{\Sigma}_{k+1|k}\mathbf{A}_k^{\text{T}} + \mathbf{C}_{\mathbf{ww}}.\end{aligned} \tag{A.12}$$

Figure A.1 represents the typical order for the operations in a Kalman filter.

A.3 Optimality of Kalman Filters

To outline the derivation of the Kalman Filter algorithm (KF) in the previous section, we posed an optimization problem to minimise the trace of the covariance of the estimation error. The optimality of the KF, however, goes beyond this. Indeed, it can be shown that for the case considered, *i.e.* a linear process with a linear measurement equation and Gaussian white process and measurement noises, the KF is also *optimal* in the sense that it minimizes the conditional covariance of the state, and thus the estimate is the conditional mean[121, 24, 146]:

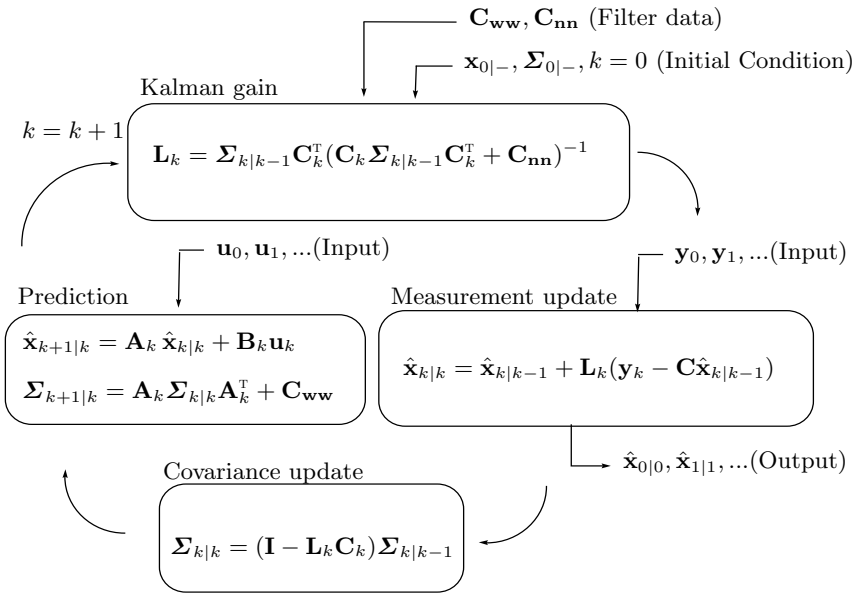

Fig. A.1. Kalman Filter Algorithm

$$\hat{\mathbf{x}}_{k|k}^{\mathrm{OPT}} = \mathbf{E}[\mathbf{x}_k|I^k] = \arg\min_{\hat{\mathbf{x}}} \mathbf{E}[(\mathbf{x}_k - \hat{\mathbf{x}}_k)(\mathbf{x}_k - \hat{\mathbf{x}}_k)^{\mathrm{T}}|I^k],$$

and

$$\boldsymbol{\Sigma}_{k|k}^{\mathrm{OPT}} = \min_{\hat{\mathbf{x}}} \mathbf{E}[(\mathbf{x}_k - \hat{\mathbf{x}}_k)(\mathbf{x}_k - \hat{\mathbf{x}}_k)^{\mathrm{T}}|I^k],$$

where $I^k = \{\mathbf{y}_k, \mathbf{u}_k, \mathbf{y}_{k-1}, \mathbf{u}_{k-1}, \mathbf{y}_{k-2}, \mathbf{u}_{k-2}, ..., \mathbf{y}_0\} = \{\mathbf{y}_k, \mathbf{u}_k, \hat{\mathbf{x}}_{k-1|k-1}^{\mathrm{OPT}}\}$ represents all the past information up to the stage k. Furthermore, because the system is linear and the disturbance and measurement noise are assumed Gaussian, the conditional probability density function (PDF) of the state is given by

$$p_{\mathbf{x}_k|I^k}(\mathbf{x}) \backsim N(\hat{\mathbf{x}}_{k|k}^{\mathrm{OPT}}, \boldsymbol{\Sigma}_{k|k}^{\mathrm{OPT}}),$$

That is, the KF gives the mean and the covariance, and this is all the information we needed to define the conditional PDF. Therefore, any statistic of interest can be determined. This, however, may not be true for the nonlinear and/or non-Gaussian cases. In these cases, other type of filters must be considered–see [7].

A.4 Correlated Disturbances

If the disturbance $\mathbf{w}_k$ in (A.8) is correlated (colored noise), as it is most common in practice, we can use statistical methods (spectral factorisation) to

obtain the model of it:

$$\begin{aligned}\mathbf{z}_{k+1} &= \mathbf{A}_{\mathbf{w}}\mathbf{z}_k + \mathbf{B}_{\mathbf{w}}\mathbf{v}_k,\\ \mathbf{w}_k &= \mathbf{C}_{\mathbf{w}}\mathbf{z}_k,\end{aligned}$$

where $\mathbf{v}_k$ is white with covariance $\mathbf{C}_{\mathbf{vv}}$. Then, we can consider a KF for the augmented model:

$$\begin{bmatrix}\mathbf{x}_{k+1}\\ \mathbf{z}_{k+1}\end{bmatrix} = \begin{bmatrix}\mathbf{A} & \mathbf{C}_{\mathbf{w}}\\ \mathbf{0} & \mathbf{A}_{\mathbf{w}}\end{bmatrix}\begin{bmatrix}\mathbf{x}_k\\ \mathbf{z}_k\end{bmatrix} + \begin{bmatrix}\mathbf{0}\\ \mathbf{B}_{\mathbf{w}}\end{bmatrix}\mathbf{v}_k,$$
$$\mathbf{y}_k = \begin{bmatrix}\mathbf{C} & \mathbf{0}\end{bmatrix}\begin{bmatrix}\mathbf{x}_k\\ \mathbf{z}_k\end{bmatrix} + \mathbf{n}_k.$$

A.5 Practical Kalman Filter: Tuning

- **Measurement Noise ($\mathbf{n}_k$)**: The measurement noise is usually associated with sensor noise. Then, if the sensors do not have biases, and $\sigma_{\mathbf{v}i}$ is an estimate of the RMS value of the component (or channel) i, we can choose

$$\mathbf{C}_{\mathbf{nn}} = \mathrm{diag}(\sigma^2_{\mathbf{n}1}, \sigma^2_{\mathbf{n}2}, \ldots, \sigma^2_{\mathbf{n}p}).$$

- **Initial State and its Covariance ($\mathbf{x}_{0|-}$, $\boldsymbol{\Sigma}_{0|-}$)**: The initial state is an initial guess, and the covariance a measure of certainty of that guess. Some components of $\mathbf{x}_{0|-}$ may be taken from y_{-1}, and the rest are set *ad-hoc*. The matrix $\boldsymbol{\Sigma}_{0|-}$ is chosen to be diagonal with high values for the non-measured states and appropriate values for measured ones.
- **Disturbance ($\mathbf{w}_k$)**: The statistics of the process disturbance are not easy to find or guess in general. Thus, the covariance $\mathbf{C}_{\mathbf{ww}}$ is usually chosen to be diagonal, and its entries are used to tune the filter—this requires trial and error. If $\mathbf{C}_{\mathbf{ww}}$ is chosen zero, $\mathbf{L}_k$ would $\to \mathbf{0}$ as k increases, because $\mathbf{C}_{\mathbf{ww}} = \mathbf{0}$ indicates high certainty in the prediction, then the optimal thing to do is ignoring the noisy update. This will never happen in practice due to uncertainty in the model. Thus, by setting $\mathbf{C}_{\mathbf{ww}} = \mathbf{0}$, one could have a filter that diverges: a dumb and happy filter ignoring measurements.

A.6 Steady State Kalman filter

When the process is stationary, *i.e.* $\mathbf{A}$ does not depend on time, and the disturbance and noise are stationary, often, after a few steps k, the KF reaches steady state values for the gain and the covariance. The steady state covariance

$$\boldsymbol{\Sigma}_\infty = \lim_{k\to\infty} \mathbf{E}[\mathbf{e}_{k|k}\mathbf{e}^{\mathrm{T}}_{k|k}],$$

can be obtained by solvong the following Discrete-time Algebraic Riccati Equation (DARE):

$$\mathbf{A}\boldsymbol{\Sigma}_\infty\mathbf{A}^{\mathrm{T}} - \boldsymbol{\Sigma}_\infty - \mathbf{A}\boldsymbol{\Sigma}_\infty\mathbf{C}^{\mathrm{T}}(\mathbf{C}\boldsymbol{\Sigma}_\infty\mathbf{C}^{\mathrm{T}} + \mathbf{C}_{\mathbf{nn}})^{-1}\mathbf{C}\boldsymbol{\Sigma}_\infty\mathbf{A}^{\mathrm{T}} + \mathbf{C}_{\mathbf{ww}} = \mathbf{0},$$

and then, the steady state Kalman gain is

$$\mathbf{L}_\infty = \boldsymbol{\Sigma}_\infty\mathbf{C}^{\mathrm{T}}(\mathbf{C}\boldsymbol{\Sigma}_\infty\mathbf{C}^{\mathrm{T}} + \mathbf{C}_{\mathbf{nn}})^{-1}.$$

This fixed gain can be used in (A.6) with $\mathbf{L}_c = \mathbf{L}_\infty$ to implement steady state KF. The advantage of the steady-state KF is that we do not need to invert matrices on-line to propagate the covariances as in the algorithm given in Section A.2. The steady-state KF will give an estimation error with a propagation equation such as (A.5) with $\mathbf{L} = \mathbf{A}\mathbf{L}_\infty$. This will be stable provided the pair is stabilisable and the pair $(A, \mathbf{C})$ detectable–see [89] for details.

A.7 Implementation Issues

The equations for the KF presented in this appendix may not be the best choice for real-time implementations. There are numerical issues associated with matrix inversion and covariance propagation; in some cases the covariance matrices could result negative definite due to numerical errors. To solve these issues, different implementations of the equations have been developed to propagate and update the estimates and the covariance. These implementations, known as *square root filtering*, are algebraically equivalent to the equations given here, but exhibit improved numerical precision and stability. For details see for example [146].

B

A Benchmark Example: Naval Vessel

The vessel model presented here corresponds to a small relatively fast monohull. This vessel was never built. The model is based on the drawing lines and load conditions of a design by ADI-Limited Australia.

The author has modified the data provided by ADI-limited so as to match the load condition and main particulars of a vessel with similar characteristics presented by Blanke and Christensen, [33]. This way the RAOs calculated by the author can be combined with the manoeuvring model from [33] to have a complete benchmark example. The hydrostatic data, as well as the RAOs, were obtained by the author using ShipX-VERES by MARINTEK AS [64].

The author would like to thank Martin Williams from ADI-Limited Australia for the shared data and also MARINTEK AS Trondheim for the use of ShipX-VERES.

B.1 Hull Shape

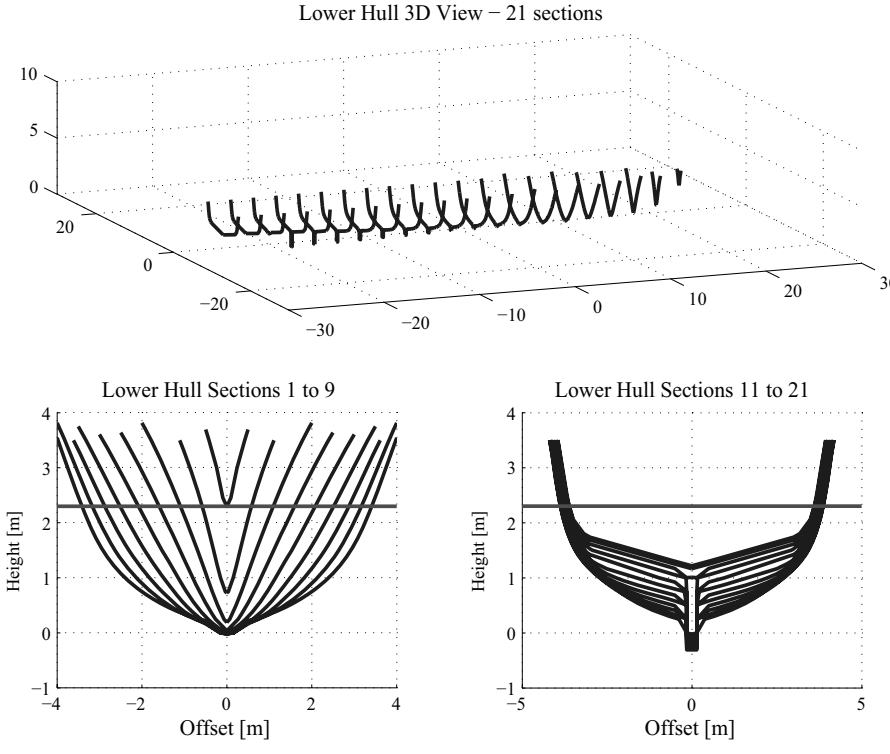

Fig. B.1. Sections of the lower hull used in the CFD code. Offsets modified by the author from ADI-Limited design. Published with permission of ADI-Limited Australia

B.2 Adopted Reference frames

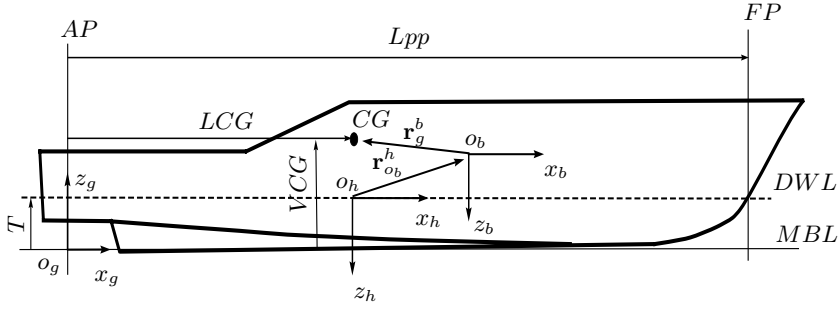

Fig. B.2. Main Particulars and reference frames: geometric (origin o_g), hydrodynamic (origin o_h), and body-fixed (origin o_b).

Table B.1. Reference frames—see Figure B.2.

Name	**Origin Coordinates**[m]	**Comments**
Geometrical	$o_g = [0, 0, 0]$	Intersection of AP and baseline
Hydrodynamic	$o_h = [LCG, 0, T]$	Measured with respect of o_g
Body-fixed	$o_b = [Lpp/2, 0, T]$	Measured with respect of o_g

B.3 Principal Hull Data and Loading Condition

Table B.2. Loading Conditions. VCG and LCG are measured with respect to the geometrical reference frame—see Figure B.2. The gyradii were approximated as $k_4 \approx 0.355\, BOA$ and $k_5 \approx 0.201\, L_{WL}$ (see [136]). The inertias were calculated using the corresponding displacements and gyradii.

Quantity	**Symbol**	**Full Load**	**Unit**
Length between perpendiculars	L_{pp}	51.5	m
Length over all	LOA	52.5	m
Beam over all	BOA	8.6	m
Nominal speed	U	15	kt
Draft at $Lpp/2$	T	2.29	m
Draft at FP	T_{FP}	2.32	m
Draft at AP	T_{AP}	2.26	m
Length Water Line	L_{WL}	47.702	m
Breadth Water Line	B_{WL}	7.726	m
Trim +ve aft	t	-0.06	m
Displacement	Δ	364.78 $\times 10^3$	Kg
Displacement vol.	∇	355.88 $\times 10^3$	m^3
Lateral Centre of Gravity from AP	LCG	19.82	m
Vertical Centre of Gravity from MBL	VCG	3.36	m
Lateral Centre of Buoyancy from AP	LCB	19.82	m
Vertical Centre of Buoyancy from MBL	VCB	1.549	m
Lateral Centre of Flotation from AP	LCF	18.27	m
Transverse Metacenter above keel	KMt	4.828	m
Longitudinal Metacenter above keel	KMl	124.15	m
Transverse Metacentric Height	GMt	1.0	m
Longitudinal Metacentric Height	GMl	113.99	m
Transverse Buoyancy to Metacentre	BMt	3.34	m
Longitudinal Buoyancy to Metacentre	BMl	114.49	m
Roll gyradius (from the CG)	k_4	3.053	m
Pitch gyradius (from the CG)	k_5	9.591	m
Inertia Roll (from the CG)	I_{44}	3.4263×10^6	Kg m^2
Inertia Pitch (from the CG)	I_{55}	3.3818×10^7	Kg m^2
Natural Roll Freq.	ω_ϕ	0.93	rad/s
Natural Roll Period	T_ϕ	6.76	s

B.4 Rudder, Fins and Bilge Keels

This vessel is equipped with two rudders.

Table B.3. Rudder data adopted by the author. CP-Rudder centre of pressure.

Quantity	Symbol	Measure	Unit
Area	A_R	2×1.5	m^2
Span	sp	1.5	m
Mean cord	$\bar{c}$	1	m
Eff. aspect ratio	a	3	-
Max. angle	α_{max}	40	deg
Max. rate	$\dot{\alpha}_{max}$	20	deg/s
Hydra. Prop. band	α_{pb}	4	deg
Long. dist. CG–CP	LCG	20.4	m
Offset CG–CP port	l_{yp}	-2	m
Offset CG–CP port	l_{ys}	2	m
Vert. Dist. CG–CP	l_z	2.61	m
Dist. CP–propeller	l_{prop}	1.5	m

Table B.4. Free stream data for rudder and fin profiles. Adopted according to data from Lewis [133].

Profile	Tip	a (eff.)	$\frac{\partial C_L}{\partial \alpha_e}$ (per deg)	C_{Lmax}	C_{D0}	α_{stall}
NACA15	Square	3	0.054	1.25	0.0065	23.0
NACA15	Square	2	0.046	1.33	0.0065	28.8

Table B.5. Fin data (adopted by the author.)

Quantity	Symbol	Measure	Unit
Area	A_R	2×1.7	m^2
Span	sp	1.3	m
Mean cord	$\bar{c}$	1.3	m
Eff. aspect ratio	a	2	-
Max. angle	α_{max}	35	deg
Max. rate	$\dot{\alpha}_{max}$	25	deg/s
Hydra. Prop. band	α_{pb}	10	deg
Tilt angle	β	34	deg
Moment Dist. to CG	r_f	4.22	m
Lat dist to CP	l_x	-2	m

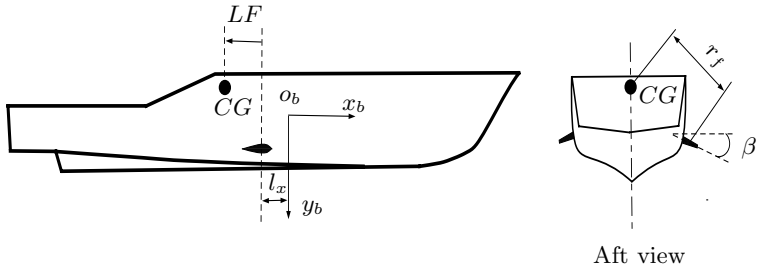

Fig. B.3. Typical fin stabilizer arrangement.

Table B.6. Bilge Keel Data.

Section from Stern	Offset [m]	Height [m]	Breadth [m]
10	2.99	1.15	0.35
11	2.93	1.15	0.35
12	2.79	1.15	0.35
13	2.58	1.15	0.35
14	2.29	1.15	0.35
15	1.98	1.15	0.35

B.5 Manoeuvring Coefficients and Motion RAO

Table B.7. Hydrodynamic derivatives for the manoeuvring model. Adapted from from Blanke and Christensen [33].

X-Coefficients	N-Coefficients	K-Coefficients	Y-Coefficients
$X_{\dot{u}} = -17400$	$N_{\dot{v}}$=538000	$K_{\dot{u}}$=296000	$Y_{\dot{v}} = -1.9022 \times 10^6$
$X_{u\|u\|} = -1960$	$N_{\dot{r}} = -4.3958 \times 10^7$	$K_{\dot{r}}$= 0.0	$Y_{\dot{r}} = -1.4 \times 10^6$
X_{vr}= $0.33 \times m$	$N_{\dot{p}}$=0.0	$K_{\dot{p}} = -0.674 \times 10^6$	$Y_{\dot{p}} = -0.296 \times 10^6$
	$N_{\|u\|v} = -92000$	$K_{\|u\|v} = 9260$	$Y_{\|u\|v} = -11800$
	$N_{\|u\|r} = -4.71 \times 10^6$	$K_{ur} = -102000$	$Y_{ur} = 131000$
	$N_{v\|v\|} = 0.0$	$K_{v\|v\|} = 29300$	$Y_{v\|v\|} = -3700$
	$N_{r\|r\|} = -202 \times 10^6$	$K_{r\|r\|} = 0.0$	$Y_{r\|r\|} = 0.0$
	$N_{v\|r\|} = 0.0$	$K_{v\|r\|} = 0.621 \times 10^6$	$Y_{v\|r\|} = -0.794 \times 10^6$
	$N_{r\|v\|} = -15.6 \times 10^6$	$K_{r\|v\|} = 0.142 \times 10^6$	$Y_{r\|v\|} = -0.182 \times 10^6$
	$N_{\phi\|uv\|} = -0.214 \times 10^6$	$K_{\phi\|uv\|} = -8400$	$Y_{\phi\|uv\|} = 10800$
	$N_{\phi u\|r\|} = -4.98 \times 10^6$	$K_{\phi\|ur\|} = -0.196 \times 10^6$	$Y_{\phi\|ur\|} = 0.251 \times 10^6$
	$N_{\phi u\|u\|} = -8000$	$K_{\phi uu} = -1180$	$Y_{\phi uu} = -74$
	$N_{\|u\|p} = 0.0$	$K_{\|u\|p} = -15500$	$Y_{\|u\|p} = 0.0$
	$N_{p\|p\|} = 0.0$	$K_{p\|p\|} = -0.416 \times 10^6$	$Y_{p\|p\|} = 0.0$
	$N_p = 0.0$	$K_p = -0.5 \times 10^6$	$Y_p = 0.0$
	$N_\phi = 0.0$	$K_{\phi\phi\phi} = -0.325\rho g \nabla$	$Y_\phi = 0.0$
	$N_{\phi\phi\phi} = 0.0$		$Y_{\phi\phi\phi} = 0.0$
			$Y_{\delta uu} = 2 \times 3.5044 \times 10^3$

NOTE: Sea water density $\rho = 1025$ Kg/m^3; Gravity constant $g = 9.81$ m/s^2.

Table B.8. Response amplitude operators at 15kts in quartering seas χ=45 deg . Roll and yaw are normalised to the wave slope, but sway to the wave amplitude.

ω[rad/s]	$\lvert H_2\rvert$	arg H_2[deg]	$\lvert H_4\rvert$	arg H_4[deg]	$\lvert H_6\rvert$	arg H_6[deg]
0.25	1.143	-82.323	0.941	-88.4	0.402	-127.483
0.412	1.179	-73.909	1.089	-86.908	0.336	-79.465
0.465	1.191	-70.761	1.138	-86.289	0.359	-66.16
0.507	1.2	-68.201	1.175	-85.741	0.385	-57.831
0.546	1.208	-65.643	1.21	-85.148	0.416	-51.292
0.574	1.213	-63.82	1.234	-84.694	0.438	-47.476
0.593	1.216	-62.537	1.25	-84.358	0.454	-45.132
0.628	1.222	-60.083	1.278	-83.674	0.485	-41.275
0.661	1.226	-57.753	1.304	-82.972	0.515	-38.222
0.668	1.226	-57.251	1.309	-82.813	0.521	-37.629
0.676	1.227	-56.738	1.314	-82.648	0.528	-37.042
0.698	1.229	-55.117	1.329	-82.109	0.548	-35.315
0.722	1.229	-53.369	1.345	-81.493	0.57	-33.639
0.736	1.23	-52.381	1.353	-81.129	0.582	-32.766
0.816	1.222	-46.462	1.389	-78.662	0.652	-28.389
0.832	1.219	-45.26	1.394	-78.093	0.665	-27.64
0.855	1.212	-43.581	1.399	-77.255	0.684	-26.655
0.879	1.204	-41.809	1.401	-76.309	0.703	-25.682
0.911	1.191	-39.454	1.4	-74.944	0.727	-24.481
0.917	1.187	-38.964	1.399	-74.642	0.732	-24.243
0.931	1.18	-37.962	1.397	-74.006	0.742	-23.765
0.935	1.178	-37.656	1.396	-73.806	0.744	-23.623
0.945	1.172	-36.932	1.393	-73.323	0.751	-23.29
0.959	1.163	-35.874	1.388	-72.586	0.761	-22.814
0.979	1.149	-34.452	1.379	-71.538	0.774	-22.194
1.06	1.076	-28.586	1.316	-66.309	0.819	-19.817
1.14	0.977	-22.81	1.202	-58.973	0.848	-17.628
1.222	0.852	-16.987	1.036	-47.294	0.86	-15.403
1.304	0.71	-11.186	0.849	-26.383	0.848	-12.987
1.343	0.637	-8.329	0.787	-10.198	0.834	-11.662
1.422	0.486	-2.175	0.898	33.335	0.787	-8.402
1.465	0.404	1.609	1.185	54.307	0.752	-6.117
1.571	0.216	15.041	2.966	85.491	0.659	2.283
1.745	0.093	110.22	15.721	103.506	0.737	22.366
1.79	0.112	137.413	15.207	107.28	0.529	32.735
1.951	0.117	179.866	1.235	134.6	0.121	146.479
2.094	0.042	171.819	0.362	-108.031	0.068	155.862
2.116	0.033	158.54	0.293	-111.449	0.054	146.38
2.353	0.071	92.218	0.162	132.391	0.016	59.094
2.618	0.116	79.625	0.052	68.818	0.013	-143.663

Table B.9. Response amplitude operators at 15kts in beam seas χ=90deg. Roll and yaw are normalised to the wave slope, but sway to the wave amplitude.

ω[rad/s]	$\lvert H_2\rvert$	arg H_2[deg]	$\lvert H_4\rvert$	arg H_4[deg]	$\lvert H_6\rvert$	arg H_6[deg]
0.25	1.576	-90.323	1.007	-89.984	0.059	-151.8
0.412	1.77	-90.685	1.019	-89.841	0.073	-132.847
0.465	1.872	-90.992	1.026	-89.798	0.078	-128.025
0.507	1.972	-91.356	1.034	-89.775	0.083	-124.691
0.546	2.089	-91.858	1.044	-89.773	0.088	-121.833
0.574	2.186	-92.33	1.052	-89.792	0.093	-120.093
0.593	2.263	-92.734	1.059	-89.821	0.097	-119.023
0.628	2.432	-93.73	1.076	-89.932	0.105	-117.369
0.661	2.628	-95.067	1.096	-90.147	0.115	-116.393
0.668	2.676	-95.416	1.101	-90.213	0.118	-116.27
0.676	2.726	-95.802	1.106	-90.29	0.12	-116.18
0.698	2.904	-97.24	1.126	-90.613	0.13	-116.18
0.722	3.128	-99.274	1.151	-91.148	0.142	-116.774
0.736	3.272	-100.717	1.168	-91.573	0.15	-117.451
0.816	4.42	-117.265	1.296	-98.022	0.216	-130.262
0.832	4.675	-123.085	1.318	-100.686	0.232	-135.512
0.855	4.975	-132.793	1.333	-105.343	0.253	-144.525
0.879	5.159	-144.572	1.315	-111.154	0.269	-155.684
0.911	5.13	-161.261	1.23	-119.254	0.276	-171.673
0.917	5.085	-164.736	1.204	-120.861	0.275	-175.016
0.931	4.957	-171.717	1.145	-123.943	0.272	178.26
0.935	4.909	-173.805	1.126	-124.817	0.27	176.246
0.945	4.781	-178.654	1.078	-126.743	0.265	171.573
0.959	4.566	174.546	1.005	-129.129	0.257	165.011
0.979	4.238	166.058	0.905	-131.388	0.243	156.821
1.06	2.842	140.327	0.594	-128.02	0.175	131.926
1.14	1.871	127.936	0.488	-114.925	0.125	119.418
1.222	1.286	122.765	0.463	-105.217	0.094	112.994
1.304	0.933	121.24	0.45	-99.355	0.075	109.146
1.343	0.812	121.245	0.444	-97.25	0.068	107.679
1.422	0.625	122.218	0.427	-93.675	0.058	105.077
1.465	0.548	123.16	0.417	-91.926	0.053	103.776
1.571	0.406	126.386	0.388	-87.75	0.045	100.725
1.745	0.264	133.538	0.336	-80.353	0.036	96.164
1.79	0.239	135.608	0.323	-78.251	0.034	95.119
1.951	0.169	143.603	0.277	-69.81	0.028	91.966
2.094	0.127	151.205	0.24	-61.12	0.025	90.166
2.116	0.122	152.357	0.235	-59.745	0.024	89.979
2.353	0.077	166.183	0.183	-42.536	0.02	89.58
2.618	0.046	-175.882	0.137	-19.681	0.016	92.534

Table B.10. Response amplitude operators at 15kts in bow seas χ=135deg. Roll and yaw are normalised to the wave slope, but sway to the wave amplitude.

ω[rad/s]	$\lvert H_2\rvert$	arg H_2[deg]	$\lvert H_4\rvert$	arg H_4[deg]	$\lvert H_6\rvert$	arg H_6[deg]
0.25	1.134	-98.692	0.568	-91.375	0.194	86.722
0.412	1.525	-105.69	0.54	-91.953	0.234	159.498
0.465	1.792	-108.782	0.54	-92.578	0.262	170.055
0.507	2.11	-112.012	0.546	-93.57	0.284	176.94
0.546	2.593	-116.613	0.563	-95.465	0.313	-176.861
0.574	3.115	-121.716	0.585	-97.994	0.344	-172.993
0.593	3.623	-127.068	0.606	-100.944	0.375	-171.038
0.628	5.013	-146.03	0.65	-112.498	0.474	-173.007
0.661	6.105	179.986	0.591	-134.489	0.564	171.585
0.668	6.123	171.398	0.552	-139.885	0.565	167.018
0.676	6.066	162.648	0.505	-145.28	0.56	162.343
0.698	5.391	136.998	0.332	-158.23	0.497	149.493
0.722	4.295	115.634	0.176	-156.117	0.402	141.941
0.736	3.712	106.776	0.126	-141.972	0.355	140.742
0.816	1.718	82.02	0.16	-82.09	0.225	152.298
0.832	1.517	79.659	0.169	-80.563	0.215	155.15
0.855	1.293	76.942	0.176	-79.303	0.203	158.831
0.879	1.108	74.575	0.179	-78.482	0.194	162.337
0.911	0.918	71.947	0.179	-77.714	0.183	166.49
0.917	0.884	71.458	0.178	-77.573	0.181	167.295
0.931	0.821	70.497	0.177	-77.297	0.177	168.882
0.935	0.803	70.215	0.176	-77.214	0.176	169.354
0.945	0.763	69.566	0.175	-77.019	0.173	170.446
0.959	0.708	68.658	0.172	-76.731	0.169	171.988
0.979	0.643	67.505	0.168	-76.336	0.164	173.972
1.06	0.444	63.274	0.144	-74.43	0.144	-178.621
1.14	0.314	59.689	0.116	-71.877	0.125	-172.181
1.222	0.22	56.464	0.085	-68.116	0.105	-166.353
1.304	0.152	53.704	0.056	-62.111	0.086	-161.139
1.343	0.125	52.581	0.044	-57.6	0.077	-158.748
1.422	0.08	50.933	0.022	-39.888	0.058	-153.837
1.465	0.06	50.611	0.014	-16.909	0.049	-150.899
1.571	0.023	54.522	0.014	71.962	0.027	-140.975
1.745	0.008	-170.333	0.02	107.978	0.006	-74.265
1.79	0.011	-161.597	0.019	113.692	0.006	-37.959
1.951	0.01	-153.039	0.008	147.605	0.007	12.666
2.094	0.004	-144.126	0.005	-111.901	0.004	36.338
2.116	0.003	-140.738	0.006	-102.191	0.003	41.757
2.353	0.002	17.082	0.004	-44.504	0.002	-168.646
2.618	0	170.95	0.003	119.574	0	-41.265

References

1. M.A. Abkowitz. Lecture notes on ship hydrodynamics–steering and manoeuvrability. Tech. report hy-5, Hydro and Aerodynamics Laboratory Lyngby, Denmark, 1964.
2. M.A. Abkowitz. Lectures on ship hydrodynamics—steering and manoeuvrability. Technical Report Rep. No. Hy-5, Hydro og Aerodynamisk Laboratorium, Lyngby, Denmark, 1964.
3. D.J. Acheson. *Elementary Fluid Dynamics*. Oxford Applied Mathematics and Computing Science Series. Claredon Press, Oxford, 1990.
4. J.F. Allan. Stabilisation of ships by activated fins. *Transactions of The Royal Institution of Naval Architects RINA*, 87:123–159, 1945.
5. R.N. Andrew, P.R. Loader, and V.E. Penn. The assessment of ship seakeeping performance in likely to be encountered wind and wave conditions. In *Proc. of RINA International Symposium on Wave and Wind Climate Worldwide. London*, 1984.
6. D. Angeli, E. Mosca, and A. Casavola. Output predictive control of linear plants with saturated and rate limited actuators. In *Proc. of American Control Conference, ACC*, pages 272–276, 2000.
7. M.S. Arulampalam, S. Maskell, N. Gordon, and T. Clapp. A tutorial on particle filters for on-line non-linead/non-gaussian bayesian tracking. *IEEE Trans on signal processing*, 50(2):174–188, 2002.
8. K. J. Åström. *Introduction to Stochastic Control Theory*, volume 70 of *Mathematics in Science and Engineering*. Academic Press, New York, 1970.
9. K.J. Åström and Witenmark B. *Computer Controlled Systems, Theory and Design*. Prentice-Hall, 3rd edition, 1997.
10. K.J. Åström and B. Wittenmark. *Adaptive Control*. Addison Wesley, 1995.
11. P.A. Bailey, W.G. Price, and P. Temarel. A unified mathematical model describing the manoeuvring of a ship in s seaway. *Transactions The Royal Institution of Naval Architects–RINA*, 140:131–149, 1997.
12. A.E. Baitis. The development and evaluation of a rudder roll stabilization system for the WHEC Hamilton class. Technical Report DDDTNSRDC/SPD-0930-02, DTNSRDC, Bethsada, MD, 1980.
13. A.E. Baitis, T.R. Applebee, and T.M. McNamara. Human factor considerations applied to operations of the FFG-8 and lamps MKIII. *Naval Engineering Journal*, 97(4), 1984.

14. A.E. Baitis, G.G. Cox, and D. Woolaver. Evaluation of V active fin roll stabilisers. *3rd Ship Control System Symposium–SCSS, Bath, UK*, 1972.
15. E. Baitis and L.V. Schmidt. Ship roll stabilization in the US Navy. *Naval Engineering Journal*, 101(3):43–53, 1989.
16. E. Baitis, D.A. Woollaver, and T.A. Beck. Rudder roll stabilization of coast guard cutters and frigates. *Naval Engineering Journal*, 95(3):267–282, 1983.
17. G. K. Batchelor. *An Introduction to Fluid Dynamics*. Cambridge University Press, 2000.
18. R.F. Beck and A.M. Reed. Modern computational methods for ships in a seaway. *SNAME Transactions*, 109:1–51, 2001.
19. J. Bell and P. Walker. Activated and passive controlled fluid tank system for ship stabilization. *Transactions of Society of Naval Architects and Marine Engineers*, 74, 1966.
20. A. Bemporad, M. Morari, V. Dua, and E. Pistikopulos. The explicit linear quadratic regulator for constrained systems. Technical Report AUT99-16, Automatic Control Laboratory, ETH-Swiss Federal Institute of Technology, 1999.
21. A. Bemporad, M. Morari, V. Dua, and E. Pistikopulos. The explicit linear quadratic regulator for constrained systems. *Automatica*, 38(1):3–20, 2002.
22. D. Bernstein and A. Michel. A chronological bibliography on saturating actuators. *International Journal of Robust and Nonlinear Control*, 5:375–380, 1995.
23. V. Bertram. *Practical Ship Hydrodynamics*. Butterworth Heinemann, 2004.
24. D. Bertsekas. *Dynamic Programming and Optimal Control*, volume 1,2 of *Optimization and Computation Series*. Athena Scientific, Belmont, Massachusetts, 2000.
25. D. Bertsekas and S.E. Shreve. *Stochastic Optimal Control: The Discrete-Time Case*. Academic Press, 1978.
26. D. P. Bertsekas. *Dynamic Programming and Stochastic Control*, volume 125 of *Mathematics in Science and Engineering*. Academic Press, New York, 1976.
27. D.P. Bertsekas, A. Nedić, and A.E. Ozdaglar. *Convex Analysis and Optimization*. Athenas Scientific, Belmont, 2003.
28. R. Bhattacharyya. *Dynamics of Marine Vehicles*. Ocean Engineering. Wiley, New York, 1978.
29. R. Bitmead, M. Gevers, and V. Wertz. *Adaptive Optimal Control: The Thinking Man's* GPC. Prentice Hall, New York, 1990.
30. M. Blanke. *Ship propulsion losses related to automatic steering and prime mover control*. PhD thesis, Servolaboratory, Technical University of Denmark, 1981.
31. M. Blanke. Uncertainty models for rudder roll damping control. In *Proc. of* IFAC *World Congress*, 1996.
32. M. Blanke, J. Adrian, K. Larsen, and J. Bentsen. Rudder roll damping in coastal region sea conditions. In *Proc. of 5th IFAC Conference on Manoeuvring and Control of Marine Craft, MCMC'2000*, 2000.
33. M. Blanke and A. Christensen. Rudder roll damping autopilot robustness to sway-yaw-roll couplings. *In: Proc. of 10th SCSS, Ottawa, Canada*, pages 93–119, 1993.
34. M. Blanke, P. Haals, and K.K. Andreasen. Rudder roll damping experience in Denmark. In *Proc. of IFAC workshop CAMS'89, Lyngby, Denmark*, 1989.
35. H. Bode. *Network Analysis and Feedback Amplifier Design*. D. van Nostrand, New York, 1945.

36. J.C.G Boot. *Quadratic Programming*. North-Holland Publishing Company - Amsterdam, 1964.
37. G.E.P. Box, G.M. Jenkins, and G.C. Reinsel. *Time Series Analysis, Forecasting and Control*. Prentice Hall, Newyork, 3rd edition, 1994.
38. C.L. Bretshneider. The generation and decay of wind waves in deep water. *Trans. American Geophysical Union*, 37, 1952.
39. R.O. Brigham. *The Fast Fourier Transform and Its Applications*. Prentice-Hall Signal Processing Series, 1988.
40. R.G. Brown and P.Y.C. Hwang. *Introduction to Random Signals and Applied Kalman filtering,*. Wiley, 1998.
41. R.L. Burden and J.D. Faires. *Numerical Analysis*. Brooks-Cole, 1997.
42. J.B. Carley. Feasibility study of steering and stabilising by rudder. *4rd Ship Control System Symposium–SCSS, The Netherlands*, 1975.
43. J.B. Carley and A. Duberley. Design considerations for optimum ship motion. *3rd Ship Control System Symposium–SCSS, Bath, UK*, 1972.
44. J.H. Jr. Chadwick. On the stabilization of roll. *Trans. of The Society of Naval Architects and Marine Engineers*, 63:237–280, 1955.
45. T.W. Chalmers. *The Automatic Stabilisation of Ships*. Chapman and Hall, London, 1931.
46. P.D. Chaplin. The effectiveness of roll stabilizers. *The Naval Architect*, April:33, 1972.
47. C.C. Chen and L. Shaw. On receding horizon feedback control. *Automatica*, 18(3):349—352, 1982.
48. J. Chen, L. Qiu, and O. Toker. Limitations on maximal tracking accuracy in tracking step signals. *In proc. of 35th IEEE Conference on Decision and Control*, 1:726–731, 1996.
49. D.W. Clark, C. Mohtadi, and P.S. Tuffs. Generalized predictive control, parts 1 and 2. *Automatica*, 23(2):137–148, 1987.
50. D. Clarke. The foundations of steering and manoeuvring. In *6th IFAC Conference on Manoeuvring and Control of Marine Craft MCMC'03, Girona, Spain*, pages –, 2003.
51. J.L. Colwel. Motion sickness habituation in the naval environment. DREA technical memorandum 94/211, Defence Research Establishment Atlantic (DREA), National Defence Research and Development Branch, Canada, 1994.
52. J.E. Conolly. Rolling and its stabilization by fins. *Transactions of The Royal Institution of Naval Architects*, 111, 1969.
53. W.E. Cowley. Development of an autopilot to control yaw and roll. *3rd Ship Control System Symposium–SCSS, Bath, UK*, 1972.
54. W.E. Cowley and T.H. Lambert. The use of a rudder as a roll stabiliser. *3rd Ship Control System Symposium–SCSS, Bath, UK*, 1972.
55. W.E. Cowley and T.H. Lambert. Sea trials on a roll stabiliser using the ship's rudder. *4th Ship Control System Symposium–SCSS, The Netherlands*, 1975.
56. P. Crossland. The effect of roll stabilization controllers on warship operational performance. In *5th IFAC Conference on Manoeuvring and Control of Marine Craft MCMC'02*, pages 31–37, 2000.
57. P. Crossland. The effect of roll stabilization controllers on warship operational performance. *Control Engineering Practice*, 11:423–431, 2003.
58. W.E. Cummins. The impulse response function and ship motion. Technical Report 1661, David Taylor Model Basin–DTNSRDC, 1962.

59. R.P. Dallinga. Hydromechanic aspects of the design of fin stabilisers. *Transactions of The Royal Institution of Naval Architects*, 1993.
60. J. A. De Doná, M. Serón, D. Q. Mayne, and G. C. Goodwin. Enlarged terminal sets guaranteeing stability of receiding horizon control. Technical Report EE01022, Dept. of Elec and Comp. Engineering, The University of Newcastle, Australia, 2001.
61. C. Edwards and I. Postlethwaite. Anti-windup and bumpless transfer schemes. *Automatica*, 34(2):199–210, 1998.
62. O. Egeland and J.T. Gravdalh. *Modeling and Simulation for Automatic Control*. Marine Cybernetics, Trondheim, 2002.
63. O.M. Faltinsen. *Sea Loads on Ships and Offshore Structures*. Cambridge University Press, 1990.
64. D. Fathi. *ShipX Vessel Responses (VERES)*. Marintek AS Trondheim, http://www.marintek.sintef.no/, 2004.
65. K.K Fedyaevsky and G.V. Sobolev. *Control and Stability in Ship Design*. State Union Shipbuilding, Leningrad, 1964.
66. T.I. Fossen. *Guidance and Control of Ocean Marine Vehicles*. John Wiley and Sons Ltd, New York, 1994.
67. T.I. Fossen. *Marine Control Systems: Guidance, Navigation and Control of Ships, Rigs and Underwater Vehicles*. Marine Cybernetics, Trondheim, 2002.
68. T.I. Fossen. A nonlinear unified state-space model for ship maneuvreing and control in a seaway. In *Lecture Note 5th EUROMECH Nonlinear Dynamics Conceference*, 2005.
69. T.I Fossen and Ø.N. Smogeli. Nonlinear time-domain strip theory formulation for low speed manoeuvring and station-keeping. *Modelling Identification and Control–MIC*, 25(4), 2004.
70. H. Frahm. Results of trials of anti-rolling tanks at sea. *Trans. of the Institution of Naval Architects*, 53, 1911.
71. B.A. Francis. The optimal linear-quadratic time-invariant regulator with cheap control. *IEEE Trans. on Automatic Control*, 24(4):616–621, 1979.
72. G. F. Franklin, J. D. Powell, and M. Workman. *Digital Control of Dynamic Systems*. Addison Wesley, 3rd edition, 1998.
73. G.F. Franklin, J. Powell, and M. Workman. *Digital Control of Dynamic Systems*. Addison-Wesley, 3rd edition, 1998.
74. J. S. Freudenberg and D. P. Looze. Right half plane poles and zeros and design tradeoffs in feedback systems. *IEEE Trans. on Autom. Cont.*, AC-30(6):555–565, 1985.
75. W. Froude. On the rolling of ships. *Trans. of the Institution of Naval Architects*, 2:180–227, 1861.
76. W. Froude. *The Papers of William Froude* M.A. LL.D. F.R.S. *1810–1879*, chapter On The Rolling Of Ships, pages 40—65. The Institution of Naval Architects, 1955.
77. W. Froude. *The Papers of William Froude* M.A. LL.D. F.R.S. *1810–1879*, chapter Appendices To Mr. Froude Paper On The Rolling of Ships, pages 65—75. The Institution of Naval Architects, 1955.
78. W. Froude. *The Papers of William Froude* M.A. LL.D. F.R.S. *1810–1879*, chapter On The Practical Limits of The Rolling Of Ships In A Sea-Way, pages 101—110. The Institution of Naval Architects, 1955.

79. P.T.K Fung and M.J. Grimble. Self-tunning control of ship positioning. *In the book Self-tunning and Adaptive Control: theory and applications, C.J. Harris and S.A. Billings (Eds.)*, pages 308–331, 1981.
80. G. Gaillarde. Dynamic behavior and operation limits of stabilizer fins. In *IMAM International Maritime Association of the Mediterranean, Creta, Greece.*, 2002.
81. C. E. Garcia, D.M. Prett, and M. Morari. Model predictive control: Theory and practice; A survey. *Automatica*, 25(3):335–348, 1989.
82. A.F.A. Gawad, S.A. Ragab, A.H. Nayfeh, and D.T. Mook. Roll stabilization by anti-roll passive tanks. *Ocean Engineering*, 28:457–469, 2001.
83. R.W.L. Gawn. *The Papers of William Froude* M.A. LL.D. F.R.S. *1810–1879*, chapter Evaluation of the Work of William Froude, pages xv—xxii. The Institution of Naval Architects, 1955.
84. A. Gelb and W.E. Vander Velde. *Multiple-Input Describing Functions and Nonlinear System Design*. McGraw Hill, London, 1968.
85. E.G. Gilbert and K. Tan. Linear systems with state and control cosnstraints: The theory and application of maximal output admissible sets. *IEEE Trans. on Autom. Control*, 36(9):1008–1020, 1991.
86. B.K. Golding. Industrial systems for guidance and control of marine surface vessels. Technical Report Project assignment, Department of Engineering Cybernetics, Norwegian University of Science and Technology NTNU, Trondheim, Norway, 2004.
87. G.J. Goodrich. Development and design of passive roll stabiliser. *Transactions of The Royal Institution of Naval Architects*, pages 81–88, 1969.
88. G. C. Goodwin and K. S. Sin. *Adaptive Filtering, Prediction, and Control*. Prentice-Hall, 1984.
89. G.C. Goodwin, S. Graebe, and M Salgado. *Control System Design*. Prentice-Hall, Inc, 2001.
90. G.C. Goodwin, T. Perez, M. Serón, and C. Y. Tzeng. On fundamental limitations for rudder roll stabilization of ships. In *Proc. of the 39th Conference on Decision and Control 2000, Sydney, Australia*, 2000.
91. G.C. Goodwin, M.M. Seron, and J.A. DeDoná. *Constrained Control and Estimation: An Optimisation Approach*. Communications and Control Engineering. Springer, London, 2005.
92. J. Gordon Leishman. *Principles of Helicopter Aerodynamics*. Cambridge University Press, 2000.
93. R. Graham. The effects of hull form on the roll damping of war ships. *Naval Engineers Journal*, 99(5):55–61, 1987.
94. R. Graham. Motion-induced interruptions as ship operability criteria. *Naval Engineers Journal*, 103(3), 1990.
95. M.J. Grimble, M.R. Katebi, and Y. Zang. $\mathcal{H}_\infty$–based ship fin-rudder roll stabilisation. In *10th Ship Control System Symposium SCSS*, volume 5, pages 251–265, 1993.
96. M.J. Grimble, R.J. Patton, and D.A. Wise. The design of dynamic positioning control systems using stochastic optimal control theory. *Optimal Control Applications and Methods*, 1:167–202, 1989.
97. S.M. Han and H. Benaroya. *Nonlinear and Stochastic Dynamics of Compliant Offshore Structures*. Solid Mechanics and its Applications. Kluwer, Dordrecht, 2002.

98. A.D. Hansen. *Predictive Control and Identification: Application to Steering Dynamics*. PhD thesis, Dept. of Mathematical Modelling (IMM), Technical University of Denmark, 1996.
99. S. Haverre and T. Moan. *Probabilistic Offshore Mechanics*, chapter On some uncertainties related to short term stochastic modelling of ocean waves. Progress in Engineering Science. CML, 1985.
100. G. Hearns and M. Blanke. Quantitative analysis and design of rudder roll damping controller. Technical Report R-1998-4243, Department of Control Engineering, Aalborg University, Denmark, 1997.
101. G. Hearns and M. Blanke. Quantitative analysis and design of rudder roll damping controllers. In *Proc. of CAMS'98*, 1998.
102. N. Hickey. *Control design for fin roll stabilisation*. PhD thesis, University of Strathclyde, Glasgow, UK, 1999.
103. N. Hickey, M. Grimble, M. Johnson, M. Katebi, and R. Melville. Robust fin roll stabilisation of surface ships. In *Proc. of the 36th Conference on Decision and Control 1997, San Diego, California, USA*, 1997.
104. N. Hickey, M. Grimble, M. Johnson, M. Katebi, and D. Wood. $\mathcal{H}_\infty$ fin roll control system design. In *Proc. of IFAC Conference on Control Applications in Marine Systems, Tronheim, Norway*, 1995.
105. N. Hickey, M. Johnson, M. Katebi, and M. Grimble. PID controller optimisation for fin roll stailisation. In *Proc. of the International Conference on Control Applications, Hawai, USA*, 1999.
106. S.F. Hoerner and H.V. Borst. *Fluid-Dynamic Lift*. Hoerner Fluid Dynamics, 2nd edition, 1985.
107. N. Hogben, N.M.C. Dacunaj, and G.F. Olliver. *Global Wave Statistics*. British Marine Technology Ltd. Feltham, UK, 1986.
108. I. Horowitz. *Synthesis of Feedback Systems*. Academic Press, New York, 1963.
109. T. Hu and Z. Lin. *Control Systems with Actuator Saturation*. Control Engineering. Birkhauser, Basle, 2001.
110. B.L Hutchison. The transverse plane motions of ships. *Marine Technology*, 28(2):.–., 1991.
111. Y. Ikeda. Prediction methods of roll damping of ships and their application to determine optimum stabilisation devices. *Marine Technology*, 41(2):89–93, 2004.
112. A. Isidori. *Nonlinear Control Systems*. Springer, 3rd edition, 1995.
113. T.A. Johansen, I. Petersen, and O. Slupphaug. On explicit sub-optimal LQR with state and input constraints. In *Proc. of the 39th IEEE Conference in Decision and Control, Sydney , Australia*, 2000.
114. J.M.J. Jouenée and W.W. Massie. *Lecture notes: Introduction to Ship Hydromechanics*. Department of Maritime Technology, Delft University of Technology, The Netherlands. http//www.shipmotions.nl, 2001.
115. J.M.J. Jouernee and L.J.M. Adegeest. *Theoretical Manual of Strip Theory Program SEAWAY for Windows*. TU Delft, Delft Unoversity of Technology, www.ocp.tudelft.nl/mt/journee, 2003.
116. A.J. Jurgens, F. van Warlee, M.X. van Rijsbergen, and P.G.M. van der Klugt. R & D on advanced ride control system for a high speed mono-hull. In *3rd International Euro Conference on High Performance Marine Vehicles HIPER'02, Bergen*, pages 248–261, 2002.

117. C. Källström and W.L. Schultz. An intergrated rudder control system for roll damping and course maintenance. *Proc. of the 9th Ship Control System Symposium*, 3:278–296, 1990.
118. C.G. Källström. *Identification and Adaptive Control Applied to Ship Steering.* PhD thesis, Lund Institute Of Technology, Lund, Sweden, 1979.
119. C.G. Källström. Control of yaw and roll by a rudder/fin stabilisation system. *In: Proc. of 6th SCSS*, 1981.
120. C.G. Källström, P. Wessel, and S. Sjölander. Roll reduction by rudder control. In *Spring Meeting*-STAR *Symposium, 3rd IMSDC*, 1988.
121. R.E. Kalman. A new approach to linear filtering and prediction problems. *Trans. of ASME Series D. of Journal of Basic Engineering.*, 82:35–45, 1960.
122. M.R. Katebi, Wong D.D.K., and M.J. Grimble. LQG autopilot and rudder roll stabilisation control system design. *Proc. of the 8th ship Control System Symposium*, 1987.
123. M.R. Katebi, N.A. Hickey, and M.J. Grimble. Evaluation of fin roll stabilizer design. In *5th IFAC Conference on Manoeuvring and Control of Marine Craft MCMC'00*, pages 31–37, 2000.
124. S. Keerthi and E. Gilbert. Optimal infinite horizon feedback laws for a general class of constrained discrete time systems: Stability and moving-horizon approximations. *Journal of Optimization Theory and Applications*, 57:265–293, 1988.
125. M. V. Kothare, P. J. Campo, M. Morari, and N. Nett. A unified framework for the study of anti-windup design. *Automatica*, 30(12):1869–1883, 1994.
126. T. Koyama. On the optimum automatic steering system for ships at sea. *Journal of the Society of Naval Architects of Japan—JSNA*, 122, 1967.
127. E. Kristansen and O. Egeland. Frequency dependent added mass in models for controller design for wave motion ship damping. In *6th IFAC Conference on Manoeuvring and Control of Marine Craft MCMC'03, Girona, Spain.*, 2003.
128. H. Kwakernaak and R. Sivan. *Linear Optimal Control Systems.* Wiley, 1972.
129. H. Kwakernaak and R. Sivan. The maximally achievable accuracy of linear optimal regulators and linear optimal filters. *IEEE Trans. Automat. Contr.*, 17(4):79–86, 1972a.
130. T. Laudval and T.I. Fossen. Nonlinear rudder-roll damping of non-minimum phase ships using sliding mode control. *Proc. of the European Control Conference, Brussel, Belgium*, 1997.
131. T. Laudval and T.I. Fossen. Rudder roll stabilization for ships subject to input rate saturation using a gain scheduling control law. *In Proc. of IFAC CAMS'98*, pages 121–126, 1998.
132. Y.I. Lee and B. Kouvaritakis. Receding horizon output feedback control for linear systems with input saturation. *IEE Proc., Control Theory and Applications*, 148(2):109–115, 2001.
133. E.V. (Ed.) Lewis. *Principles of Naval Architecture vol III: Motions in Waves and Controllability.* Society of Naval Architects and Marine Engineers, New York, 3rd edition, 1988.
134. K.P. Lindegaard. *Acceleration Feedback in Dynamic Positioning.* PhD thesis, Faculty of Information Technology, Dept. of Engineerign Cybernetics, Norwegian University of Science and Technology NTNU, 2003.
135. A.R.J.M. Lloyd. *Seakeeping: Ship Behaviour in Rough Weather.* Ellis Horwood Series in Marine Technology. Ellis Horwood, 1989.

136. A.R.J.M. Lloyd. *Seakeeping: Ship Behaviour in Rough Weather*. A.R.J.M. Lloyd, 26 Spithead Av., Gosport, Hampshire, UK, 1998.
137. A.R.M.J. Lloyd. Design considerations for optimum ship motion. *3rd Ship Control System Symposium–SCSS, Bath, UK*, 1972.
138. A.R.M.J. Lloyd. The hydordynamic performance of roll stabiliser fins. *3rd Ship Control System Symposium–SCSS, Bath, UK*, 1972.
139. A.R.M.J. Lloyd. Roll stabilisation by rudder. *4th Ship Control System Symposium–SCSS, The Netherlands*, 1975.
140. A.R.M.J. Lloyd. Roll stabiliser fins: A design procedure. *Transactions of The Royal Institution of Naval Architects*, 1975.
141. J.M. Maciejowski. *Predictive Control with Constraints*. Prentice Hall, New York, 2002.
142. C.A. Marchaj. *Aero-Hydrodynamics of Sailing*. Tiller Publishing, 3rd edition, 2000.
143. P Marquis and J. Broustail. SMOC, a bridge between state space and model predictive controllers: application to the automation of hydrotreating unit. In *Proc. of IFAC workshop on model based process control*, pages 37–43. Oxford: Pergamon Press, 1988.
144. Martec. *Trident Seakeeping: advanced hydrodynamic analysis for ships moving in waves*. Martec TM, `http://www.martec.com/trident_seakeeping.html`, Website accessed by the author in April 2005.
145. B. Massey. *Mechanics of Fluids*. Stanley Thornes Ltd, 7 edition, 1998.
146. Peter S. Maybeck. *Stochastic Models, Estimation and Control*, volume 141 of *Mathematics in Science and Engineering*. Academic Press, 1979.
147. D. Q. Mayne, J. B. Rawlings, C. V. Rao, and P. O. M. Scokaert. Constrained model predictive control: Stability and optimality. *Automatica*, 36:789–814, 2000.
148. D.Q. Mayne. *Modelling, Control and Optimization of Complex Systems*, chapter 6. Kluwer, 2003.
149. M.E. McCauley, J.W. Royal, J.F. O'Halon, and R.R. Mackie. Motion sickness incidence: Exploratory studies of habitutation, pitch and roll, and the refinement of a mathematical model. Technical report 1733-2, Human Factors Research, 1976.
150. R.G.A. Melville, C. Källströ, and K Theorén. Rudder roll stabilisation-an improved control law. *Proc. of the Third IEEE Conference on Control Applications*, 2:1099–1105, 1994.
151. N. Minorsky. Problems of anti-rolling stabilization of ships by the activated tank method. *American Society of Naval Engineers*, 47, 1935.
152. K. Monk. A war ship roll criterion. *Royal Institute of Naval Architects*, pages 219–240, 1988.
153. S. Motora. Studying device of the rolling of ships. *US Patent,April 14*, 1925.
154. K. R. Muske and J. B. Rawlings. Model predictive control with linear models. *AIChe Journal*, 39(2):262–2872, 1993.
155. D. Myrhaug. Probabilistic theory of sealoads. Lecture notes, Department of Marine Technology, NTNU, Trondheim, Norway, 2004.
156. NA. Sistemas dinámicos y modelos matemáticos (in Spanish). Lecture Notes A-SisDin&MM (http://www.fceia.unr.edu.ar/dsf/), Chair of System Dynamcis and Control, Dept. of Electronics, Universidad Nacional de Rosario, Argentina, 2000.

157. NATO. *Standarization Agreement: common procedures for seakeeping in the ship design process (*STANAG*) 3rd ed N0.4154.* North Atlantic Treaty Organization (NATO), Military Agency for Standarization (MAS), 2000.
158. D.E. Newland. *An Introduction to Random Vibrations, Spectral and Wavelet Analysis.* Pearson Education, 1993.
159. J.N. Newman. *Marine Hydrodynamics.* MIT Press, 1977.
160. J.N. Newman. The theory of ship motions. *Advances in Applied Mechanics*, 18:222–283, 1978.
161. V. Nicolau and E. Ceanga. Fuzzy rudder-roll damping system based on analysis of autopilot command. In *IFAC Conference on control Applications Of Marine Systems—CAMS*, pages 285—290, 2004.
162. N.H. Norrbin. Theory and observation on the use of a mathematical model for ship manoeuvring in deep and confined waters. *8th Symposium on Naval Hydrodynamics, USA*, 1970.
163. M.K. Ochi. *Ocean Waves: The Stochastic Approach.* Ocean Technology Series. Cambridge University Press, 1998.
164. H. Oda, K. Ohtsu, and T. Hotta. A study on roll stabilisation by rudder control. *Journal of Japan Institute of Navigation*, 1995.
165. H. Oda, K. Ohtsu, and T. Hotta. Statistical analysis and design of a rudder roll stabilization system. *Control Engineering Practice*, 4(3):351—358, 1996.
166. H. Oda, K. Ohtsu, and T. Hotta. A simulation study and full scale experiment of rudder roll stabilisation system. *In Proc. of 11th Ship Control System Symposium SCSS, Southampton, U.K.*, 1:299–313, 1997.
167. H. Oda, M. Sasaki, Y. Seki, and T. Hotta. Rudder roll stabilisation control system through multivariable autoregressive model. *In Proc. of IFAC Conference on Control Applications of Marine Systems–CAMS*, 1992.
168. T. Ogilvie. Recent progress towards the understanding and prediction of ship motions. In *6th Symposium on Naval Hydrodynamics*, 1964.
169. J.P. O'Halon and M.E. McCauley. Motion sickness incidence as a function of frequency and acceleration of vertical sinusoidal motion. *Aerospace Medicine*, 45(4):366–369, 1974.
170. P.R. Payne. On quantazing ride comfort and allowable accelerations. In *Proc. of AIAA/SNAME Advanced Marine Vehicles Conference, Arlington VA, USA*, 1976.
171. Y. Peng, D. Vrancic, R. Hanus, and S. Weller. Anti-windup designs for multivariable controllers. *Automatica*, 34(12):1559–1665, 1998.
172. T. Perez. Dynamic models and performance of tank stabilizers for preliminary seakeeping analysis. Commenrcial in confidence, ADI-Limited, Major Projects Group, Australia, 2002.
173. T. Perez. *Performance Analysis and Constrained Control of Fin and Rudder-based Roll Stabilizers for Ships.* PhD thesis, School of Electrical Eng. and Computer Sc., The University of Newcastle, Australia., 2003.
174. T. Perez, T.I. Fossen, and A.J. Sørensen. A discussion about seakeeping and manoeuvring models for surface vessels. Technical report MSS-TR-001, Centre for Ships and Ocean Structures (CESOS), Norwegian University of Science and Technology NTNU, Trondheim, Norway. Available at http://www.cesos.ntnu.no/mss/, 2004.
175. T. Perez and G. C. Goodwin. Constrained control to prevent dynamic stall in ship fin stabilizers. In *6th IFAC Conference on Manoeuvring and Control of Marine Craft MCMC'03*, pages 173–178, 2003.

176. T. Perez, G. C. Goodwin, and M. Serón. Cheap control fundamental limitations of input constrained linear systems. *In Proc. of 15th IFAC World Congress, Barcelona, Spain*, 2002.
177. T. Perez, G. C. Goodwin, and M. Serón. Performance degradation in feedback control due to constraints. *IEEE Trans. of Autom. Contr.*, 48(8):.–., 2003.
178. T. Perez and G.C. Goodwin. On constrained control of fin, rudder or combined fin-rudder stabilisers: A quasi-adaptive control strategy. In *IFAC Conference on Control Applications of Marine Systems—CAMS*, pages 113—118, 2004.
179. T. Perez, G.C. Goodwin, and C.Y. Tzeng. Model predictive rudder roll stabilization control for ships. In *5th IFAC Conference on Manoeuvring and Control of Marine Crafts. (MCMC2000), Aalborg, Denmark*, 2000.
180. T. Perez, H. Haimovich, and G.C. Goodwin. On optimal control of constrained linear systems with imperfect state information and stochastic disturbances. *International Journal of Robust and Nonlinear Control (IJNRC)*, 14:379–393, 2004.
181. W.J. Pierson and L. Moskowitz. A proposed spectral form for fully developed wind seas based on the similarity theory of S.A. Kitaigorodskii. *Trans. American Geophysical Union*, 69, 1964.
182. W.C. Price and R.E.D. Bishop. *Probabilistic Theory of Ship Dynamics*. Chapman and Hall, London, 1974.
183. S. Qin and T. Badgwell. An overview of industrial model predictive control technology. *Chemical Process Control-V,*, CACHE, AIChE:232–256, 1997.
184. L. Qiu and E.J. Davison. Performance limitations of non-minimum phase systems in the servomechanism problem. *Automatica*, 29(2):337–349, 1993.
185. Royal Australian Navy RAN. Standard materiel requirements for RAN ships and submarines: Part 6 seakeeping. Technical Report A016464 Revison 1, Naval Platform System Engineering Directorate, Department of Defence, Royal Australian Navy, Unclassified, Jan 2003.
186. S.O. Rice. Mathematical analysis of random noise. *Bell System Technical Journal*, 23:282–332, 1944.
187. S.O. Rice. Mathematical analysis of random noise. *Bell System Technical Journal*, 24:46–156, 1945.
188. M.V. Ricketts and P.A. Gale. On motions, wetness and such: The USS MIDWAY blister story. *Trans. SNAME*, 97:., 1989.
189. G. N. Roberts. A method to determine the applicability of rudder roll stabilization for ships. *In Proc. of IFAC World Congress*, 5:405–408, 1993.
190. G. N. Roberts. A note on the applicability of rudder roll stabilization for ships. *In Proc. of ACC, San Francisco, California, USA*, pages 2403–2407, 1993.
191. G.N. Roberts, M.T. Sharif, R. Sutton, and A. Agarwal. Robust control methodology applied to the design of a combined steerign/stabiliser system for warships. *IEE Proc. Control Theory Applications*, 144(2):128–136, 1997.
192. J.B. Roberts and P.D. Spanos. *Random vibration and statistical linearization*. John Wiley and Sons, 1990.
193. H. Rosenbrock and P. McMorran. Good, bad, or optimal? *IEEE Trans. on Automatic Control*, pages 552–554, 1971.
194. A. Saberi and P. Sannuti. Cheap and singular controls for linear quadratic regulators. *IEEE Trans. on Automat. Contr*, 32(3):208–219, 1987.
195. N. Salvesen, E.O. Tuck, and O.M. Faltinsen. Ship motions and sea loads. *Trans. The Society of Naval Architects and Marine Engineers–SNAME*, 10:345–356, 1970.

196. M. Sasaki, H. H. Oda, Y. Seki, K. Ohtsu, and T. Hotta. Actual experiences in designing rudder roll control systems. *In Proc. of IFAC Conference on Control Applications of Marine Systems–CAMS*, 1992.
197. O. Schlick. Gyroscopic effects of flying weels on board ships. *Transactions of The Institution of Naval Architects INA*, 1904.
198. F.H. Sellars and J.P. Martin. Selection and evaluation of ship roll stabilization systems. *Marine Technology, SNAME*, 29(2):84–101, 1992.
199. M. Serón, J. Braslavsky, and G.C. Goodwin. *Fundamental Limitations in Filtering and Control*. Springer, 1997.
200. M. Serón, J. A. De Doná, and G. C. Goodwin. Global analytical model predictive control with input constraints. In *Proc. of the 39th Conference on Decision and Control, Sydney, Australia*, 2000.
201. M.M Serón, J. H. Braslavsky, P.V. Kokotović, and D.Q. Mayne. Feedback limitations in nonlinear systems: From Bode integrals to cheap control. *IEEE Trans. on Automatic Control*, 44(4):829–832, 1999.
202. J.N. Sgobbo and M.G. Parsons. Rudder/fin roll stabilization of the USCG WMEC 901 class vessel. *Marine Technology*, 36(3):157–170, 1999.
203. A.A. Shabana. *Dynamics of Multibody Systems*. Cambridge University Press, 2nd edition, 1998.
204. J.S. Shamma and K.Y. Tu. Output feedback for systems with constraints and saturations: scalar control case. *System Control Letters*, 35:265–293, 1998.
205. M.T. Sharif, G.N. Roberts, and R. Sutton. Robust fin/rudder roll stabilization. *Proc. IEEE 3rd Conference on Control Applications*, 2(.):1107—1112, 1994.
206. M.T. Sharif, G.N. Roberts, and R. Sutton. Sea-trial experimental results of fin/rudder roll stabilization. *Control Eng. Practice*, 3(5):703—708, 1995.
207. M.T. Sharif, G.N. Roberts, and R. Sutton. Final experimental results of full scale fin/rudder rudder roll stabilisation sea trials. *Control Engineerign Practice*, 4(3):377–384, 1996.
208. C.D. Simonsen. *Rudder, propeller and hull interaction by RANS*. PhD thesis, Dept. of Naval Architecture and Offshore Eng., Technical University of Denmark, 2000.
209. R.E Skelton. *Dynamic Systems Control: Linear Systems Analysis and Synthesis*. Wiley, New York, 1988.
210. S. Skogestad and I. Postlethwaite. *Multivariable Feedback Control*. Wiley, 1996.
211. A.J. Sørensen. Structural properties in the design and operation of marine control systems. *IFAC Journal on Annual Reviews in Control*, 2005.
212. M.T. Srarif, G.N. Roberts, S.A. French, and R. Sutton. Lateral force stabilization: A comparison of controller designs. In *10th Ship Control System Symposium SCSS*, volume 5, pages 149–169, 1993.
213. M. St Denis and W.J. Pierson. On the motion of ships in confused seas. *SNAME Transactions*, 61:280–332, 1953.
214. J. Stoustrup, H.H. Niemann, and M. Blanke. A multi objective $\mathcal{H}_\infty$ solution to the rudder roll damping problem. In *Proc. of CAMS'95*, 1995.
215. R. Taggart. Anomalous behavior of merchant ship steering systems. *Marine Technology*, April:205–215, 1970.
216. A. Tang and P.A. Wilson. Lateral force estimator stabilization. In *IFAC CAMS*, 1992.
217. A. Tang and P.A. Wilson. Ship stabilization using lateral force estimator. *The Naval Architect, RINA*, 1992.

218. A. Tang and P.A. Wilson. LFE stabilization using rudder. In *IFAC MCMC*, 1992.
219. H. Tanguy, G. Lebret, and O. Doucy. Multi-objective optimisation of pid and h_∞ fin/rudder roll controllers. In *5th IFAC Conference on Manoeuvring and Control of Marine Craft MCMC'03*, 2003.
220. M.J. Tucker. *Waves in Ocean Engineering: Measurement, Analysis, Interptretation*. Ellis Horwood, 1991.
221. C.-Y. Tzeng, C.-Y., and Y-L Chu. A sensitivity function approach to the design of rudder roll stabilization controller. *Journal of Marine Science and Technology*, 9(2):100—112, 2001.
222. C.-Y. Tzeng and C.-Y. Wu. On the design and analysis of ship stabilizing fin controller. *Journal of Marine Science and Technology*, 8(2):117—124, 2000.
223. J. van Amerongen. *Adaptive steering of ships–A model reference approach to improved maneouvering and economic course keeping*. PhD thesis, Delft University of Technology, The Netherlands., 1982.
224. J. van Amerongen and J.C. van Cappelle. Mathematical modelling for rudder roll stabilization. In *Proc. of 6th Ship Control System Symposium SCSS*, 1981.
225. J. van Amerongen, P. van der Klugt, and H. van Nauta Lemke. Rudder roll stabilization for ships. *Automatica*, 26:679–690, 1990.
226. J. van Amerongen and H.R. van Nauta Lemke. Optimum sterring of steering of ships with an adaptive autopilot. In *Proc. of 5th Ship Control system Symposium—SCSS, Anapolis, USA*, 1978.
227. P.G.M van der Klught. *Rudder roll stabilization*. PhD thesis, Delft University of Technology, The Netherlands, 1987.
228. P.G.M. van der Klugt. *Rudder roll stabilization*. PhD thesis, Delft University of Technology, The Netherlands., 1987.
229. F.F. van Gunsteren. Analysis of roll stabilizer performance. *Trans. of The Society of Naval Architects and Marine Engineers*, 21:125–146, 1974.
230. J. Vasta, A.G. Giddings, A. Taplin, and J.J. Stilwell. Roll stabilization by means of passive tanks. *Transactions of The Society of Naval Architects and Marine Engineers SNAME*, 69:411–439, 1961.
231. F. Warhurst. Evaluation of the performance of human operators as a function of ship motion. Report 2828, Naval Ship Research and Development Centre, 1969.
232. P. Watt. On a method of reducing the rolling of ships at sea. *Trans. of the Institution of Naval Architects*, 24, 1883.
233. P. Watt. The use of water chambers for reducing the rolling of ships at sea. *Trans. of the Institution of Naval Architects*, 26, 1885.
234. W.C. Webster. Analysis of the control of activated anti-roll tanks. *Transactions of Society of Naval Architects and Marine Engineers*, 75, 1967.
235. G. Weinblum and M. St. Denis. On the motion of ships at sea. *Trans. SNAME*, 1950.
236. Sir A. Wescostt. *The Papers of William Froude* M.A. LL.D. F.R.S. *1810–1879*, chapter The Papers of William Froude M.A. LL.D. F.R.S. A Memoir, pages xi—xiii. The Institution of Naval Architects, 1955.
237. L.F. Whicker and L.F. Fehlner. Free stream characteristics of a family of low aspect ratio control surfaces for application to ship design. Report 933, DTRC, 1958.
238. Sir W. White. Experiemts with Dr. Schlicks's gyroscopic aparatus for steading ships. *Transactions of The Institution of Naval Architects INA*, 1907.

239. A.G. Wills. *Barrier Function Based Model Predictive Control*. PhD thesis, School of Electrical Eng. and Comp. Science, The University of Newcastle, Australia, 2003.
240. C. Yang and M. Blanke. Rudder roll damping controller design using μ synthesis. *In Proceeding of IFAC CAMS'98*, pages 127–132, 1998.
241. W.-W. Zhou, D.B. Chercas, and S. Calisal. Identification of rudder-yaw and rudder-roll steering models using prediction error techniques. *Optimal Control Applications and Methods*, 15:101–114, 1994.
242. W.W. Zhou, D. Chercas, S. Calisal, and A. Tiano. A new approach for adaptive rudder roll stabilisation control. *Proc. of the 9th Ship Control System Symposium*, 1:115–127, 1990.
243. G. Zhu, M.A. Rotea, and R.E. Skelton. A convergent feasible algorithm for the output covariance constraint problem. In *30th American Control Conference*, pages 1675–1679, 1993.
244. M. Zoccola and E. Baitis. Division-patented rudder roll stabilization system invention honored by CNR. Wavelengths online; Official publication of Naval Surface Warfare Center Carderock. http://www.dt.navy.mil/pao/wavelengths/waves1999.html, 1999.

Index